Caribbean Sea Level Change: observational analysis from millennial to decadal timescales

Luke Peter Jackson

Submitted in accordance with the requirements for the degree of
Doctor of Philosophy

The University of Leeds
School of Earth and Environment
4th November 2013

Declaration

The candidate confirms that the work submitted is his own and that appropriate credit has been given where reference has been made to the work of others.

Acknowledgements

My first thanks go to Him who is not visible, but who walks beside me. To Him, whose Spirit lives in my heart and is my hope and my cornerstone. To Him be the glory, the splendour and the majesty. For everything in heaven and on Earth is yours. All things come from you. I pray this work would be acceptable in your sight, Father, Son and Holy Spirit. Amen.

At times during this project, I have felt as if I have been ploughing a lonely furrow by studying sea level change at Leeds. However, this could hardly be further from the truth. Thank you Jon. You have been a wonderful supervisor, full of patience, kindness and wisdom. Thank you also to Greg and Andy, who have grilled me a few times to make sure I really do know what I'm talking about. Thanks to the other members of the great post-graduate fraternity, especially Sandra, Barbara, Tom, Julia, Hannah, Paddy, Matt and Andy.

Thank you to my brothers and sisters in Christ. You have been Christlike and for that there is no need to say more.

Lastly, to my dear wife Sara and little Sam. You are the lights of my life. Thank you for helping me to enjoy research and study, for keeping me grounded and loved.

Abstract

Sea-level rise continues to be an issue of societal concern. It is a fact that millions of people live close to the coast and will be at risk both directly and indirectly from sea-level rise. Understanding the future begins in the past and so this thesis considers Holocene and modern sea-level variations in the Caribbean region, an area particularly at risk from long term sea-level rise.

I construct a catalogue of 561 published Holocene sediment ages and depths, primarily fossil corals and mangrove peats. I derive probability distributions of the habitable ranges of corals and peat using modern growth and abundance records. These distributions are used to simulate realisations of sea-level position in the past. The relative sea-level (RSL) position and RSL rate are calculated at 500 year time slices to construct sub-regional sea-level histories. At each time slice, I select the realisations that fall within a 2000 year time window and calculate the least-squares estimate of RSL rate and RSL position. Results show Caribbean wide spatio-temporal RSL changes. From 7000 to 4000 cal yr BP, RSL rates were $\sim$2 mm yr^{-1} in the north (Cuba and Florida), $\sim$1 mm yr^{-1} in the east (Lesser Antilles and US Virgin Islands) and $\sim$2.5 mm yr^{-1} in the south west. From 4000 to 1000 cal yr BP, sea level rose between 3 (US Virgin Islands, Venezuela and Trinidad) and 5 metres (Florida, Belize). During the last 1000 years, RSL rates fell below 1 mm yr^{-1} and by 500 cal yr BP lay between 0 to 0.5 mm yr^{-1}.

The spatial variation between sub-regional RSL histories is also investigated by using a spherically symmetric, rotating numerical model that simulates sea-level change and vertical ground motion (VGM). I derive model RSL histories at the sub-regions in the Caribbean using a single deglaciation model and a range of earth parameters. By minimising the misfit of the model RSL curves to the data driven RSL curves, I find a representative model fit where lithospheric thickness is 71 km, upper and lower mantle viscosities are 0.5 and 10 $\times$ 10^{21} Pa s respectively.

To find the change in sea-level rise in modern (1960 to 2012) times compared to the late Holocene, I calculate RSL and absolute sea-level (ASL) rates using 49 tide gauge records and satellite altimetry. I apply three corrections to remove seasonal and regionally coherent noise and calculate a least-squares estimate of sea-level change. Results show that present day RSL rise is up to three times greater than in the late Holocene, though there remains a small ($\leq$ 1 mm yr^{-1}) long term contribution from the last deglaciation. For individual sites, I found that variations in VGM can exacerbate long term sea-level change enhancing the risk of coastline communities.

Contents

List of Figures

List of Tables

Chapter 1

Introduction

The waters rose and increased greatly on the earth. (Genesis 7:18)

Sea-level rise remains a pressing societal concern given the significant proportion of the global population that live on or near the coastline. Developing a full scientific understanding of how sea level has changed and is changing over the full spectrum of time scales (millions of years to hours) is critical to informing policy makers and the wider non-academic community of the complexity and potential risk of sea-level rise.

Over the longest timescales sea level is dictated by the formation and breakup of continents (200 - 400 Myr, Miall (1990)). Over the shortest timescales, sea-level changes due to tidal variations that occur over minutes and hours caused by ocean-atmosphere interaction and the Moon orbiting the Earth. In between the two ends of the spectrum lie numerous cycles, which include the glacial-interglacial that occurs roughly every 100,000 years. The last deglaciation of ice sheets (at high latitudes, primarily the Northern hemisphere) occurred from ∼21,000 to ∼1,000 years before present (BP) and caused a spatio-temporally varying sea-level change (average change ∼+120 m) and land uplift/subsidence. These global scale changes are augmented by local variations depending upon the location on the Earth. These local variations include the local coastal environment, tides, vertical ground motion caused by local tectonics, ocean temperature and salinity.

Changes in sea level at millennial timescales are recorded by fossils, sediments, uplifted shorelines, erosion features, and more recently archaeological remains (Pirazzoli, 1991). In the tropics, fossil corals and mangrove sediments (peat) dominate the record of past sea-level change.

Over the last century, the time resolution at which sea-level change can be recorded

has increase markedly. Tide gauges measure relative sea-level (RSL) change, that is sea level observed from a land-based reference frame. Satellite altimeters measure absolute sea-level (ASL) change, that is sea level observed outside the land-based reference frame. These two instruments provide detailed records of short timescale variations, which can primarily be attributed to climate-ocean interactions. By performing time series analysis upon such time series, it is possible to learn about long timescale variations, for example the effect of the last deglaciation. Such evidence shows modern global mean sea-level rise, which amounted to 1.8 mm yr^{-1} in the 20^{th} century (Church et al., 2004) and 3.4 mm yr^{-1} for the last 20 years (Nerem et al., 2010).

Table 1.1 shows a list of the major contributing factors to global sea level (as of 2007) in the form of a budget as compared to observed changes. Estimates of the thermal expansion contribution account for almost a third of the global budget from 1961 - 2003 and 1993 - 2007. Both thermal expansion and total ice sheet contributions have risen since the end of the 20^{th} century. The focus of my thesis is to try to quantify the spatio-temporal variations in sea level caused by these contributions across the Caribbean region from the Holocene to the present.

Table 1.1: Contributors to global mean sea-level rise for tide gauge and satellite eras

Source	Mean Sea-Level Rise (mm yr^{-1})		
	1961–2003	1993–2007	2003–2007
1. Thermal Expansion	0.42 ± 0.12	1.0 ± 0.3	0.25 ± 0.8
2. Glaciers & Icecaps	0.5 ± 0.18	1.1 ± 0.25	1.4 ± 0.25
3. Greenland Ice Sheet	0.05 ± 0.12		
4. Antarctic Ice Sheet	0.14 ± 0.41		
5. Total Ice Sheets	0.19 ± 0.53	0.7 ± 0.2	1.0 ± 0.2
6. Land Water	–	–	-0.2 ± 0.1
Sum (1 + 2 + 5 + 6)	1.1 ± 0.5	2.85 ± 0.35	2.45 ±0.85
Observed	1.8 ± 0.5	3.3 ± 0.4	2.5 ± 0.4

Source: 1961–2003: IPCC 2007 (Solomon et al., 2007), 1993–2007 and 2003–2007: Cazenave and Llovel (2010)

1.1 Study area: the Caribbean

The region I am investigating is centred upon the Caribbean, shown in Figure 1.1. I include in my study the Southern half of Florida (south of 27^oN), the eastern part of the Gulf of Mexico, the extreme western part of the Atlantic Ocean and the Caribbean

Sea. Although the Pacific Ocean is important to global sea-level variation, only the climatic effects associated with it are used and it is not discussed at any length in the text. The following three sections outline, in a simplified manner, the tectonic setting, climate, and risk due to sea-level rise of the Caribbean.

1.1.1 Tectonics

The region defined then, covers a surface area of ∼7,257,000 km^2, the Caribbean Sea covering ∼2,754,000 km^2 similar to that of the Mediterranean. An extensive diversity of tectonic regimes characterises the Caribbean. Figure 1.1 shows the seven plates lying adjacent to one another. Zones of deep earthquakes coupled with volcanic arcs indicate the presence of subduction of the Cocos plate beneath the Caribbean plate and the Atlantic plate beneath the Caribbean plate (forming the Lesser Antilles). Shallow seismicity and geodetic studies indicate transform fault and pull-apart basin tectonics between Caribbean and North American (which is deemed stable) plates (e.g. Mann et al. (2002), Benz et al. (2011), DeMets et al. (2010)). This shallow seismicity has resulted in a number of damaging earthquakes including the 12$^{\text{th}}$ January 2010, 7.0 moment magnitude event at Port-au-Prince, Haiti that killed an estimated 300,000 people (*earthquake.usgs.gov*). There are complex plate interactions between the South American, Panama, North Andean and Caribbean plates in the south giving rise to subduction, transform and spreading boundaries.

The summary above shows that active tectonics occur in the study region, therefore local sites may be subject to uplift and deflection. This is important to note as these changes can be direct contributors to observed sea-level rise or fall.

1.1.2 Ocean-Atmosphere Climate

The Caribbean Sea is a semi-enclosed sea, separated from the Atlantic Ocean by the Greater Antilles in the north and the Lesser Antilles in the east. Seasonal variability in the region is dominated by the Inter-Tropical Convergence Zone (ITCZ), which controls wind and rainfall (Torres and Tsimplis, 2012). The trade winds (Caribbean Low Level Jet, CLLJ) enter the region from the south east and tend to follow the South American coast before turning north towards the Yucatan Straits. Fresh water outflow is significant in the South Colombia Basin from the Magdalena and Atrato Rivers.

The Caribbean current, that dominates ocean circulation in the region, begins where

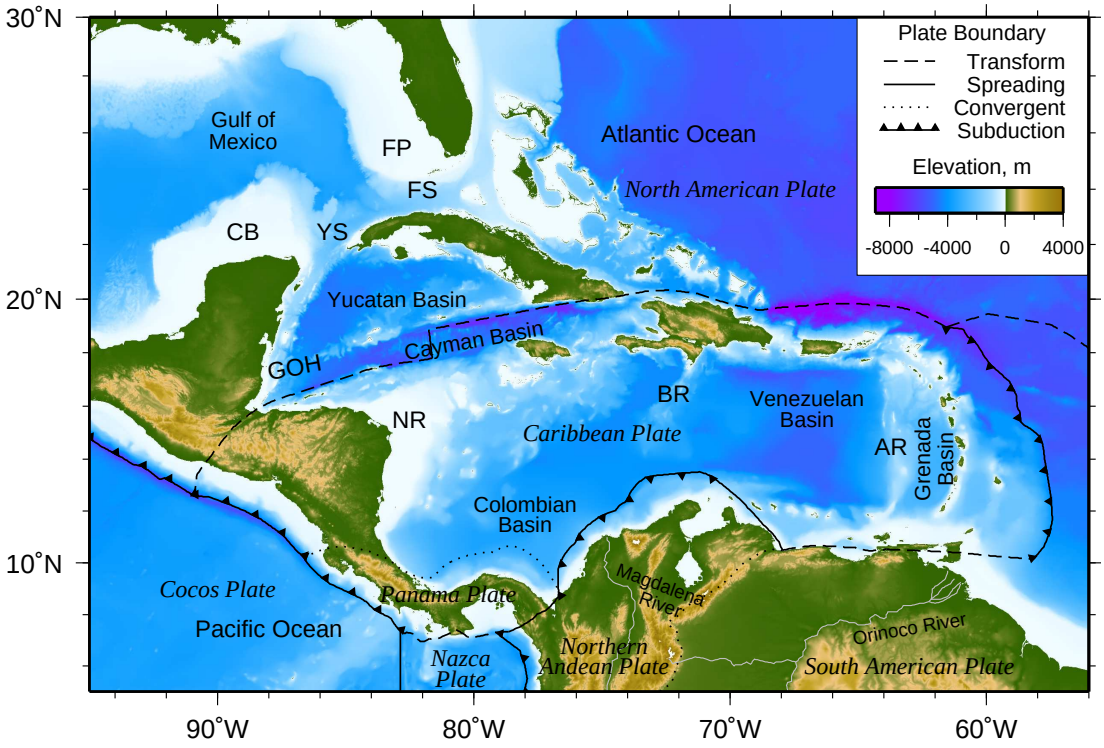

Figure 1.1: Topography, bathymetry and tectonic map of Caribbean region. Topography and bathymetry from GEBCO 1 arc-minute gridded data from *http://www.bodc.ac.uk/*. Acronyms: FP, Florida Platform; FS, Florida Shelf; YS, Yucatan Strait; CB, Campeche Bank; GOH, Gulf of Honduras; NR, Nicaragua Rise; BR, Beata Ridge; AR, Aves Ridge. Tectonic plates labelled in italics.

the Guyana Current flows into the Lesser Antilles and continues westward along the northern coast of South and Central America (Torres and Tsimplis, 2012). The current then flows north into the Gulf of Mexico through the Yucatan Chanel, where it is called the Yucatan Current. The Panama-Colombia gyre dominates the circulation in the South of the Colombia Basin, but its structure and variability is not well understood. The region generally exhibits a micro-tidal range of around 0.5 m (Kjerfve, 1981, Granger, 1985, Hill et al., 2011) though this can vary according to the coastal setting.

Laying as it does in the tropics, the Caribbean has a climate that is generally warm and humid. Rainfall occurs seasonally from May to November. With long term increases in temperature due to climate change, comes an inevitable increase in precipitation, though there are uncertainties about how this might vary spatially. This is combined with the risk from hurricanes (May to October) across the region, which is certainly the most feared hazard in the present climate (Biasutti et al., 2012).

1.1.3 Climate Change Risk

The Intergovernmental Panel on Climate Change (IPCC 2007: Parry et al. (2007)) identified the Caribbean as being at risk to sea-level rise and exposure to geological and hydro-meteorological disasters (earthquakes and tsunamis, hurricanes and storm surges). Below is a summary of the risks highlighted by IPCC 2007 for the regions of interest to this study.

1. Small Islands (Mimura et al., 2007)

    - The vulnerability of islands of limited size and that lie in regions currently at risk from natural hazards will only be enhanced due to climate change. In most cases they have low adaptive capacity, and adaptation costs are high relative to gross domestic product.
    - Almost without exception, international airports, roads and capital cities in the small islands of the Caribbean are sited along the coast or on tiny coral islands. Sea-level rise will exacerbate inundation, erosion and other coastal hazards, threatening vital infrastructure.
    - Climate change is likely to heavily impact coral reefs, fisheries and other marine-based resources.
    - The effects of climate change on tourism are likely to be both direct and indirect, and largely negative.

2. Florida and Gulf of Mexico (Field et al., 2007)

    - Sea-level rise will exacerbate the impacts of progressive inundation, storm-surge flooding and shoreline erosion. Storm impacts are likely to be more severe.
    - Salt marshes, other coastal habitats, and dependent species are threatened by sea-level rise, fixed structures blocking landward migration, and changes in vegetation.
    - Population growth and the rising value of infrastructure in coastal areas increases vulnerability, whilst current adaptation is uneven and readiness for increased exposure is low.

3. South and Central America (Magrin et al., 2007)

    - With most of their population, economic activities and infrastructure located at or near sea-level, coastal areas will be very likely to suffer floods and erosion, with high impacts on people, resources and economic activities.
    - Coral reef and mangroves are expected to be threatened, with consequences for a number of endangered species: e.g., the green, hawksbill and loggerhead turtles, the West Indian manatee, and the American and Motelet's species of crocodile.

Further syntheses of risk due to climate change in the Caribbean, Florida and Gulf of Mexico have been made by Stanton and Ackerman (2007), Bueno et al. (2008), Simpson et al. (2010) and Biasutti et al. (2012). Table 1.2 shows the difference between the potential cost caused by high-impact ("business as usual") and low-impact ("rapid stabilisation") climate scenarios for a selection of regions across the Caribbean (Stanton and Ackerman, 2007, Bueno et al., 2008). The "rapid stabilisation" scenario can be summarised by 50% and 80% reduction in global and U.S. emissions by 2050, whilst rainfall and hurricane intensity remains constant. The "business as usual" case is summarised by increasing emissions following IPCC A2 scenario (sea-level rise 0.23 to 0.51 m, Solomon et al. (2007)), whilst rainfall patterns change and hurricane intensity increases.

Table 1.2: Cost of inaction in $US billions (2006: Florida and 2007: Caribbean) at 2050 AD, where cost is difference between high-impact and low-impact emission scenarios (see text).

Site	Cost due of various infrastructures, $ billions (total % of GDP)				
	Hurricanes	Tourism	Electricity	Real Estate	Summary
United States of America					
Florida	$25	$40	$5	$23	$92 (2.8%)
Selected Caribbean countries			Infrastructure		
Bahamas	$0.24	$0.31	$0.23		$0.80 (13.9%)
Cuba	$0.77	$0.38	$3.63		$4.78 (12.5%)
Saint Kitts & Nevis	$0.08	$0.02	$0.03		$0.13 (35.5%)
Trinidad & Tobago	$0.0	$0.06	$0.94		$1.01 (7.0%)
All Caribbean	$3.2	$2.8	$15.9		$21.9 (10.3%)

Source: Florida data, (Stanton and Ackerman, 2007) and Caribbean data, (Bueno et al., 2008)

The methods employed to calculate these costs use climate change models and static stereographic methods to calculate inundation of coastlines. These estimates demon-

strate the importance, financial and socio-economic, of accurately measuring and calculating sea-level change at the local scale. This accurate, numerically consistent approach must begin with the prehistoric record and extend to the present so that these results can be used as starting conditions for future projections.

1.2 Sea-level research in the Caribbean

There has been a wealth of published literature on sea-level change in the Caribbean over the timescales I consider. Here I highlight a few key publications, widening the discussion in forthcoming chapters.

Attempts to describe the sea-level history of the region using sea-level indicators culminated in the production of the Western Atlantic Sea-Level (WASL) curve (Toscano and Macintyre, 2003). This has come under much scrutiny, not least because the WASL curve uses sea-level indicators from sites across the Caribbean, averaging the compilation to a generic curve. This approach has some utility, but fails to acknowledge the unique conditions at each locality from which indicators were taken. Another important contribution to the sea-level literature is the sea-level record from Barbados (Fairbanks, 1989, Bard et al., 1990, Peltier and Fairbanks, 2006), which catalogues the entire deglacial history from 32,000 to 700 Cal years BP. The Barbados record has been used as a means of calculating global deglaciation histories (e.g. Tushingham and Peltier (1991), Peltier (2004)) because of its long continuous record and its position relative to the centres of deglaciation (North America, Scandinavia, Greenland and Antarctica).

The Barbados sea-level record moves one into the numerical applications to model sea level globally and regionally. Of particular note, the work by Milne et al. (2005) used sea-level indicators at specific locations in the Caribbean and the Atlantic coast of South America to find model parameters for their symmetrical, visco-elastic, rotating, shoreline migrating Earth model that simulates sea-level rise and land deformation due to GIA (Mitrovica and Milne, 2003). Recent work by Toscano et al. (2011a) has sea-level indicators from the US Virgin Islands to calibrate a new deglaciation model (ICE-6G, improved from ICE-5G Peltier (2004)) and test the latitudinal extent of the fore-bulge region (the area affected directly by inundation of melt-water from centres of deglaciation).

Regional sea-level changes in the Caribbean since 1950 have been explored by

Palanisamy et al. (2012) using tide gauge and satellite altimetry. This work sought to estimate sea-level trends and ocean-climate interactions. Palanisamy et al. (2012) found that mean sea-level rate closely aligned to the global mean sea-level rise of 1.8 mm yr^{-1}. Furthermore, the inter-annual mean sea level was strongly correlated with the El-Nino Southern Oscillation and hurricane activity (Palanisamy et al., 2012).

Work by Kjerfve (1981) and Torres and Tsimplis (2012) helped to describe the present seasonal sea-level signal, whilst Hill et al. (2011) modelled tidal variation in the Holocene across the region. Johnson and Purkey (2009) conducted a numerical ocean modelling experiment for the Caribbean Sea and suggested that deep sea warming contributes about 1.2 mm yr^{-1} of sea-level rise in areas with bottom depths around 5000 m.

1.3 Contributions and Outline of Thesis

This thesis contributes to knowledge of sea-level change in the Caribbean at two timescales, millennial and decadal. There is insufficient data available to make specific comments upon century scale variations since tide gauges and satellite altimetry are too short in their time extent and geological records (coral and mangrove sediments) are not of sufficient quality or time resolution.

The thesis is separated into this introduction, four "research and discussion" chapters and a summary chapter. Chapter 2 introduces the prehistoric data available and describes and executes a method to construct sea-level histories at 500 year time slices for sub-regions across the Caribbean. The purpose of the chapter is to derive a sea-level history from sea-level data numerically, rather than relying upon qualitative assessments (e.g. Toscano and Macintyre (2003)). Chapter 3 utilises these local sea-level histories to ascertain the optimal model parameters (lithospheric thickness, upper and lower mantle viscosity) for use in an Earth model that simulates sea-level rise and land deformation due to a global deglaciation history. Chapter 4 considers the sea-level change across the Caribbean during the 20^{th} and 21^{st} Centuries. I use a series of numerical corrections on tide gauge and satellite altimetry time series to remove short timescale sea noise (e.g. seasonal and annual cycles; 6 and 12 months). I estimate long term rates of sea-level change from the time series. In Chapter 5, I synthesise the results from Chapters 2, 3 and 4 to assess the difference between prehistoric and modern sea-level change, the difference between model versus observed sea-level change

and vertical ground motion and if the modern budget for sea-level rates can be closed. Finally, I summarise sea-level change across the Caribbean over the last 10,000 years, discuss the shortcomings of this research, suggest a series of implications and impacts of sea-level rise upon the Caribbean, and recommend areas for further research.

Chapter 2

Sea-level change since the Last Glacial Maximum

2.1 Introduction

The last 20,000 years of sea-level change are the best recorded of pre-instrumental history. Many publications have focused upon the Western Atlantic and its sub-regions (Lighty et al., 1982, Digerfeldt and Hendry, 1987, Boardman et al., 1989, Fairbanks, 1989, Blanchon and Shaw, 1995, Toscano and Macintyre, 2003, Gischler and Hudson, 2004, Blanchon, 2005). These studies use *in situ* coastal and near shore marine deposits, which have a known relationship to the position of sea level due to their tidal range, habitable depth or minimum elevation (Toscano and Macintyre, 2003). By ascertaining the sample age and depth relative to present day sea level, non-numerical by-eye curves are used to define sea-level rise histories.

In this chapter, I investigate the spatial variations of sea-level change in the Caribbean by constructing local sea-level curves using a probabilistic method. I collate, quality control and calibrate observations from more than 60 publications in the Caribbean. By performing age calibration, these data can be combined with TIMS U/Th dated samples to extend the catalogue for this region (e.g. Toscano and Lundberg (1998), Toscano and Macintyre (2003)). Each age has an associated probability distribution function. I then devise probability distribution functions (pdf) to describe the habitable range of different coral species and different types of mangroves. These pdfs are used to construct multiple data sets by randomly sampling the time and depth distributions many times. I then apply a numerical method to calculate the elevation and rate of sea level and sea-level rise in different time windows. This methodology is used

for small geographical regions of the original data set to study regional variations in sea-level position and sea-level rise.

The curves produced are relative to land motion (i.e. relative sea-level curves); assumptions are not made about tectonic stability in the Caribbean (a micro-plate surrounded by subduction, extension and transform zones). Tectonic signals may exist for the solutions presented that affect the region at a variety of length scales, from thousands of kilometres (isostatic adjustment) to tens of metres (faults) (Mann et al., 1990, McCann and Pennington, 1990).

2.2 Sea-level indicators

A sea-level indicator is an organic or inorganic object, which lies in a stratified context and has a depth relationship to the position of sea level. Man-made indicators (e.g. Roman fish tanks, Lambeck et al. (2004)) whose position was designed to be at a specific elevation relative to the sea level allow one to accurately (within 25 cm) position sea level in the past. Similarly, natural indicators (e.g. corals, mangroves and certain molluscs) have habitable depth/elevation ranges, which can be tied (within metres) to the position of sea level. By ascertaining the age, and understanding the vertical position of these organic materials, one can attempt to reconstruct sea-level position in the past.

The indicators around the Caribbean come from different localities, which lie in a variety of tectonic settings and have experienced varying degrees of glacio-isostatic adjustment. Some localities contain multiple types of indicators whilst others only contain one. Different indicators have different relationships to past sea-level position. Critical to the selection and use of indicators are detailed published descriptions of the essential features of their growth (Davies and Montaggioni, 1985). The numerical method for the sea-level curve construction is based upon a regression method that fits the indicator data while explicitly respecting habitable uncertainty.

2.2.1 Coral

Coral reefs are resistant structures that stand above their surroundings and exert an influence over local ocean circulation (Hubbard, 2009). They distribute themselves (in patterns) radially off-shore to form reef complexes ((Goreau and Goreau, 1973): Figure 2.1). They might emerge as fringing and barrier reefs or form submerged features

along shelf margins (e.g. Gischler and Hudson (2004), Hubbard et al. (2005)). Since corals do not live in a sufficiently narrow depth range it is important to devise a quantitative vertical distribution based on species growth and distribution across the reef complex related to wave energy (Davies and Montaggioni, 1985), water depth (Huston, 1985), salinity and sediment influx (Cuevas et al., 2009). Furthermore, corals will never live above sea level although tidal variation can be a factor. This is not significant in the Caribbean where present-day tidal ranges are <0.5 m (Kjerfve, 1981, Weiss, 1979). The variation of depth habits for a single species demonstrates that fossil corals are in most cases indicative, rather than definitive of sea-level position (Lambeck et al., 2010).

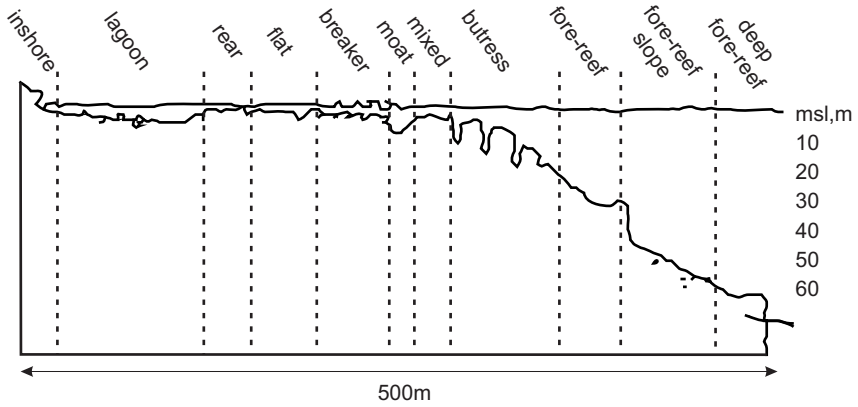

Figure 2.1: Typical reef complex profile showing different zones with their related water depth, after Goreau and Goreau (1973)

2.2.2 Mangroves

Mangrove sediments indicate pre-historic shoreline locations in sheltered tropical environments. Mangroves generally grow inter-tidally, they are often restricted within the tidal range and deposits are usually *in situ*. The dominant species of mangrove in the Caribbean Sea is *Rhizophora mangle*, though others include *Conocarpus erectus* and *Cladium jamaicense*. These species generally grow at or within 1 m above sea-level (Figure 2.2), though there are possibilities of errors due to the potential effects of root penetration (up to 1 m; Woodroffe (1981)), compaction and subsidence. A way of mitigating these effects is using samples taken from within 1m of a pre-Holocene (basal) surface.

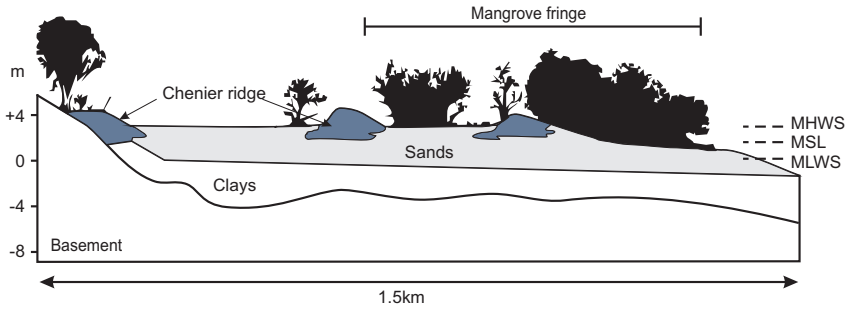

Figure 2.2: Near shore profile with mangroves at (or above sea level) (typical *Rhizopora mangle* location) after Barham and Harris (1983). MHWS: mean high water springs; MSL: mean sea level; MLWS: mean low water springs

2.2.3 Other indicators

Though mangroves and corals dominate sea-level indicator information, other indicators exist. These include shells of clams (e.g. *Tagelus plebius*), mussels (e.g. *B. modiolus*) and oysters (e.g. *I. alatus*), wood and leaf fragments. Most of the shell samples found lived in the swash-zone, that is the high to low tide range, which in the Caribbean is less than 0.5m (Weiss, 1979, Kjerfve, 1981). Some publications utilise these samples in sea-level curve construction (e.g. Gischler and Hudson (1998), Macintyre et al. (2004)). However, the reworking and movement of shell fragments up or down slope after deposition means there is more uncertainty about the position of these indicators relative to former sea level than either mangroves or corals. Therefore, I choose to reject all wood, leaf and shell samples with one exception. The exception is a shell that lies within a narrow peat deposit on the Holocene/Pleistocene interface (Boardman et al., 1989).

The final indicator is archaeological, from a fire pit in a limestone cave near the Mexican Caribbean coast now submerged by salt water (Coke et al., 1991). This indicator is used since its position was at terrestrial limiting elevation relative to past sea level.

2.3 Data around the Caribbean

There are more than 60 publications documenting Late-Pleistocene and Holocene coastal marine deposits in the Caribbean region. The following discussion outlines the dated Holocene marine deposits available in the literature to the best of by knowledge and

explains what data I retain for my catalogue following the criteria of no wood, leaf or shell fragments, no peat samples obviously emplaced or affected by compaction and no coral samples not in situ. Appendix A lists these sea-level indicators, their age and depth relative to present mean sea level. The data are either corals or mangrove peat deposits with two exceptions that are justifiable to use as sea-level indicators. Figure 2.3a shows the data presented in this study and the sub-regions (boxes) into which they are grouped. The Colombian coastline is extremely poorly sampled. The only data I could find available was a palaeontological study from four uplifted marine terraces (Martínez et al., 2010). Furthermore, my extensive survey of the literature found no publications for coastal marine deposits along the coast of Costa Rica, Honduras and Guatemala (south west Caribbean).

2.3.1 Florida

The Florida region has been systematically sampled along the length of its reefs, from Tortugas in the west to Miami in the north east (Figure 2.3b). Furthermore, the swamp regions of the Everglades and central Florida Keys contain mangrove deposits that are well preserved.

Shinn et al. (1977) sampled Holocene corals at eight coral reefs from Dry Tortugas to Carysfort along the Southern Florida Keys. Most of the coral reefs along the Florida Keys are localised by pre-existing Pleistocene topography. Toscano and Lundberg (1998) sampled three reef tracts in south-east Florida (Two at Sand Keys and one at Carysfort). This and other head corals, from reef crest, shallow back-reef and deeper fore-reef facies fill a time gap between late Holocene peats and early Holocene corals. Acropora palmata (hence forth, *A palmata*) framework corals form a minor part of the Holocene reef portions (Shinn et al., 1977, Toscano and Lundberg, 1998)). Although Toscano and Lundberg (1998) corrected sample depths for subsidence in Florida (0.015 mm yr^{-1}: Mullins and Neumann (1979)), I use the uncorrected depths since no other data in the region have been corrected.

Further east, Lighty et al. (1978) sampled a relict oceanic reef (Shelf Edge Reef), ∼40 km north off-shore Miami and ∼95 km long, which is thought to have ended its growth (primarily *A palmata*) when the shelf region was inundated in the early Holocene. *A palmata* samples are also available from Upper Florida Keys (*Precht et al.,* unpublished in Toscano and Macintyre (2003)).

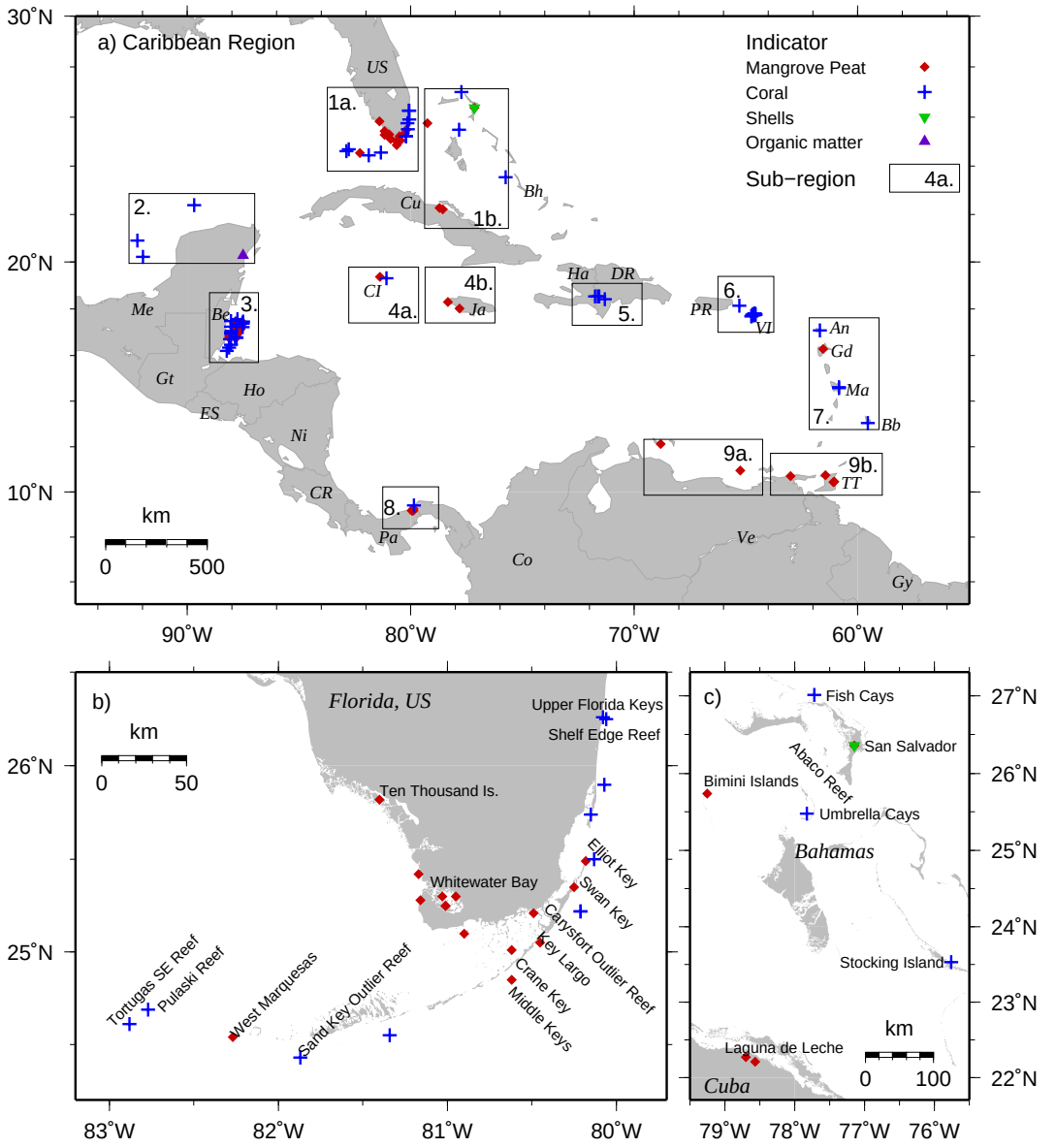

Figure 2.3: Late Pleistocene and Holocene coastal marine samples from publications for, **a**: whole Caribbean, **b**: Florida and **c**: Bahamas/North Cuba region. In **a**, boxes represent sub-regions used in this analysis. Acronyms for countries (clockwise): US, United States of America; Bh, Bahamas; Cu, Cuba; Ha, Haiti; DR, Dominican Republic; CI, Cayman Islands; Ja, Jamaica; PR, Puerto Rico; VI, US Virgin Islands; An, Antigua; Gd, Guadeloupe; Ma, Martinique; Bb, Barbados; TT, Trinidad & Tobago; Gy, Guyana; Ve, Venezuela; Co, Colombia; Pa, Panama; CR, Costa Rica; Ni, Nicaragua; Ho, Honduras; ES, El Salvador; Gt, Guatemala; Be, Belize; Me, Mexico

In the central Florida Keys, mangrove (Rhizophora mangle) deposits were sampled by Robbin (1984) (Elliot to Middle Keys and West Marquesas: Figure 2.3b) and their habitable range is controlled by the tidal range (± 0.5 m). To the north in the Everglades, the incursion of marine water into fresh-water swamps brings about the deposition of mangrove peat over calcitic mud along the banks of penetrating waterways (Scholl and Stuiver, 1967). This contact forms over a vertical range of 0.0 to 0.12 m above sea level in back swamp areas where tidal range is less than a few centimetres and the environment is essentially fresh water. With a rise in sea level, deposition of mangrove peat spreads landward over fresh-water deposits. Scholl and Stuiver (1967) sampled these deposits between Ten Thousand Islands and Whitewater Bay (Figure 2.3b), identifying mangrove/fresh water peat contacts to give ages of former sea-level positions.

Peat samples at Crane Key are from Rubin and Suess (1955) (in Woodroffe (1981)). Woodroffe (1981) add that Rhizophora communities begin in water less than 0.6 m deep and are easily established in sediments with thick growths of turtle grass and algae.

The mangrove and fresh water peat are marine and terrestrial limiting data respectively. I removed samples that appeared to be vertically inconsistent compared to others at the same depth. These are likely to be root contaminated samples, caused by roots from above growing down into older sediments. I also removed organic matter, sand and shell deposits whose life position though theoretically well constrained by surrounding samples cannot be defined certainly.

2.3.2 Bahamas

Boardman et al. (1989) use a peat-on-bedrock approach to measurement to minimise problems with compaction for their peat samples on San Salvador (Figure 2.3c). In addition to these measurements, I use a shell indicator from a peat-on-bedrock position Boardman et al. (1989).

Woodroffe (1981) include peat samples from Broecker and Kulp (1957) (Bimini Islands) and Toscano and Macintyre (2003) use *A palmata* samples published in Lighty et al. (1982) (Fish and Umbrella Cays).

A coral-algal ridge reef complex at Stocking Island was sampled by Macintyre et al. (1996). Four coral and nine gastropod samples were dated in cores spanning fore-reef to back-reef. The corals sampled here are framework based (Montastrea and Porites,

in shallow habitable range). I include the corals but exclude the gastropod samples.

Although some research suggests the Bahamas is undergoing measurable subsidence (0.02 mm yr^{-1}: Carew and Mylroie (1995)), I use uncorrected depths to maintain regionally consistent relative sea-level rise, particularly between the Bahamas and Florida, which shall also be grouped together (1a and 1b, Figure 2.3a).

2.3.3 Cuba

Peros et al. (2007) took sediment cores from a low lying ($\leq$1 m above sea level) mangrove region on the north coast of Cuba surrounding a coastal lake (Laguna de la Leche, 50 cm above mean sea level: Figure 2.3c). Deposits contain mangrove peat, organic matter and gastropods. I exclude the organic matter and gastropods from my catalogue. The peat samples are included because the coastal lake is oligohaline (low salinity level) indicating an underlying connection to the sea (otherwise it would be a fresh water lake since the tidal range is $\pm$30 cm). Peros et al. (2007) considered the mangroves lie at 50 - 100 cm above mean sea level at most. Therefore, I shift the peat samples by the elevation of the top of the core (1 m) to align them with present mean sea-level position.

2.3.4 Belize

Off-shore Belize has been extensively surveyed and contains the longest reef system in the Atlantic. It can be partitioned into three localities (from East to West): carbonate platforms, Belize barrier reef (BBR) system, and patch reefs that lie behind the the BBR (Figure 2.4a). I will discuss each in turn, but treat them as a whole when performing the sea-level curve reconstruction.

Carbonate Platforms

There are three carbonate platforms offshore Belize: Glovers Reef, Lighthouse Reef and Turneffe Islands. Gischler (2003) took cores from the interior lagoons of these platforms and sampled basal peats extending to $\sim$8000 yrs BP. Peat samples of cores from Turneffe Islands (Wooler et al., 2009) correlate with Gischler (2003). I exclude two data from Wooler et al. (2009) because of habitable depth uncertainty. Gischler and Hudson (1998) sampled the edges of the reef platforms and found Acropora, Montastrea and Diploria species. Gischler and Lomando (2000) primarily sampled Lighthouse Reef

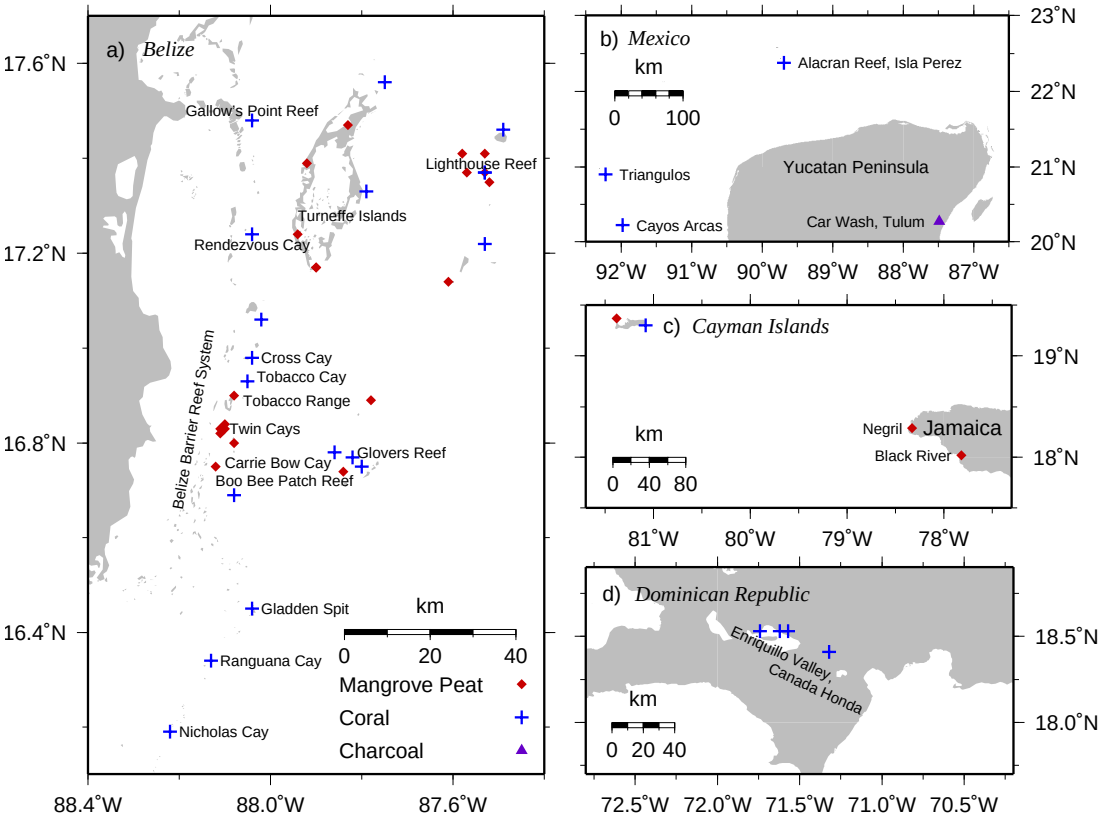

Figure 2.4: Late Pleistocene and Holocene coastal marine samples from publications for, **a**: Belize, **b**: Mexico, **c**: Cayman Islands/Jamaica and **d**: Dominican Republic

finding mangrove basal peats and three corals (Montastrea and Diploria). The carbonate platforms and mangrove sediments are formed upon faulted Pleistocene basement. The variable depth of this basement relative to present sea level explains the significant difference in reef and mangrove tract thicknesses (Gischler, 2003).

Belize Barrier Reef system

Gischler and Hudson (2004) sampled the numerous small Reefs, Cays and Spits that comprise the BBR finding Acropora and Montastrea corals. It is not possible to distinguish between in-situ corals and those transported from growth position, but in this case I use all the dated samples because of the continuous nature of the cores sampled (Gischler and Hudson, 2004). As with the carbonate platforms, the elevation (north-south decreasing) and structural (Pleistocene faulting) variability are thought to be the primary cause of timing differences in Holocene reef growth along the BBR system (Gischler and Hudson, 2004).

Patch reefs behind BBR

Halley et al. (1977) give a peat sample age from the base of the slope of Boo Bee Patch Reef. The sample overlies 2 - 3 m of clay material, which in turn lies on Pleistocene basement.

Wooler et al. (2004, 2007) analyse the palaeoecology of mangroves from Twin Cays. Age-depths correlate with Macintyre et al. (2004) other than a 1 m thick break in mangrove peat, which occurs in one of the cores. The break contains sediment of the tropical evergreen, Myrsine. This unit appears to have accumulated in a short time 80 - 240 years (4280 - 4040 cal yr BP) and may be attributed to the vegetation in this area of the patch reef being felled during hurricanes (Wooler et al., 2004). This break does not exist in nearby cores sampled by Wooler et al. (2007) but a sharper, thinner section of Myrsine lies around 5100 cal yr BP.

Purdy (1974), Halley et al. (1977) and Shinn et al. (1982) (in Toscano and Macintyre (2003)) all sample mangrove communities and infer that they were well established when the continental shelf was flooded in the early Holocene. Most drowned later in the Holocene and were buried under marine sediments. In areas of high elevation, mangrove communities continued to flourish forming very thick sections of peat. Two such locations are Tobacco Range (Macintyre et al., 1995) and Twin Cays (Macintyre et al., 2004), which have thick mangrove sections (up to 10 m). These began accumulating at $\sim$4.3 mm yr^{-1} around 7000 cal yr BP. Accumulation allowed the mangroves to "keep-up" with Holocene sea-level rise.

2.3.5 Mexico

Blanchon and Perry (2004) collected 13 cores across reef front, flat and back-reef positions of Cayos Arcas and Triangulos (Figure 2.4b). I exclude four of the Acropora dated samples because the rubble is interpreted as a hurricane deposit (Blanchon and Perry, 2004, Gischler, 2006, Toscano and Macintyre, 2006). I exclude other samples that are not in situ because they form part of a gravel facies.

Macintyre et al. (1977) sample the extensive Holocene reef tracts at Isla Pérez (870 m by 150-180 m in area). The Holocene tracts overlie a Miocene/Pliocene limestone surface at 33.5 m depth, and contain *A cervicornis* and *M annularis* coral remains. Three *M annularis* head coral samples have ^{14}C dates.

A single ^{14}C date of charcoal from a fire pit in a limestone cave is recorded by

Coke et al. (1991). As mentioned earlier, the fire pit must have been above sea level when in use, and the fire pit lies submerged at 27.5 m below present sea level. The age-depth is in line with the uplifted and reservoir corrected Barbadian sea-level curve (Fairbanks, 1989), indicating close link between terrestrial and marine ^{14}C dates (Coke et al., 1991).

2.3.6 Cayman Islands

Figure 2.4c shows the locations of mangrove peat samples from Barkers Peninsula (Woodroffe, 1981). To the east of Grand Cayman, a relict coral reef dated to early Holocene was discovered by Blanchon (2000). Seven down-slope Acropora samples are older than 8000 yr BP whilst two younger samples (5000 - 6000 yr BP) lie in an up-slope position.

2.3.7 Jamaica

Digerfeldt and Hendry (1987) sample two locations in Jamaica, Black River and Negril (Figure 2.4c). The peat samples vary from salt-water (Rhizophora and Rhizophora Conocarpus) to fresh-water (Cladium) types with salt-fresh water transitional types (Cladium Rhizophora and Cladium Conocarpus). I select any types of peat, where the sample is less than 1 m from bedrock (BP) and basal peat on clay (BC), which immediately overlies bedrock. This reduces the probability of sediment compaction.

2.3.8 Dominican Republic

Figure 2.4d shows the position of a Holocene fossil reef (Canada Honda) at the edge of Enriquillo Basin in Dominican Republic. The site presents an unusual case of a sub-aerially exposed reef, due to damming of the valley mouth in the late Holocene. Samples are devoid of Acropora and show low growth rates perhaps because of a high sediment environment, which would limit sub-surface light intensities (Mann et al., 1984, Cuevas et al., 2009). Corals sampled by Taylor et al. (1985) include Montastrea and Siderea species. Although the region is tectonically active, recent studies suggest little or no significant vertical uplift has occurred for the last 10000 yrs BP (Mann et al., 1984, 2002).

2.3.9 Puerto Rico

A palmata dates in Bahia Salina del Sur, Vieques Island (Figure 2.5a) are sampled by Macintyre et al. (1982). The present reef framework communities appear to have migrated leeward across loose, back-reef sediment since the Holocene.

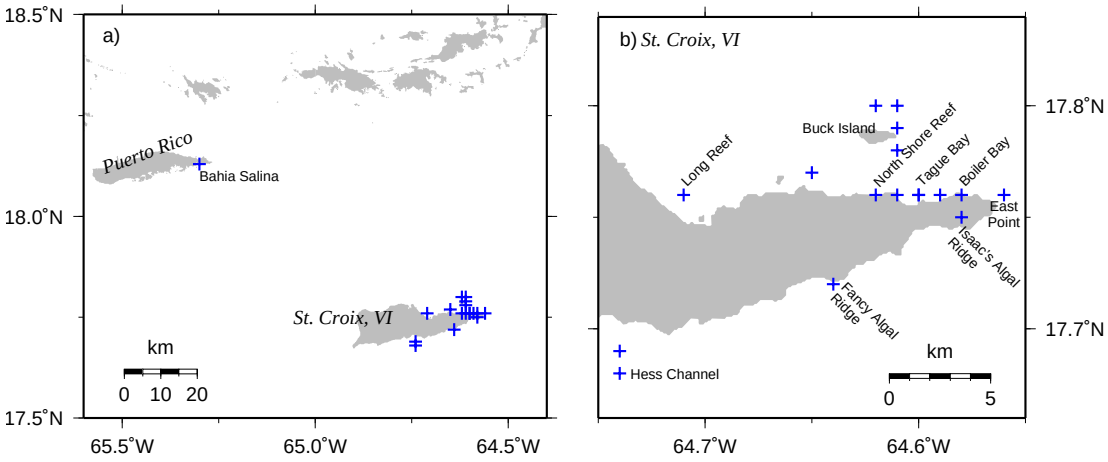

Figure 2.5: Late Pleistocene and Holocene coastal marine samples from publications for, **a**: Puerto Rico and US Virgin Islands, **b**: St. Croix, US Virgin Islands

2.3.10 US Virgin Islands

The reefs surrounding St. Croix, like off-shore Belize, have been extensively sampled (Figure 2.5b). Cretaceous sediments of volcaniclastic origin form the basement of the eastern end of St. Croix. The basement has been tilted, uplifted and eroded to form a topography that is thought to play an important role in the timing and location of reef development (Hubbard et al., 2005).

Corals along the south coast, from Hess Channel to East Point are sampled by Adey (1975), Adey et al. (1977), Lighty et al. (1982) and Toscano and Macintyre (2003). *A palmata* dominates present day reefs primarily between 0 - 6 m below sea level, though extending to 12 m dependent on water clarity (Hubbard, 2009).

On the north coast, staggered Acropora samples are recorded on the reef between Tague and Boiler Bay, which began as a series of isolated platforms Lighty et al. (1982), Burke et al. (1989), Toscano and Macintyre (2003), Macintyre et al. (2008). Buck Island, off mainland St. Croix is sampled by Macintyre and Adey (1990) and Hubbard et al. (2005). Frequent storms have disrupted reef growth on Buck Island Bar

at the shelf edge and have prevented the reef from catching up with the rising seas of the Holocene Transgression. Two time intervals exist where no coral reef is present (Hubbard et al., 2005).

Long Reef forms the western extent of the Outer Shelf-Edge reef system (which extends east through Buck Island and Lang Bank, ∼20km in length). Samples from Macintyre et al. (2008) indicate the reef tract on Long Reef is shallower than central and eastern sections of Outer Shelf-Edge Reef complex at Buck Island Bar and Lang Bank.

2.3.11 Panama

Bartlett and Barghoorn (1973) made detailed palynological analyses in the man-made Gatun Basin (Figure 2.6a: Gatun Lake was formed when the Panama canal was constructed by damming the Chagres river in 1907). Rhizophora (red mangrove) forms 45 - 95% of pollon assemblage in the peat sections. The peat is highly unconsolidated, but autocompaction has probably occured as well as compaction caused by overlying clays and gravels deposited by the meandering Trinidad River. Pollon analysis shows a transition from salt to fresh water influence occured around 4200 yrs BP (Bartlett and Barghoorn, 1973), therefore I exclude samples younger than 4900 yrs BP. Peat samples at depths between 8.5 - 35 m (below present mean sea level) must have been deposited at or below mean sea level, since oyster shells associated with the swash zone are found in situ within section (Bartlett and Barghoorn, 1973).

On the north coast of Panama, a relict reef containing *A palmata* and other head corals overlies middle Miocene Gatun formation at Galeta Point (Macintyre and Glynn, 1976). Macintyre and Glynn (1976) took samples from across the reef and found datable material from a variety of coral species. I eliminate potential storm rubble and fore/back reef samples and use only Acropora (framework forming with a narrow habitable range to sea level).

2.3.12 Lesser Antilles

The Windward reef colony, Antigua (Figure 2.6b) whose Holocene reef tract comprises primarily *A palmata*, gives way to head corals down slope (Macintyre et al., 1985). Older Acropora are found to have lain in deep water (more than 6 m), compared to those in the last 3000 years, which caught up with sea level.

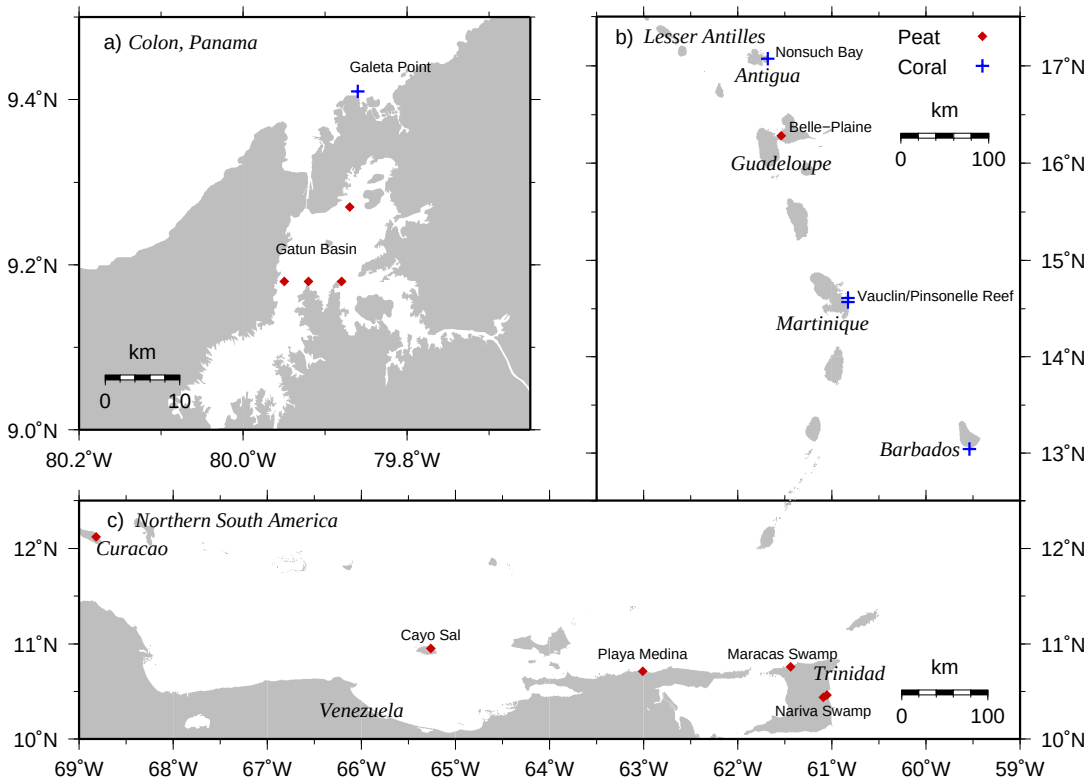

Figure 2.6: Late Pleistocene and Holocene coastal marine samples from publications for, **a**: Colon, Panama, **b**: Lesser Antilles and **c**: Northern South America

Mangrove peat samples from Guadeloupe (Feller et al., 1990) suggest a marine depositional environment. Volcanic activity on the island does not appear to have vertically altered accumulation rates compared to those of peats on passive tectonic margins. The last 1000 years show ∼1 m of accumulation, which might be explained by any of the historic eruptions of Soufrière Guadeloupe from 1530 to 1976 (Feuillet et al., 2011).

Adey and Burke (1976) took samples from two algal ridges running north-south off the east coast of Martinique and found *A palmata* in growth position. In addition, Acropora is also sampled by Lighty et al. (1982). It is worth noting that both reefs and ridges do not quickly develop on recent, rapidly eroding volcanic shores.

Peltier and Fairbanks (2006) presented U/Th dated coral record off the south coast of Barbados extending back to the last glacial maximum (LGM). The original data set (Fairbanks, 1989) and (Bard et al., 1990) was augmented in Fairbanks et al. (2005) and corrected for assumed constant tectonic uplift rate 0.34 mm yr^{-1} Fairbanks (1989). This coral record has been pivotal in developing an understanding of global sea-level change

since LGM (e.g. Tushingham and Peltier (1991), Peltier (2004)). The Barbados record, where it overlaps with others in the Lesser Antilles is in agreement in its corrected state. Recently however, the corrected Barbados record has come under scrutiny for over simplifying the vertical uplift rate where different cores in the sequence span different neotectonic segments (Bard et al., 2010). Since there is little available information regarding different uplift rates across the Barbados reef tracts to enhance the original record, I choose to leave it in its vertically corrected state.

2.3.13 Venezuela

Rull et al. (1999) present one date of a stratified peat sample in Playa Medina (Figure 2.6c). Other depth/times plotted in Rull et al. (1999) are inaccessible (except Weiss (1979)) therefore only the stated time/depth is used here. Weiss (1979) present core samples taken on Cayo Sal off-shore Venezuela. One sample appears to be an in-situ peat, which I include whilst others comprise mud layers and an emplaced peat (possibly due to hurricanes) both of which I exclude.

2.3.14 Curacao

Milne et al. (2005) cite an unpublished work by Klosowska (2003) who "provide four index points which are likely to have been lowered from their original elevation by compaction." In spite of this statement and the disregard for data from Rull et al. (1999) (which includes Weiss (1979)) because of local tectonic movement, Milne et al. (2005) retain Klosowska (2003) with very small error bounds (25 cm). Rull et al. (1999) comment that tectonic activity along this part of the South American coastline is dominated by strike-slip motion, and vertical components are only significant in a few secondary faults.

2.3.15 Trinidad

Ramcharan (2004) took a series of peat cores in two localities, Maracas and Narivas swamps on the Caribbean and Atlantic coasts of Trinidad. Ramcharan and McAndrews (2006) comment that Maracas Swamp mangroves became less marine influenced after 3000 yr BP. Furthermore, Ramcharan (2004) comment that at Narivas swamp, the transition from saline to fresh water habitat was complete by 2700 yr BP. Therefore, I exclude samples after 2700 yr BP from the Narivas site. One Maracas Swamp peat

sample is dated to 2930 ± 80 ^{14}C yr BP, which I retain.

The sample elevations in Trinidad are systematically lower than those in Venezuela/Curacao. There is no consensus over this difference that I have found in the literature. Given the limited vertical tectonic movement in Venezuela/Curacao (Rull et al., 1999), the systematic vertical offset is likely to be related to either compaction or tectonic effects in Trinidad. It is an open question whether one or other of these effects is the primary cause.

2.3.16 Western Atlantic Sea-Level curve

In Chapter 1 I referred to two key publications on sea level in the Caribbean since the LGM. Whilst the Barbados sea-level record Fairbanks (1989) is important for understanding global sea-level change, the Western Atlantic Sea-Level (WASL) curve of Toscano and Macintyre (2003) is important in describing Holocene sea-level change in the Caribbean. This curve is constructed from a suite of carefully selected, published and unpublished, *A palmata* corals and Rhizophora mangrove peats from 10 sites around the Caribbean. The WASL curve is designed as a reference model for further investigations in this region: "in future studies of the history of western Atlantic coral reefs, scientists will be able to relate calibrated radiocarbon dates to this sea-level curve to determine palaeo-water depths and rates of sea-level rise" (Toscano and Macintyre, 2003). It should be noted however that the data used still contains deviations within vertical sample positions (particularly peat deposits). For example Florida basal peats deviate from Belize basal peats (∼5500 cal yr BP) such that the sea level in Florida appears to arrive within 5 m of present ∼9000 cal yr BP, whilst Belize arrives within 5 m of present ∼6000 cal yr BP. I utilise many of the referenced indicators in their database and use the WASL curve as a tool to compare with my sub-regionally constructed sea-level curves.

2.4 Methods: Sample Dating

Radiocarbon dating and calibration

The publications used in this synthesis span 40 years during which time the standard method of reporting radiocarbon dates has changed significantly. All records pre-1990 give only basic ^{14}C dates based on the Libby half life (5568 years), relative to 1950 AD.

To calibrate the radiocarbon ages so that they can all be compared to each other, I first calculate the conventional radiocarbon ages (CRA) of each sea-level indicators by correcting them for their isotopic fractionation.

The isotopic fractionation refers to the fluctuation in the carbon isotope ratios as a result of natural biochemical processes. It is expressed as a δ^{13}C value, which represents the parts per thousand ($‰_{PDB}$) difference from the international standard carbonate (Keith et al., 1964, Aitken, 1990) at the Cretaceous belemnite formation at Peedee (PDB) in the USA. The resultant ages are termed "normalised", meaning the measured activity is corrected with respect to -25 $‰_{PDB}$ (Stuiver and Polach, 1977).

Where a CRA is published, but not a ^{14}C age, I use the CRA. For ^{14}C ages that do not specify $^{14}C/^{12}C$ or $^{14}C/^{13}C$ fractionation method, I assume the original ^{14}C date was derived from $^{14}C/^{12}C$ ratio (Macintyre et al., 2008). I use the Calib spreadsheet d13ccorr.xls (online Calib manual: http://calib.qub.ac.uk/calib) to calculate $\delta^{13}C_{PDB}$ values and corresponding conventional radiocarbon dates for each sample. The four suggested δ^{13}C per mil values to use (for this study) are marine carbonate (CO_3^{-2}) 0 ± 2‰, marine organisms -15 ± 2‰, charcoal -24 ± 2‰, and peat -27 ± 3‰(Stuiver and Polach, 1977).

After the indicators are corrected from ^{14}C dates to CRA, I calibrate them using the CALIB 6.0 Radiocarbon calibration program (Stuiver and Reimer (1993); http://calib.qub.ac.uk/calib; on-line version Stuiver et al. (2005)) with the marine calibration data set (marine04.14C) except for the charcoal fragment, which uses the terrestrial calibration data set (intcal04.14C). The calibration calculates the probability distribution of the CRA's true calendar age using an independently dated calibration curve. There are different curves with which to calibrate data depending upon whether the sample data is marine or terrestrial.

Organisms from marine environments have been exposed to different levels of ^{14}C than those in the atmosphere. To account for these elevated values, the marine04.14C calibration data set incorporates a time-dependent global ocean reservoir correction of about 400 years (Stuiver and Reimer, 1993). To accommodate local reservoir effects, the difference (ΔR) between the local region and an atmospheric-ocean carbon circulation model needs to be determined (Stuiver and Braziunas, 1993). I use a global database of ΔR values (http://www.calib.qub.ac.uk/marine) to determine the average for the Caribbean. 56 records spanning 6 publications give a weighted mean

ΔR = 15 $\pm$ 40 (standard deviation) (Broecker and Olson, 1961, Druffel and Linick, 1978, Lighty et al., 1982, Hughen et al., 2004, Guilderson et al., 2005, Kilbourne et al., 2007, Wagner et al., 2009).

The result of the age calibration (including reservoir correction for marine organisms) is a set of adjacent age ranges, each with an associated probability that the sample age lies within that range. For each calibrated sample, I concatinate the adjacent age ranges with their associated probabilities to form a stepwise probability distribution function.

Absolute dating

Five publications from the catalogue use the Thermal Ionization Mass Spectrometric (TIMS) U-Th dating technique. The ages presented in these publications do not require any calibration. I use the standard deviations published with each U-Th dated sample age to define a Gaussian probability age distribution.

2.5 Methods: Indicator relationship to sea level

2.5.1 Corals

I approach the problem of probabilistic vertical distributions for different coral species by searching through the literature for records of growth, abundance and reef coverage at various depths. Table 2.1 shows the weighted median coral depths using growth rate data (Huston, 1985, Dullo, 2005, Cuevas et al., 2009), abundance (Bak and Engel, 1979, Rogers et al., 1984, Horta-Puga and Barba-Santos, 1999) and coverage (Weil and Knowlton, 1994). These publications sample corals at different, discontinuous depths.

To account for this vertical sampling I use weighted median depths. The median of the sample is the halfway point when the sample values x_i, $\{i = 1, 2, ..., N\}$ are arranged in ascending (or descending) order. If N is odd then the median is equal to $x_{(N+1)/2}$, whereas if N is even the median is $\frac{1}{2}(x_{N/2} + x_{(N/2)+1})$.

After collating the records for a given coral species, I have a series of depths, $\{z_i\}$ with a corresponding set of measures (e.g. growth rates), $\{m_i\}$. First the measures are normalised by the maximum measure for the given species to give a dimensionless fraction, $\{g_i/g_{max}\}$. Next I scale the depths by the normalised measures, $\{z_i \times g_i/g_{max}\}$.

Table 2.1: Documented coral species with median depths (m) based on growth rate, abundance and coverage records. The fifth column states the chosen probability distribution (Grow, Growth; Logi, Logistical) and column six shows final calculated median depth ($\pm\sigma$ required for logistical pdf)

Coral species	Growth rate m	Abundance m	Coverage m	Grow/Logi PDF	Median depth ($\pm\sigma$), m
A cervicornis	3.80	9.00		G	6.4
A palmata	4.40			G	4.4
C natans	9.26	10.19		L	9.73 (4.0)
D clivosa	1.60			L	1.6 (2.5)
D labyrinthiformis		16.35		G	16.35
D stokesi		15.89		G	15.89
D strigosa	1.30	10.25		G	5.78
M annularis	7.20	13.68	5.00	G	7.2
M cavernosa	22.0	10.21		L	16.11 (4.0)
M faveolata	6.20		2.42	G	4.31
M franksi			15.19	L	15.19 (3.0)
P astereoides	6.40	14.97		G	10.69
S michelinii		18.56		L	18.56 (3.5)
S radians	1.97			L	1.97 (2.5)
S siderea	11.0	15.0		L	13.0 (3.0)

Finally, the weighted median depth (z_{med}) is solved by dividing the median scaled depth $\mathbf{med}\{z_i \times g_i/g_{max}\}$ by the median normalised fraction $\mathbf{med}\{g_i/g_{max}\}$. The weighted median depth for a given depth-measure for each coral species is shown in columns 2 to 4 in Table 2.1.

The weighted median depth is used as the starting point for two probability distribution functions (pdfs), which describe coral depth distributions. The first is a scaled form of the equation for coral reef growth (Bosscher and Schlager, 1992) and the second is the logistical distribution. Figure 2.7 shows the two probability distributions, which I aim to fit to the published data. The other coral species and mangrove vertical distributions are shown in Appendix A. I acknowledge that the pdfs for different coral species are subjective in their selection to a certain extent (see Figure 2.7b). I use *a priori* information (such as common statements about coral depths used in various publications, e.g. Lighty et al. (1982), Peltier and Fairbanks (2006)), coupled with the coral species depth-measures to decide on the more appropriate distribution of the two. The choice of distribution is shown in Table 2.1 (column 5). Column 6 in Table 2.1 shows the median depth of the different measures for a given coral species (a scale parameter is in brackets for logistical distributions).

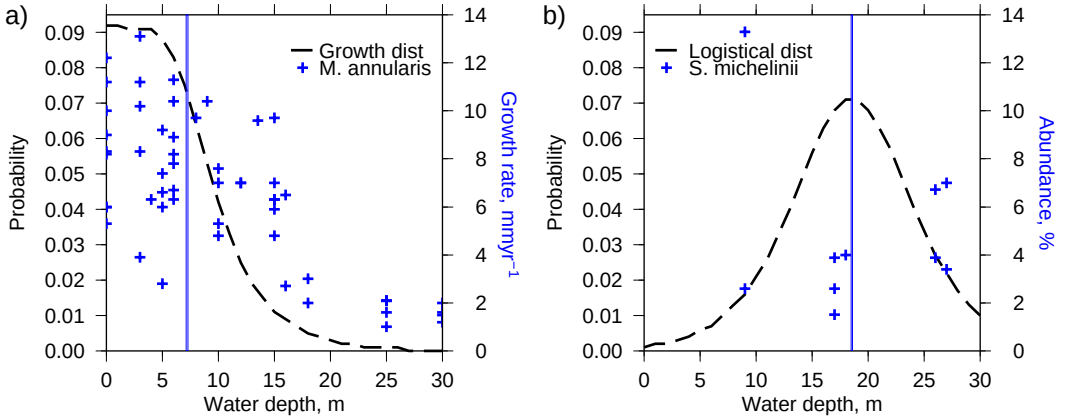

Figure 2.7: Probability distributions derived from (**a**: growth) M. annularis depth/growth rates and (**b**: logistical) S. Michelinii depth/abundance respectively. Vertical blue line corresponds to weighted median depth (shown in Table 2.1), M. annularis: 7.2 m; S. michelinii: 18.56 m

Scaled Growth Distribution

Chalker (1981) and Chalker et al. (1988) hypothesised that coral growth rate, G is proportional to vertical light intensity, I_z using the hyperbolic tangent function.

$$G = G_m \tanh(I_z/I_k) \tag{2.1}$$

where G_m is maximum growth rate and I_k is saturating light intensity (typically 50 to 450 μE m^{-2} s^{-1}). The light intensity for a given depth z follows the Beer-Lambert's law (Chalker, 1981),

$$I_z = I_0 e^{-kz} \tag{2.2}$$

where I_0 is the surface light intensity (typically 2000 to 2250 μE m^{-2} s^{-1} in the tropics) and k is the extinction coefficient, a measure of the extinction of photosynthetically active radiation (range from 0.04 - 0.16 m^{-1}: Chalker (1981)). To incorporate the weighted median depth, I simplify equation 2.1 such that $I_0/I_k = 2000/250 = 8$ and $k = 2/z_{med}$. The probability, P_g for growth rate is defined as,

$$P_g = \tanh(8e^{-2z/z_{med}}) \tag{2.3}$$

To use this growth function as a pdf, it is scaled such that its integral over the range

0 - 30m is one (Figure 2.7a). The growth function pdf is useful to use for reef building corals, which tend to dominate shallow depths in the breaker to fore-reef environments (Figure 2.1a, e.g. *M annularis*).

Logistical Distribution

The logistical distribution is a continuous probability distribution, which resembles the normal distribution in shape but has heavier tails. The peak lies at the weighted median of the published coral depths. The probability distribution (P_l) is defined by,

$$P_l = \frac{e^{\frac{z-z_{med}}{\sigma}}}{(1+e^{\frac{z-z_{med}}{\sigma}})^2} \tag{2.4}$$

where z is the depth, z_{med} is the weighted median depth and σ is a scale parameter loosely related to standard deviation. Figure 2.7b shows the logistical pdf is useful to use for non-reef building corals, which tend to have greater abundance down the fore-reef slope (e.g. S. michelinii)

2.5.2 Mangroves

There is a wide variety of opinion about the relationship between mangroves and sea level (e.g. Woodroffe (1981, 1990), Toscano and Macintyre (2003)). It is commonly held that compaction and subsidence of a substrate can give false age-depth relationships of peats to sea level (Woodroffe, 1981, 1990). As a result, basal peats are thought to be reliable indicators if the underlying substrates are assumed to be unaffected by compaction (Horton et al., 2009). In these circumstances, basal peats give the most accurate position of former sea levels. For example, Woodroffe (1981) use a deposition range of 0 - 0.3 m above mean sea level for basal marine mangrove peats for samples within 0.05 m of Pleistocene carbonate on Grand Cayman. Scholl and Stuiver (1967) ascribe the same magnitude of depth error by identifying the deposition of mangrove peat over calcitic mud (inferring a fresh to saline water contact, hence a tidal limit therefore a sea-level position). Milne et al. (2005) employ height uncertainties of $\pm$ 1.0 m for Jamaican mangroves and Digerfeldt and Hendry (1987) state *Rhizophora mangle* forms within 1m above mean sea level.

Many of the samples in the catalogue are non-basal. These samples can also be used to help constrain a minimum curve for sea-level if used in a conservative manner

with much larger uncertainties than those of basal samples to account for such vertical movement as compaction.

I ascribe three categories for vertical uncertainty for mangrove peats. All three assume that sea-level position lies within a Gaussian vertical probability distribution. All the high precision basal samples with published sea-level ranges lie within $\pm$ 0.25 m. For basal samples that do not have published sea-level ranges I use a range of $\pm$ 0.5 m. For non-basal samples, I use a range of $\pm$ 1.0 m.

As with corals, mangrove peats help to establish a limit to sea-level position. With this is mind, I also ascribe the type of limit the mangrove represents: terrestrial (fresh water mangroves at or above sea level), inter-tidal (mangroves at sea level) or marine limiting (marine mangroves at or below sea level).

2.6 Methods: Sea-Level Curve Reconstruction

Sea-level curve reconstruction has tended to be a qualitative affair, primarily drawing a by-eye curve onto a plot of sea-level indicators assuming a fixed vertical distribution such that the bulk of corals plot below sea level and the bulk of peats plot above sea level. A number of publications have taken a numerical approach: Boardman et al. (1989) fit a cubic polynomial function to best fit their basal samples. Pinter and Gardner (1989) attempted a Lagrange polynomial interpolation whereby sea-level indicators would be sectioned chronologically and fitted using boundary conditions at adjacent sections to give a smooth function (akin to spline fitting). Pinter and Gardner (1989) use this method for multi-glacial sea-level cycles but its temporal resolution is too coarse for a Holocene study such as this. Milliken et al. (2008) fit a third order polynomial using non-linear regression to derive an R^2 value, but their data are exclusively intertidal peats and shells. This short assessment begs the question, is there another appropriate manner of reconstructing past sea level that does not rely exclusively on intertidal samples or use a single continuous polynomial function?

In the previous section, I reviewed the evidence supporting the hypothesis that corals and peats display vertical depth probability distributions. Mangrove peats can be marine, inter-tidal or terrestrial limiting and different coral species can lie at very different depths and that their probability of lying at a particular depth can be described by one of two pdfs. This means that I can take a quantitative approach towards calculating past sea-level positions using the age-depth pdfs for sea-level indicators and

a windowing method.

In the subsequent figures, the zero in the age scale for calibrated radiocarbon and U/Th dated samples is AD 1950. Also, elevation is presented as upwards positive and downwards negative. Although gradients in subsequent plots will be negative, I will present these as rates of sea-level rise with the opposite sign (e.g. gradient of -1.5 mm yr^{-1} will be presented as rate of sea-level rise, 1.5 mm yr^{-1}).

Figures 2.8 and 2.9 show the maximum depth and age ranges for corals, peats and the shell/charcoal samples. Regardless of distribution type, these figures show their measured sample depth at the limiting position of sea level for all the samples in the catalogue I have assembled. There is a strong bias in the data sampling towards Florida and Belize. As highlighted earlier, the Lesser Antilles data are dominated by the Barbados data (Fairbanks, 1989, Peltier and Fairbanks, 2006) whilst indicators along the north South American coast are very sparse. Elsewhere, significant gaps in time exist in the data in the Bahamas (1700 - 3500 cal yr BP), Cayman Islands (2000 - 5000 cal yr BP), Jamaica (0 - 3000 cal yr BP), Dominican Republic (0 - 6000 cal yr BP) and Panama (0 - 2200 cal yr BP). These gaps mean that I will not be attempting to fit unbroken sea-level curves to the regional data sets, but identifying the position of sea level where the data do exist. This removes the problem of interpolating across time spans with no data, in fact I require at least three data points to calculate a theoretical former sea-level elevation.

I adapt a method originally used by Holgate and Woodworth (2004) for studying modern global sea-level rise using tide gauges. Holgate and Woodworth (2004) used successive, overlapping, ten year trends calculated for each year of a tide gauge record to study accelerations in present day sea level. My method uses the same idea of calculating successive, overlapping trends but instead of using a densely sampled tide gauge record, I use sea-level indicators and instead of using 10 year time windows I use millennial scale time windows.

To account for the variability in time and depth of the sea-level indicators, I generate 1000 realisations (using the Matlab © function: *randsample*) that sample the pdfs and are adjusted for the limiting factor. This is shown for four samples in Figure 2.10. Figure 2.10a shows a terrestrial limiting peat sample with the narrowest of the three vertical distributions. The position of sea level must be below this sample elevation, so the distribution is shifted vertically by 0.25 m (the range of the pdf). Figure 2.10b shows

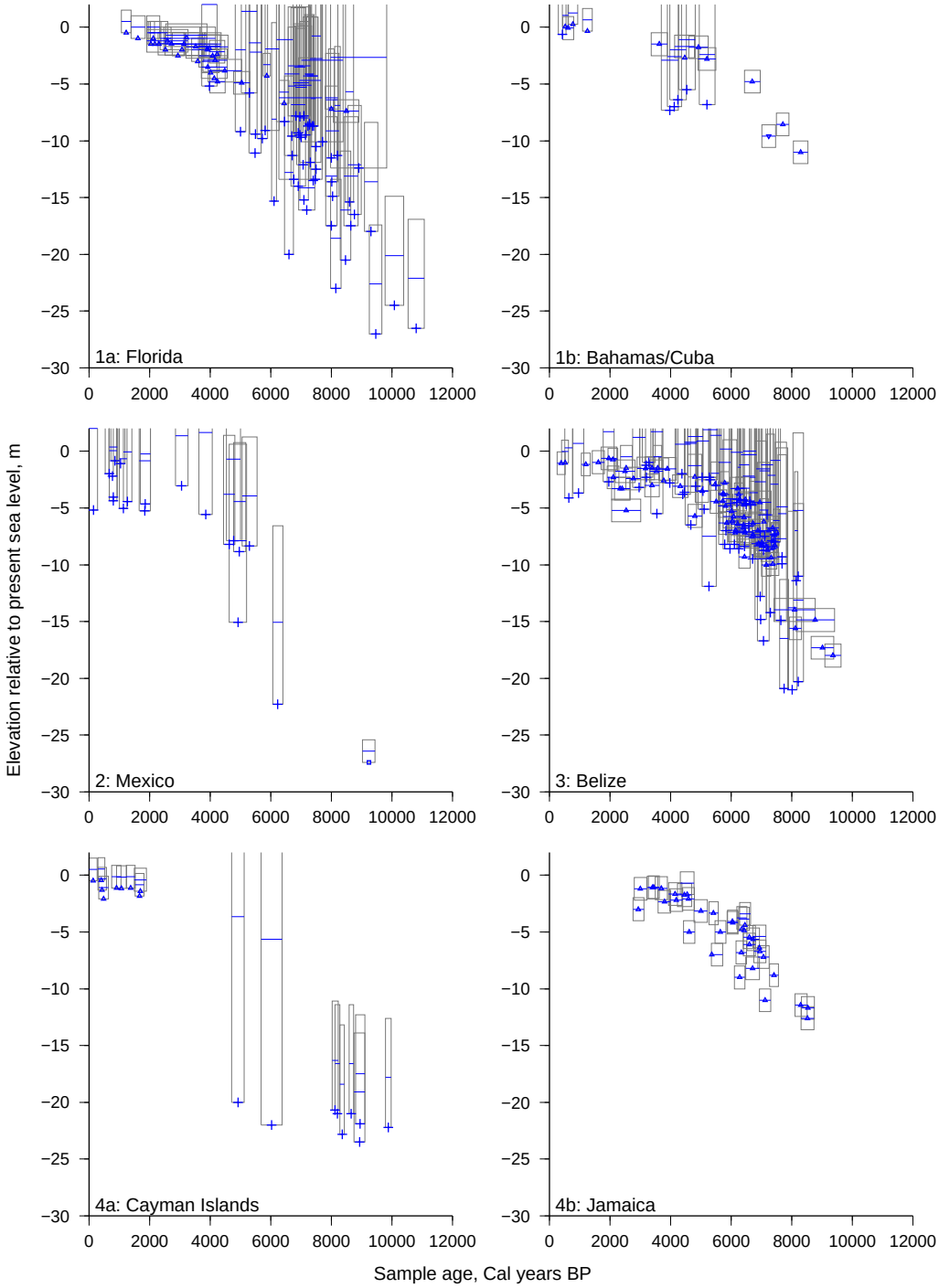

Figure 2.8: Maximum age-depth ranges of sea-level indicators for regions 1a to 4b. Sea-level indicator symbols for peat, shell, charcoal and coral are upward triangle, downward triangle, square and cross respectively

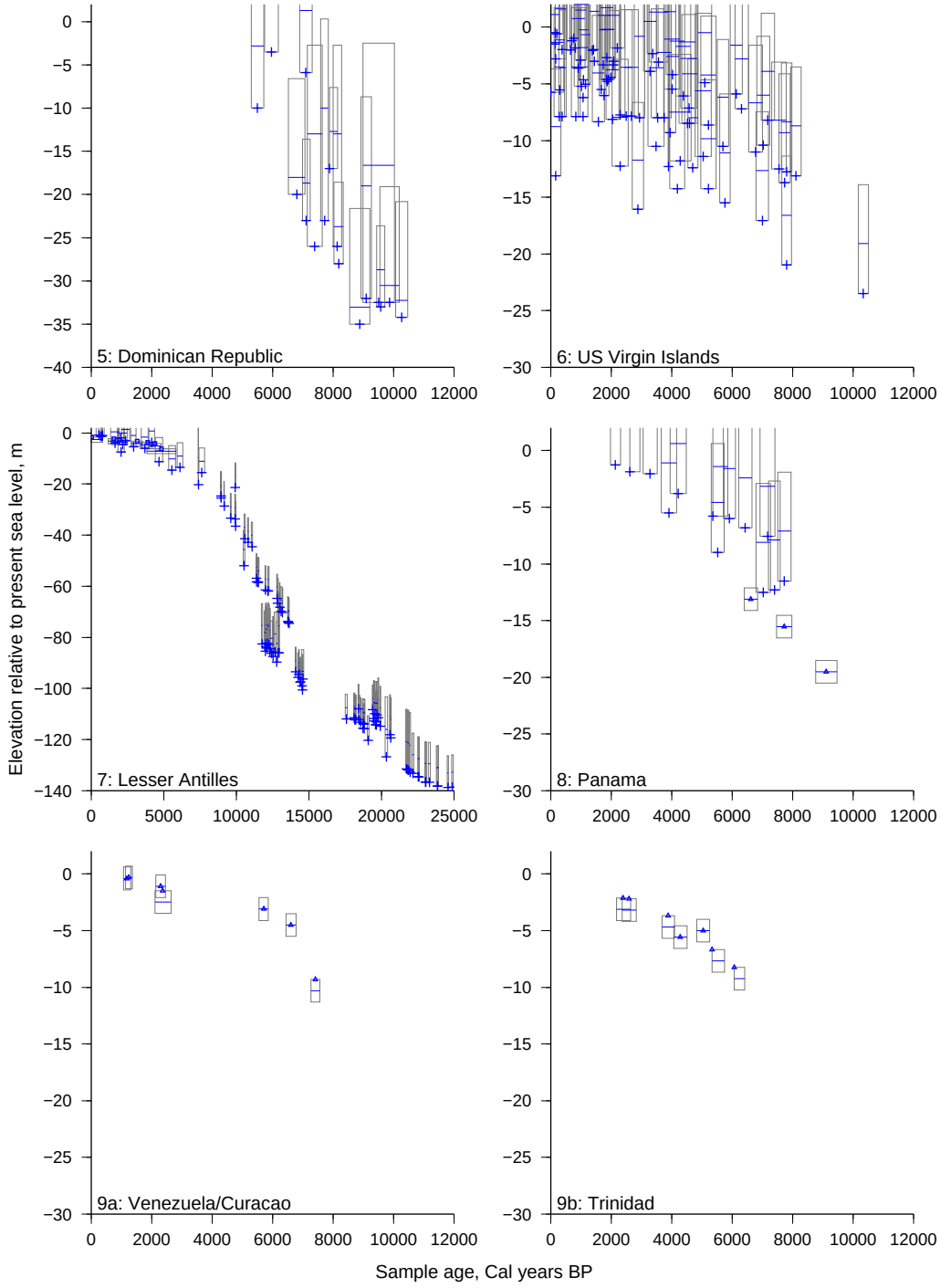

Figure 2.9: Maximum age-depth ranges of sea-level indicators for regions 5 to 9b. Symbols as in Figure 2.8

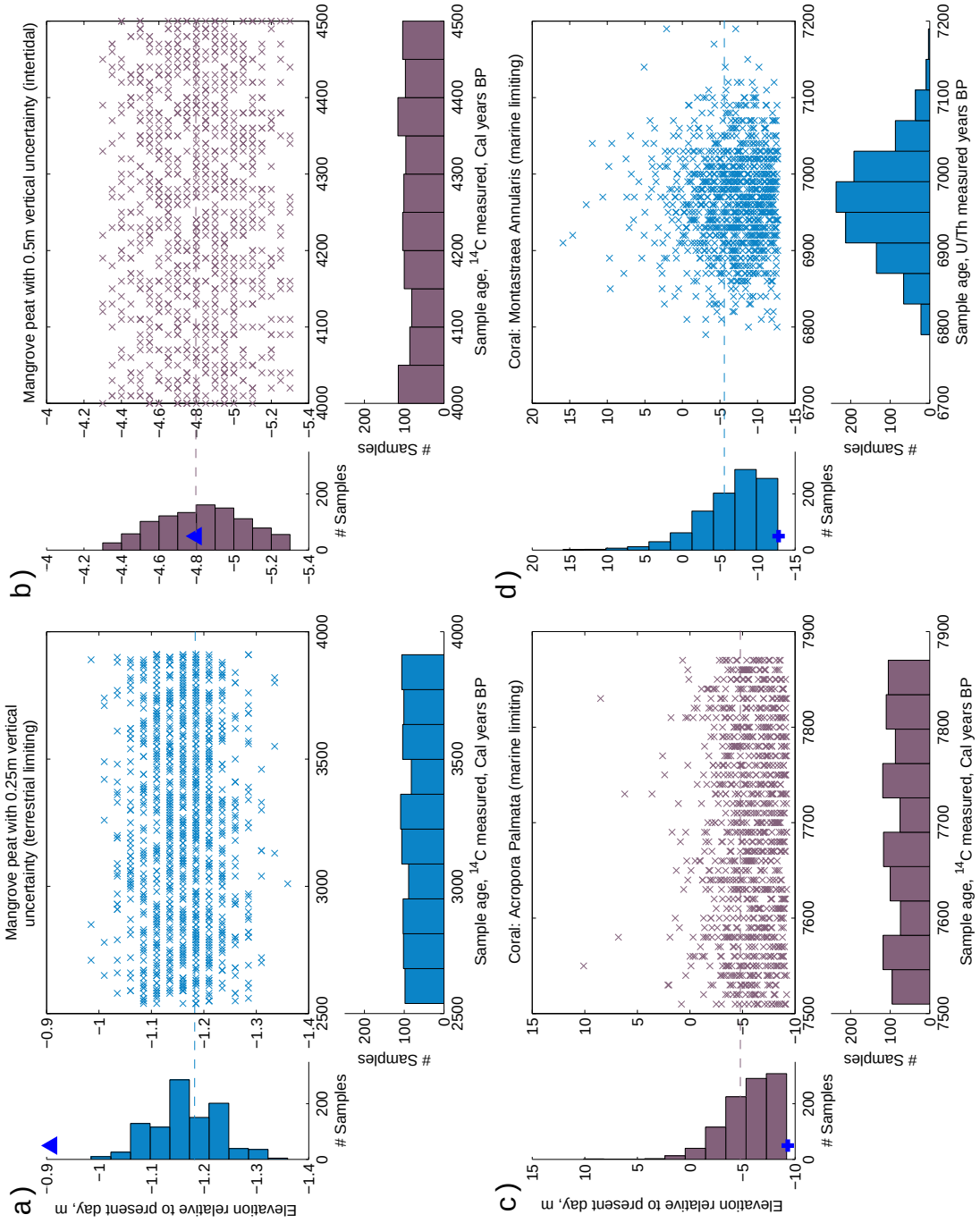

Figure 2.10: Time-depth samples of sea-level indicators for age and depth probability distributions. Actual vertical sample position shown by blue symbol. Dashed line shown at highest probability of former sea-level position. ^{14}C calibrated age samples: (**a**) Terrestrial limiting mangrove peat with 0.25 m habitable depth range, (**b**) Inter-tidal mangrove peat with 0.5 m habitable depth range. (**c**) Marine limiting coral, A. palmata. U/Th measured age samples: (**d**) Marine limiting coral, M. annularis.

an inter-tidal peat with a 0.5 m habitable range. The position of sea level lies at the centre of this distribution. Figure 2.10c and d show marine limiting corals (*A palmata* and *M annularis*) whose sample elevation lies at the base of their distributions. Again, the highest probability of the position of sea level is at the weighted median depth above the sample elevation. Figure 2.10a-c also show sampling of the age distributions from calibrated ^{14}C ages before present whilst Figure 2.10d shows the U/Th dating age distribution.

I will now outline and then discuss the windowing method, which is applied to each sub-region, for the 1000 realisations of sea-level indicator age-depth probability functions as follows:

1. Set the length of time window (e.g. 2000 years)

2. Set up a vector with 500 year step size that covers the maximum time extent of the data.

3. For each realisation (1000 total) and each 500 year step size, search for sample points within time window (e.g. 0 - 2000 years or 3500 - 5500 years).

   (a) Remove sample points greater than +1 m.

   (b) If the number of points is less than 3, ascribe null rate and intercept.

   (c) Otherwise calculate gradient and intercept of points.

   (d) If gradient exceeds 50 mm yr^{-1} ascribe null value. Otherwise record gradient and intercept.

4. Calculate the fraction of non-null gradient values for a given time slice (i.e. number of values divided by 1000).

5. For each time slice, if the fraction exceeds 0.4 (i.e. more than 400 realisations are solved), calculate the theoretical vertical positions of sea level using rate and intercept information.

6. Then calculate mean and standard deviation of vertical positions to give most probable position of sea level at time slice (i.e. average over all acceptable realisations for given time slice).

The length of the time window inside which I search for ages is dictated by the time density of the sea-level indicators. For a very dense, regularly spaced set of sea-level indicators, I could use a narrow time window and small step size to calculate local sea levels without significant deviations. The wider the time window, the more smoothed the average rate and sea-level position becomes. I test time windows at 1000, 2000 and 3000 years.

Within each iteration I remove sample sea-level positions, which are greater than 1 m above present sea level. This is because the Caribbean region lies far from any centre of deglaciation. Sea-level response to deglaciation suggests curves in this region should reach present sea level or just emerge above present sea level ($\leq$ 1 m) giving a small sea-level fall in the late Holocene (Clark et al., 1978). None of the published sea-level curves (e.g. Lighty et al. (1982), Toscano and Macintyre (2003)) for this region indicate sea level rising above present sea level, so the boundary condition applied is conservative.

I also ascribe null values to gradients exceeding 50 mm yr^{-1}. This is because there is little evidence that during the Holocene at tropical latitudes, sea level rose at rates above 50 mm yr^{-1}. A rise of more than 50 mm yr^{-1} would result in catastrophic reef drowning events in which reef growth would not be able to keep up with sea-level rise (Blanchon and Shaw, 1995). The melt water pulses commonly tied to late-Pleistocene/Holocene sea-level rise are not thought to exceed 25 mm yr^{-1} therefore this boundary condition is conservative as well.

Figure 2.11 shows the resulting average RSL curve (in red) and one standard deviation from the results of the 1000 realisations for the Florida region (1a: Figure 2.3a/b). The grey dots show the theoretical sea-level positions at the centre of each time window for each of the realisations. I only include the average sea-level position if more than 40% of the realisations are successful in deriving a sea-level position (that is at any time slice, there are more than 400 grey dots). Figure 2.11 also shows the probability distributions of the theoretical sea-level positions for each time slice to show that a mean and standard deviation is applicable for estimating the best fit sea-level position.

As a short test to validate the use of the probability distributions described above, I calculate a set of RSL curves using uniform depth probability distributions for coral and mangrove sea-level indicators. The results (Appendix B: Figures B-1 to B-3) show RSL curves with much larger vertical errors, especially where corals are present.

Furthermore, the shapes of the curves are unrealistic compared to the WASL curve (Toscano and Macintyre, 2003). Interestingly there does not appear to be a significant change to the RSL curves where only mangroves are present (e.g. 1a: Florida, see 2000 - 3500 Cal yr BP in Figures 2.11 and B-1), however I retain the Gaussian probability distribution (Figure A-1:16-18) for the results sections of this chapter.

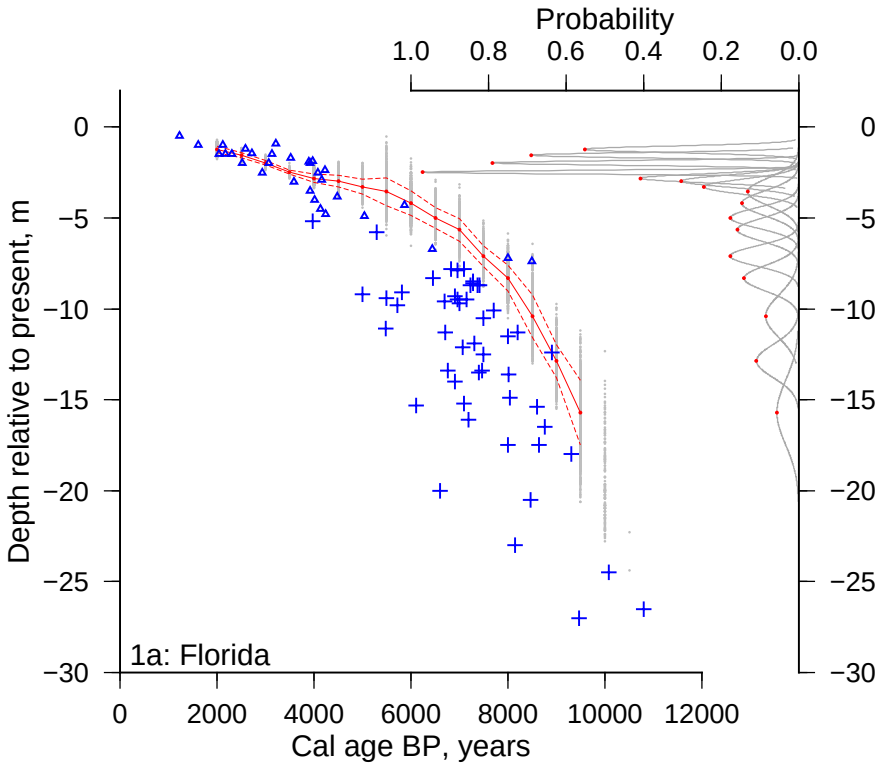

Figure 2.11: Florida sea-level realisations at 500 year time steps (grey dots). The solid red line joins the red dots, which show the mean of the sea-level realisations. The dashed red lines represent the envelope of standard deviations. The probability distribution of each set of sea-level realisations are shown with depth (grey lines).

2.7 Results

2.7.1 Sea-Level Curves

I use a 2000 year time window to calculate average sea-level curves for the sub-regions shown in Figure 2.3a. The results of the construction methods are shown in Figures 2.12 and 2.13 along with the WASL curve (Toscano and Macintyre, 2003) for comparison. I also show the result of combining regions 1a and 1b, 4a and 4b, 9a and 9b in Figure 2.14. This is of particular importance for 9a/9b where the data are sparse. I do not plot the habitable ranges of the indicators in these figures, but as a rule corals (crosses) and peats (triangles) should lie below and straddle the curve respectively.

Appendix A shows the curves at all sub-regions across the Caribbean for 1000 year (Figure A-2 - A-4) and 3000 year (Figure A-5 - A-6) time windows. Generally, there are no significant differences between the results of the different time windows, particularly where there is a high time density of sea-level indicators (e.g. Florida, 1a). However, the 1000 year time window does not give any sea-level curve results for the regions 9a or 9b and the 3000 year window prevents one from ascertaining rates and sea-level position closer to the present than 1500 cal yr BP. Furthermore, I wish to use a fixed window across the different regions to allow direct comparison between results, therefore I concentrate on the findings from the 2000 year window.

Regions with a high proportion of peats have small standard deviations (e.g. Florida: 0.57 m, Belize: 0.33 m and Jamaica: 0.15 m), which delineate the position of sea level in the past. Those regions with a greater proportion (or composed exclusively) of corals have larger standard deviations (e.g. Mexico: 1.92 m and Dominican Republic: 2.06 m).

Holocene sea level approaches the present day position at different times depending upon the region considered. For example, in Florida sea level has not reached that of present day around 2000 cal yr BP where as in Belize sea level had been at present day level since 3000 - 4000 cal yr BP. This point argues in favour of the need for sub-regional sea-level curves particularly in these two localities. The debate over the utility and construction methods of the WASL curve has centred on the differences between indicators from Florida and Belize (Toscano and Macintyre, 2003, Blanchon, 2005, Toscano and Macintyre, 2005, Gischler, 2006, Toscano and Macintyre, 2006).

The results presented are in agreement with published sea-level curves for the

Caribbean (e.g. WASL curve of Toscano and Macintyre (2003)) and have been constructed using a numerical method rather than a qualitative approach. The WASL curve uses corals and peats from across the Caribbean but remains a regional average. The results of the window method presented here show persistent and consistent differences from this averaged curve. Also, the shapes of the curves themselves are different, there is not just a systematic offset. The Florida (1a), Bahamas (1b) and Belize (3) curves (Figure 2.12) deviate from WASL curve by more than the standard deviations indicating that they are distinct. The Mexico (2) curve deviates from the WASL curve until 5000 cal yr BP. The deviation is probably due to the deep coral samples at 5000 and 6200 cal yr BP whose position must lie outside the habitable range ascribed in my methodology. The US Virgin Islands (6) curve follows the WASL curve the most closely as does the Panama (8) curve in the time range 5000 - 8500 cal yr BP. The Lesser Antilles (7) curve appears to deviate from the WASL curve prior to
5000 cal yr BP and there can be a high level of confidence in this curve as the samples are framework *A palmata*, which have a narrow habitable depth range (e.g. Lighty et al. (1982) and Table 2.1).

The last 4000 years of all the calculated sea-level curves are aligned with the WASL curve except Belize (3), Jamaica (4a) and Panama (8) curves. Likewise, the last 4000 years of the averaged sea-level curves (Figure 2.14) are aligned with the WASL curve. Prior to 4000 cal yr BP, the Florida/Bahamas (1) and Caymans/Jamaica (4) curves lie above and below the WASL curve respectively.

2.7.2 Rates of Sea-Level change

In Figure 2.15, I show the time varying rates of change of sea level for each region. These rates are the average of the rates calculated in the suite of 1000 realisations for each region. The figure reveals certain patterns of spatial variation of sea-level change with time, which are less easy to identify in Figures 2.12 - 2.14. Sampling with 500 year step size gives rates at individual time slices rather than a continuous function; i.e., the rates plotted are not necessarily the slope of the lines joining the points plotted in Figures 2.12 - 2.14.

All of the Caribbean has experienced rates of less than 1 mm yr^{-1} from 3500 cal yr BP to present. As mentioned in the previous section, the North and West Caribbean have been in this state for approximately 1500 years longer than the South Eastern

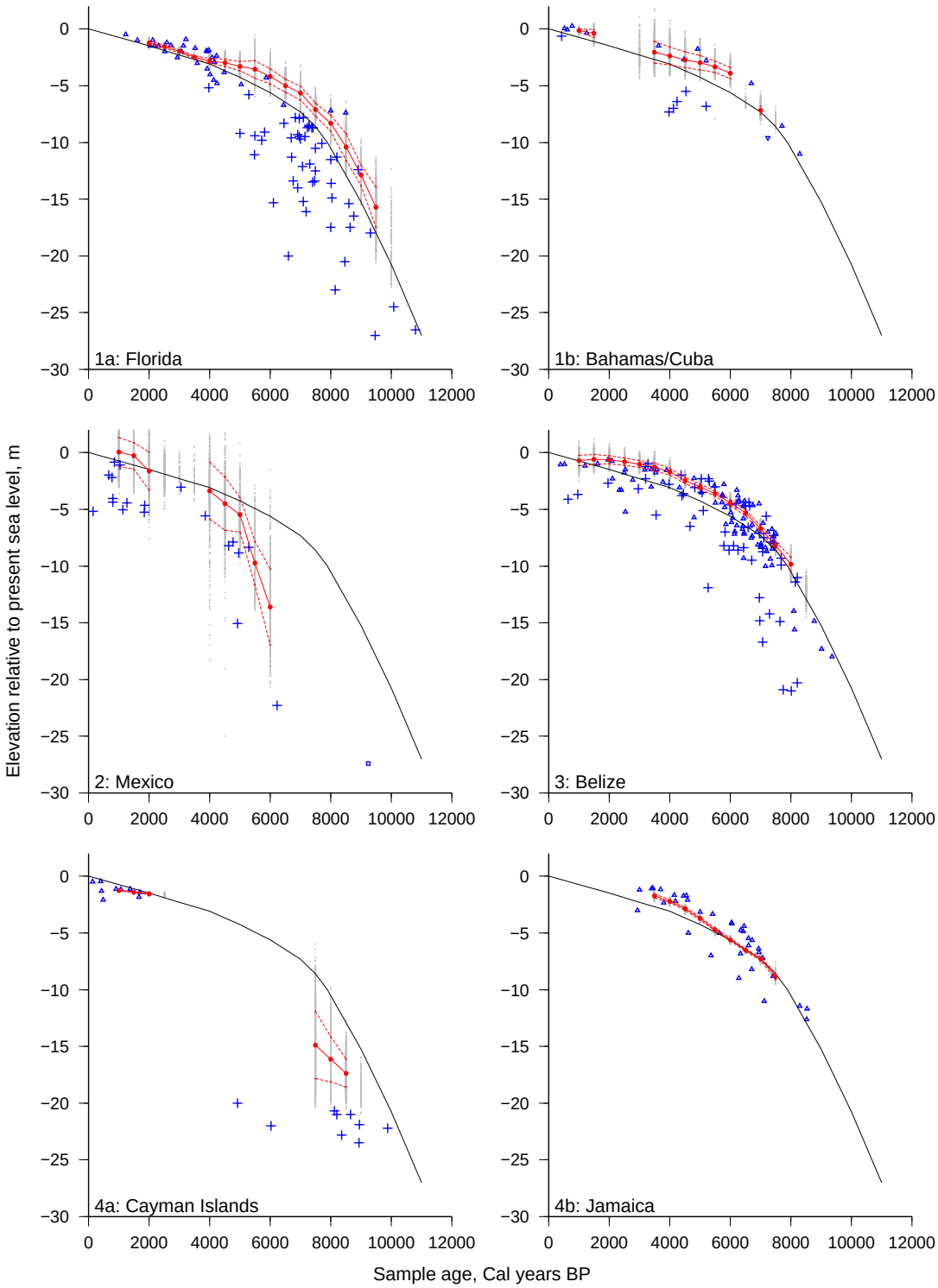

Figure 2.12: Regional sea-level curves for regions 1a to 4b (2000 year time window). Western Atlantic Sea-Level (WASL) curve (Toscano and Macintyre, 2003) plotted in black.

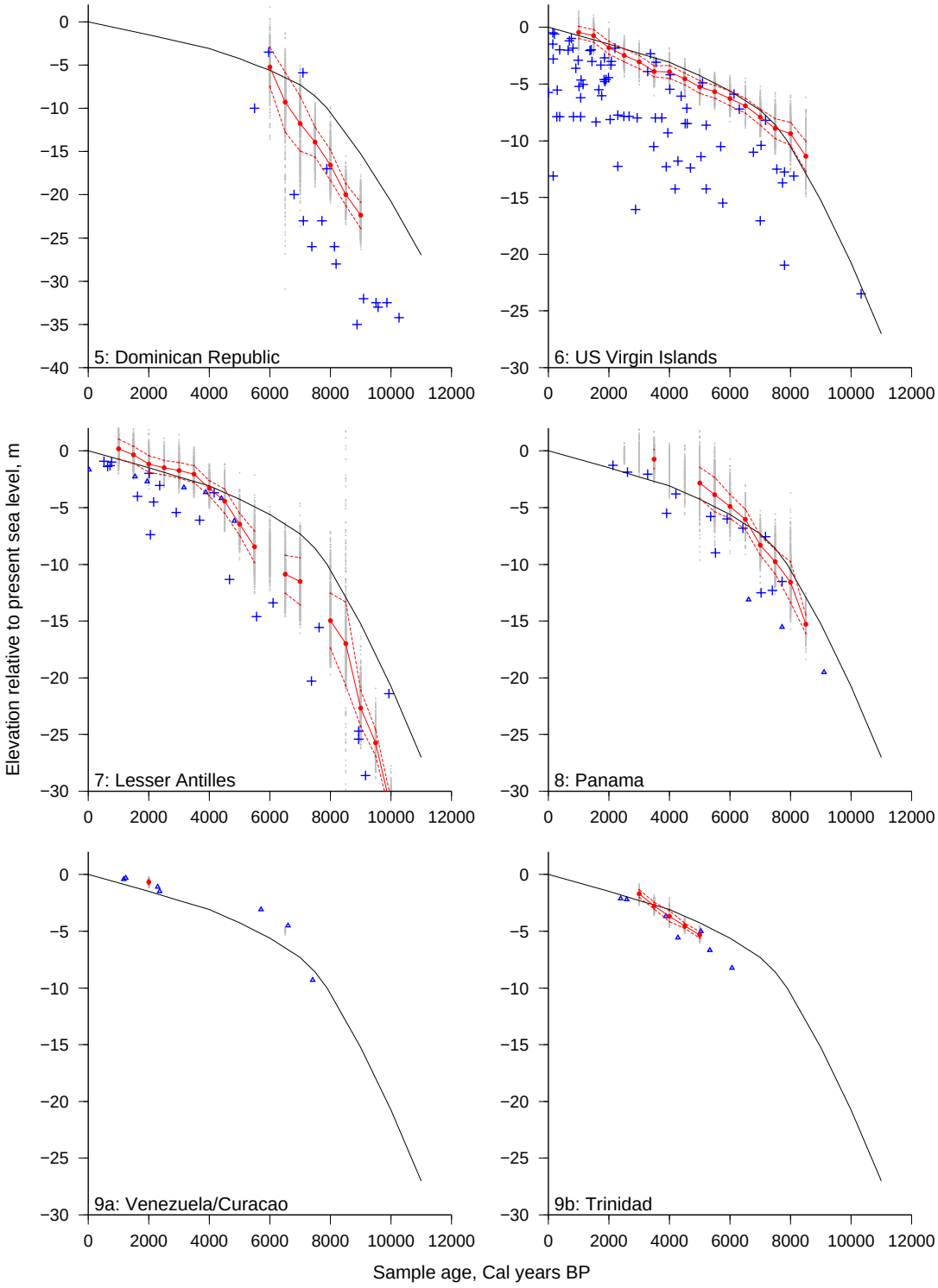

Figure 2.13: Regional sea-level curves for regions 5 to 9b (2000 year time window). Western Atlantic Sea-Level (WASL) curve (Toscano and Macintyre, 2003) plotted in black.

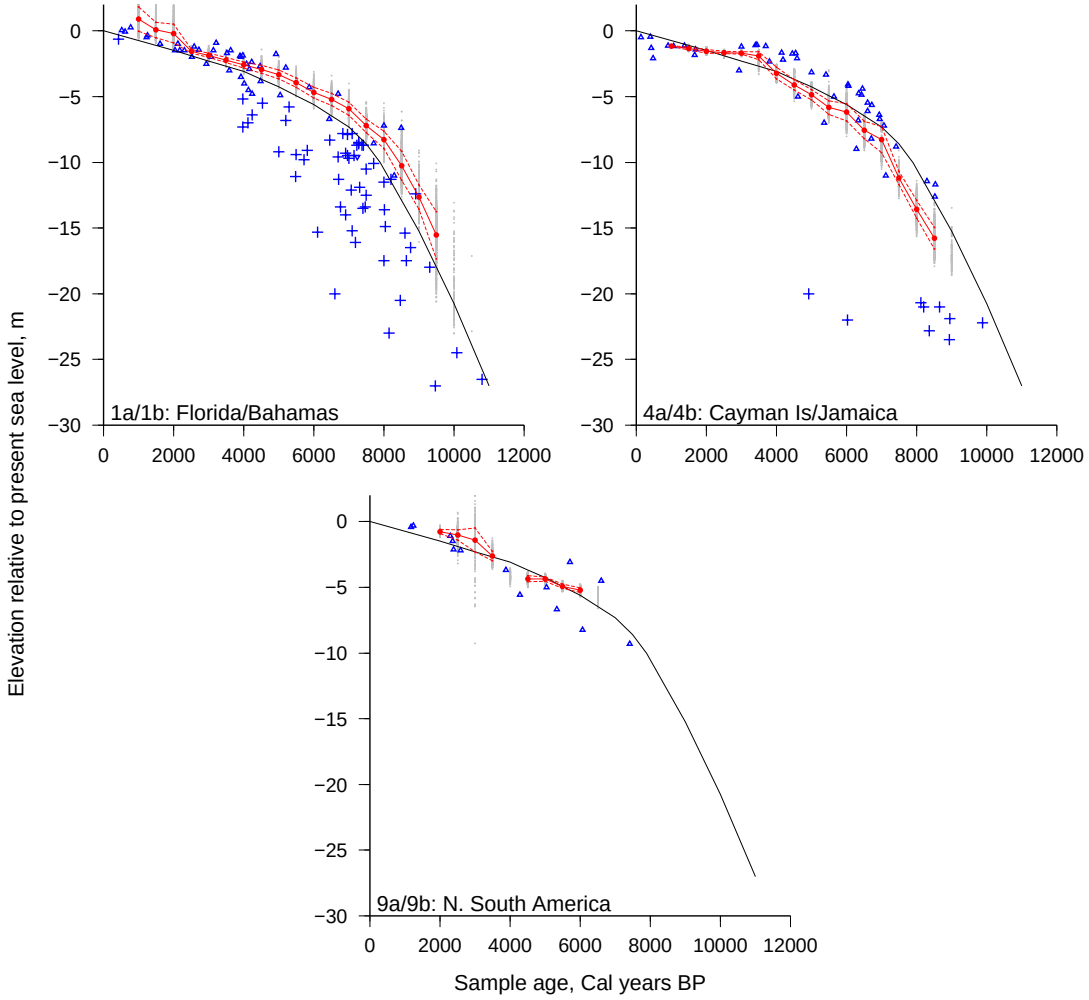

Figure 2.14: Regional sea-level curves for collated regions 1 (1a,1b), 4 (4a,4b) and 9 (9a,9b) (2000 year time window). Western Atlantic Sea-Level (WASL) curve (Toscano and Macintyre, 2003) plotted in black.

Caribbean. The Florida, Bahamas and Belize sub-regions show rates of 1 - 2 mm yr^{-1} occurring between 7000 - 5500, 7000 - 5500 and 7000 - 4500 cal yr BP respectively, whilst Barbados and Trinidad show the same rates between 6500 - 4000 and 4500 - 3000 cal yr BP respectively.

Other points of note are the slowing down of sea-level rise in the early Holocene (12000 - 8000 cal yr BP) across the Caribbean after the bulk of global deglaciation had been completed (Peltier, 2004). The $\geq$ 3 mm yr^{-1} rise occurs in Florida prior to 8500 cal yr BP, in Barbados prior to 7500 cal yr BP (at 10000 cal yr BP it was 12 mm yr^{-1}), at Panama prior to 8500 cal yr BP, at the Dominican Republic prior to 8000 cal yr BP.

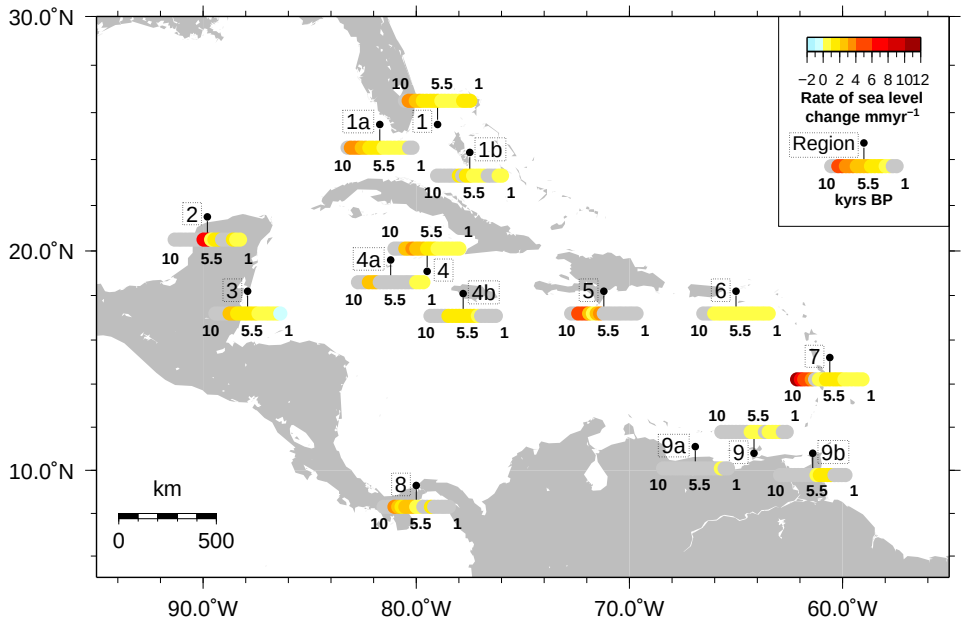

Figure 2.15: Average rates of relative sea-level change (circles) as measured within in each 500 year time window for each regional subset (labelled in dashed box) of the indicator catalogue. Grey circles are where no rate is obtainable.

2.8 Discussion

2.8.1 Characterisation of Holocene sea-level rise

The Holocene sea-level curves and the associated rates calculated using this probabilistic, windowing approach are dominated by a large scale sea-level rise common to all the sub-regions. This is due to the input of melt-water from the formerly glaciated regions of the polar regions, particularly the Northern hemisphere. To quantify where this melt water has come from, the next chapter will consider numerical models of an Earth-like globe, which experiences stepwise deglaciation over a 25000 year period, simulating the vertical ground motion and sea-level responses.

As mentioned in the Results, there are a number of time variations in the rise of sea level across the sub-regions of the Caribbean. This is shown in Figure 2.16, which shows six of the sub-regional sea-level curves and the WASL curve. The primary result is a lag of 1500 years in the South Eastern Caribbean compared to the North and Western Caribbean sea-level curves (compare 1 and 3 with 7 in Figure 2.16). Furthermore, there are shape differences between curves in Florida and Belize, which demonstrates that sea level in Belize rose to present level before Florida.

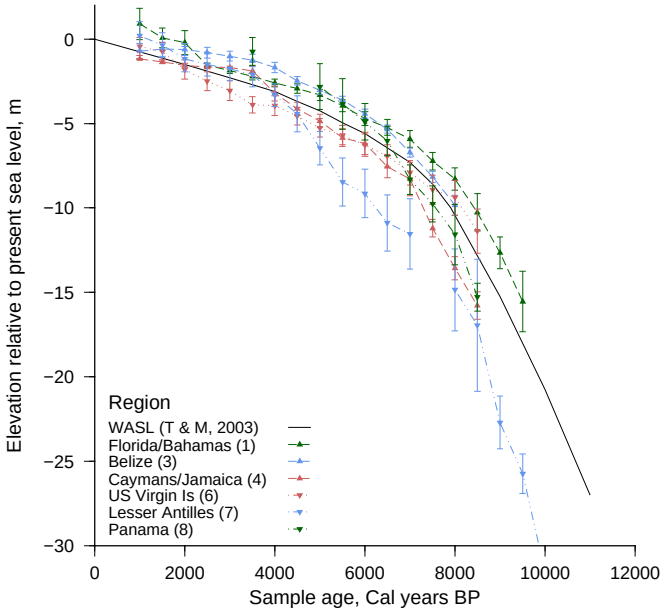

Figure 2.16: Compilation of relative sea-level curves and the standard deviation in their vertical position for regions Florida/Bahamas (1), Belize (3), Caymans/Jamaica (4), US Virgin Islands (6), Lesser Antilles (7) and Panama (8). WASL curve (Toscano and Macintyre, 2003) shown in black.

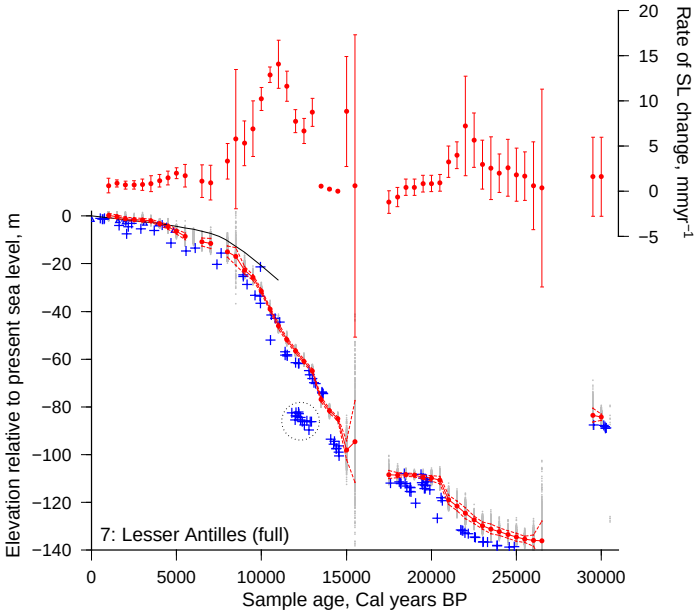

Figure 2.17: Relative sea-level curve (lower) and calculated rates of sea-level change (upper) of full Lesser Antilles (8) time span. See Holocene section in Figure 2.13. Indicators (*M annularis*) inside dashed circle omitted from calculation of sea-level curves because difference in vertical position compared to indicators directly above them (*A palmata*) is greater than vertical distribution ascribed. WASL curve (Toscano and Macintyre, 2003) shown in black.

Figure 2.17 shows the full Lesser Antilles curve and the averaged calculated rates for each time slice. Indicators prior to 7500 cal yr BP all belong to Barbados (Fairbanks, 1989, Peltier and Fairbanks, 2006). This curve shows the rapid rises in sea level during the Late Pleistocene/Early Holocene, where rates ranged between 5 and 15 mm yr^{-1}. I note that indicators inside the dashed circle (*M annularis*) in Figure 2.17 were omitted from the calculation of the calculated relative sea-level curves. This is because the difference in stratigraphic position between the circled *M annularis* and *A palmata* indicators above them is greater than the vertical distribution ascribed to the *M annularis* ($\geq$20 m). Since the *A palmata* has a narrower habitable depth range than the *M annularis*, I favour the former samples given that the latter could still live at the depths predicted by the resultant curve (i.e. *M annularis* could live at greater than 20 m below sea level, but *A palmata* can not live above sea level).

Although the Caribbean region is tectonically active (e.g. Pindell and Kennan (2009)), the common published consensus is that vertical ground motion has been limited, or non-existent at the coastal localities used in this study during the Holocene: Florida, Mullins and Neumann (1979); Bahamas, Carew and Mylroie (1995); Belize, Dillon and Vedder (1973); Dominican Republic, Mann et al. (1984, 2002); US Virgin Islands, Hubbard et al. (2005), Macintyre et al. (2008); Barbados, Fairbanks (1989); Venezuela, Rull et al. (1999). The only region I question this assumption is in the Dominican Republic (5), whose calculated sea-level curve (Figure 2.13a) deviates significantly from the curves in adjacent regions (Jamaica (4b) and US Virgin Islands (6)). It is probable that the proximity of the Enriquillo Basin to the Enriquillo fault, whose trace follows the Enriquillo Valley (Mann et al., 2002) and the present sub-sea elevation of the valley have contributed to this deviation, particularly prior to 7000 cal yr BP. Alternatively, if one follows Cuevas et al. (2009), the low coral growth rates imply a sediment heavy environment coupled with a deeper species habitat than the vertical distribution allowed (similar to the problem of *M annularis* in Barbados outlined above). This strong deviation of the Dominican Republic (5) sea-level curve from the WASL curve raises a number of questions regarding the windowing method used for sea-level curve construction, which I discuss below.

2.8.2 Methodological comments

A visual comparison between the WASL curve (Toscano and Macintyre, 2003) and the constructed sub-regional sea-level curves demonstrates that the methods applied in this chapter produce successful results. The best curves are produced from dense temporally spaced, inter-tidal peat samples (e.g. Jamaica (4b), Figure 2.12f) or
A palmata coral samples (e.g. US Virgin Islands (6) and Lesser Antilles (7), Figure 2.13b and c). Furthermore, the combination of the two indicator types (coral and peat) is preferable although the dense time spacing of the indicators is the most important factor for sea-level curve reconstruction.

The two areas of the methodology that require consideration are the vertical depth distributions of the coral habitable ranges and the window length used for the curve construction. As stated earlier, the coral vertical distributions are derived from growth, abundance and distribution measures from published literature for the Caribbean. The measures for each species are at discontinuous depths and I have had to perform a normalisation to obtain weighted median depths. Furthermore, the growth, abundance and distribution measures are used as modern analogues for Pleistocene/Holocene coral depth distributions. Also, the coral depth ranges are averaged across the Caribbean, rather than reef/regionally specific species depth ranges.

As I mentioned in section 2.6, the window length used for the sea-level curve construction dictates the smoothness of the curve and the accuracy of the vertical position of sea level in the past. The window length needs to be long enough for most time slices to contain more than three data points, but short enough to describe the nature of the sea-level rise during a section of the Holocene/Pleistocene. Based on the region with the sparsest data (region 9a/9b), I elected to use 2000 years. This allows the Holocene (12000 years to present) to be considered in at least 6 sections.

2.8.3 Searching for the global meltwater signal

One of the opportunities the Caribbean provides is to use sub-regional sea-level curves to identify areas that mimic the global meltwater sea-level signal, termed eustatic sea level (this will be discussed more fully in the next Chapter). This component is defined as a globally uniform height shift of the ocean surface that would occur (in the absence of gravitational effects and Earth deformation) due to mass input from continental ice reservoirs (e.g. Farrell and Clark (1976), Milne and Mitrovica (2008)). To test the

locations one might expect to observe eustatic sea level, scientists use computer models to simulate deglaciation on an Earth-like sphere. The regions that predict the eustatic sea-level signal are sensitive to deglacial ice model and Earth structure.

Milne and Mitrovica (2008) predicted the regions one might expect to find records of eustatic sea-level change for different deglaciation models (Figure 2.18). For the ICE-5G deglaciation model (Figure 2.18b, Peltier (2004)), the Barbados (7), Panama (8) and Venezuela/Trinidad (9) regions lie in the eustatic zone (Milne and Mitrovica, 2008). Although none of the three sea-level curves in question rise above present sea level, the large standard deviations in vertical sea-level position for Panama and sparse data in Venezuela/Trinidad make the true eustatic curve difficult to define. The ICE-5G model uses the Barbados data set as a proxy for eustatic sea-level rise. Since the Barbados data set has been the subject of much debate (e.g. Milne and Mitrovica (2008), Bard et al. (2010)), I will investigate the question of eustatic sea-level change in the next chapter.

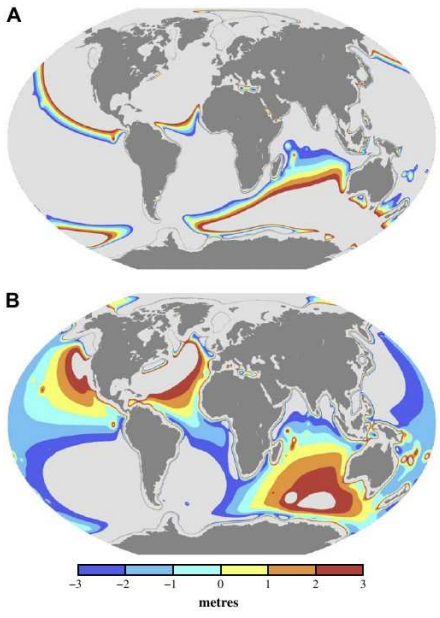

Figure 2.18: Predicted total RSL change minus the model eustatic component from 21000 cal yr BP to the present-day with restricted contour range ±3 m. (A) Prediction based on the Bassett et al. (2005) ice model and the associated Earth model. (B) Prediction based on the ICE-5G/VM2 ice-earth model (Peltier, 2004). The zero contour is where RSL is equal to model eustatic value. Reds and blues indicate sea levels that are above and below the eustatic value. Figure reproduced with permission from Milne and Mitrovica (2008).

Chapter 3

Modelling Caribbean Sea-level change

3.1 Introduction

In the previous chapter, I implemented a method to construct relative sea-level (RSL) curves at the sub-regional scale across the Caribbean. All the curves are dominated by a large scale sea-level rise during the Holocene, this tens of metres scale rise is attributed to the deglaciation of the polar regions.

In this chapter, I use a numerical model to simulate the deglaciation on an Earth-like sphere to investigate the temporal and spatial variation of sea level during the Holocene deglaciation. I will compare the results of sea-level change from the model with the RSL curves I derived in the previous chapter in order to define a best fitting Earth model to the Caribbean region, develop an understanding of which ice centre (e.g. Antarctica, Greenland) dominated sea-level rise for the Caribbean and ascertain what differences in Earth model occur across the Caribbean.

3.2 Glacial Isostatic Adjustment

3.2.1 Glacial cycles and sea-level response

The deglaciation from around 21000 cal yr BP is the most recent of numerous glacial cycles primarily controlled by periodicities in orbital eccentricity (100,000 years), obliquity (40,000 years) and precession (22,000 years) resulting in significant heating and cooling in the polar regions (e.g. Lambeck et al. (2010)). The last glacial cycle extends back to approximately 125,000 year BP (Lambeck and Chappell, 2001), resulting in

100,000 years of ice accumulation and sea-level fall. The result of the deglaciation was a rapid melting of ice, particularly ice on land, and a global rise in RSL. Figure 3.1 shows a schematic diagram of the effect of deglaciation.

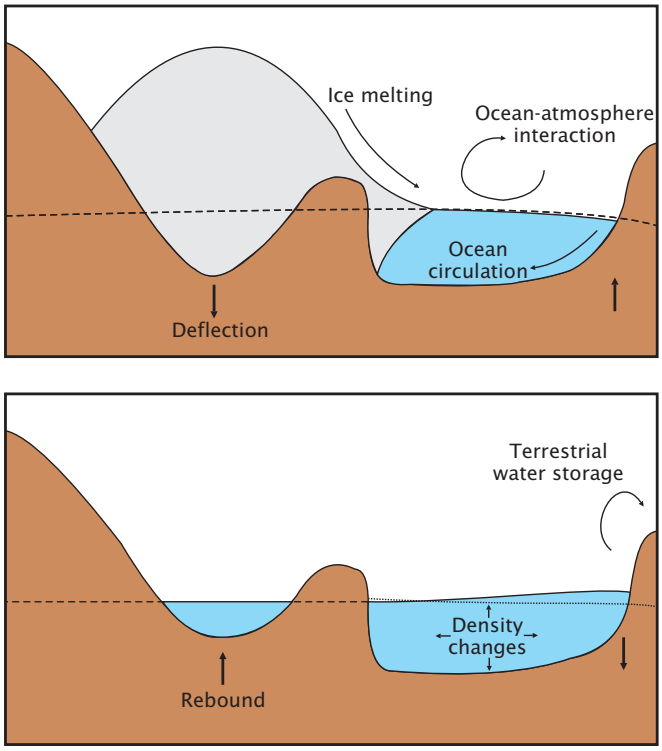

Figure 3.1: Schematic diagram showing the Earth, ocean and atmospheric response to loading (top) and unloading (bottom) of an ice sheet.

Sea-level change occurs in response to a number of interrelated factors: (1) ice volume variation, (2) land surface displacement due to load change, (3) changes in gravitational potential due to deformation and mass redistribution, (4) ocean basin shape change, and (5) water redistribution to retain an equipotential surface. Glacial Isostatic Adjustment (GIA) is defined as the combination of surface deformation and geoid changes of the ocean surface. It is important to understand these factors completely because they are global, are dominant during glacial cycles and continue long after ice volumes have stabilised.

The simplest method to calculate how much sea level rises or falls due to ice loss or gain on the Earth is to assume that sea-level changes by the same amount everywhere on the Earth. This assumes a rigid, non-rotating sphere with no gravitational effects. If I know the surface area of the world's oceans and the melt water equivalent of the ice to be lost or gained, I can calculate the eustatic change in sea level using,

$$\Delta \text{SL} = \frac{\Delta \text{Ice volume} \times 0.917}{\text{Surface area oceans}} \tag{3.1}$$

where 0.917 is the density ratio between water and ice and the oceans cover 71 % of the Earths surface. Therefore, if I observe a 10 mm sea-level rise and assume that this is the same change everywhere in the oceans, I use equation 3.1 to infer an equivalent ice volume loss of 3949 km^3. The complexity of this model is made more realistic by considering the effect of gravitational attraction.

The theory of gravitational attraction due to a point ice mass was first considered by Woodward (1888) who derived an equation for RSL change on a rigid Earth when water from the ocean is "frozen" a point in time,

$$R = \frac{\left(\frac{1}{2\sin(\theta/2)} - 1 - \frac{\rho_E}{3\rho_w}\right)}{\frac{\rho_E}{3\rho_w}} \tag{3.2}$$

where R is the ratio between the actual sea-level change and the change neglecting the effect of attraction. ρ_E and ρ_w are the densities of the Earth (5500 kg m^{-3}) and water (1000 kg m^{-3}) respectively and θ is the angular distance from the point ice mass. Table 3.1 shows that there is virtually no change in sea level 20^o away from the ice; within this angular distance sea level falls and beyond this angular distance sea level rises. If one were to change the geometry of the equation to allow multiple point masses on a spherical body, one could study how sea level would be distributed at the "frozen" time slice. The next stage in GIA modelling was to combine equations 3.1 and 3.2 in a method to model the redistribution of water whilst accounting for the variations shown in Figure 3.1.

Table 3.1: The vertical position of sea level for a fixed moment in time at increasing distance from a point ice mass (at $\theta = 0^o$ using the theory of Woodward (1888) (Equation 3.2). After Farrell and Clark (1976)).

θ (^{o})	R
1	+ 29.7
10	+ 1.6
20	0.0
45	-0.8
60	-1.0
90	-1.2

3.2.2 Retrospective sea-level prediction

The seminal paper by Farrell and Clark (1976) presented for the first time a method of calculating changes in sea level that occur when ice and water masses are rearranged on an Earth-like surface, that is elastic/viscoelastic and non-rotating. The numerical modelling methods first expounded by Farrell and Clark (1976) were made more computationally efficient and accurate with the introduction of a pseudo-spectral algorithm for a gravitationally self-consistent sea-level solution that would allow much higher spherical harmonic degrees ($l \gg 100$) (Mitrovica and Peltier, 1991). This method has become the standard tool to model GIA (e.g. Spada and Stocchi (2007); Mitrovica and Milne (2003)). The introduction of time varying shoreline geometry (e.g. Johnston (1993); Milne and Mitrovica (1998a)) and Earth rotation (Milne and Mitrovica, 1998b) has greatly improved sea-level change estimates (due to GIA). The generalised sea-level equation has been explicitly defined by Mitrovica and Milne (2003) and Kendall et al. (2005). By selecting a specific glaciation/deglaciation model and 1-dimensional Earth structure, the numerical implementation of this equation gives theoretical RSL change and vertical ground motion (VGM). These GIA model RSL curves can be used retrospectively to compare to indicators of RSL to improve the Earth model and ice model.

Clark et al. (1978), for an instantaneous uniform melting scenario of the Northern hemisphere ice sheets, determined a series of regions across the globe each of which have diagnostic GIA model RSL curves (Figure 3.2). These depend upon their distance from centres of deglaciation and the contribution of ocean basin subsidence/ land uplift due to GIA.

The Caribbean region overlaps the intermediate (zone III) to far field (zone IV) regions relative to the Northern hemisphere distribution of the ice sheets. These two types of diagnostic GIA model RSL curves are shown in Figure 3.2b. The intermediate (zone III) curve shows a time dependent emergence in the late Holocene implying raised beaches and RSL above present day. The far-field (zone IV) curve is not emergent and is affected by the subsidence of the ocean basin due to the flux of water from the distant ice centres (Mitrovica and Milne, 2002). At tectonically stable locations within the Caribbean, one would expect that the RSL signal would be of small ($\sim$0.5 m) emergence in the mid-Holocene in the north and a zone of no emergence for the same time in the south (Clark et al., 1978).

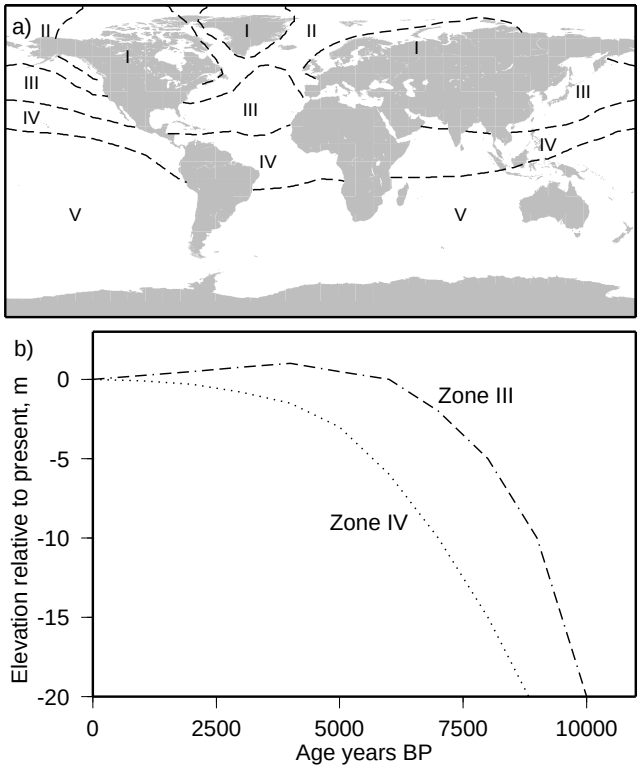

Figure 3.2: **a**: Illustration of five sea-level zones for a uniform instantaneous melting of Northern hemisphere ice sheets during the last deglaciation. Zones represent: I, glaciated areas; II, fore-bulge to ice margin; III, time dependent emergent zone; IV: oceanic submergence, V: oceanic emergence. Within each zone the sea-level signatures at all locations are similar to one another. Reproduced with permission from Clark et al. (1978). **b**: Sea-level signatures expected from zones III and IV, which partition the Caribbean in this model

3.2.3 Numerical modelling

The sea-level model solves the generalised sea-level equation (Mitrovica and Milne, 2003, Kendall et al., 2005). It contains time-varying shoreline migration and Earth rotation parameters, which are both calculated at each time step of ice/melt redistribution. The algorithms to solve the problem are in the spectral domain. The pseudo-spectral approach of Mitrovica and Peltier (1991) allows one to represent any geometrically spherical field (ice mass distribution, bathymetry, surface deformation, ocean distribution and rotational deformation) as a set of harmonics to a certain truncation level. The degree of the harmonics defined the resolution of the model. I use spherical harmonics up to degree 256, which gives a resolution of approximately 150 km (east-west) by 75 km (north-south). The FORTRAN 95 code used in this study was provided by Mark Tamisiea (National Oceanographic Centre, Liverpool).

For any position, (θ, ψ) and time (t_j), the sea level ($\mathrm{SL}(\theta, \psi, t_j)$) is defined as the difference between the geoid (gravitational equipotential; $\mathrm{G}(\theta, \psi, t_j)$) and the radial position of the solid surface ($\mathrm{R}(\theta, \psi, t_j)$),

$$\mathrm{SL}(\theta, \psi, \mathrm{t_j}) = \mathrm{G}(\theta, \psi, \mathrm{t_j}) - \mathrm{R}(\theta, \psi, \mathrm{t_j}). \tag{3.3}$$

The change in sea level (ΔSL) is simply the difference between geoid height change (ΔG) and solid Earth height change (ΔR) over a given time,

$$\Delta\mathrm{SL}(\theta, \psi, \mathrm{t_j}) = \Delta\mathrm{G}(\theta, \psi, \mathrm{t_j}) - \Delta\mathrm{R}(\theta, \psi, \mathrm{t_j}) \tag{3.4}$$

where

$$\begin{aligned} \Delta\mathrm{G}(\theta, \psi, \mathrm{t_j}) &= \mathrm{G}(\theta, \psi, \mathrm{t_j}) - \mathrm{G}(\theta, \psi, \mathrm{t_0}) \\ \Delta\mathrm{R}(\theta, \psi, \mathrm{t_j}) &= \mathrm{R}(\theta, \psi, \mathrm{t_j}) - \mathrm{R}(\theta, \psi, \mathrm{t_0}). \end{aligned} \tag{3.5}$$

t_0 is a time prior to the onset of glaciation (Mitrovica and Milne, 2003).

In the previous chapter RSL was measured with respect to present day sea level (e.g. present day sea level has an RSL elevation of zero),

$$\mathrm{RSL}(\theta, \psi, \mathrm{t_{past}}) = \mathrm{SL}(\theta, \psi, \mathrm{t_{past}}) - \mathrm{SL}(\theta, \psi, \mathrm{t_{present}}). \tag{3.6}$$

To remain consistent, I correct modelled sea-level changes ($\Delta\mathrm{SL}(\theta, \psi, \mathrm{t_j})$) by the value of the sea-level change predicted at present to give RSL change. Unlike the modelled RSL values, RSL indicators are affected by more than just eustatic, isostatic and rotational variations. Changes relating to a number of environmental and geophysical factors can be described by (Shennan et al., 2012),

$$\begin{aligned} \Delta\mathrm{RSL}(\theta, \psi, \mathrm{t}) &= \Delta\mathrm{EUS}(\mathrm{t}) + \Delta\mathrm{ISO}(\theta, \psi, \mathrm{t}) + \Delta\mathrm{TECT}(\theta, \psi, \mathrm{t}) \\ &\quad + \Delta\mathrm{LOCAL}(\theta, \psi, \mathrm{t}) + \Delta\mathrm{UNSP}(\theta, \psi, \mathrm{t}). \end{aligned} \tag{3.7}$$

where ΔEUS is the eustatic signal, ΔISO is the total isostatic contribution of the glaciation history, ΔTECT is the local tectonic effect, ΔLOCAL is the effect due to local coastal environmental and ΔUNSP are all other unspecified factors.

The eustatic signal has been described in section 3.2.1. ΔISO describes the spatially

varying ice load, water load and rotational contributions of GIA (e.g. Milne et al. (2005)). Whilst oceanic areas some thousands of kilometres from the glaciated regions (Figure 3.2 zones IV and V) are dominated by the water loading signal (termed hydro-isostasy), those areas close to the glaciated regions (zones I and II) are dominated by ice loading signal (Clark et al., 1978, Mitrovica and Milne, 2002, Milne et al., 2005). GIA models can be used to estimate ΔEUS and ΔISO.

Long term local uplift or subsidence caused by regional tectonics can contribute millimetres to centimetres per year to the position of sea level. An earthquake containing a vertical component of slip can cause rapid (within hours) uplift or subsidence to alter sea-level indicator positions and tide gauge measurements (discussed in Chapter 5). Measurements of VGM, either total change or rates of change are not well resolved across the Caribbean.

The coastal environment and the local dynamical processes of sedimentation and tidal variation are difficult to quantify. They rely upon high resolution near-shore sediment cores, coupled ocean-climate models and palaeo-bathymetry (Shennan et al., 2012). Most regional scale studies assume the sum of local and unspecified factors to be close to zero (Shennan et al., 2012).

3.3 Deglaciation and Earth models

As mentioned in the previous section, the computer model used to solve the generalised sea-level equation requires two inputs: an ice model and an Earth model. The two are interrelated, since Earth viscosity-depth profiles are often derived from time dependent uplift measurements (e.g. relaxation-time spectrum from Scandinavia: Wieczerkowski et al. (1999)), a direct result of deglaciation. Ice glaciation/deglaciation models are tuned to fit dated RSL measurements, which rely upon known viscosity-depth models. The problem is non-unique. In this study, I choose to use a single ice model, ICE-5G (Peltier, 2004) and vary the Earth model to best fit my dated RSL measurements.

3.3.1 Ice model: ICE-5G

Any successful model of the last deglaciation must satisfy the available global constraints upon the net amount of water that was added to the oceans (Peltier, 2004). Furthermore, the veracity of a particular ice model is dependent upon the quality of

the observational evidence and level of glaciological complexity (Mitrovica et al., 2010). Geological evidence provides information on ice sheet extent and flow direction, whilst GIA observables (e.g. RSL, gravity changes, crustal deformation) are useful to quantify total ice volumes.

The ICE-5G deglaciation model (Peltier, 2004) attempts to reconcile these two types of observational evidence. This model is the fifth iteration in a series (prior models: ICE-1,-2,-3G and -4G, Peltier and Andrews (1976), Wu and Peltier (1983), Tushingham and Peltier (1991), Peltier (1994) respectively) and represents the global deglacial history as a series of gridded ice thicknesses at 1000 (32,000 years BP to 17,000 years BP) and 500 year (17,000 years BP to present) time slices. Figure 3.3a-c shows the distribution and thickness of the ICE-5G model at three of these time slices. Figure 3.3d shows the equivalent eustatic sea-level rise of the deglaciation and the contributions of the major ice sheets during this time period. Various aspects of the ICE-5G model have been questioned, for example the volume of Antarctic melt water (17.3 m eustatic equivalent) appears to be too high compared to other studies of the same region (e.g. 6.1 - 13.1 m: Bentley (1999)). However, ICE-5G has been tuned primarily to fit the total global eustatic sea-level rise, which is in part constrained by the Barbados sea-level record Fairbanks (1989), Bard et al. (1990), Peltier (2004). It is also important to note that ICE-5G is coupled to a specific Earth model, VM2 (see Figure 3.4) demonstrating the trade-off between the two model components (ice and Earth input) to best fit global observables.

3.3.2 Earth model

The Earth model required is one-dimensional and is characterised by user-defined lithospheric thickness, upper and lower mantle viscosities, and the elastic and density structure of seismic model PREM (Dziewonski and Anderson, 1981). Much work has been done on calculating appropriate user-defined model inputs since it is one of the few ways of estimating mantle viscosity (e.g. Peltier (1974), Mitrovica and Forte (1997, 2004), Milne et al. (2005), Bradley et al. (2011)).

The definition of the lithosphere for GIA modelling is the rheological contrast at the lithosphere - asthenosphere boundary. Although the crust - mantle transition is a more distinct boundary from a chemical point of view, the region below the crust can be approximated to the lithosphere because it still behaves elastically on time scales of

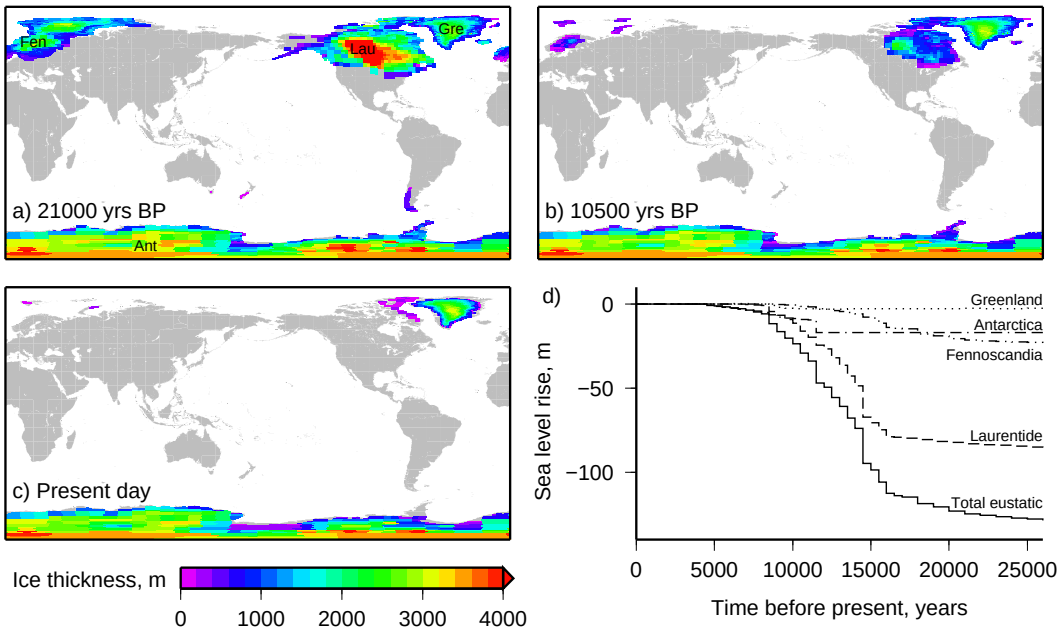

Figure 3.3: **a-c**: Ice extent and thickness of ICE-5G deglaciation model (Peltier, 2004) at 21000, 10500 and 0 years BP. **d**: Meltwater equivalent RSL rise of ICE-5G model and the contributions of major ice centres (Lau: Laurentide, Fen: Fennoscandia, Ant: Antarctica, Gre: Greenland).

thousands of years (typical GIA time scale).

Haskell (1935) first estimated the viscosity of the mantle theoretically using the loading of an isoviscous, incompressible half-space to approximate the post-glacial uplift and uplift rate in Scandinavia. The result, dynamic viscosity of 10^{21} Pa s, has been widely accepted as the average mantle viscosity (Mitrovica, 1996). I, like other researchers in this field, use this value as a centre point from which to refine the Earth model into upper and lower mantle viscosities.

Figure 3.4 shows the range of results from Mitrovica and Forte (2004) who infer mantle viscosity with depth using a joint inversion of convection and GIA data. Figure 3.4 also shows the best fitting Earth model of Peltier (2004), VM2, which is coupled to the ICE-5G deglaciation model. The depth averaged parameters for VM2 (Peltier, 2004) give a lithospheric thickness of 90 km and upper and lower mantle viscosities of 0.5 and 2.7 x 10^{21} Pa s respectively (Spada and Galassi, 2012). All the authors referred to above record that viscosity significantly increases (up to three orders of magnitude: Mitrovica and Forte (2004)) from the upper mantle to the lower mantle.

I choose to run the sea-level solving programme at lithospheric thicknesses, 71,

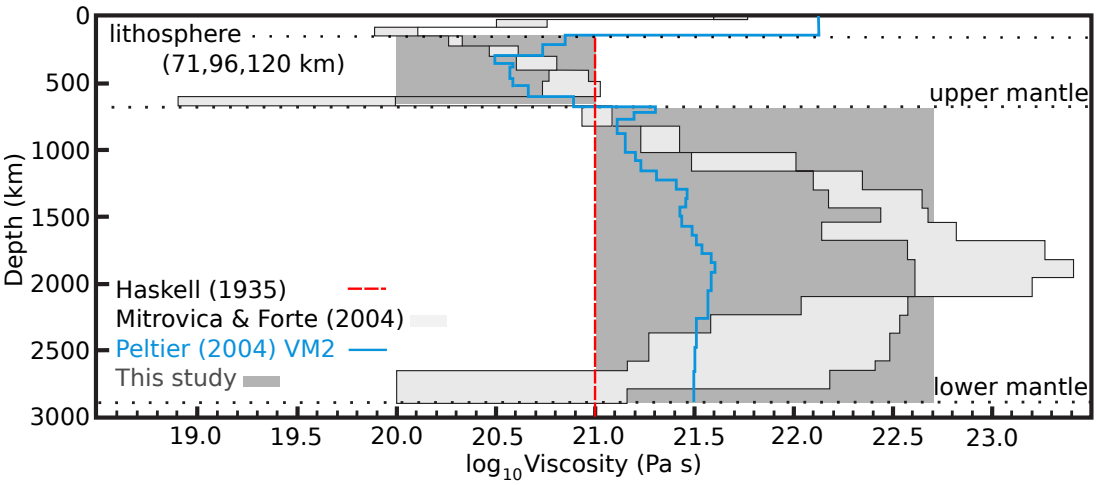

Figure 3.4: Viscosity-depth profile showing the major interfaces within the Earth (lithosphere, upper and lower mantle). Solutions from Mitrovica and Forte (2004) (light grey) and Peltier (2004) (blue) show the range of viscosities theorised (VM2 of Peltier (2004) is coupled to ICE-5G deglaciation model). Viscosity range for model Earth parameters used in this study shown in dark grey and specified in Table 3.2.

Table 3.2: Range of model Earth parameters used in this study as inputs for generalised sea-level equation (Mitrovica and Milne, 2003).

Parameter	Unit	Values
Lithospheric thickness	km	[71 96 120]
Upper mantle viscosity, υ_{UM}	x 10^{21} Pa s	[0.1 0.2 0.4 0.5 0.6 0.8 1.0]
Lower mantle viscosity, υ_{LM}	x 10^{21} Pa s	[1 2 5 10 20 30 40 50]

96 and 120 km and in the upper and lower mantle viscosity ranges highlighted in Figure 3.4 and specified in Table 3.2. These ranges are typical of those used amongst the GIA research community (e.g. Milne et al. (2005)). The ranges encompass VM2 (Peltier, 2004) and cover the bulk of the parameter space of Mitrovica and Forte (2004), exempting their extreme values at the base of the upper mantle and the centre and base of the lower mantle.

3.4 Determining model Earth parameters

The RSL derived curves constructed in the previous chapter and the coupled age-depth probability distributions of the RSL indicator catalogue are utilised here to ascertain the best model Earth parameters for each of the sub-regions in the Caribbean. For a particular region, I calculate the χ^2 misfit between the GIA model predicted RSL curve (SL_i^{p}) and either the RSL indicator realisations or the RSL derived curve (SL_i^{obs}). The misfit is given by,

$$\chi^2 = \frac{1}{(N-1)} \sum_{i=1}^{N} \left(\frac{(\mathrm{SL}_i^p - \mathrm{SL}_i^{\mathrm{obs}})}{\sigma_i} \right)^2 \tag{3.8}$$

where σ_i is the observed depth error of the sea-level data and N is the total number of data (e.g. Bradley et al. (2011)). The determination of χ^2 misfits varies slightly depending upon if I compare the GIA model RSL curves to the derived RSL curves or the RSL indicator realisations, therefore I describe each in turn. Since the derived RSL curves are directly linked to the RSL indicator realisations, I expect there to be agreement between their χ^2 misfits for the range of GIA model RSL curves used.

I also calculate the 95% confidence region to the minimum misfit by using statistical look-up tables of the F-distribution given the number of data, N (Riley et al., 2006). For example, 15 data points gives both 15 degrees of freedom in the numerator and denominator giving a scale factor of 2.40. This scale factor is multiplied by the minimum χ^2 misfit to give a contour of 95% confidence. The more data that is available, the lower the scale factor. There is a trade off between the number of data and the position of the realisations or derived RSL curve points compared to the GIA model RSL curve.

3.4.1 χ^2 misfit: RSL curves

The misfit calculation between model and data derived RSL curves is trivial. Each data derived RSL curve has a given elevation and a standard deviation, which represent $\mathrm{SL}_i^{\mathrm{obs}}$ and σ_i respectively. These elevations are spaced at 500 year time steps. I linearly interpolate the GIA model RSL curve to 500 year time steps (this is not required post 17,000 years BP, see section 3.3.1) and solve equation 3.8 for each Earth model.

3.4.2 χ^2 misfit: RSL indicators

In the previous chapter I showed that coral sea-level indicators do not have a Gaussian depth distribution, that is they can't be described by a mean and standard deviation. To solve the misfit calculation then, I utilise random sampling of the age-depth distributions of the RSL indicators. Firstly, for a given region I derive 1000 sea-level positions for each RSL indicator based upon the age-depth distribution of the sample (e.g. coral or peat). Then for each suite of RSL indicator realisations (1000 total) I calculate the χ^2 misfit with the model RSL curve. σ_i is the standard deviation of the 1000 RSL positions for each indicator (i). This results in 1000 χ^2 misfit values between

a single model RSL curve and a set of RSL indicator realisations. The average of this suite of misfit values is used as the χ^2 misfit for that Earth model parameterisation.

3.5 Results and Discussion

3.5.1 Model curves and misfits

Figures 3.5 and 3.6 show for Florida and Lesser Antilles respectively, the suite of GIA model RSL curves (using the parameters in Table 3.2), the χ^2 misfit and 95% confidence region between the GIA model RSL curves and the data derived RSL curves and the χ^2 misfit between the GIA model RSL curves and the RSL indicator derived realisations. The χ^2 plots for the other sub-regions are shown in Appendix C. In addition, Figure 3.7 shows the overall χ^2 misfit and 95% confidence regions using all the data derived RSL curves (a, c, e) and RSL indicator derived realisations (b, d, f). Note the change in colour scale between the sub-regional misfit contour plots (e.g. Figure 3.5) and the full-region misfits (Figure 3.7).

It is evident that the two methods of deriving the χ^2 misfit give similar patterns of contouring, although the magnitude of the misfit varies between them. Visually, the misfit appears to be invariant to lithospheric thickness and there generally appears to be a tighter bound upon the range of lower mantle viscosities than those in the upper mantle (Figure 3.5). These Figures show that a trade off exists between upper and lower mantle viscosities. For example, in Figure 3.6 so long as upper and lower mantle viscosities are both reduced, the misfit between model and data derived RSL curves will remain within the 95% confidence interval. Although the Lesser Antilles region contains the longest record of sea level (since 32,000 cal years BP) with many data points (115) and RSL curve points (49), the wide 95% confidence interval limits it as a location to specify an optimal set of model Earth parameters. The 95% confidence interval of the full-region solution (Figure 3.7) appears tightly constrained for all three lithospheric thicknesses (χ^2 minimum at 1 x 10^{21}/20 - 30 x 10^{21} Pa s, Upper/Lower mantle viscosities) when compared to the Lesser Antilles solution (Figure 3.6). However, the ranges of χ^2 misfit values are similar, which shows the difference in misfit between the parameters within the 95% confidence interval and the parameters at the edge of the parameter space is small.

This fact is particularly important for the full-region since the 95% confidence in-

terval (Figure 3.7) lies within four of the sub-regional 95% contour intervals (Mexico, Figure C-2; Cayman Islands, Figure C-4; Lesser Antilles, Figure 3.6; Trinidad, Figure C-10), which makes those sub-regions of little use when ascertaining optimal model parameters. Five sub-region's 95% confidence intervals partially overlap with the full-region 95% confidence interval (Florida, Figure 3.5; Bahamas, Figure C-1; US Virgin Islands, Figure C-7; Panama, Figure C-8; Venezuela, Figure C-9), whilst the remaining sub-region's 95% confidence intervals do not overlap with the full-region 95% confidence interval (Belize, Figure C-3; Cayman Islands, Figure C-4; Jamaica, Figure C-5).

Table 3.3 summarises the model parameter configurations, which minimises the χ^2 value for the three lithospheric thicknesses used in the model runs for each sub-region and the full-region, for both data derived RSL curves and the RSL realisations. The model parameters with the minimum χ^2 value are highlighted. The optimal model Earth parameters for the full-region (Figure 3.7) are lithospheric thickness, 71 km, upper and lower mantle viscosities, 1 x 10^{21} and 30 x 10^{21} Pa s respectively. Although there are a larger number of absolute minimum misfits for 120 km lithospheric thickness, the minima for each lithospheric thickness are close in value to each other. This demonstrates the broad invariance of the misfit calculation to lithospheric thickness across the region.

I test if model invariance to lithospheric thickness is a valid statement by calculating the standard deviation of the three minimum misfit values for each region. Then, I divide this standard deviation by the smallest of the three minimum misfit values (final column, Table 3.3). This normalisation allows me to study the relative deviations of all the region's minimum χ^2 values. Most of the regions (both for misfits calculated using derived RSL curves and RSL indicator realisations) display low (≤ 0.2) fractions supporting the argument that the GIA model RSL curves are invariant to lithospheric thickness. However there are two exceptions whose fractions are greater than 0.6, Belize (0.61) and Dominican Republic (0.82). Although the fraction is high for Dominican Republic, the optimal upper and lower mantle viscosities are the same for all lithospheric thicknesses. The range of minimum misfits for the Belize derived RSL curve shows significant variation, compared to the other regional misfit ranges, for the three lithospheric thicknesses (Table 3.3).

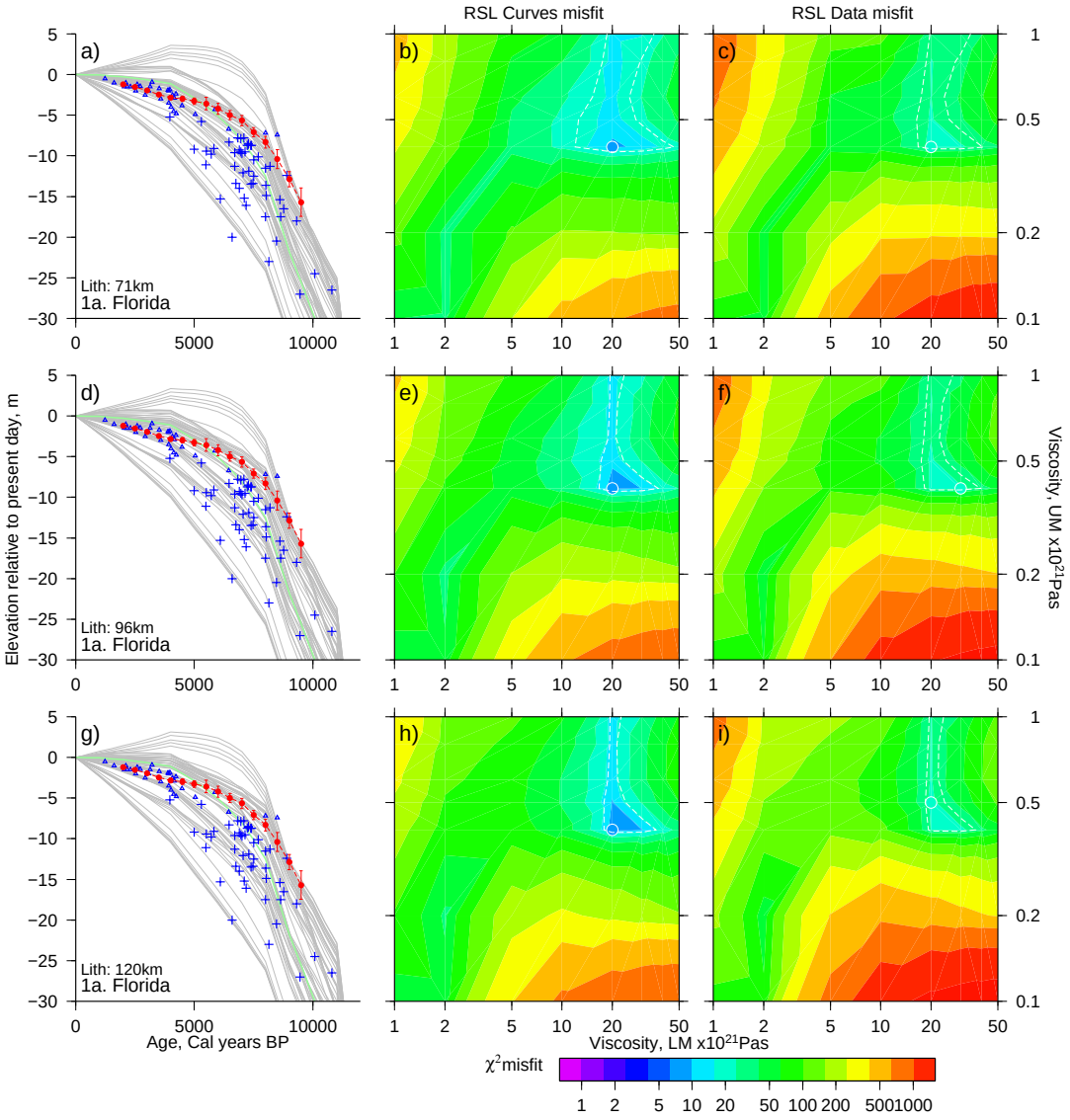

Figure 3.5: Florida region (1a) χ^2 misfit: model, data and sea-level curves. **a**, **d**, **g**: age-elevation plots for lithospheric thicknesses, 71, 96 and 120 km respectively. GIA model RSL curves (grey), VM2 (Peltier, 2004) GIA model RSL curve (green), data derived RSL curve (red), RSL indicators (blue symbols). Contour plots **b**, **e**, **h** show χ^2 misfit between GIA model and data derived RSL curves ($N = 20$ points). Contour plots **c**, **f**, **i** show χ^2 misfit between GIA model RSL curves and RSL indicator realisations ($N = 81$ points). In both cases, the white outlined coloured circle represents the model upper and lower mantle viscosities, which minimise the misfit and the dashed white line represents the 95% confidence contour (inside which the minimum χ^2 value lies).

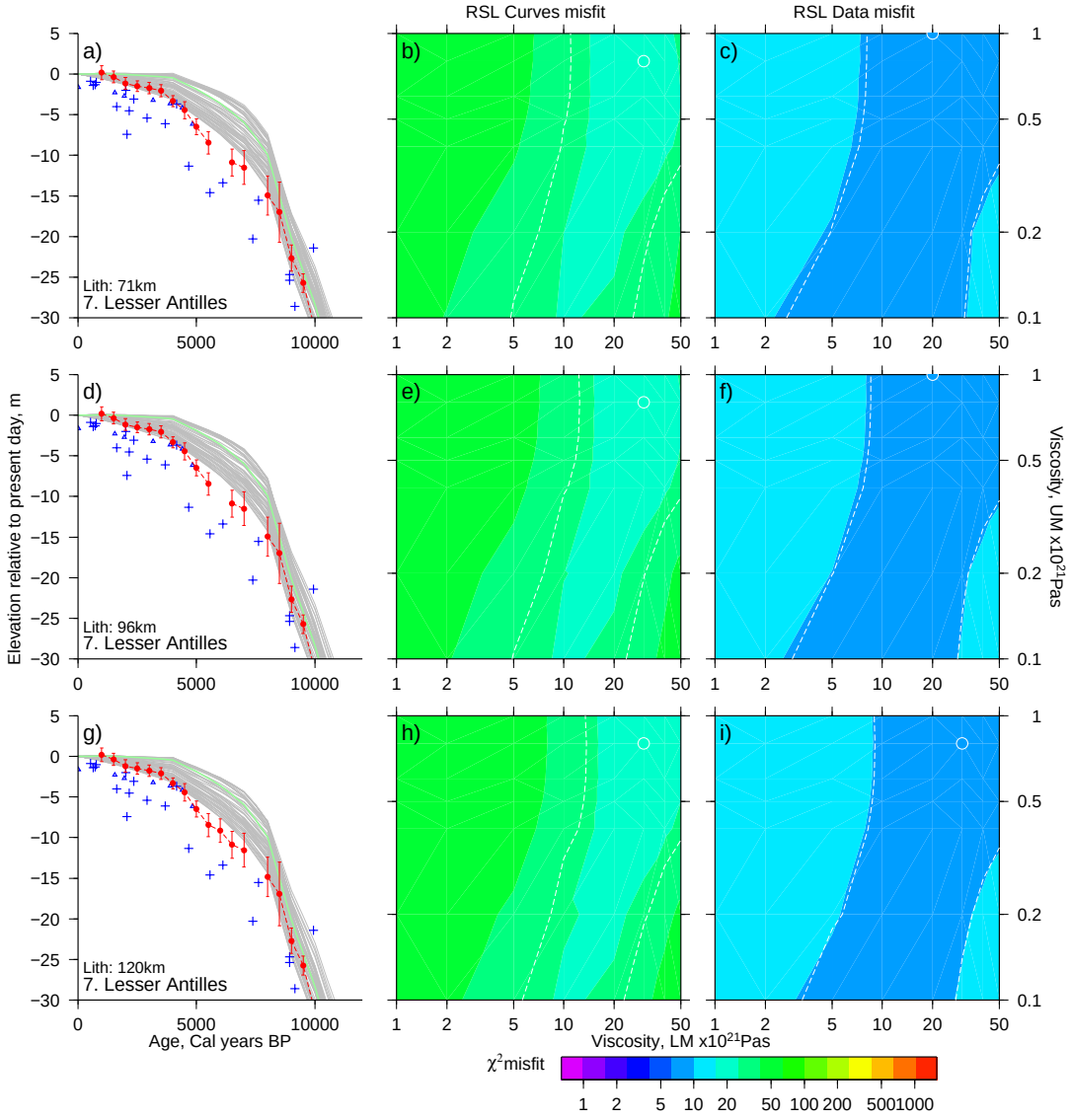

Figure 3.6: As in Figure 3.5 but for Lesser Antilles region (7). Data derived RSL curves (N = 49 points). Sea-level indicator derived RSL position (N = 115 points)

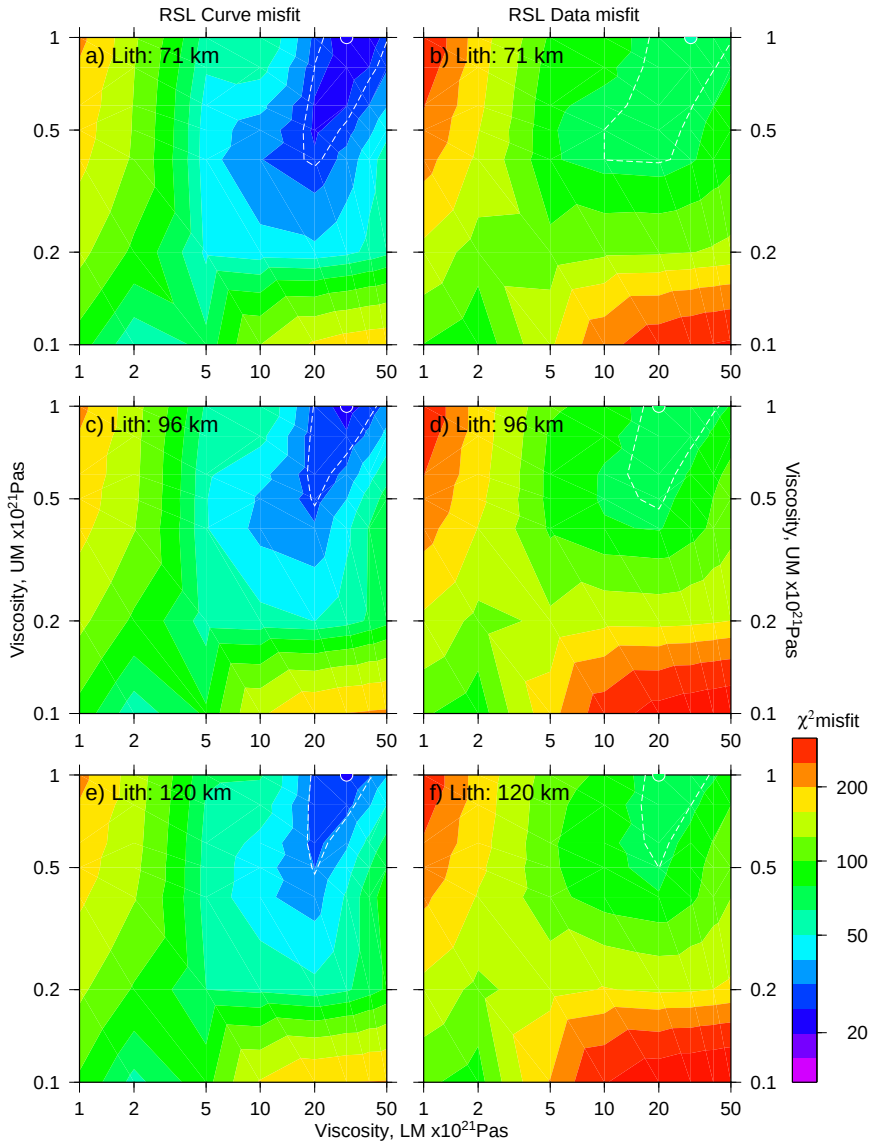

Figure 3.7: Contour plots **a**, **c**, **e** show χ^2 misfit between GIA model and full-region data derived RSL curves ($N = 150$ points). Contour plots **b**, **d**, **f** show χ^2 misfit between GIA model RSL curves and full-region RSL indicator realisations ($N = 546$ points). Minimum misfit and 95% confidence contour shown by white outlined circle and white dashed line respectively. Note different colour scale to Figures 3.5 and 3.6.

It is useful to note that the number of data derived RSL curve points or RSL indicators (N) varies significantly across the sub-regions (Table 3.3 and Figure 2.3a). The χ^2 misfit values follow a loose trend, which increases with the number of the data, N. This means that the full-region optimal model parameters are potentially biased to sub-regions with larger numbers of points in either data derived RSL curves or RSL indicator derived realisations. Given the potential bias in the full-region optimal model parameters, I use an additional approach to ascertain representative rather than optimal GIA model parameters (Section 3.5.2). The aim is to have a set of model parameters that are a good fit to all of the sub-regions rather than an optimum fit, which might bias certain sub-regions in favour of fitting others better. The representative parameters and range should certainly overlap with the full-region 95% confidence interval.

3.5.2 Representative model Earth parameters

The optimal model Earth parameters from the full-region solution that minimises the χ^2 misfit (Figure 3.7) are lithospheric thickness, 71 km, upper and lower mantle viscosities, 1 x 10^{21} and 30 x 10^{21} Pa s respectively. However, since there is likely to be a sub-regional bias of the parameters, I use a separate method to identify representative model Earth parameters, which use the regions whose 95% confidence regions cover a smaller parameter space. I pair adjacent sub-regions in a series of Figures where I show for each lithospheric thickness, the three misfit minima positions in terms of their upper and lower mantle viscosity and their associated 95% confidence region (Figure 3.8 and 3.9). The representative model parameters should be close to the optimal model parameters and the resultant predicted RSL curves should fit the spatial trends found in the sub-regional data derived RSL curves to the first order.

Mantle viscosities

Figures 3.8 and 3.9 show six regional pairings and reveal the general (also shown in Table 3.3) invariance of model solution to lithospheric thickness and the range of upper and lower mantle viscosities best satisfying the RSL observations. There is consistency between most pairs. All regions appear to be satisfied by an upper mantle viscosity of 0.5 - 0.8 x 10^{21} Pa s and a lower mantle viscosity of 10 - 30 x 10^{21} Pa s although there are some regions for which solutions lie at the extreme of these ranges. These ranges are in agreement with the reference (and optimal) upper/lower mantle viscosities of

Table 3.3: Model Earth upper and lower mantle viscosities corresponding to the minimum χ^2 misfit for each lithospheric thickness for each sub-region and full-region, for data derived RSL curves and sea-level indicator derived RSL positions. The number of points (N) used in the χ^2 calculation is shown in column 2. Highlighted upper/lower mantle viscosities are those corresponding to the absolute minimum χ^2 value (also highlighted).

		71 km			96 km			120 km			
Region	N	υ_{UM} x 10^{21} Pa s	υ_{LM} Pa s	χ^2	υ_{UM} x 10^{21} Pa s	υ_{LM} Pa s	χ^2	υ_{UM} x 10^{21} Pa s	υ_{LM} Pa s	χ^2	$\frac{\sigma_{\chi^2}}{\chi^2_{\text{min}}}$
Relative sea-level curves											
1a	16	0.4	20	8.64	0.4	20	6.88	0.4	20	6.75	0.16
1b	9	0.8	20	1.22	0.8	20	1.14	0.2	2	0.88	0.20
2	8	1	10	0.73	1	10	0.71	1	10	0.67	0.05
3	15	1	20	0.53	0.8	10	1.12	0.8	10	1.06	0.61
4a	6	1	10	58.34	1	10	65.68	1	10	77.81	0.16
4b	9	0.8	50	0.95	1	50	0.92	0.2	20	1.24	0.19
5	7	1	10	2.7	1	10	1.65	1	10	1.03	0.82
6	16	0.1	50	2.5	0.1	50	2.3	0.1	50	1.75	0.22
7	49	0.8	30	18.92	0.8	30	18.74	0.8	30	18.59	0.01
8	9	0.4	30	0.42	0.5	10	0.36	0.6	10	0.41	0.09
9a	1	-	-	-	-	-	-	-	-	-	-
9b	5	1	20	80.96	1	20	68.13	1	30	58.81	0.19
Full	150	1	30	20.73	1	30	22.40	1	30	24.43	0.09
Relative sea-level indicators											
1a	81	0.4	20	21.82	0.4	30	22.29	0.5	20	21.23	0.03
1b	18	0.6	20	15.76	0.8	20	14.89	0.8	20	15.17	0.03
2	20	0.1	5	1.3	1	5	1.25	1	5	1.16	0.06
3	132	0.1	5	22.02	0.1	5	22.05	0.1	5	22.28	0.01
4a	35	1	10	68.15	1	10	70.43	0.1	10	68.96	0.02
4b	18	0.2	40	18.41	0.2	30	18.05	0.2	30	18.24	0.01
5	16	1	10	3.72	0.1	10	3.37	0.1	10	3.2	0.08
6	79	0.1	50	2.14	0.1	50	2.11	0.1	50	2.11	0.01
7	115	1	20	7.25	1	20	7.3	0.8	30	7.36	0.01
8	18	1	50	51.72	1	50	53	1	50	54.04	0.02
9a	7	0.5	50	41.64	0.6	50	37.24	0.8	50	33.09	0.13
9b	7	1	20	90.24	1	20	78.3	1	20	69.75	0.15
Full	546	1	30	62.84	1	20	65.19	1	20	65.32	0.02

Milne et al. (2005) (0.5 x 10^{21} Pa s and 10 x 10^{21} Pa s respectively), which I choose as representative viscosities. Certainly one exception is region 4b whose RSL curve and RSL indicators are tightly constrained to a very limited range of suitable viscosity models, most of which lie outside the aforementioned ranges.

Lithospheric thickness

Although the three model lithospheric thicknesses used do not greatly change the misfit values, there is other evidence to promote the thinnest of the three (71 km) to use as the representative solution. A similar GIA study to this by Milne et al. (2005) applied a range of viscosity and lithospheric models to RSL indicators at sites in the Caribbean (Jamaica and Curacao) and the Atlantic coast of South America. The reference Earth model used had a lithospheric thickness of 96 km. After adjusting the model parameters, Milne et al. (2005) found a best fit to their complete data using a lithospheric thickness of 71 km. This thickness is supported by seismic studies of the region as well. González et al. (2007) imaged crust and upper mantle structure using seismic tomography and performed a series of S-wave inversions across the Caribbean to derive S-wave velocity with depth. All of their regions show an increasing velocity to a depth of ∼70km after which it remains constant.

It is important to add that other authors record thinner crustal thicknesses. For example Miller et al. (2009) performed surface wave tomography onshore Venezuela and calculated a crustal thickness of 45 km. This area like many in the Caribbean is tectonically complex, where major accretionary zones (Dominican Republic and US Virgin Islands, González et al. (2007)) and underthrusting of the Caribbean plate (Lesser Antilles, Miller et al. (2009)) occurs. These effects are likely to result in thickened lithosphere (e.g. the overriding plate causing the lithosphere to appear to be two plate thicknesses deep). To support this evidence, the bulk of Lesser Antillean seismicity occurs between depths of 50 to 100 km though the subducted Atlantic plate (beneath the Caribbean) causes earthquakes to occur at deep as 160 km (Benz et al., 2011, Bezada et al., 2010). The existence of a thicker lithosphere from the Lesser Antilles north-west towards Florida is supported by the results in Table 3.3, which show regions 6, 7 and 9b showing absolute minimum misfits for 120 km lithospheric thickness. The representative thickness for the Lesser Antilles then is likely to be averaging the complex lithospheric and upper mantle plate interactions. This being said, I retain a whole

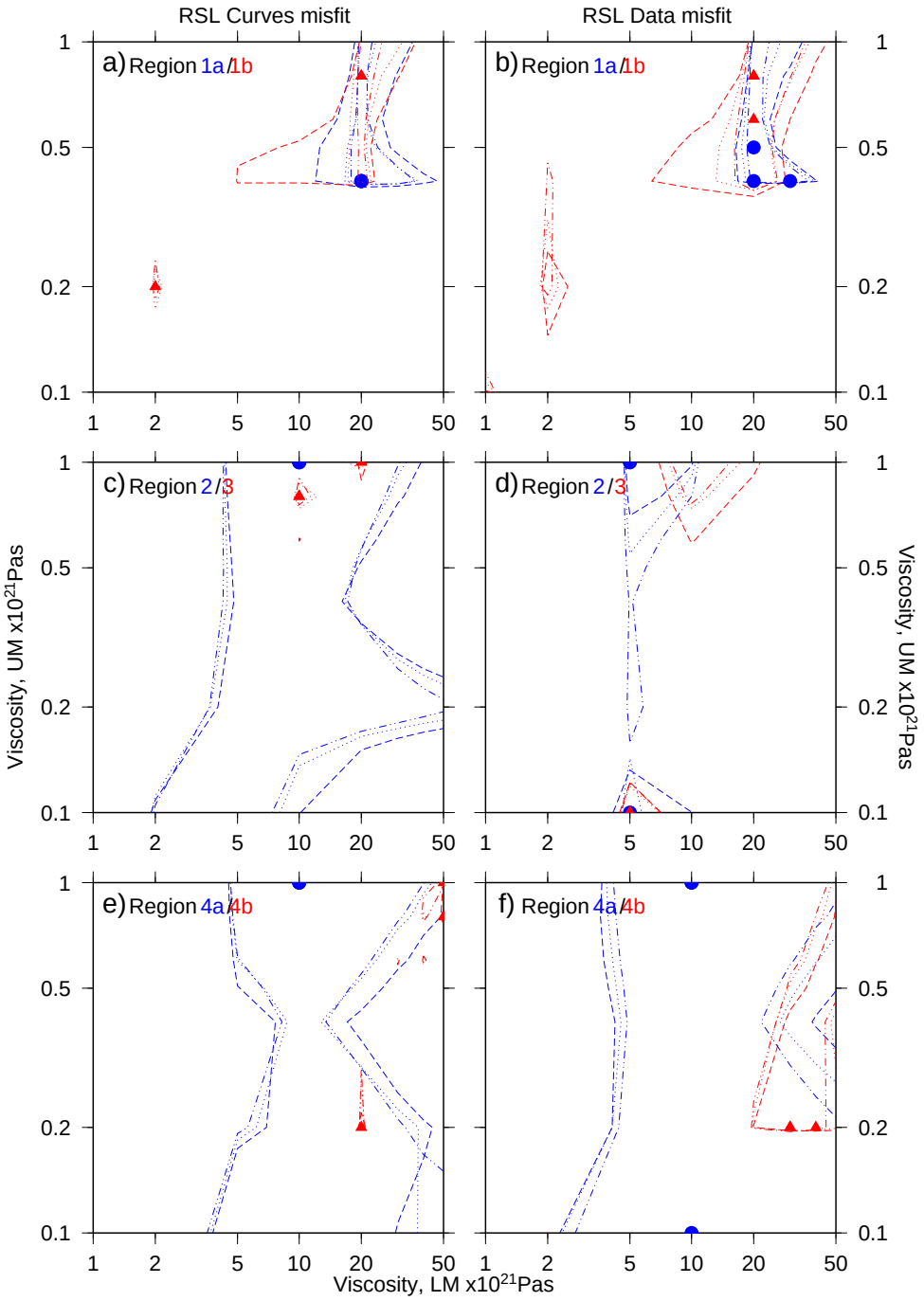

Figure 3.8: 95% confidence regions (dashed lines) and model upper/lower mantle viscosities, which minimise the misfit (symbols) for two geographically adjacent regions for misfit between model sea-level curves and (**a**,**ce**) data derived RSL curves or (**b**,**df**) sea-level indicator derived RSL positions. **a** & **b**: Florida (blue) and Bahamas (red), **c** & **d**: Mexico (blue) and Belize (red), **e** & **f**: Cayman Islands (blue) and Jamaica (red). Contours represent three lithospheric thicknesses: 71 km - dashed, 96 km - dotted, 120 km - dot-dashed.

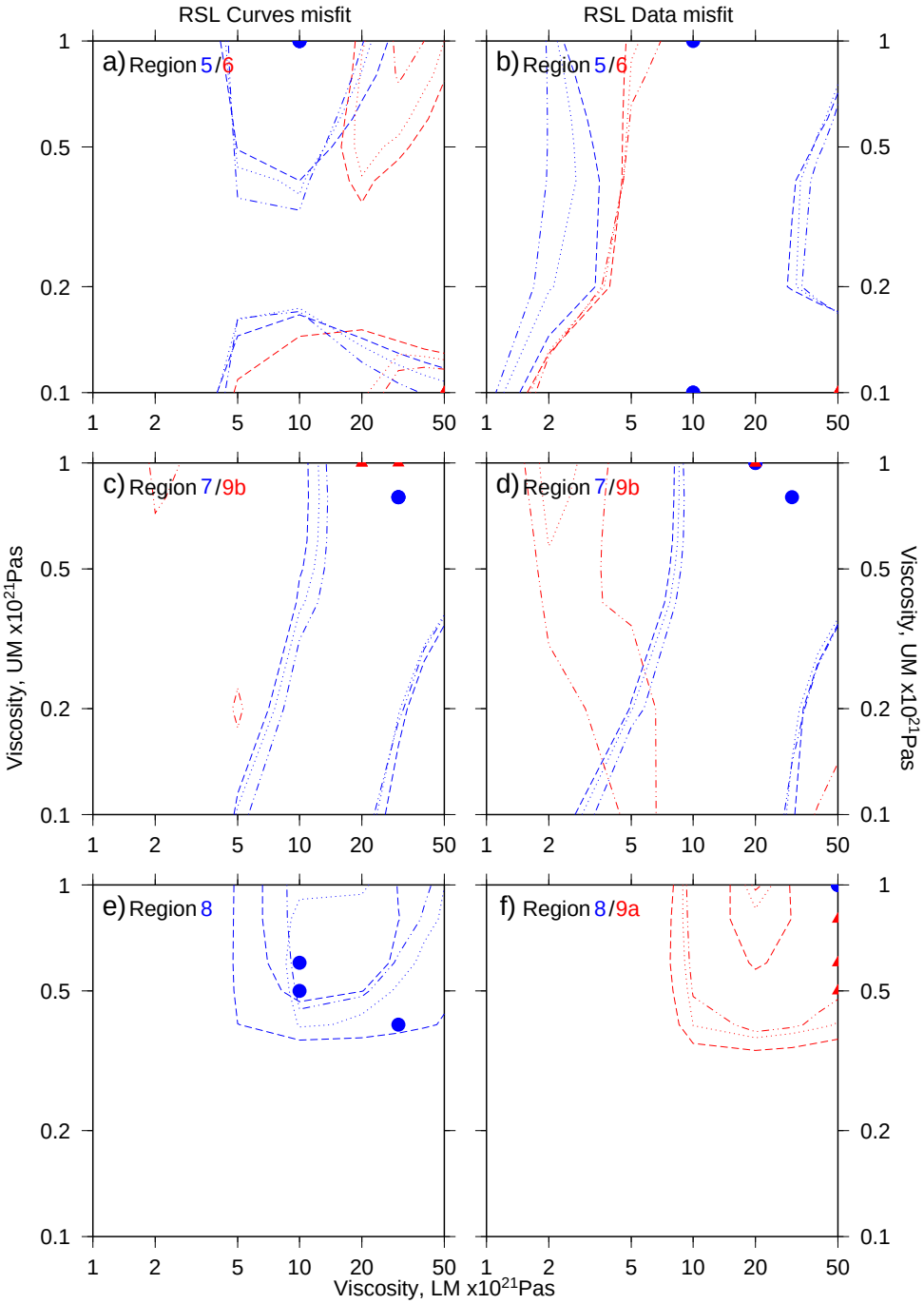

Figure 3.9: As in Figure 3.8. **a** & **b**: Dominican Republic (blue) and US Virgin Islands (red), **c** & **d**: Lesser Antilles (blue) and Trinidad (red), **e** & **f**: Panama (blue) and Venezuela (red). Note that Venezuela region has only one data derived RSL curve position therefore misfit calculation was not attempted.

Caribbean regional lithospheric thickness of 71 km and upper/lower mantle viscosities of 0.5 x 10^{21} Pa s and 10 x 10^{21} Pa s respectively. I will also study the effect of a thicker lithosphere in Florida and the Lesser Antilles.

3.5.3 Comparison of VM2 to representative model Earth parameters

It is important to note that my chosen upper mantle viscosity is in agreement with the depth averaged VM2 (Figure 3.4) of Peltier (2004) though my lower mantle viscosity is ∼3.7 times larger ($\upsilon_{\mathrm{LMopt}}/\upsilon_{\mathrm{LMVM2}}$ = 10 x 10^{21} Pa s/2.7 x 10^{21} Pa s). This means that the ICE-5G model will no longer be tuned to the viscosity model and hence slight variations in the position of eustatic sea level (assumed to be at Barbados: Peltier (2004), Peltier and Fairbanks (2006)) will occur. Figure 3.10 shows the differences between modelled present day sea-level rates (a and b) and prehistoric RSL curves (c, d, e and f) across the region due to GIA for the ICE-5G (VM2) (Peltier, 2004) and ICE-5G with representative viscosity model (Lith: 71 km, υ_{UM} = 0.5 x 10^{21} Pa s, υ_{LM} = 10 x 10^{21} Pa s). In this region, a thinner lithosphere and more viscous lower mantle has the following effects: a higher present day rate of sea-level change due to GIA across the region by up to a factor of three, a localising of the area where there is zero sea-level rise to only the northern Central and South American coastline, and a generally later arrival of the sea level to its present day position compared to the VM2 (Peltier, 2004) model. The representative GIA model RSL curves also track below the eustatic sea-level rise (Figure 3.10) for the duration of the Holocene.

3.5.4 Spatial trends across the Caribbean

In the previous chapter, I described the spatial pattern of RSL across the Caribbean. The region-wide sea-level rise of up to 30 m in the Holocene with little or no evidence of emergence above present day levels in the south is confirmed by the modelling study for the representative Earth parameters (and VM2: Peltier (2004)). A lag of 1500 years in the South Eastern Caribbean compared to the North and Western Caribbean RSL curves is evident (Figure 2.16a), along with shape differences between Florida and Belize showing sea level rose to present level in Belize before Florida. The model RSL curves show this distinctive feature (Figure 3.10c,d) for VM2 and the representative Earth parameters. Furthermore, there does appear to be a lag between Eastern and Western sites in the arrival of sea level at present day position (Figure 3.10d,e).

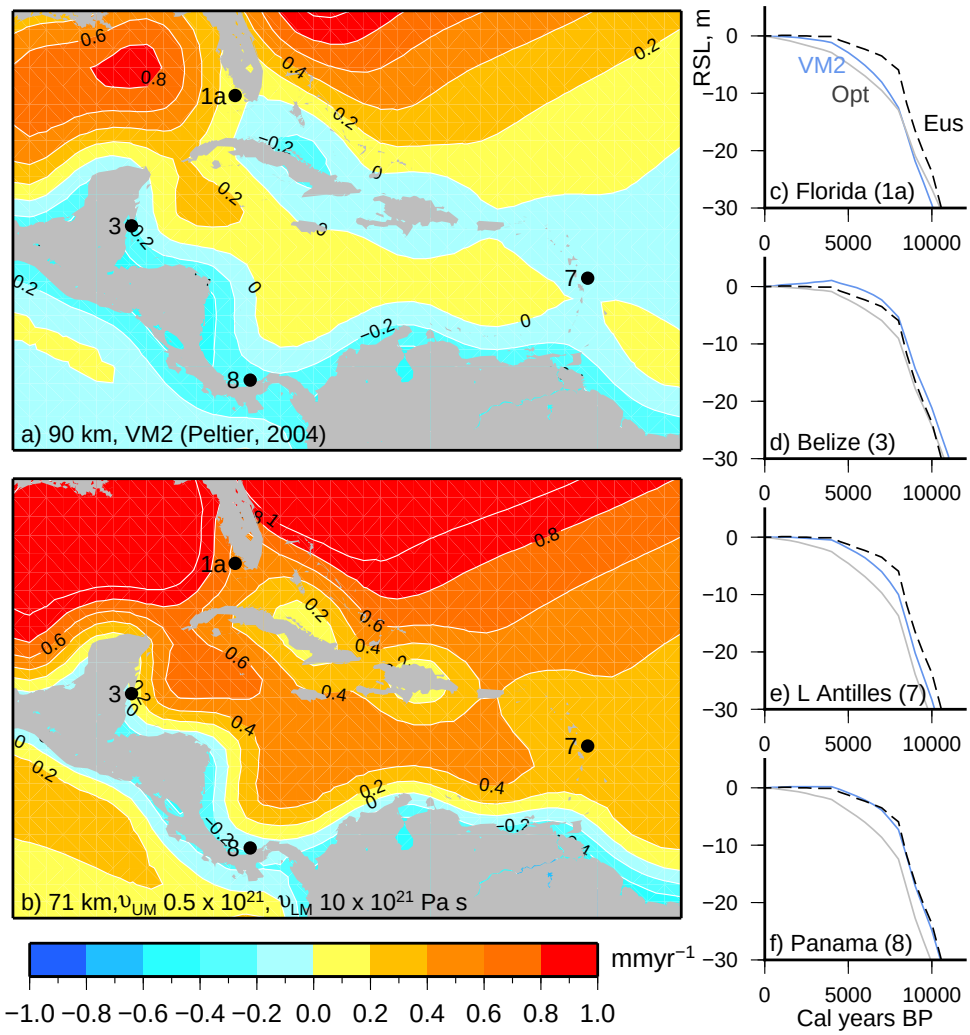

Figure 3.10: Present day predicted sea-level rise due to GIA using model Earth parameters: **a** 90 km lithospheric thickness, VM2 (Peltier, 2004) and **b** 71 km lithospheric thickness, $\upsilon_{\mathrm{UM}} =$ 0.5 x 10^{21} Pa s and $\upsilon_{\mathrm{LM}} =$ 10 x 10^{21} Pa s. Labelled black dots correspond to location of predicted RSL curves in **c** - **f**, where VM2 (blue), representative parameters (grey) and eustatic RSL curves (black, dashed) are plotted.

3.5.5 Testing GIA model parameters: non-eustatic correction

It is useful to test how robust the chosen GIA and ice deglaciation models are, other than performing χ^2 misfits. I calculate the GIA model non-eustatic RSL contribution in each sub-region and correct the RSL data (RSL derived curves and RSL indicators) to see if it aligns with the ICE-5G eustatic sea-level curve Milne et al. (2005). This difference is subtracted from the RSL derived curves and RSL indicators to adjust their position. The results are shown in Figure 3.11.

The first thing to identify is if a regionally consistent discrepancy exists between the ICE-5G eustatic curve and the corrected RSL derived curve and RSL indicators. The corals should still remain below the eustatic curve whilst the peats should straddle the line. Such a residual could be interpreted directly as *the* correction required to the eustatic signal of the ice model (by recalculating the total ocean equivalent and adjusting the ice model as required).

The corrected data (Figure 3.11, lower graph in each box) follow a trend similar to that of the ICE-5G eustatic curve (plotted in blue). Other than Trinidad (9b), all of the sub-regions agree with the low global ice sheet loss due to deglaciation ($\leq$ 1.5 m) over the last 5000 years. Prior to 5000 cal yr BP, the match between the model and data is good for the Bahamas (1b), Belize (3), Cayman Island (4a), US Virgin Islands (6), Lesser Antilles (7) and Panama (8).

Other sub-regions' corrected RSL data deviate from the ICE-5G eustatic curve. Florida (1a) and Jamaica (4b) display over corrected RSL data. Certain corals lie above the eustatic line in Florida around 7500 cal yr BP. The deviation of the corrected RSL indicators in Jamaica is in agreement with the findings of Milne et al. (2005). These two results, if there has not been any significant tectonic or local effects upon sea-level indicator position (Equation 3.7), imply a lower melt rate between $\sim$ 7000 - 8000 cal yr BP (Milne et al., 2005).

Sub-regions 5 and 9b may show subsidence effects that caused the corrected RSL data to plot below the eustatic line, even though the indicators tracked sea level when they were alive (similar to the Holocene reef in US Virgin Islands where Buck Island reef tracked sea level but had systematic vertical offset, Macintyre and Adey (1990)). The deviation of the Mexico (2) sub-region after 5000 cal yr BP is either a local effect or a failure of the sea-level curve construction method. The good agreement between GIA model, non-eustatically corrected RSL data and the ICE-5G eustatic RSL curve across

the sub-regions in the Caribbean supports the hypothesis that the ICE-5G deglaciation model coupled with the χ^2 minimising, model parameters is correct from the mid Holocene to present.

3.5.6 Testing alternate GIA model parameters: non-eustatic correction

There is significant deviation from the ICE-5G eustatic RSL curve prior to 5000 cal yr BP for Florida (Figure 3.11a). I attempt to find a better set of model Earth parameters that satisfies the RSL derived curves of this sub-region and those along the eastern Caribbean because of the thickened lithosphere likely to exist along the subduction zone (Figure 1.1). I correct sub-regions (Florida, Bahamas, US Virgin Islands, Lesser Antilles and Trinidad) for the non-eustatic RSL component in the same way as the previous section using an alternate model, 120 km lithospheric thickness,
υ_{UM} = 0.8 x 10^{21} Pa s and υ_{LM} = 30 x 10^{21} Pa (Figure 3.12). This set of model parameters were chosen because they minimise the χ^2 misfit across the eastern Caribbean regions (Figures 3.8a - b and 3.9a - d).

Figure 3.12a shows that the Florida region is extremely well corrected by the GIA model non-eustatic component. Furthermore, there is little change in the other corrected RSL data, compared to the corrections in Figure 3.11. These results imply a greater lithospheric thickness improves the misfit between model and observations for regions along the northern and eastern Caribbean.

Since there is still no uniform offset from the eustatic curve across the sub-regions (Milne et al., 2005), I will use the aforementioned model parameters as my representative model but I introduce a range, 71 - 120 km (lithospherically invariant), upper mantle viscosity 0.5 - 0.8 x 10^{21} Pa s and lower mantle viscosity 10 - 30 x 10^{21} Pa s, to quantify errors in the GIA modelling results. I will use the representative model and errors for GIA corrections and inter-comparisons of modern RSL data in Chapter 5.

Of the suite of model Earth parameters I have used for this study, there is no single earth-ice model that can fit every observation well. The larger residuals could be associated to observation and model limitations. A classic limitation of the modelling is the lack of the ability to compute the effect of lateral viscosity variations in the Earth, whilst on the observation side one can not neglect the possible influence of vertical tectonics, which are not accounted for in any model. Recent GIA publications have

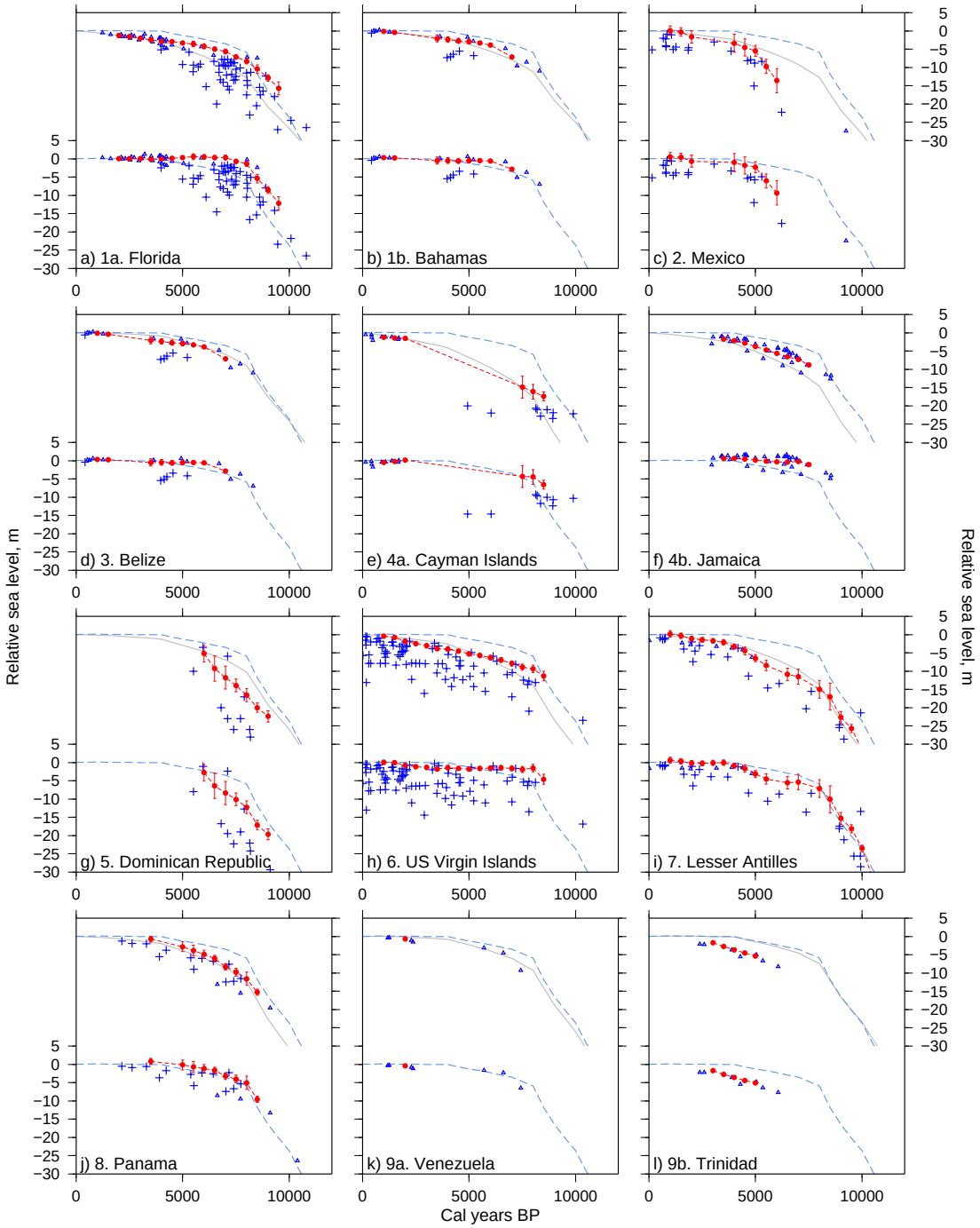

Figure 3.11: For representative model Earth parameters (71 km lithospheric thickness, υ_{UM} = 0.5 x 10^{21} Pa s and υ_{LM} = 10 x 10^{21} Pa s), sea-level curves and observations at each site corrected for non-eustatic GIA contribution of the best fitting model. For each sub-region, upper graph shows originally data derived RSL curve (red), RSL indicators (blue), representative GIA model derived RSL curve at site (grey) and eustatic RSL curve (blue, dashed). Lower graph shows data derived RSL curve (red) and RSL indicators (blue) corrected by difference between eustatic and representative GIA model derived RSL curve. The eustatic curve is plotted (blue,dashed).

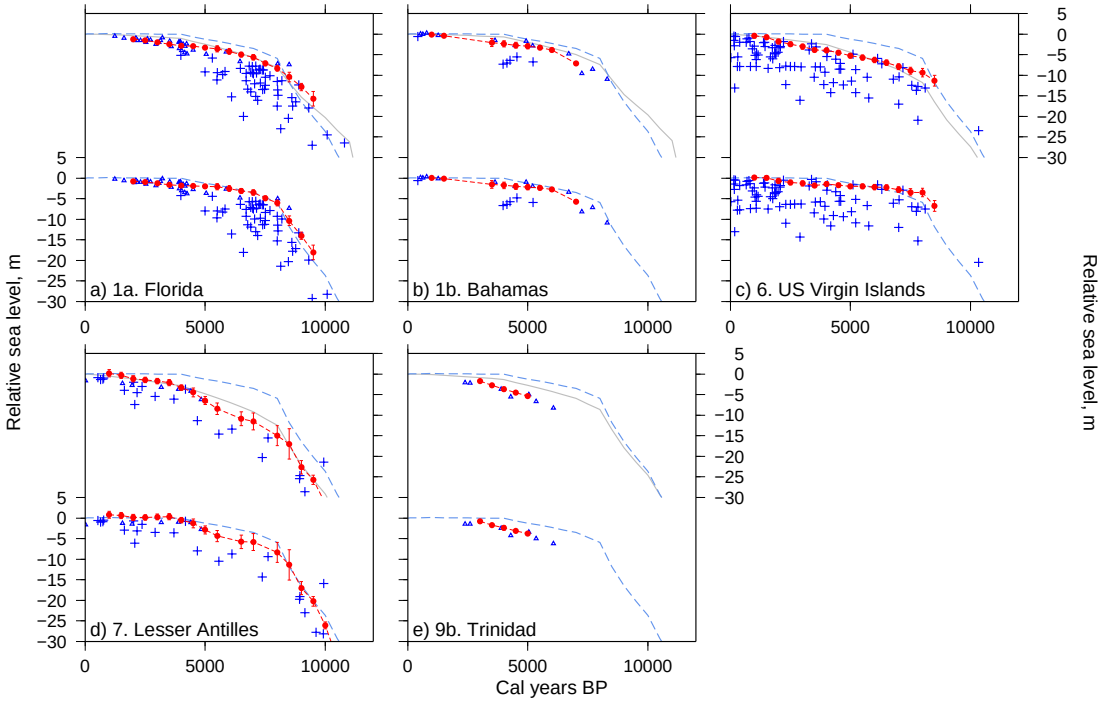

Figure 3.12: As in Figure 3.11 for Florida, Bahamas, US Virgin Islands, Lesser Antilles and Trinidad for thickened lithospheric parameter (120 km). Upper and lower mantle viscosities remain the same.

attempted to include the three-dimensionality of the lithospheric-mantle structure in sea-level calculation (Paulson et al., 2009, van der Wal et al., 2010) though this added complexity appears to have negligible effects on predictions (Mitrovica et al., 2011). Perhaps more relevant to this study is the introduction into the sea-level equation of sediment influx in to oceanic basins (Dalca et al., 2013). This could have significant influence in the Caribbean due to the large sediment output of the Orinoco and Magdalena rivers from South America.

3.5.7 Fingerprints: ice centre contributions

One of the questions posed at the beginning of this chapter was, what is the contribution to RSL change of the individual ice sheets during the deglaciation? The geographically distinct patterns of sea-level change due to melting of different ice sheets are described as "fingerprints" (Mitrovica et al., 2001a, Tamisiea et al., 2001, Mitrovica et al., 2010, 2011). The combination of the fingerprints result in the global pattern of sea-level change. Although the deglaciation model remains the same so that the eustatic contributions are consistent (Figure 3.3d) I run the sea-level model using the representative

model Earth parameters for each of the major ice complexes: Laurentide, Fennoscandia, Greenland and Antarctica. Figure 3.13 shows the contribution to present day sea level and the contribution to RSL curves at different sites around the Caribbean to assess the dominant ice centre. The present day response is overwhelmingly due to the deglaciation of the Laurentide ice sheet (Figure 3.13a - d). In prehistory (Figure 3.13e - h) the Antarctic contribution was significant (∼17 m) though the dominant contributor was still the Laurentide (∼50 m). The combined contribution from Fennoscandia and Greenland totals ∼22.5 m (∼20 m ∼2.5 m respectively). The spatial variations in the RSL curves come exclusively from the melting of the Laurentide ice sheets. This is due to the proximity of this former ice sheet to the Caribbean. In contrast, the Caribbean lies in the far-field to the other ice centres hence the similarities in their curves at the four sites (Figure 3.13e-h).

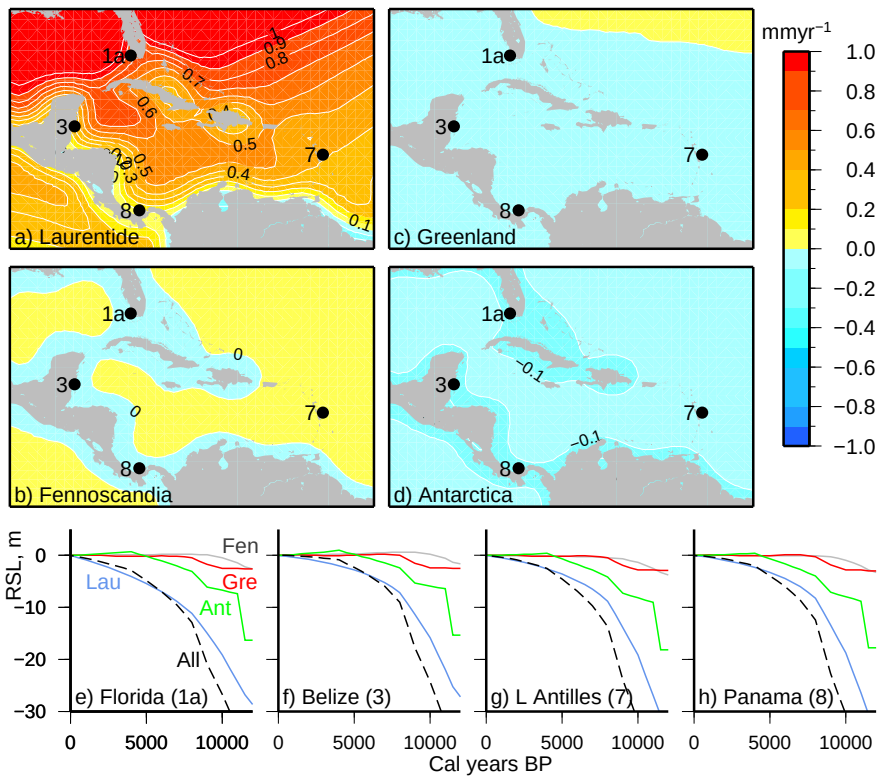

Figure 3.13: For model Earth parameters, 71 km lithospheric thickness, $\upsilon_{\mathrm{UM}} = 0.5$ x 10^{21} Pa s and $\upsilon_{\mathrm{LM}} = 10$ x 10^{21} Pa s. **a-d** Present day sea-level contribution from the four major ice centres. **e-h** RSL contributions from the four major ice centres and the RSL curve (ALL) for the full ICE-5G (Peltier, 2004) model.

3.6 Conclusions

By solving the sea-level equation numerically for a range of model Earth parameters and comparing the resultant RSL curves from the same locations as those from which I have data, I have found an representative Earth model in agreement with the findings of Milne et al. (2005). This investigation extends the Milne et al. (2005) study geographically to the north and whilst the ice models used in their study is different from ICE-5G (Peltier, 2004), the similarly in the results is encouraging. It is apparent that the model output is generally invariant to different lithospheric thicknesses.

The spatial variations of the modelled RSL curves do not reveal any emergent sea levels during the late Holocene as originally predicted by Clark et al. (1978). In fact, model predictions suggest that emergent sea-level curves will occur south of the equator along the South American coastline (Milne et al., 2005).

By assuming a representative Earth model (71 km lithospheric thickness, υ_{UM} = 0.5 x 10^{21} Pa s and υ_{LM} = 10 x 10^{21} Pa s) for this region, the deviations of the RSL curves derived in the previous chapter can now be considered to represent sub-regional variations due to isostacy, tectonics and local environmental changes as described in Section 3.2.3. Figure 3.11 justifies this claim because the correction of observations to the eustatic RSL curve at each locality is successful over the last 5000 cal yr BP (Figure 3.11). In view of the uncertainties of the model non-eustatic correction prior to 5000 cal yr BP posed by the Florida (and to a lesser extent Jamaica) RSL data, I will use the aforementioned model parameters as my representative model but I introduce a range, 71 - 120 km (lithospherically invariant), upper mantle viscosity 0.5 - 0.8 x 10^{21} Pa s and lower mantle viscosity 10 - 30 x 10^{21} Pa s, to quantify errors in the GIA modelling results. I will use the representative model and errors for GIA corrections and inter-comparisons of modern RSL data in Chapter 5.

The probabilistic-windowing method I devised in Chapter 2 calculates RSL derived curves and rates from sea-level indicator realisations. The GIA predicted RSL rates shown in Figure 3.14 are calculated from GIA model sea-level curves, which minimise the χ^2 misfit across the sub-regional RSL derived sea-level curves. Figure 3.14 shows how closely the RSL rate of the data derived RSL curves matches the GIA model predicted RSL rates. The youngest (1000 cal yr BP) predicted-observed pairs lie within 0.25 mm yr^{-1} and the remaining pairs match within 1.0 mm yr^{-1} until

~7000 cal yr BP. After this age, the GIA model parameters appear to over predict the RSL rates. This could be a symptom of sub-regional scale tectonics, local and unspecified effects as described by Equation 3.7 (Section 3.2.3).

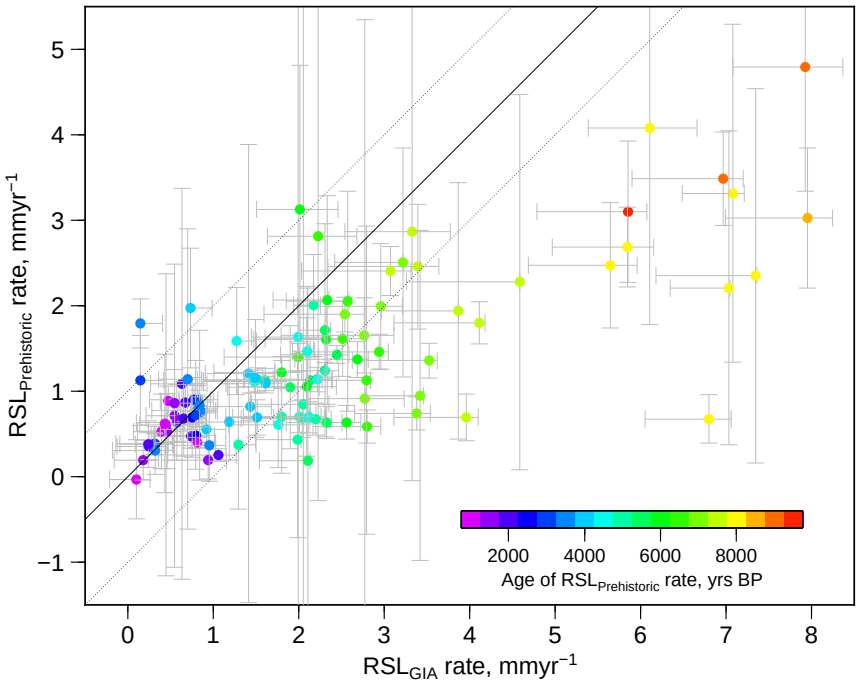

Figure 3.14: Predicted prehistoric RSL rate from representative model Earth parameters versus observed prehistoric RSL rate calculated from sea-level curve construction method. Each coloured circle represents the age of the calculated RSL rate in a sub-region. Horizontal error bars represent GIA model RSL rates from range of model Earth parameters. The black lines are the line of equality (continuous) plus or minus 1 mm yr^{-1} (dashed).

The modelling from this chapter has allowed an explanation of the glacial cycle time scale sea-level trends for the Caribbean. A question that can now be addressed is what proportion of present day sea-level change is due to GIA in this region and can the deviations in the observationally derived RSL curves be explained by regional tectonics or other factors? Both of these questions will be addressed in Chapter 5, but first I consider present day sea-level change from an observational perspective.

Chapter 4

Sea-level observations over the last century

4.1 Introduction

Tide gauges provide the primary source for 20th century relative sea-level (RSL) measurements. These records though are confined to coastlines whilst deeper oceans are poorly sampled, if sampled at all. In contrast to this satellite altimetry records absolute sea level (ASL), which is spatially uniform across much of the world though it only spans the last ∼20 years. The sea-level time series recorded by both methods contain long term trends, which are masked by short term signal and noise.

For the purpose of this chapter, the long term trends described exist consistently across multiple decades during the 20th century to present. They are distinct from the late-Holocene trends considered in the previous chapters since global sea level deviated from these trends in the early 20th century (Gehrels and Woodworth, 2013). Over the length of the sea-level series, long term sea-level rises can be much smaller in amplitude than short term variations. For tide gauges and satellite altimetry, oceanic signals such as seasonal tides, annual, quasi-multiannual oscillations (e.g. North Atlantic Oscillation: NAO) and atmospheric pressure changes distort the long term volumetric and steric changes desired for sea-level projection. In addition to short term high amplitude sea-level changes (e.g. extreme weather events), very long term changes in land uplift due to the glacial cycle (Glacial Isostatic Adjustment: GIA) and tectonic effects (active faulting/inflation of volcano flanks) further complicate the assessment of sea-level change. These will be considered in the next chapter.

In this chapter I use a time series analysis procedure, which is applied to tide gauge

and satellite altimetry observations. The method removes sub-decadal and regionally coherent sea-level change to find long term relative and absolute modern sea-level trends.

4.2 Present day observations

Tide gauges and satellite altimetry are the primary observations used to study modern sea-level change. The spatio-temporal distribution of Caribbean tide gauges and the satellite altimetry grid is shown in Figure 4.1a.

4.2.1 Tide gauges in the Caribbean

48 tide gauge records exist in the Caribbean region spanning between 99 (Key West) and 2 (Palm Beach) years in length. The average series length for the region's tide gauges is 23 years (compared to 26 years global average: Woodworth and Player (2003)) and when restricting to tide gauges that overlap with the satellite altimetry era (1992.9 - present) the average series length is 25 years. Although the gauges appear to be well distributed, there are still significant gaps along the southern and western coastlines of the Caribbean Sea. Furthermore, the distribution of tide gauges for the altimetry era is significantly biased to the northern Caribbean (Figure 4.1b).

Monthly mean sea-level (MMSL) tide gauge time series were obtained from the Permanent Service for Mean Sea Level (PSMSL, *http://www.psmsl.org*). The stability and reference of the stations are regularly monitored (Woodworth and Player, 2003) such that each tide gauge time series is in a Revised Local Reference (RLR) frame with respect to a tide gauge bench mark. The RLR MMSL records can be used for time series analysis at global and local scales over a variety of timescales (e.g. Church et al. (2011), Church and White (2011)).

Tide gauge records were individually examined and gaps of less than 3 months were linearly interpolated. Otherwise, larger gaps are retained through the processing and analysis. For the Panama region, two tide gauge records (Cristobal and Coco Solo) are combined to form a single series because of their close proximity to one another (4 km, Figure 4.2) and their coherent RLR frame.

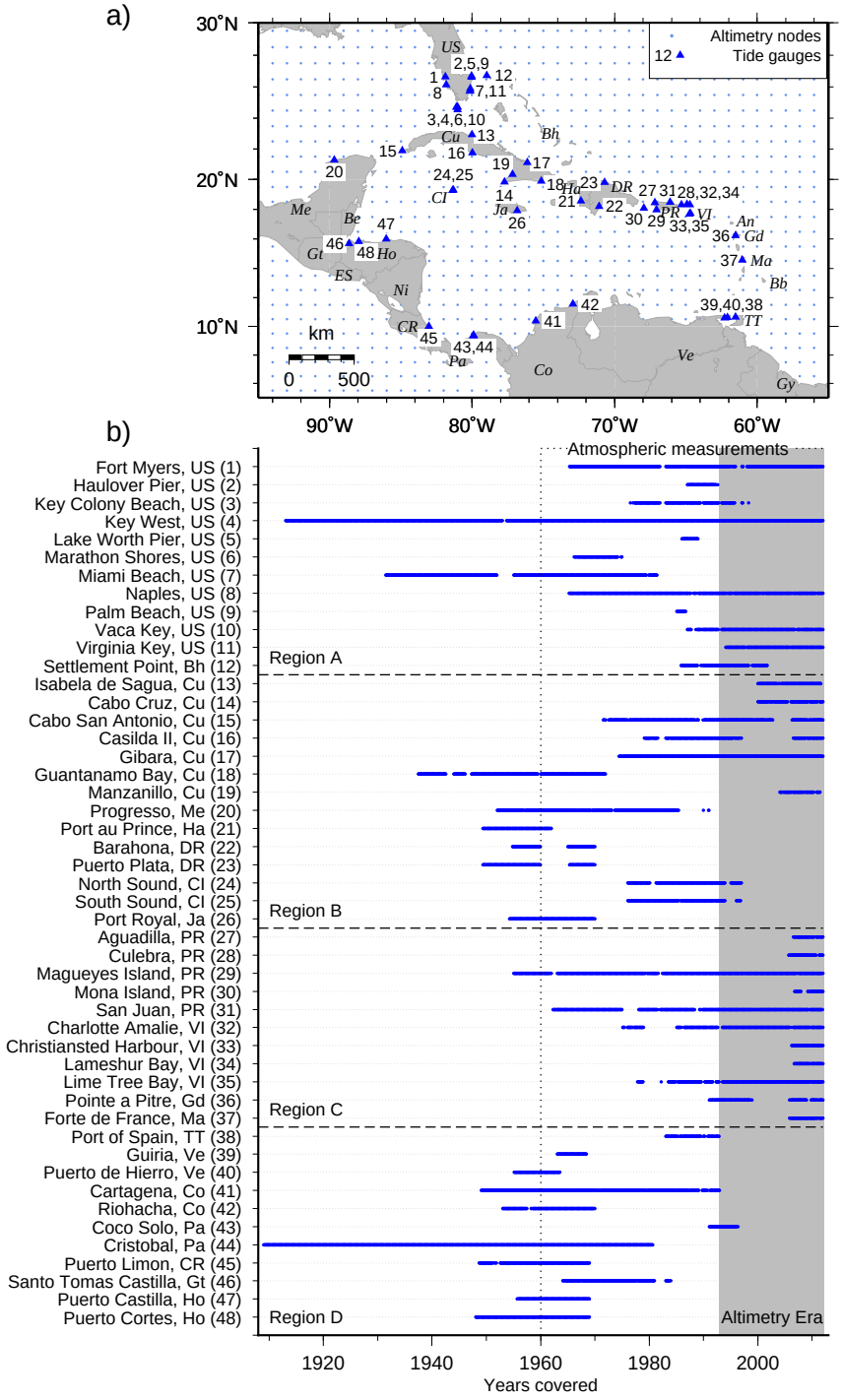

Figure 4.1: **a**: Spatial distribution of tide gauges (1909-present) and nodes from altimetry (sealevel.colorado.edu). **b**: Tide gauges (numbers in parentheses correspond to those on map) in the Caribbean region (from *http://www.psmsl.org/*), their data coverage and to which region (for processing purposes) they have been assigned. Atmospheric pressure readings are available since 1960 and complete altimetry since 1993. Acronyms for countries (clockwise): US, United States of America; Bh, Bahamas; Cu, Cuba; Ha, Haiti; DR, Dominican Republic; CI, Cayman Islands; Ja, Jamaica; PR, Puerto Rico; VI, US Virgin Islands; An, Antigua; Gd, Guadeloupe; Ma, Martinique; Bb, Barbados; TT, Trinidad & Tobago; Gy, Guyana; Ve, Venezuela; Co, Colombia; Pa, Panama; CR, Costa Rica; Ni, Nicaragua; Ho, Honduras; ES, El Salvador; Gt, Guatemala; Be, Belize; Me, Mexico

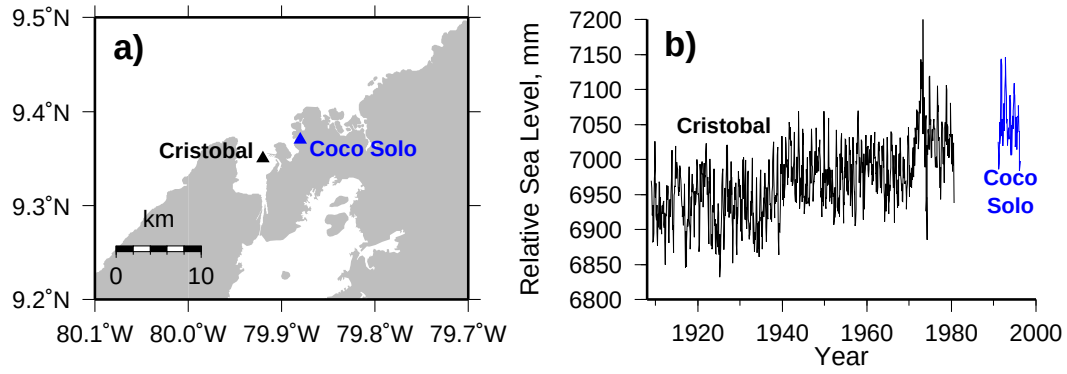

Figure 4.2: **a**: Tide gauges locations for Coco Solo(43) and Cristobal(44), Panama region. **b**: Tide gauge records plotted to same baseline (7000mm).

4.2.2 Altimetry across the Caribbean

Satellite altimetry observations consist of ten day sea surface height (SSH) measurements supplied by AVISO (http://www.aviso.oceanobs.com). The raw TOPEX (1993-2001), Jason-1 (2001-2008) and Jason-2 (2008-present) satellite missions data are calibrated to common ground tracks (Leuliette et al., 2004) and referenced onto a regularised $1^o \times 1^o$ global grid (nodes in Figure 4.1a) using a cross-track gradient correction. This grid, spanning 1993-present was downloaded for this study from the University of Colorado Sea-Level Research Group (http://sealevel.colorado.edu). Further details of the processing methods are available in Wang and Rapp (1994) and Leuliette et al. (2004). Each 10-day point has a precision of 4-5 mm (Mitchum et al., 2010). As with tide gauges, time series show seasonal variations due to annual water exchange from continents and thermal expansion. I resample the altimetric grid from 10 day to monthly values by taking median values of observations within a monthly time window.

4.2.3 Near-shore versus off-shore sea-level change

Before describing the process of analysing the sea-level change for both tide gauges and satellite altimetry, it is worth considering the differences between near-shore and off-shore (open ocean) measurements.

In the open ocean sea-level change is primarily caused by density (steric) variations, which assume that the ocean bottom pressure is constant (Bingham and Hughes, 2012). This is what satellite altimetry measures. Along coast lines, where tide gauges are commonly situated, the ocean depth falls towards zero and the assumption of constant

bottom pressure breaks down. The differences then, between coastal sea level and ocean sea level will alter the interpretation of tide gauge measurements. A common approach to dealing with this problem is by making a steric correction to the measurements by ascribing a vertical water section near to the tide gauge (i.e. a false bottom pressure variation), though not so near or far to give a meaningless steric correction.

Near to the shore, the sea level can be strongly controlled by longshore wind and wave propagation (Calafat et al., 2012). In fact, Bingham and Hughes (2012) demonstrated a decoupling of coastal and ocean sea-level signals at inter-annual time scales.

These issues highlight the problems associated with direct intercomparisons between the two measurement types. However, it as been demonstrated that for multi-annual time scales there is agreement between coastal trends (derived from tide gauges) and the true global mean sea-level rate (derived from altimetry) (Calafat et al. (2012), e.g. Church et al. (2004), Jevrejeva et al. (2006)).

4.3 Time series decomposition: estimation of the rate

The rate of change of sea level is calculated as a function of time. The most common approach to calculate sea-level change is to find a time dependent fit to the following functions using a least-squares approach for both local and global assessments (Baart et al., 2012a),

$$H(t) \quad = \quad at + b \tag{4.1}$$

where a and b denote sea-level change rate and intercept at $t = 0$, and $H(t)$ is the sea level at a given time.

The function $H(t)$ will be a sum of sea and land contributions that occur on different time scales. Those on centuries to millennial time scales stem from global variations in ice volume, temperature, salinity, earth rotation and seafloor subsidence (Baart et al., 2012a). Contributions on decadal time scales include global atmospheric phenomena like the El-Nino Southern Oscillation (ENSO) and the North Atlantic Oscillation (NAO).

Although the monthly time series do not record daily tides, the seasonal changes (months to years) in the tides are recorded. These short term variations are primarily

caused by orbital variations and local basin scale effects have much higher amplitudes than the cumulative long term sea-level change in sea-level records (e.g. Figure 4.2b).

The challenge of separating long term and short term signals with comparable amplitudes has been tackled by numerous studies (e.g. Douglas (2001), Sturges and Hong (2001), Feng et al. (2004), Zhang and Church (2012)). To provide stable estimates of long term sea-level change, Douglas (1991) proposes that only tide gauges spanning more than 50 years should be used, because records over a few decades contain large local and regional inter-annual fluctuations. Figure 4.3a shows the raw and 5 year bin median filtered tide gauge record for San Juan, Puerto Rico (station 31, Figure 4.1). Figure 4.3b shows the variation in sea-level trend computed from successive 20-year spans of these two time series, with their respective means. Although the average values are similar (1.66 and 1.68 mm yr^{-1}), the variations in rate range from -0.79 to 3.56 mm yr^{-1} (raw) and 0.25 to 3.11 mm yr^{-1} (filtered). This means that attention should be given to tide gauge record trend estimates as they are sensitive to the length, start and end period of time windows. Baart et al. (2012a) comment that it is useful to use time windows that include known decadal cycles (e.g. 18.6 year lunar nodal cycle) so as to limit their effect upon trends.

The dilemma faced in the Caribbean is that only three tide gauge stations exceed 50 years in length and 24 have lengths less than the lunar nodal cycle. By removing short term sea-level variations from the tide gauges and altimetry I should be able to derive long term sea-level rates and lower the associated rate uncertainty.

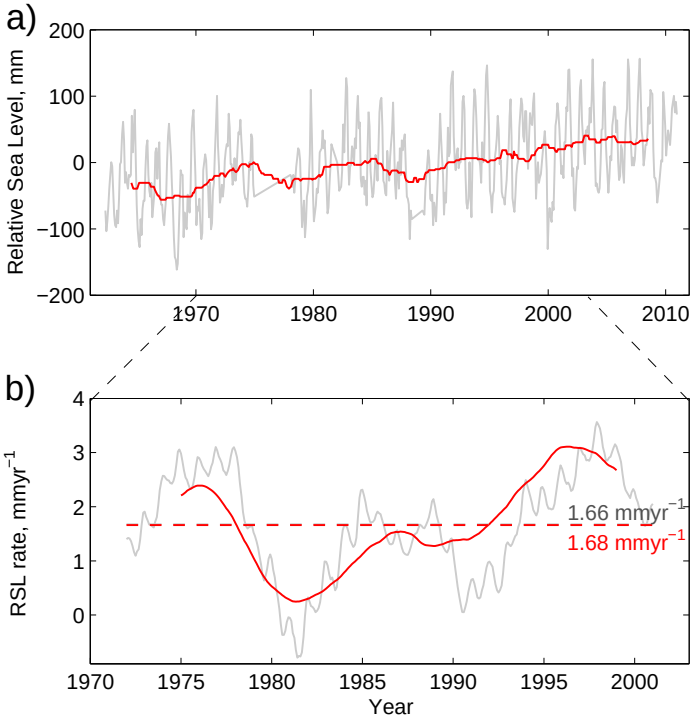

Figure 4.3: **a**: Monthly mean (tide gauge) sea-level data (grey) for San Juan (Puerto Rico) and 5 year bin median filtered sea level (red). **b**: Sea-level trends of series in **a** calculated using sliding 20-year spans, hence rates only cover years 1972-2001. Dashed lines show average of rates through time, with respective values printed.

4.3.1 Method of Mazzotti et al., (2008)

To calculate long term sea-level trends, short term non-linear effects upon RSL and ASL time series must be accounted for. These effects occur over a range of temporal and spatial scales, which have the effect of aliasing mid-high (0.1 to 2 yr^{-1}) frequency sea-level variability into the sea-level trend (Zhang and Church, 2012). This study focuses upon the annual cycle and basin scale climatological variations, which account for a large part of sea-level variability in regions where tidal amplitudes are small such as the Caribbean.

Mazzotti et al. (2008) proposed a method to calculate long term trends whilst accounting for these short term variations. Three corrections are applied cumulatively to preserve the long term signal: an inverse barometric correction, removal of the annual cycle and removal of detrended high frequency signals that are coherent to multiple sea-level time series at the basin scale. These corrections are summarised in Table 4.1

Table 4.1: Corrections applied to tide gauge and altimetry time series

Correction	Tide gauge	Altimetry
1	**Inverse barometric correction**	
	Linearly detrend converted pressure series and subtract from sea-level time series.	Downloaded data already corrected.
2	**Seasonal annual signal correction**	
	Stack 1-year data slices of sea-level time series. Take average of 1-year stack and subtract from sea-level time series.	
3	**Regional common mode correction**	
	Divide region into sub-regions. Sum all detrended time series within given region and average to give pseudo-regional tide gauge series.	For each node, construct an average time series of nodes within 5^o radius whose correlation exceeds 0.129 (95% confidence level).
	Subtract this averaged series from tide gauge/altimetry time series in question. This removes regionally coherent noise at the basin scale.	

and explained in the following sections.

Figure 4.4 shows the cumulative result of applying these corrections to San Juan tide gauge (Puerto Rico). It is obvious that the amount of scatter is reduced by comparing the root mean square (RMS) variability of the estimate trend to the processed data. There is an overall 39 mm reduction in RMS variability (see Section 4.3.2) from raw (a, RMS: 50.4 mm) to regional common mode correction (g, RMS: 11.4 mm). Furthermore, the amplitude spectra shows the removal of the annual signal (f and h) from inverse barometric (c, RMS: 45.9 mm) to annual signal corrected series (e, RMS: 32.2 mm). The regional common mode correction (g) significantly improves the error term, which falls by 0.59 mm yr^{-1} from $\pm$0.72 to $\pm$0.13 mm yr^{-1}. Appendix D shows the same series of corrections for a selection of the 48 tide gauges.

Figure 4.5 shows the improvements made by the corrections upon all the Caribbean tide gauges and a subset (to be discussed later). The mean error falls significantly for both tide gauge sets with the exception of the inverse barometric correction for all tide gauges, though this is mainly due to the shortening of the tide gauge records to 1960 onwards. The greatest reduction occurs with the annual signal correction ($\sim$50%).

Inverse Barometric correction

The inverse barometric correction accounts for the influence of changing atmospheric pressure upon sea level, which responds to the weight of the atmosphere. A theoretical

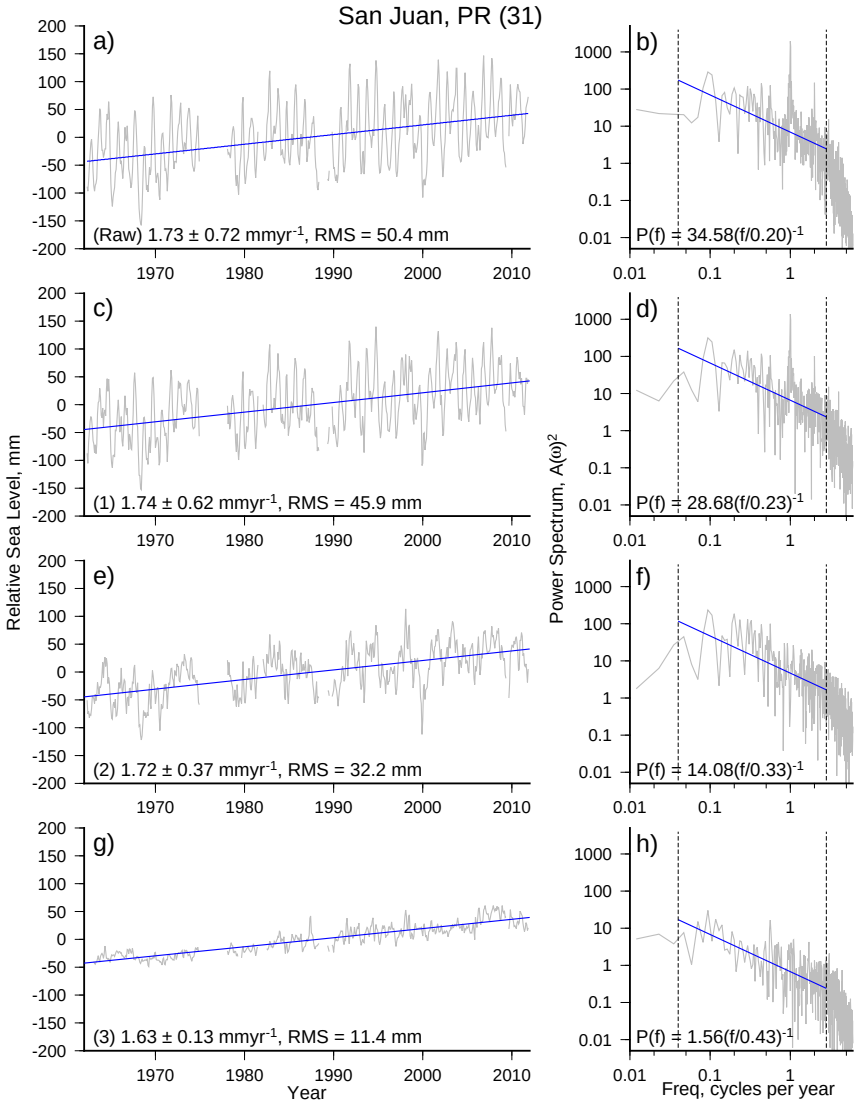

Figure 4.4: Monthly mean tide gauge record for San Juan (Puerto Rico) (**a**, **c**, **e** and **g**). Raw observations (**a**) and the cumulative result after each correction (**c**, **e**, **g**) with linear RSL trends (blue). **c** (1) inverse barometric correction, **e** (2) mean seasonal correction, **g** (3) regional common mode correction (region C for San Juan). **b**, **d**, **f** and **h** show power spectra of raw and corrected observations. **b**/**d** show dominant annual signal whilst **f**/**h** show suppression after corrections.

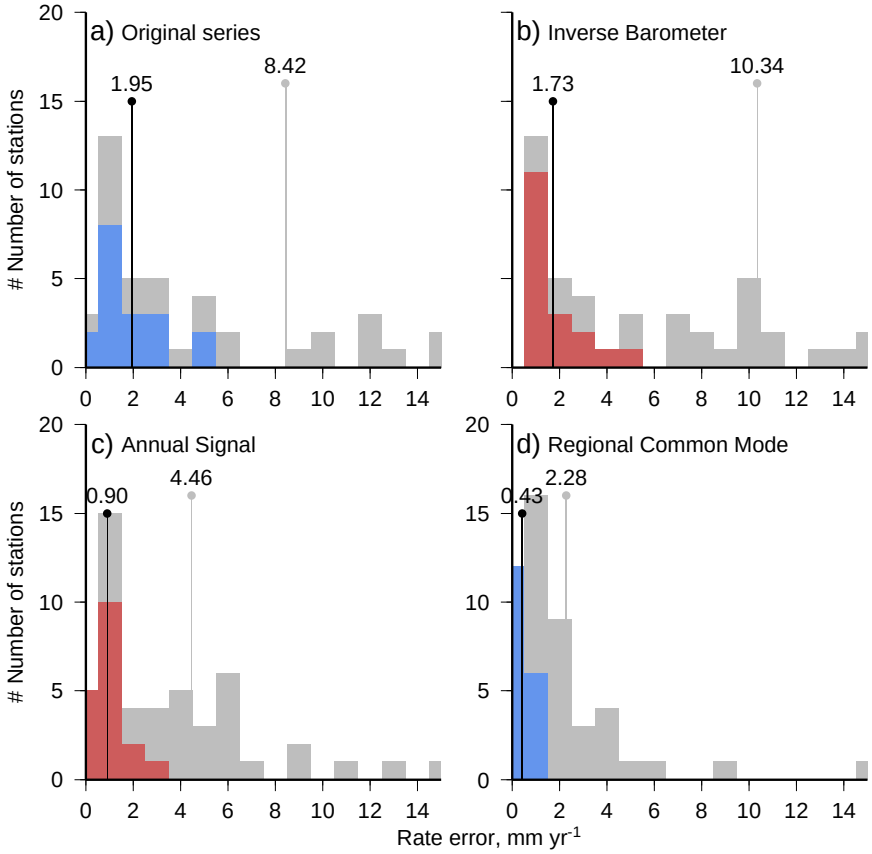

Figure 4.5: Distribution of errors for all and selected Caribbean tide gauges. **a**: Uncorrected tide gauge record, **b**: Inverse barometric correction, **c**: Annual signal correciton, **d**: Regional common mode correction. Mean values shown for each distribution.

value of height change (δh) of water due to 1 mbar pressure change ($\Delta P = 100$ Pa) can be calculated using,

$$\delta h = \frac{\Delta P}{g\rho} = \frac{100\text{kg m}^{-1}s^{-2}}{-9.81\text{ms}^{-2} \times 1000\text{kg m}^{-3}} \quad (4.2)$$

$$= -10.2 \text{ mm} \quad (4.3)$$

where g is acceleration due to gravity at Earth surface and ρ is the density of water. This reveals that as atmospheric pressure drops, sea-level rises and likewise as atmospheric pressure rises so sea level falls. The atmospheric pressure, essentially weather varies on seasonal time scales, thus the monthly sea-level measurements need to be corrected for this variation.

Monthly atmospheric pressure measurements are provided by the NOAA

(*http://www.cdc.noaa.gov*) in the form of ICOADS 1-degree grid measurements for the globe (Kalnay et al., 1996). The measurements span 1960 to present, which limits the length of sea-level time series to 52 years. To test the relationship between atmospheric pressure and the tide gauge records, the correlation coefficient is taken between the two where they overlap. Figure 4.6a shows an example of this correlation for San Juan tide gauge. The average of the correlation coefficients for all tide gauge stations is -0.42 (Figure 4.7a). Next, a least squares trend is calculated between tide gauges and pressure series in mm/mb (e.g. San Juan tide gauge, Figure 4.6b). This empirical relationship gives an average of -17.3 mm/mb for all tide gauge stations (Figure 4.7b).

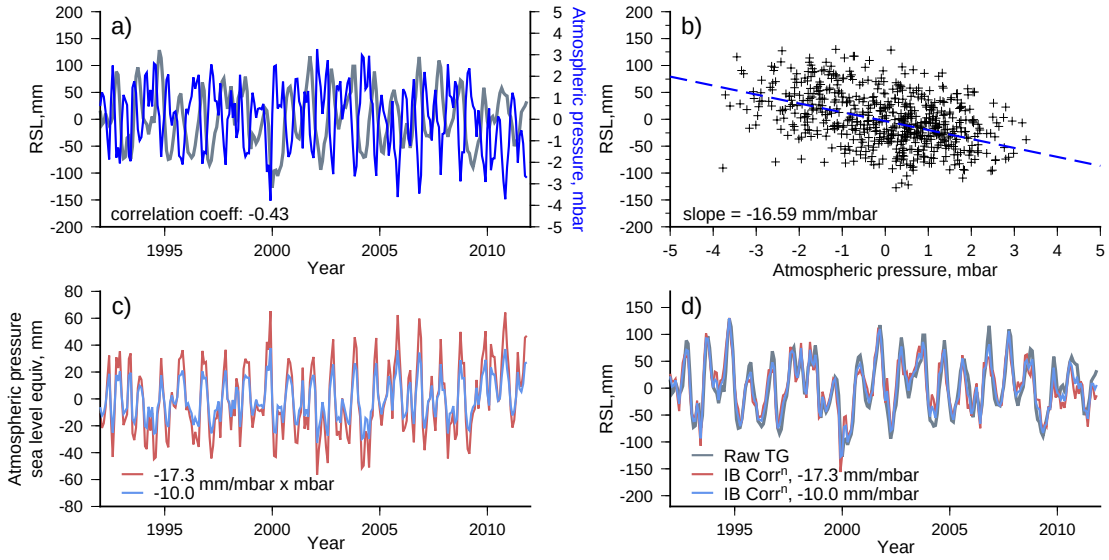

Figure 4.6: Inverse barometric correction used for tide gauge San Juan (Puerto Rico). **a**: paired tide gauge (grey) and atmospheric pressure (blue) time series with associated correlation coefficient at zero lag. **b**: Empirical, linear relationship between relative sea-level height (mm) and pressure (mbar). **c**: Detrended, sea-level height equivalent atmospheric pressure, calculated by multiplying the atmospheric time series by the average of all tide gauge/pressure linear gradients (-17.3 mm/mb, red) and the standard correction (-10 mm/mb, blue). **d**: Uncorrected (grey) and inverse barometer corrected (as in **c**) tide gauge time series.

The theoretical -10 mm/mbar value is generally used to correct monthly mean sea-level records, though it is smaller than the average empirical value for the Caribbean tide gauges. The Caribbean value may be elevated due to the effects of wind stress, ocean currents and resonance effects (Thomson and Tabata, 1982). Furthermore, the deviation is even larger when compared to trends as low as 5 mm/mbar found by Gaspar and Ponte (1997) in the equatorial regions.

In the Caribbean Sea, wind stress (at its extreme causing hurricanes) is caused

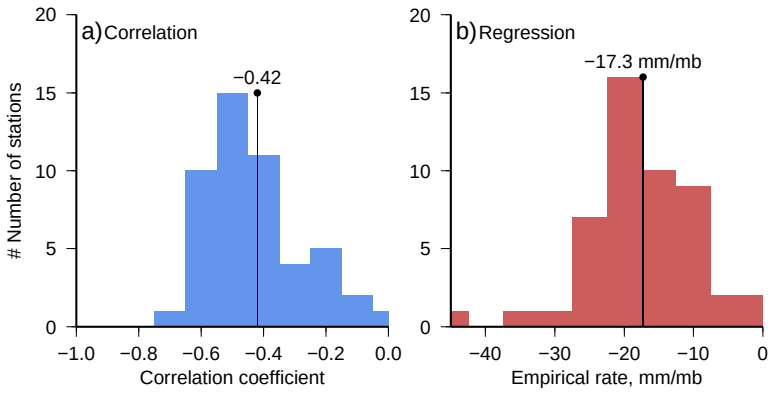

Figure 4.7: Distributions of, **a**: correlation coefficients and **b**: empirical trends, between tide gauges and nearest atmospheric pressure series from 1-degree grid

by sea surface temperature, which rises above 28°C from July to October each year (Wang and Enfield, 2001, Wang and Lee, 2007). Along the northern coast of South America, there is an axis of strong trade winds that drive ocean upwelling, inhibiting convection across the Antilles Islands particularly in mid-summer (Granger, 1985, Jury et al., 2007, noz et al., 2008, Jury and Malmgren, 2012).

Since the scatter about the average of the empirical trends is large (e.g. Figure 4.6b), I use the theoretical sea level-pressure relationship (-10mm/mb). Although this would appear to be conservative, applying the full empirical relationship at each tide gauge would likely introduce noise to the signal since the correlation between the two series is not greater than -0.7. Furthermore, the atmospheric time series (e.g. Figure 4.6a, blue) shows an annual component, whose influence upon the tide gauge record will be removed after the annual signal correction (see next section). For each tide gauge record, I multiply the paired atmospheric pressure time series by -10 mm/mb and linearly detrend the new series (e.g. Figure 4.6c). The tide gauge correction is then performed by subtracting this new series from the tide gauge time series (e.g. Figure 4.6d).

The altimetry is already processed for atmospheric effects when downloaded.

Annual signal correction

The second correction removes an empirically calculated annual signal that is unique to each sea-level time series. The annual signal is caused by periodic variations in distance between the Earth and the Sun, changes in solar declination, atmospheric pressure, wind effects and steric expansion (Torres and Tsimplis, 2012). The mean annual cycle

has amplitudes of up to 200 mm (Tsimplis and Woodworth, 1994, Vinogradov and Ponte, 2010). Within the Caribbean, the annual cycle has amplitudes between 25 - 90 mm, peaking between April and October (Torres and Tsimplis, 2011, 2012).

Incorporated into the annual signal is a semi-annual signal that varies from Northern South America (30 - 50mm) to Greater Antilles (0 - 20 mm) to Southern Florida (30 - 40 mm) whose maximum occurs from October to November. Shorter period signals include a mean micro-tidal range of 200 mm (Kjerfve, 1981) that rises to ∼400 mm on the Nicaraguan Shelf and the extreme South East Caribbean. Two dominant climate forcing parameters have been suggested to account for the observed semi-annual signal; the Panama-Colombia gyre driven by wind stress and the Caribbean low level jet modulating sea level along the north coast of South America (Torres and Tsimplis, 2012).

For each tide gauge/altimetry series (e.g. San Juan tide gauge, Figure 4.8), 1-year data slices are stacked over the length of the time series, then averaged by the number of stacks (i.e. average the sum of all January's, February's, etc of time series). Figure 4.8b shows the determined annual signal for tide gauge San Juan, which is repeated to produce a time series that spans the length of the tide gauge series. The correction is then subtracted from the whole series (resulting curve for San Juan in Figure 4.4c).

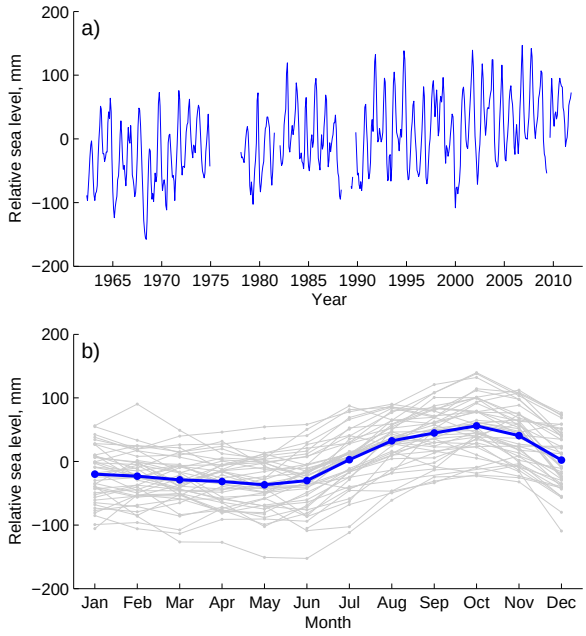

Figure 4.8: Annual signal correction used for tide gauge San Juan (Puerto Rico). **a**: Tide gauge data after inverse barometric correction (Figure 4.6). **b**: Stacks of 1-year bins (grey lines) over the whole time series and the average of these (blue) giving 12, monthly averaged seasonal sea-level data points.

Regional common mode correction

The final correction is designed to remove regionally coherent noise between sea-level time series on the basin scale. The time series in a given region are summed, averaged and detrended producing a pseudo-tide gauge coherent noise time series. This pseudo-series is subtracted from each tide gauge time series, having already been through processing steps 1 and 2, within the given region.

Since I am interested in 20$^{\text{th}}$ century and modern RSL and ASL rates, the regional common mode correction does not retain accelerations in the final corrected time series. This is caused by linearly detrending the regional summation of time series, hence any accelerations would become part of the noise content. The globally averaged ASL acceleration over the last 100 years is estimated by Church and White (2011) as 0.009 $\pm$ 0.004 mm yr^{-2}. This gives a total ASL rise of $\sim$ 200 mm for the last 100 years and a maximum of 86.2 $\pm$ 16.3 mm (1986 - 2009) for the average length of the Caribbean tide gauges (23 years). Although the total ASL rise due to acceleration would be comparable to that of a linear rise for many of the tide gauge time series, publications searching

for long term sea-level acceleration have used time series of more than 100 years (e.g. Jevrejeva et al. (2008), Church and White (2011)) and comment that to make robust acceleration estimates requires the removal of 2 to 30 year signal variability. Since the average time series lengths of the Caribbean tide gauges and satellite altimetry are 23 and 20 years respectively, it is reasonable to concentrate upon solving for two degrees of freedom (slope and intercept) rather than three with the addition of a quadratic term.

Grouping the tide gauges into regions requires care because of the discontinuous time spans and geographical variability. I approach the problem by trying to satisfy two caveats. One, the tide gauges in a given region need to show some positive correlation to each other. Two, at least two tide gauges in a given region need to overlap in time to produce an average pseudo-tide gauge time series. The tide gauges in the Caribbean are partitioned into four sub-regions (Figure 4.9) whose inter-tide gauge correlations are considered in the next section.

The regional common mode correction is applied to satellite altimetry but because of the high and even distribution of nodes (Figure 4.1a), the method is implemented slightly differently (see Altimetry correlation).

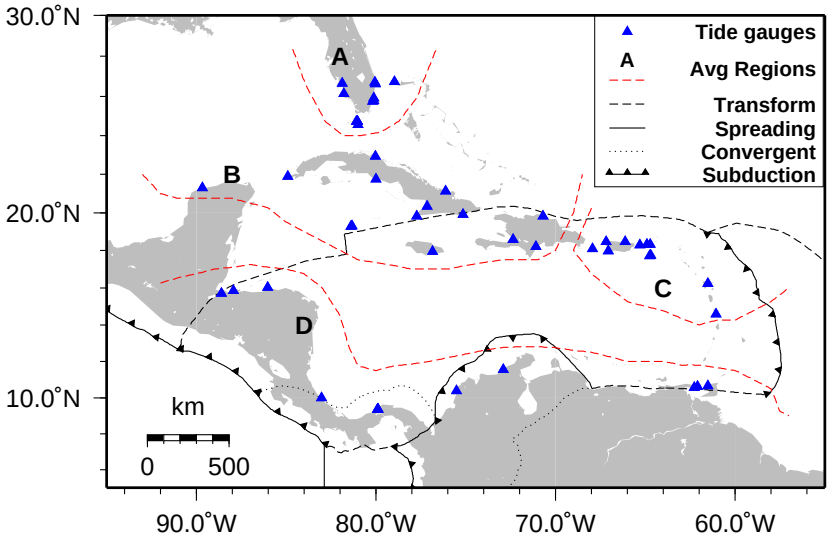

Figure 4.9: Map of tide gauges and sub-regions into which they are binned to perform regional common mode correction

Inter-tide gauge correlation

Calculating correlation between tide gauges across the Caribbean allows one to delimit sub-regions for the third step of the correction process (regional common mode correction). For two time series, x and y consisting of discrete points x_i and y_i, the correlation coefficient (r_{xy}) is defined by,

$$r_{xy} = \frac{V_{xy}}{s_x s_y} \tag{4.4}$$

$$V_{xy} = \frac{1}{N-1}\sum_{i=1}^{N}(x_i - \bar{x})(y_i - \bar{y}) \tag{4.5}$$

$$s_x = \sqrt{\frac{1}{N-1}\sum_{i=1}^{N}(x_i - \bar{x})^2} \tag{4.6}$$

$$s_y = \sqrt{\frac{1}{N-1}\sum_{i=1}^{N}(y_i - \bar{y})^2} \tag{4.7}$$

where V_{xy} is the covariance between two time series (e.g. tide gauges) and s_x and s_y are the standard deviations of each series ($\bar{x} = \frac{1}{N}\sum_{i=1}^{N} x_i$ and $\bar{y} = \frac{1}{N}\sum_{i=1}^{N} y_i$ is the mean of the time series) (Riley et al., 2006).

Figure 4.10 shows the correlation coefficients between all 48 tide gauges in the study region after the inverse barometric correction and annual signal is removed. The figure shows the stations ordered into their respective regions. There is a strong correlation between stations across the Caribbean region prior to annual signal removal (Figure 4.10a). The correlation of the off-diagonal elements drop significantly after this correction has been made (Figure 4.10b). Most of the stronger positive correlation lies near the diagonal (where the 1:1 line is each station correlated with itself) indicating that stations near to each other record similar sea-level signals. The average of the correlation coefficients for regions A, B, C and D are 0.53, 0.36, 0.65 and 0.39 respectively. Although regions B and D show weaker correlations, due in part to the large geographical areas they cover, complete overlapping records with two or more tide gauges is achieved in all regions. Therefore, using these groupings of tide gauges I am able to apply the regional common mode correction, such that each time series is not being subtracted from itself.

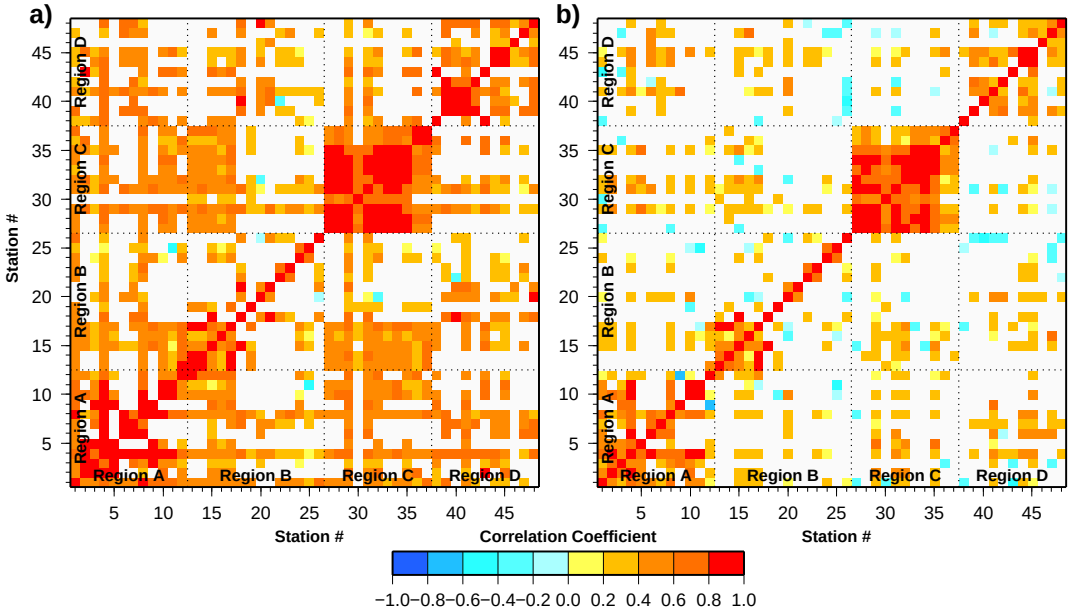

Figure 4.10: Correlations between tide gauges across Caribbean after (**a**) inverse barometric correction and (**b**) removal of seasonal signal. Station number corresponds to numbers shown in Figure 4.1. White areas are those without correlations due to no overlap of time series or correlations that lie below the 95% significance level, which we do not consider.

Altimetry correlation

Figure 4.11a - f shows maps of correlation coefficients between a node (marked by black point) and all other nodes of the satellite altimetry grid for a suite of geographic positions. It is evident that whilst certain parts of the Caribbean correlate regionally, others are correlated at the sub-regional level.

A local correlation anomaly can be seen at the entrance to the Gulf of Mexico, by the Yucatan Straits (Figure 4.11a). Chérubin et al. (2005) modelled deep ocean flow variability in the Yucatan Straits and found that long-lived loop current rings were produced (6 year period) that propagated into the eastern Gulf. The area delineated by this loop is the same as that of the zero-negative correlation anomaly. As a result of this loop current, this region would be subject to distinct sea-level change, in comparison to the shallow areas of the Campeche bank and Florida shelf either side of it.

The Atlantic portion of the gridded region (Figure 4.11b) is correlated consistently between 0.4 - 0.6, though zero correlation exists in the south eastern extreme of the region. The area of zero correlation is located at the outflow of the Orinoco river, which has seen large local sediment output during the Holocene (Warne et al., 2002)

and continues to affect local sea level. It is likely that tide gauge observations in the south eastern Caribbean will be affected by this source (Sheng and Tang, 2003).

There are some complex correlation patterns in the Caribbean Sea (Figure 4.11c, d, f), which appear to delineate ocean basins (Figure 4.11h: Colombian, Venezuelan and Yucatan Basins). Grid nodes lying in the Colombian Basin displays very high, localised positive correlations (Figure 4.11f). This basin, as with the other four basins composing the Caribbean Sea is controlled by the Caribbean current running from southeast to northwest. The Colombian Basin is also affected by the Panama-Colombian gyre caused by the interaction of the current with the Magdalena river outflow. This produces pronounced local effects (Mooers and Maul, 1998, Sheng and Tang, 2003).

Figure 4.11e shows that the Pacific nodes are strongly correlated to each other, whilst the Caribbean has little or no correlation with the Pacific.

The correlation study here results in an adjusted regional common mode correction method. For each node, an average time series is constructed from those nodes within 5^o radius and that have a correlation coefficient greater than 0.129. This value is the 95% confidence value of statistical significance for time series of 234 data points. This averaged psuedo-time series is detrended and subtracted from the node time series in the same way as the tide gauge. This process is applied after the altimetry grid have been processed for the annual signal.

4.3.2 Calculating uncertainties

Empirical rate error estimate

In geodetic studies, it has been normal practise to calculate a linear rate of change and uncertainty of the signal. The uncertainty is calculated using the assumption that the individual measurements are uncorrelated (white noise power spectrum) and that the normal (Gaussian) distribution would be the most appropriate noise model (Williams, 2003). However, recent geodetic studies have found error sources that are correlated and therefore a different noise model needs to be used. A common statistical model that describes many geophysical processes is the power-law model, which has been preferred in many GPS (e.g. Agnew (1992), Zhang et al. (1997), Mao et al. (1999)) and tide gauge studies (e.g. Snay et al. (2007), Mazzotti et al. (2008)).

The time domain behaviour of the signal in the power spectrum takes the form (Agnew, 1992),

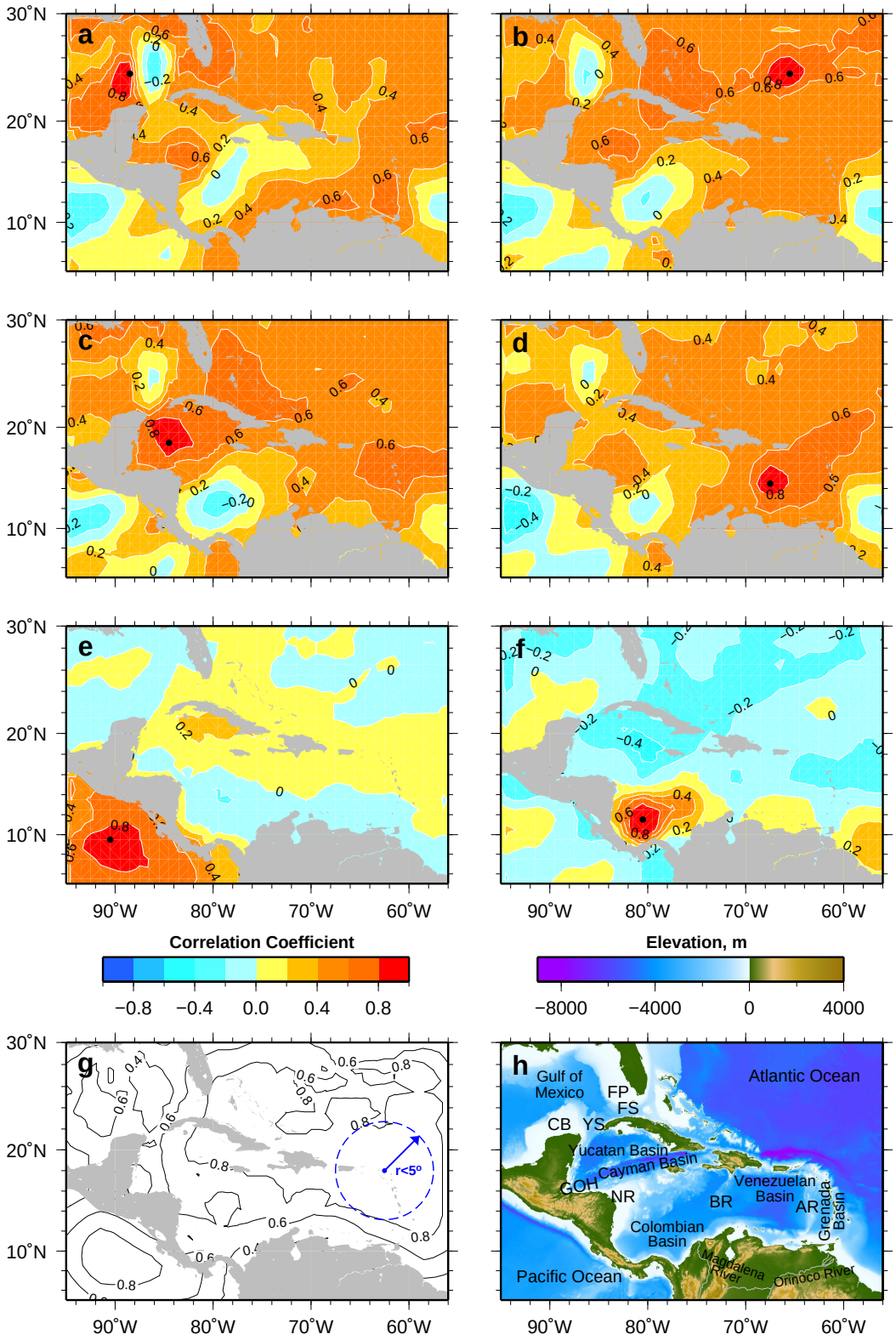

Figure 4.11: a-f: Correlation between time series at the marked node (black dot) and other time series from nodes in gridded region. g: Fraction of nodes within 5^o of central node and greater than correlation coefficient (0.1288) for regional common mode correction h: Topography and bathymetry of Caribbean (GEBCO 1 arc-minute gridded data from *http://www.bodc.ac.uk/*). Acronyms for bathymetric locations: FP, Florida Platform; FS, Florida Shelf; CB, Campeche Bank; YS, Yucatan Shelf; GOH, Gulf of Honduras; NR, Nicaragua Rise; BR, Beata Ridge; AR, Aves Ridge

$$P(f) = P_0 \left(\frac{f}{f_0} \right)^{\nu} \tag{4.8}$$

where P is spectral power at a given frequency f, ν is the spectral index, P_0 and f_0 are normalising constants. The spectral index normally lies between -3 and -1 for strongly correlated processes with high energy at low frequencies (Agnew, 1992, Williams, 2003, Mazzotti et al., 2008) meaning energy at low frequencies exceeds that at high frequencies ("red" spectrum). The spectral index ν = 0, -1, -2 give white (Gaussian), flicker and random walk (Brownian motion) noise respectively (Williams, 2003). In the RSL studies of Snay et al. (2007) and Mazzotti et al. (2008), a white and flicker noise model ($\nu = -1$) was applied to tide gauge time series. I choose this value for the spectral index in this study, which gives equation 4.8 as,

$$P(f) = P_0 \left(\frac{f}{f_0} \right)^{-1} \tag{4.9}$$

The normalising constant P_0 is the average power (in the frequency domain) of the time series. This could also be thought of as the white noise amplitude, when $\nu = 0$. The normalising constant f_0 is calculated by taking logarithms of equation 4.9,

$$\begin{aligned} logP(f) &= log\left[P_0 \left(\frac{f}{f_0} \right)^{-1} \right] && (4.10) \\ &= logP_0 + logf_0 - logf && (4.11) \end{aligned}$$

and performing standard linear least squares ($logP(f) = c + mlogf$) to calculate the intercept at $log(f) = 0$ (since m = -1) to give equation 4.14.

$$\begin{aligned} c - logf &= logP_0 + logf_0 - logf && (4.12) \\ c &= logP_0 + logf_0 && (4.13) \\ f_0 &= \frac{10^c}{P_0} && (4.14) \end{aligned}$$

Having defined the constants in equation 4.8, which can be calculated by taking the power spectrum of the tide gauge or altimetry time series and calculating its average power and the intercept at $log(f) = 0$, I define the white (σ_w^2) and flicker (σ_f^2) noise amplitudes respectively,

$$\sigma_w^2 = \frac{f_s}{2} P_0 f_0^{-1},\ \sigma_f^2 = \pi \sqrt{f_s} P_0\ . \tag{4.15}$$

f_s is the sampling frequency of the time series. Following these definitions, Mao et al. (1999) proposed a formula regarding the uncertainty in the rate using the white and flicker ($\nu = -1$) power law assumption,

$$\sigma_{wf} \approx [(12\sigma_w^2/gT^3) + (9\sigma_f^2/16T^2)]^{0.5} \tag{4.16}$$

where g is the average number of points per year in the time series: 12 (tide gauge), 36.5 (altimetry) and 12 (altimetry after resampling). T is the series time span in years. Although the completeness of the time series and the spectral power affect the level of uncertainty in the determined rate, the dominant factor is the length of the time series (Equation 4.16).

In this study, I use equation 4.16 to estimate the rate uncertainty of both tide gauge and altimetry time series. As has been mentioned, previous work using tide gauges and GPS have used this method to estimate rate uncertainty (e.g. Snay et al. (2007), Mazzotti et al. (2008), Bouin and Wöppelmann (2010)).

I calculate the white-flicker noise error (σ_{wf}) for each tide gauge and altimetry node at each processing step. I use the individual error models for each tide gauge or satellite altimetry node to calculate the error as described in the results and subsequent chapters. Figure 4.12 shows the average of each of the processing steps error models for (a) all tide gauges and (b) tide gauges whose span is longer than 15 years, whilst ending at or after 1997. The satellite altimetry has a fixed span from 1992 to 2012, which gives an average error ± 1.04 mm yr^{-1} after processing. In the results section, the error varies spatially due to different levels of noise depending upon the location in the Caribbean.

Table 4.2 shows how the error drops with each correction for the three scenarios outlined. It is obvious that the corrections reduce the error estimates significantly. The average error after all the corrections are performed falls by more than half compared to the uncorrected time series. A subset of tide gauges, longer than 15 years and ending at or after 1997, is constructed to study longer term sea-level trends with greater confidence. the average error model (Figure 4.12) after processing gives an error of ± 0.65 mm yr^{-1} at 15 years span.

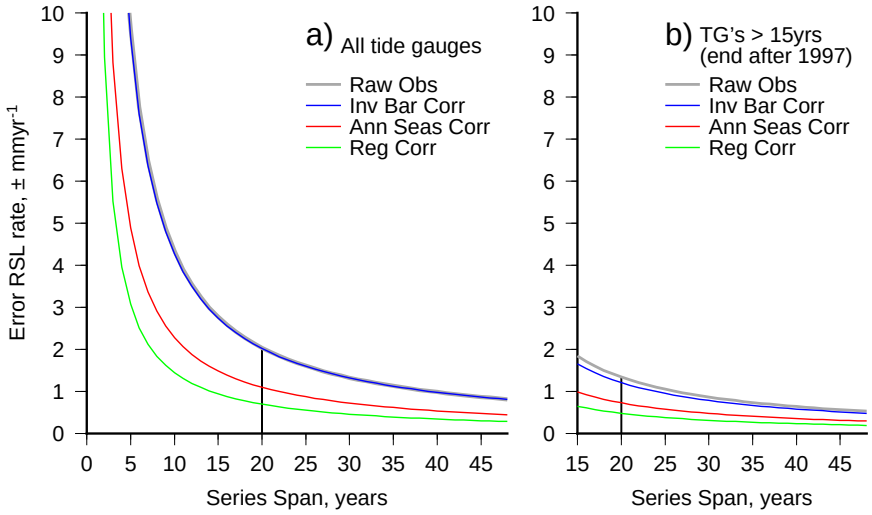

Figure 4.12: Error models derived from average of individual error models from each processed tide gauge record. Each model corresponds to a processing step from raw data, inverse barometer correction, annual seasonal correction and regional common mode correction. **a**: all tide gauges, **b**: tide gauges whose span is longer than 15 years, whilst ending at or after 1997.

Table 4.2: Average of white-flicker noise error models at 20 year span, for all and selected (see text) tide gauges and satellite altimetry after each correction stage: IB, Inverse Barometer; AS, Annual Signal; RCM, Regional Common Mode.

	Error for time series span of 20 years			
Sea-level records	Raw	IB	AS	RCM
All tide gauges	±2.04	±2.02	±1.10	±0.70
Tide gauges >15 years, post-1997	±1.34	±1.21	±0.73	±0.48
	Raw	Resampled	AS	RCM
Satellite altimetry	±3.27	±3.16	±1.95	±1.04

Root mean square variability

In addition to the empirical rate error estimate, I refer to RMS variability. This is calculated as the degree of scatter of the detrended time series about zero. The RMS variability is calculated as follows,

$$\mathrm{RMS} = \sqrt{\frac{1}{N}\sum_{n-1}^{N} |X_n - (a \times t_n + b)|^2} \tag{4.17}$$

where X_n is the time series at an altimetry node of length N . t_n, a and b are the time at n and least squares estimated rate and intercept of the time series X_n. This

is another way of showing how the corrections described above denoise the time series and improve the fit of the trend. Figure 4.4 shows the reduction in RMS variability after each correction step, described in section 4.3.1.

4.4 Tide gauge results

4.4.1 Long term rates of relative sea-level change

Figure 4.13 shows the rates of RSL with their associated errors for tide gauges in the Caribbean region. These rates extend across different, overlapping time-spans (Figure 4.1). Therefore, all trends calculated using series post-1960 are presented in Figure 4.13a, whilst modern rates are presented in Figure 4.13c using a subset of tide gauges as described in the previous section. Figure 4.13b shows uncertainties and demonstrates the power law relationship such that increasing record length results in decreasing errors. The uncertainties of the modern rates (Figure 4.13d) lie near to the average error model (Figure 4.12b) with a RMS misfit of 1.01 mm yr^{-1}. In all regions, present relative sea level is rising. After the three corrections are applied, averaging tide gauge trends for Regions A, B and C give rates of 2.1 $\pm$ 0.5, 1.7 $\pm$ 0.6 and 1.4 $\pm$ 0.2 mm yr^{-1} respectively.

Table 4.3 shows a comparison between some of the results in this study with those calculated from local (Palanisamy et al., 2012) and global (Wöppelmann et al., 2007) studies. The average difference between my raw rates and those of Palanisamy et al. (2012) is 0.28 mm yr^{-1} but this is skewed by Lime Tree Bay, which differs by 1.13 mm yr^{-1}. Excluding this site gives an average difference of 0.11 mm yr^{-1}. The close agreement between the rates of Palanisamy et al. (2012) (except Lime Tree Bay) and Wöppelmann et al. (2007) gives me confidence to trust the raw rates I have calculated.

The discrepancies between the error terms come from the different ways errors are derived. The errors of this study are generally larger because of the assumption that the deviations from the mean are not a white noise spectrum, where as Wöppelmann et al. (2007) and Palanisamy et al. (2012) use formal standard deviations from their least squares linear regression. Wöppelmann et al. (2007) note that their errors are optimistic due to the many parameters involved in the processing. Another difference between this study and the published errors is that my corrected time series (fourth

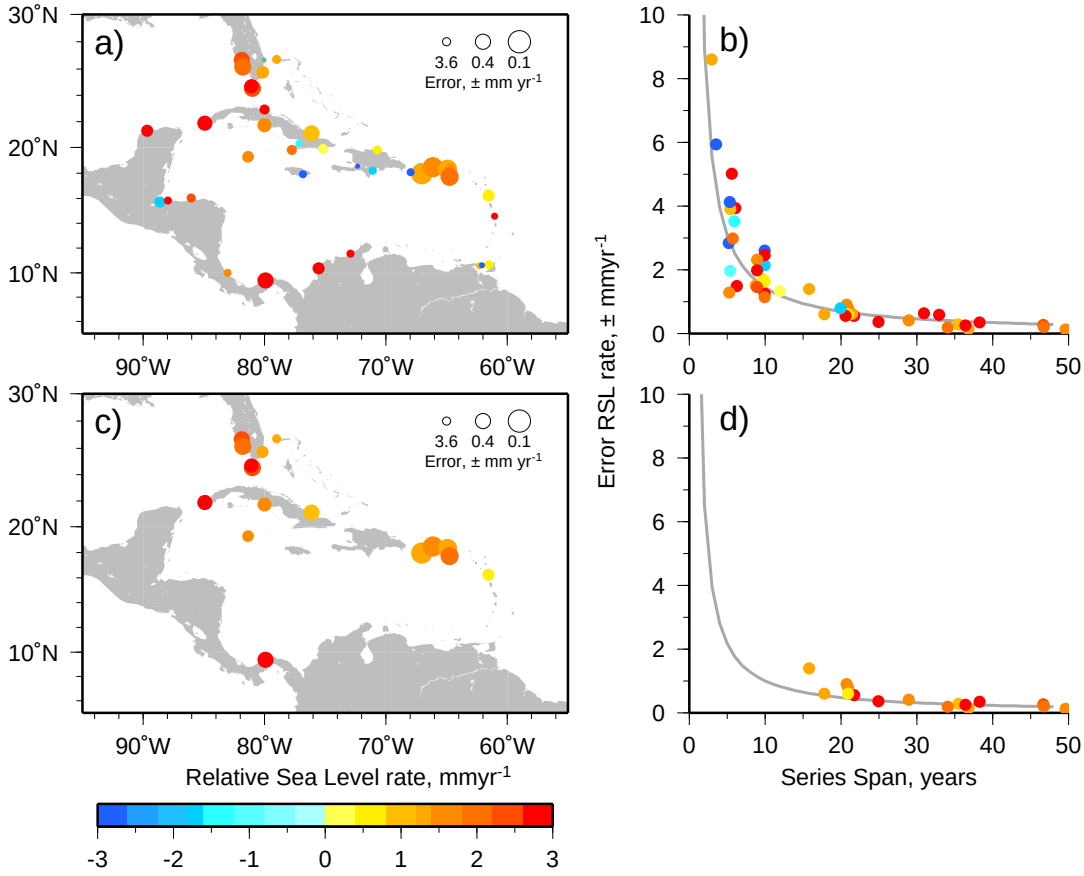

Figure 4.13: Rates and their errors (**a**,**c**) and tide gauge spans and errors (**b**,**d**) of corrected relative sea level. **a**,**b**: all tide gauges in region since 1960. **c**,**d**: tide gauges that span > 15 years, whilst ending at or after 1997. Average error model after all corrections from Figure 4.12 plotted in grey.

column in Table 4.3) begin (at the earliest) at the start of the barometric record (1960), thereby reducing the tide gauge spans. Key West and Magueyes Island tide gauge records are reduced by 47 and 5 years respectively.

There is a trade off between reducing sea-level record length and the enhancement of the rate and its associated error. For example, the error at Key West tide gauge is smaller for the unshortened record ($\pm$ 0.41 mm yr^{-1}) than the uncorrected shortened record ($\pm$ 0.82 mm yr^{-1}). However, after the corrections, the error ($\pm$ 0.20 mm yr^{-1}) is reduced below that of the original. The removal of the regional common mode signal suppresses climate-ocean effects and gives a true measure of long term RSL rate. The variations from site to site across the Caribbean is therefore caused by site effects at the tide gauge (e.g. land uplift) and the long wavelength

Table 4.3: Relative sea-level rates (mm yr^{-1}) of tide gauges, this study and published sources

		This analysis		Palanisamy	Wöppelmann
Station (no.)	Start/End	Raw	Corrected	et al. (2012)	et al. (2007)
Key West (4)	1913/2012	2.26±0.41	2.53±0.20		2.25±0.09
Cabo San Antonio (15)	1971/2010	3.22±1.26	3.13±0.35	3.50±0.7	
Gibara (17)	1974/2010	1.39±1.46	1.10±0.28	1.50±0.5	
Magueyes Island (29)	1955/2012	1.41±0.68	1.27±0.10	1.40±0.2	
San Juan (31)	1962/2012	1.73±0.72	1.63±0.13	1.60±0.3	
Lime Tree Bay (35)	1978/2012	2.13±1.40	2.00±0.19	1.00±0.5	

Note: Key West (4) and Magueyes Island (29) use shorter spans for their corrected rates (beginning at 1960 or later because of the atmospheric record).

sea-level variability.

Although the tide gauges are sparsely distributed (Figure 4.13c) the modern RSL rate appears to decrease from west to east along the Greater Antilles. Trends decrease from 2.5 ± 0.2 (Key West) to 1.1 ± 0.3 (Gibara) to 0.8 ± 0.6 mm yr^{-1} (Pointe a Pitre).

4.4.2 Quindecadal variations of relative sea level

To contrast with the the long term rates of relative sea-level change, changes over 15 year time spans are analysed since 1967. The same correction methods are applied and a bin size of 15 years is chosen to investigate these shorter term changes. It is acknowledged that the best error will be ∼0.65 mm yr^{-1} (Figure 4.12) for a full 15 year series. At this timescale, the RSL rates are likely to be affected by climate oscillations (e.g. El-Nino Southern Oscillation: ENSO). Figure 4.14a-c shows the rates of RSL change from 1967 - 1982, 1982 - 1997 and 1997 - 2012 with their associated errors. Figure 4.14d shows sub-regional and Caribbean averaged tide gauge RSL rates and their associated errors.

At any of the three time slices, it is obvious that rates of RSL across the Caribbean are positive (with minor large error exceptions). Within any sub-region (A, B, C and D: Figure 4.14a), RSL rates are similar though with varying degrees of error depending upon the completeness of tide gauge records. There is a qualitative agreement between RSL rates in the northern Caribbean, though upon closer inspection the 1997 - 2012 rates in region C are 1 - 1.5 mm yr^{-1} greater than those in regions A and B. To identify any long term RSL change I average all RSL rates within each time window. Although the results point to increasing RSL rate (1.3 ± 1.2, 1.6 ± 1.5, 2.1 ± 0.9 mm yr^{-1} for 1967 - 1982, 1982 - 1997, 1997 - 2012 respectively), the change is not statistically significant enough to support this hypothesis.

The northern Caribbean regions display a certain coherence in their RSL rates. By comparison, the Colombian Basin (south-western) area of region D shows strongly elevated rates from 1966 - 1982 (Figure 4.14d). Although the resolution of the 15 year windows is very poor, there is some indication that the rates are anti-correlated to the ENSO oceanic index. This is shown by a high RSL rate (5.0 ± 1.2 mm yr^{-1}, 1967 - 1982) corresponding to a negative index and a low RSL rate (0.5 ± 2.5 mm yr^{-1}, 1982 - 1997) corresponding to a positive index.

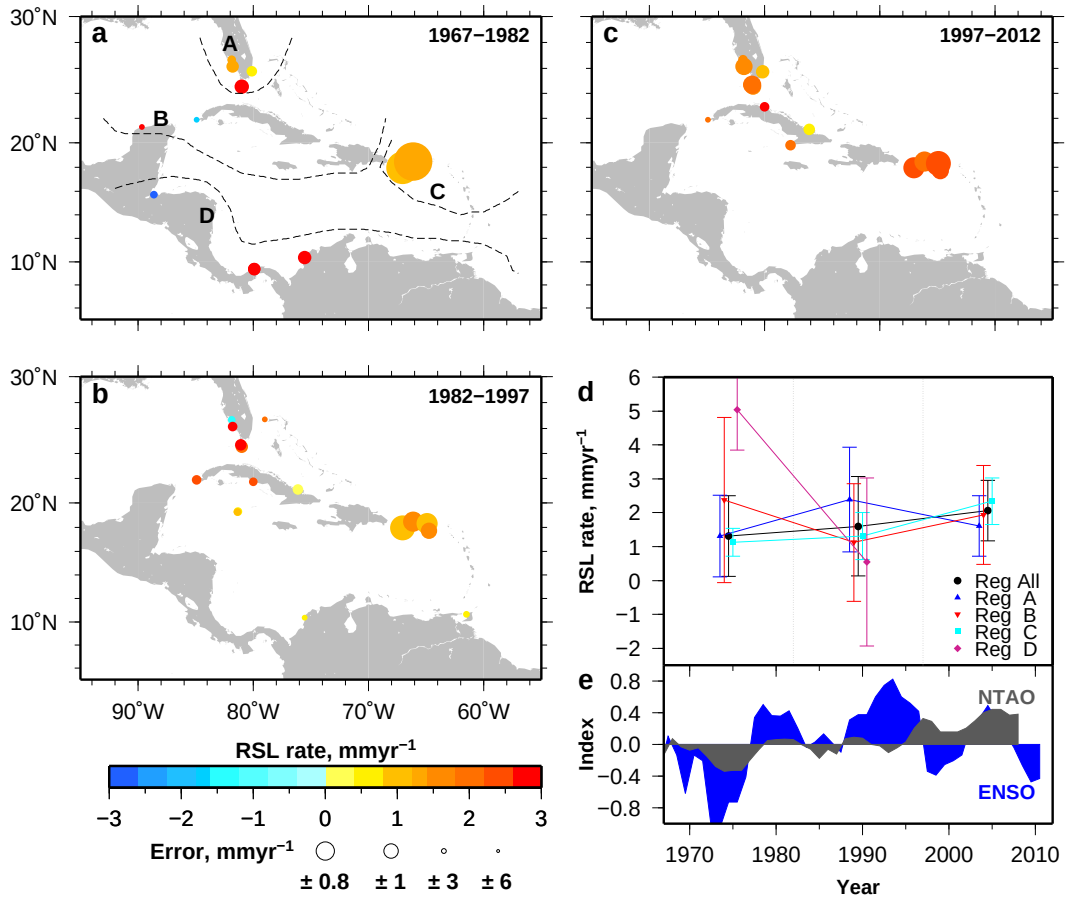

Figure 4.14: **a-c**: Rates of relative sea-level change (coloured circles) calculated from tide gauges in 15 year bins. Size of circle denotes error of calculated rate. Tide gauge time series have been corrected as described in text and rates are plotted in each bin if the time series has > 50% completeness. Subregions for regional common mode correction denoted in **a**. **d**: Regionally averaged tide gauge rates plotted at centre of each 15 year bin. **e**: Oceanic indices of ENSO and NTAO, with median 5 year bins.

4.5 Satellite Altimetry results

4.5.1 Absolute sea-level change: 1992-2012

Figure 4.15 shows the rate of ASL change, the rate error and the RMS variability for all satellite altimetry nodes across the Caribbean calculated at each of the processing stages.

The monthly resampled ASL rates (Figure 4.15b) are in agreement with those calculated by Palanisamy et al. (2012). The trends vary spatially with ASL rates from -0.5 (Southern Cuba) to 5 mm yr^{-1} (Gulf of Mexico). Elsewhere, the northern South American coast and central Gulf of Mexico show elevated values ($\geq$2 mm yr^{-1}). The central Caribbean displays trends closer to 0 mm yr^{-1}. No part of the Caribbean have rates greater than the global average (3.4 $\pm$ 0.4 mm yr^{-1}, Nerem et al. (2010)). A strong spatial gradient in the Gulf of Mexico exists north of the Yucatan Peninsula. This corresponds to the transition from Campeche Bank to Yucatan Strait. Regional averages of rates using areas delineated for the tide gauges (Figure 4.9) give ASL trends of 1.1 $\pm$ 0.9, 0.6 $\pm$ 0.9, 2.4 $\pm$ 0.7, 2.7 $\pm$ 0.9 mm yr^{-1} for regions A, B, C and D respectively showing that sea-level trends in the southern and eastern Caribbean are greater than those in the northern and central Caribbean.

Figure 4.15e-h shows the error in the rates as estimated for each time series of each node for each processing step. From resampling (Fig 4.15f) to seasonal correction (Fig 4.15g), errors are reduced by between 0.2 to 0.6 mm yr^{-1}. Further reduction is evident from the regional common mode correction (Fig 4.15h), on the order of 0.2 mm yr^{-1}.

Figure 4.16 shows that there is little change (less than 0.5 mm yr^{-1}) in the calculated rates with each processing stage. Further to this, the error and RMS variability is reduced after each step at each node (Figure 4.15e - h, i - l respectively). Resampling from 10-day to monthly medians (Figure 4.15i to j) does not greatly alter the variances. The seasonal and regional common mode corrections reduce the variances by around 30% (Figure 4.15k) and 20% (Figure 4.15l) respectively. The most problematic region is that of the Gulf of Mexico, where the variance remains relatively high after corrections ($\sim$80 mm, Figure 4.15l), but has been halved from its original variance.

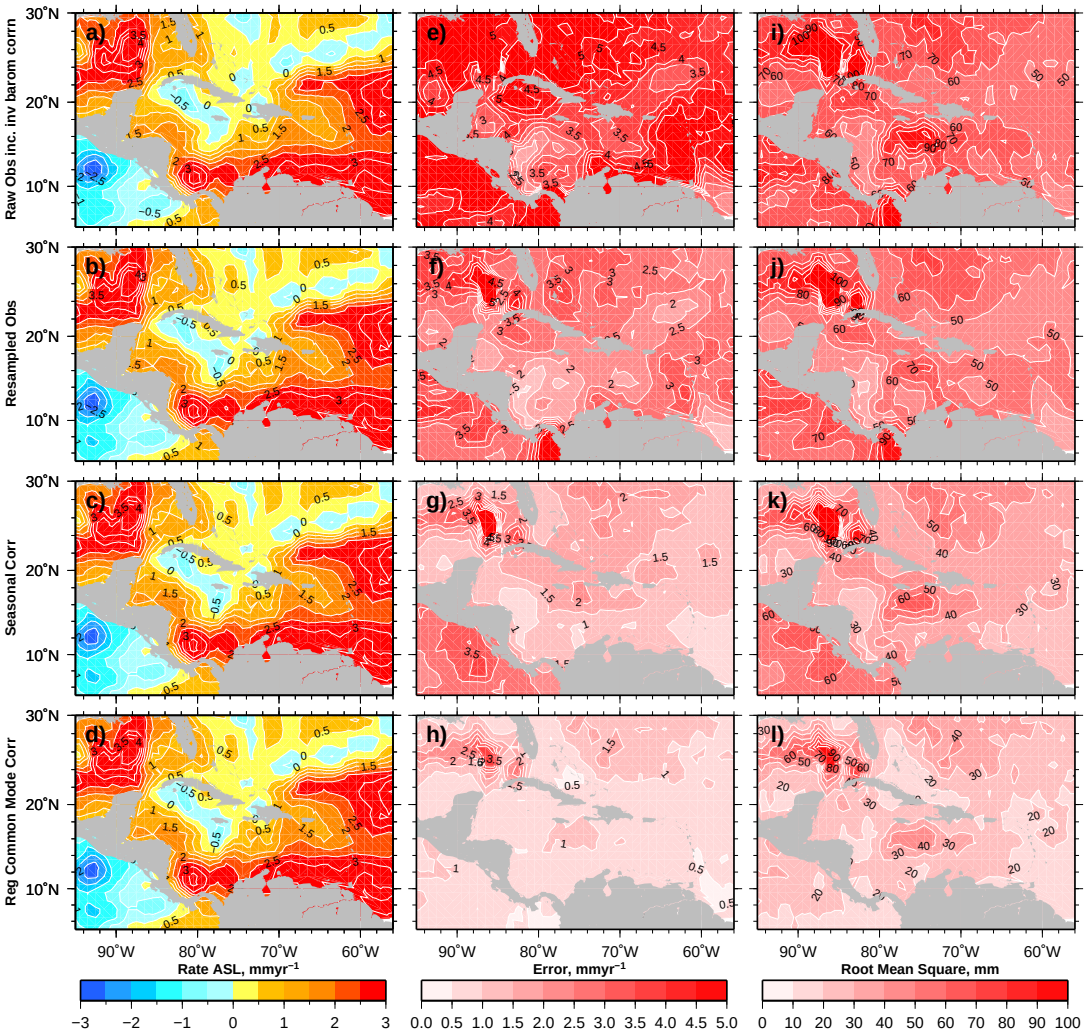

Figure 4.15: Absolute sea-level change between 1992-2012 for **a**: Raw altimetry (10-day sampled), **b**: After monthly median resampled altimetry, **c**: After seasonal correction (devised to remove average annual signal at each node) and **d**: After regional common mode correction (for each node, construct average time series from all nodes within 5^o and whose series are correlated above 0.1288. Subtract linearly detrended averaged time series from selected node). **e-h**: Errors in rates calculated after each of the three processing steps. **i-l**: Root mean square variability (see section 4.3.2) for raw altimetry and after each of the three processing steps.

4.5.2 Absolute sea-level change: 15 year variation (1997-2012)

In the same way as RSL trends are considered in 15 year bins for tide gauges (Figure 4.14), the same procedure is applied to the altimetry to assess ASL change for a bin spanning 1997-2012. Figures 4.17 show calculated rates (a), errors (b) and RMS variability (c) for the raw data and three processing steps.

The first observation is the difference in the trends of ASL over the 15 year span

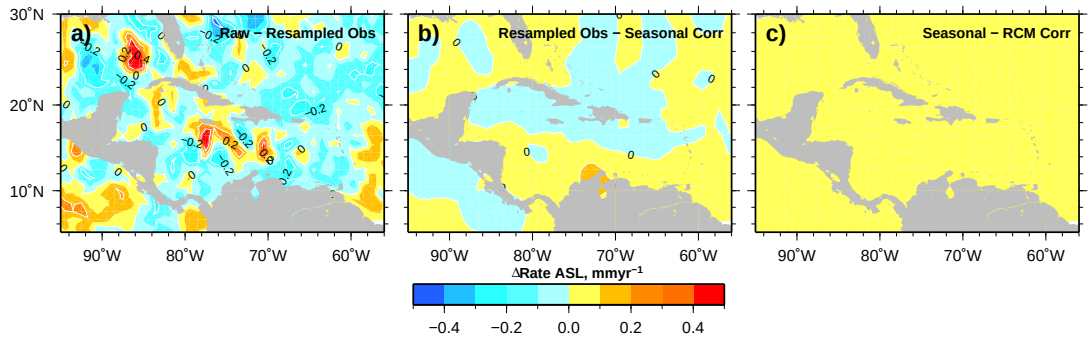

Figure 4.16: Differences in rates between correction stages. **a**: Raw (10-day sampled) minus resampled (monthly), **b**: resampled (monthly) observations minus seasonal cycle correction, **c**: seasonal cycle correction minus regional common mode correction

compared to the full 19.5 year span. The period of 1997-2012 displays a similar spatial pattern to the full 19.5 year series (compare Figure 4.15a - d to Figure 4.17a - d), though the range of rates is greater for the shorter time series (-2 to 5.5 mm yr^{-1}) where climate induced ocean dynamics contribute on yearly-decadal timescales. There is a larger error in the rates calculated for the shorter time series (Figure 4.17e-h), though the magnitude of RMS variability is comparable to those of the full series calculation (Figure 4.17i-l).

When the seasonal correction is applied (Figure 4.17c), slight changes are evident in the rates though their spatial pattern remains unchanged. This correction reduces the errors by around 1 mm yr^{-1}, though some regions are unchanged (e.g. Northern Colombian Basin).

The regional common mode correction (Figure 4.17d) significantly reduces the amplitudes of ASL rates across the Caribbean. In fact, this correction reveals the same trends over the 15 year period as those over the full span (Figure 4.15d). Figure 4.18 shows the difference between regional common mode corrected ASL rates (a), errors (b) and RMS variability (c) of full and shortened altimetry time spans. The difference in the rates is not statistically different from zero when one considers the difference between the errors. Interestingly, the difference between RMS variabilities is almost zero across the Caribbean. These results show that underlying the decade length oceanic variations there has been a spatially consistent sea-level rise on the local scale for the duration of the time series.

I have now calculated long term rates of sea-level change from tide gauges and

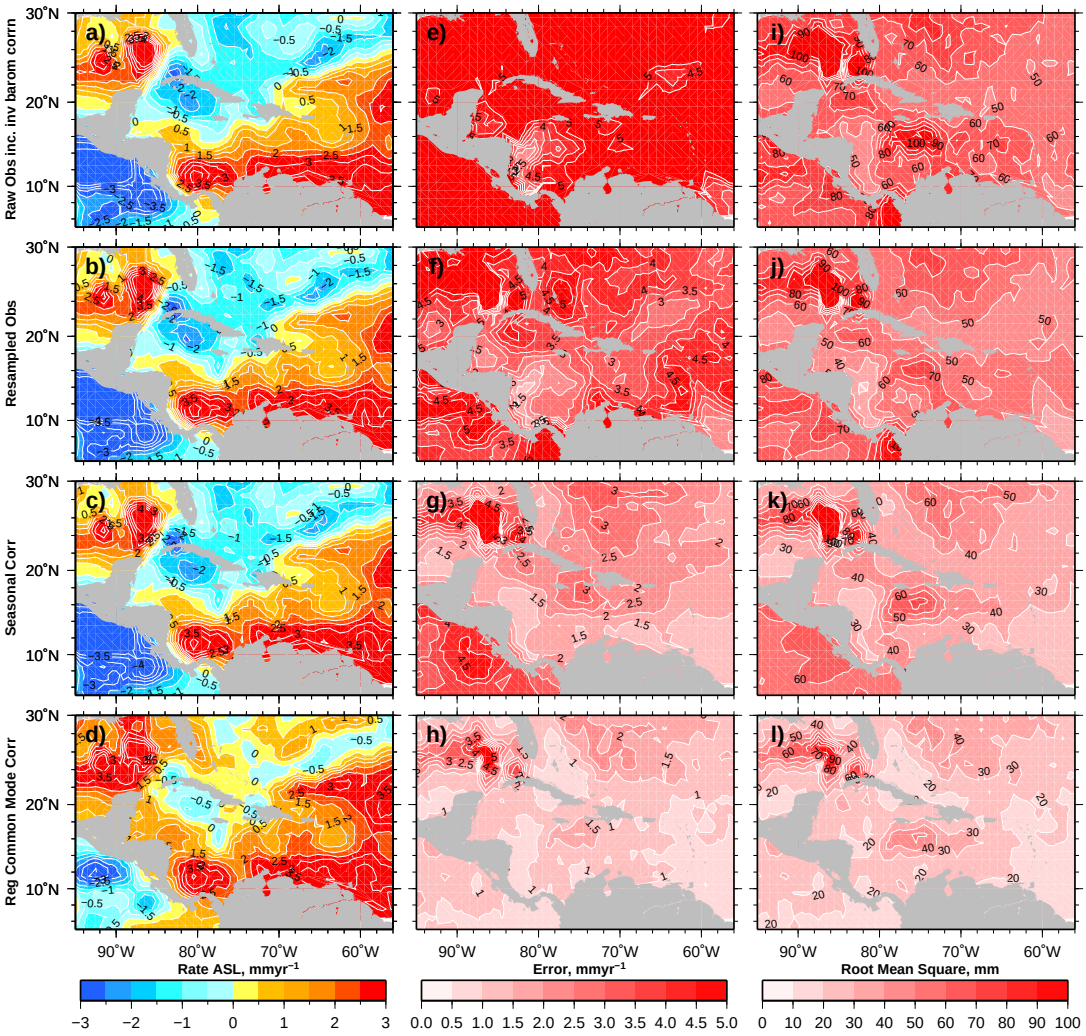

Figure 4.17: Absolute sea-level rate for 15 year time window between 1997-2012. Pattern of figures shown as in Figure 4.15.

satellite altimetry at different timescales. I will compare the two sets of corrected results in the discussion section (4.7) of this chapter. The next section considers the potential influence of short-term climatological variations upon the corrected sea-level rates.

4.6 Oceanic index correlation with sea-level observations

4.6.1 Ocean indices

Climate-induced changes in sea level result from ocean temperature increase, from re-distribution of heat within oceans, as well as from long-term fluctuations in atmospheric

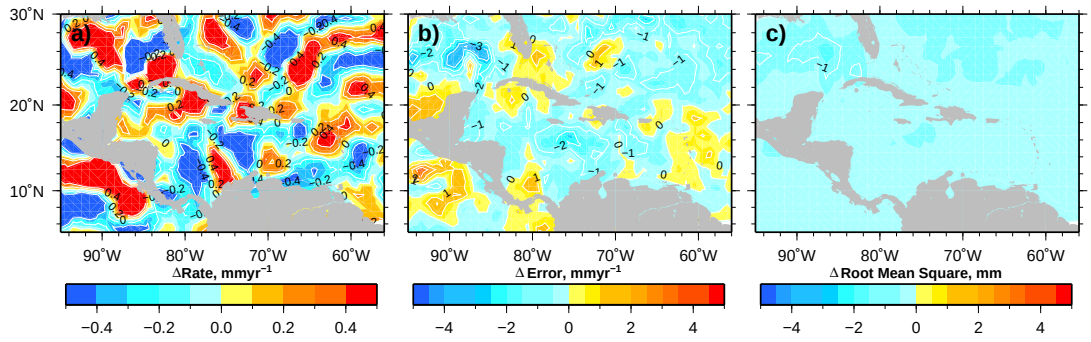

Figure 4.18: Differences between rates **a**, errors **b** and root mean square **c** of 1992-2012 and 1997-2012 time series of absolute sea level after all corrections.

pressure and wind fields (Lambeck et al., 2010). Hence, climate modes that are known to show global teleconnections may express themselves as sea-level fluctuations on regional scales. This section considers the primary climate modes that drive inter-annual to multi-decadal sea-level variability. As shown in Figure 4.10 and Figure 4.11a-f, significant correlations exist in sea-level time series within the same sub-region inferring basin scale dynamic relationships. Similarly, significant correlations between climate indices and sea-level change will indicate certain climatic systems driving oceanic variability at the time scales of the length of sea-level time series, i.e. greater than 15 years. This is one of the reasons Douglas (1991) argues monthly mean tide gauge records less than 50 years should not be used to investigate long term rates of sea level.

Climate indices time series are obtained from the National Oceanic & Atmospheric Administration (*www.esrl.noaa.gov/psd/data/climateindices/*). Three climate indices are tested; El-Nino Southern Oscillation (ENSO; Wolter and Timlin (1998)), Northern Tropical Atlantic Oscillation (NTAO; Penland and Matrasova (1998)) and the Caribbean Oscillation (CAR; Penland and Matrasova (1998)), which are the indices whose climate related effects are the most likely to effect Caribbean sea level. These series are monthly averaged indices (1950 to present) composed of different observed variables that are measured over well defined regions (Figure 4.19). The ENSO multivariate index is calculated as the first principal component of six variables: sea-level pressure, zonal and meridional surface wind, sea surface and air surface temperature and fraction of cloudiness of the sky (Wolter and Timlin, 1998). NTAO and CAR (Penland and Matrasova, 1998) are calculated from sea surface temperature anomalies within the regions over the central Atlantic and the Caribbean.

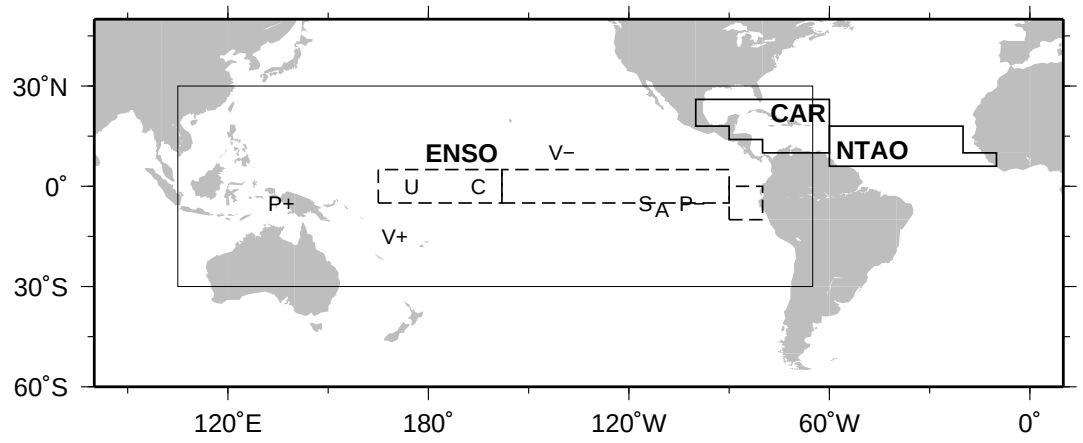

Figure 4.19: Regions (solid boxes) used to calculate oceanic indices, ENSO, CAR and NTAO. For ENSO, dashed boxes are prominent Nino regions. Letters in Pacific represent position of dominant index contribution. P+/P-, pressure; U/V+/V-, wind anomalies; S, sea surface temperature; A, surface air temperature; C, cloudiness.

4.6.2 Correlation results

Correlation coefficients, between oceanic index and sea surface height (altimetry) or relative sea level (tide gauge) at each correction step, are calculated using equations 4.5 - 4.7. The relative importance of the correlation coefficient is found by using the length of the series and statistical tables, which define the Pearson product moment correlation coefficient. For altimetry, there are 234 degrees of freedom (19.5 years $\times$ 12 months = 234 sample pairs of altimetry and climate index). The statistically significant correlation value (r) at the 95% ($\alpha = 0.05$) confidence level is 0.1288. Taylor (1990) has pointed out that the r statistic is an abstract measure and does not allow precise interpretation. The square of r gives the coefficient of determination (r^2), which is defined as the percent of the variation in the values of the dependent variable (y) that can be explained by variations in the value of the independent variable (x) (Mason et al., 1983, Taylor, 1990). Therefore, climate indices that are related to more than 20% (0.2) of sea-level observations need to have correlation coefficients of at least 0.45 ($\sqrt{0.2}$).

Figure 4.20 shows maps of the correlation coefficients between climate indices and sea-level time series (uncorrected and fully corrected). For both uncorrected and corrected sea-level time series low correlations exist are prevalent across the Caribbean. The CAR index has low positive correlations (0.2 - 0.4) in the northern Caribbean, the

bulk of which are removed in the corrected sea-level time series.

Evidence that the correlation is working can be seen for the ENSO index correlations in the Pacific region for the uncorrected sea-level time series. Elsewhere, correlation with ENSO is low, though this rises after the corrections are made to the sea-level time series. It would therefore seem that the narrow land bridge between north and south America acts to limit the effect of ENSO upon sea-level change in the Caribbean. NTAO correlation increases along the South American coast to the extreme south-east, which is consistent between corrected and uncorrected sea-level time series. The location of elevated correlations are in agreement with the position of regions delimited in Figure 4.19.

The oceanic index-tide gauge correlation coefficients (tide gauges whose series length exceeds 15 years and ends after 1997) show similar values and spatial variation to the index-altimetry results (Figure 4.20). Deviations between index-tide gauge and index-altimetry correlation coefficients at the same location are likely due to the stations' close proximity to the land and the local sea-level variation.

4.6.3 Index contribution to sea-level change

Having derived correlation coefficients that indicate a weak linear relationship between sea level and oceanic indices, I must decide whether the observed correlation could have arisen by chance (even if there is no direct relationship, the correlation coefficient is unlikely to be zero). Following Machin et al. (2010), the associated statistical test of the null hypothesis $\rho = 0$ is $t = r/\mathrm{SE}(r)$, where

$$\mathrm{SE}(r) = \sqrt{\frac{1 - r^2}{n - 2}} \tag{4.18}$$

The standard error (SE) follows the Students' t-distribution with degrees of freedom, $df = n - 2$ where n is the number points of the time series. For the altimetry data in Figure 4.20, with n = 234, the maximum correlation coefficient is selected for each oceanic index. Table 4.4 shows the results from equation 4.18. By using statistical look up tables (e.g. Riley et al. (2006), Machin et al. (2010)) it is possible to test if the t value is valid at a given significance level. If r = 0 lies within the resultant confidence interval (r at 95%), the null hypothesis can not be rejected thus the two data are unrelated statistically. The null hypothesis is rejected for correlations between CAR, ENSO and NTAO oceanic indeces and altimetry time series. The percentage

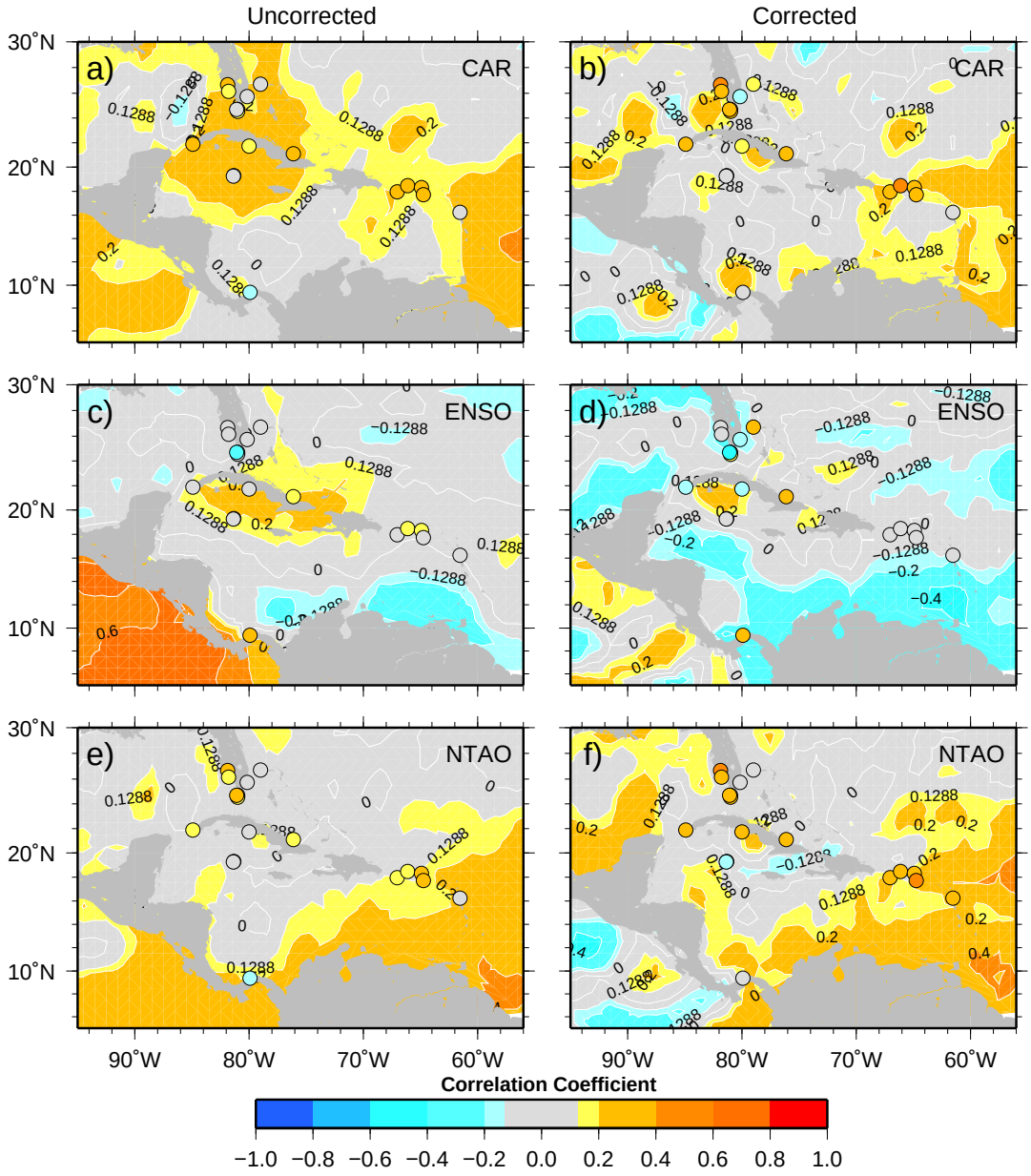

Figure 4.20: Correlation coefficients (r) between between altimetry (contoured) or selected tide gauges (coloured circles) and oceanic indices greater than 0.1288 for (**a**,**c** and **e**) uncorrected sea-level time series and (**b**,**d** and **f**) corrected sea-level time series. **a** and **b**: Caribbean Oscillation, **c** and **d**: El Nino Southern Oscillation, **e** and **f**: Northern Tropical Atlantic Oscillation.

contribution of these indices to the variance of the sea-level signal (r^2) are 9, 49 and 9% respectively.

Table 4.4: Statistical importance of maximum correlation coefficient (r) between oceanic indices and altimetry data

Oceanic Index	Maximum r	SE(r)	t_r	p-value	r(at 95%)	Reject null hypothesis?
CAR	0.3	0.063	4.79	≤ 0.0001	0.18 to 0.41	Yes
ENSO	0.7	0.047	14.93	≤ 0.0001	0.63 to 0.76	Yes
NTAO	0.3	0.063	4.79	≤ 0.0001	0.18 to 0.41	Yes

I calculate the contribution to sea-level change associated with each oceanic index/sea-level time series using an empirical scheme similar to the atmospheric correction of tide gauges (see Decomposition Methods). For nodes in the altimetry or tide gauge time series, whose absolute correlation with an index exceeds 0.1288 ($r \geq 0.1288$), I calculate the regression of the index per year (index year^{-1}). This gradient is multiplied by the gradient of the sea level per index (mm index^{-1}). This gives an empirical estimate for sea-level change due to the index value (mm yr^{-1}).

The empirical contributions to sea-level rate caused by the processes measured by each of the oceanic indices are shown in Figure 4.21. The change from uncorrected to corrected rates are reduced across the Caribbean, though it is still noticeable that up to half of the ASL rate ($\sim$1.2 mm yr^{-1} in the extreme south east) can be accommodated by the sum of these contributions (compare Figure 4.21f to Figure 4.15d). Over much of the central Caribbean, where correlations were essentially zero, contributions are similarly small, if not zero. Since the correlation between each of the oceanic indices and sea-level time series is weak, except in the Pacific for ENSO and along the northern South American coast for NTAO, it is likely that these regions experience some effect of the long term variation in the climatological effects governing their respective oceanic indices.

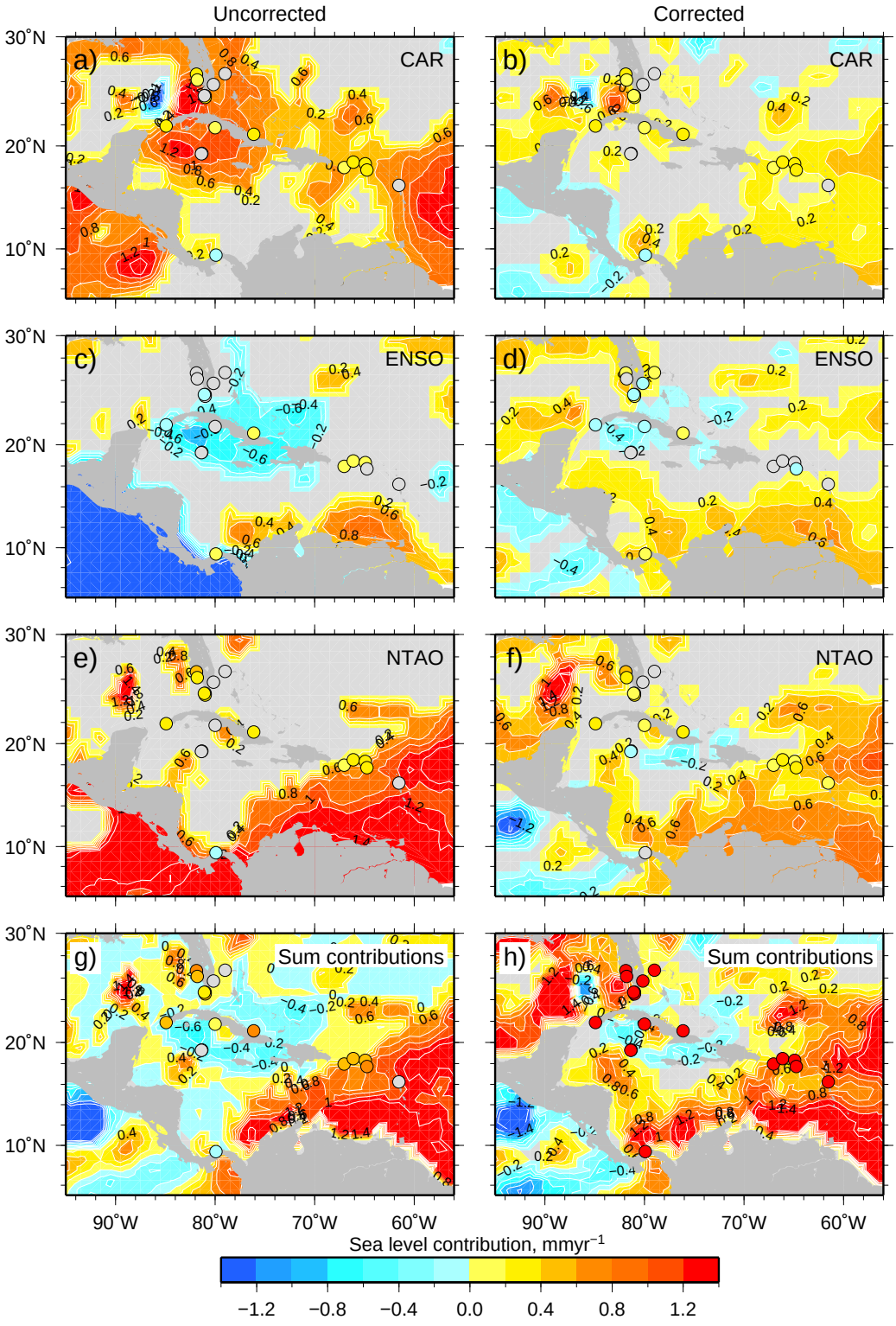

Figure 4.21: Empirical sea-level contribution of ocean-climate interaction where correlation between altimetry (contoured) or selected tide gauges (coloured circles) and oceanic indices greater than 0.1288 for (**a**,**c** and **e**) uncorrected sea-level time series and (**b**,**d** and **f**) corrected sea-level time series. **a** and **b**: Caribbean Oscillation, **c** and **d**: El Nino Southern Oscillation, **e** and **f**: Northern Tropical Atlantic Oscillation, **g** and **h**: Sum of contributions for uncorrected and corrected sea-level time series.

4.7 Discussion and Conclusions

Figure 4.22a shows the corrected RSL (tide gauge) and ASL (altimetry) rates for a period extending up to 52 and 20 years respectively. Figure 4.22b shows the same information for the last 15 years. The long term ASL rise is consistent across both time spans. To see how RSL rates have changed between the two spans and how RSL rates in general compare to ASL rates, I interpolate ASL rates from the altimetry grid to the tide gauge locations. Table 4.5 shows the full span and 15 year span of RSL rates and ASL rates at selected tide gauge locations.

The full span regionally averaged RSL rates are greater than the ASL rates by $\sim$1 mm yr^{-1} for regions A and B. In region C, this difference switches so that the RSL rate is $\sim$1 mm yr^{-1} less than the ASL rates. In region D (only Panama) the difference is negligible within error. The 15 year span (1997 - 2012) shows the two types of rate allying together, particularly when comparing the regionally averaged rates for RSL and ASL. The errors in the 15 year spans are much larger than those in the full spans. Part of this is due to the shorter time series and the reduction of completeness of the tide gauge time series for this range. Also, the amplitude of the short time scale noise (climate related) has a greater effect for shorter time series, which is the main the reason for limiting the 48 Caribbean tide gauges to this subset of 18 (19 but Panama is combination of two tide gauges, Figure 4.2).

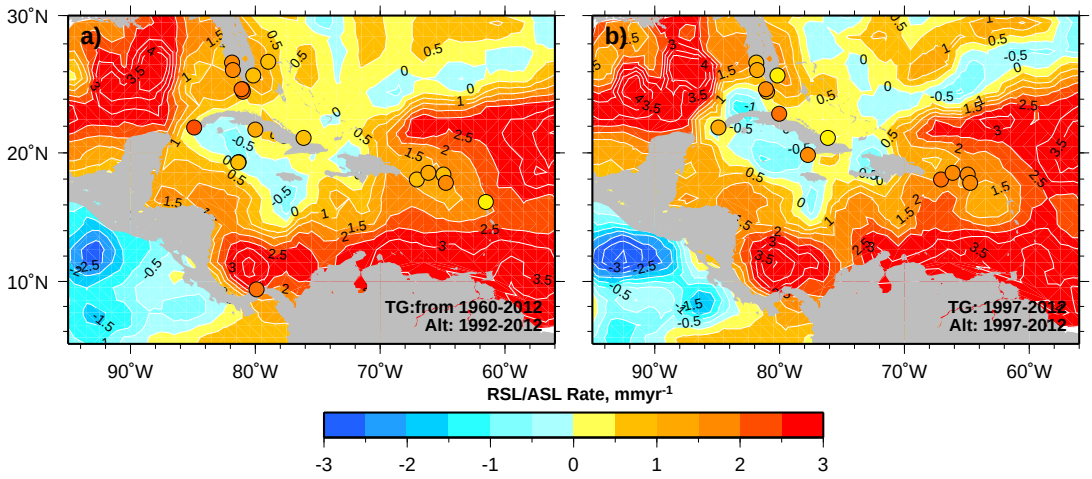

Figure 4.22: Absolute (altimetry - contours) and relative (tide gauge - circles) sea-level rates of processed observations. **a**: Tide gauges span from minimum 1960 to 2012 and altimetry spans 1992-2012. **b**: Tide gauges and altimetry span from 1997 to 2012

Table 4.5: Relative and absolute sea-level rates (mm yr^{-1}) from tide gauge subset and altimetry. Altimetry rates are those interpolated at tide gauge locations. Regional average has two rows: the first is average of values in column above, the second (in parentheses) are average altimetry rates using areas delimited in Figure 4.9 to calculate regional common mode correction.

			Full span		1997-2012	
Region	Station	Start/End	TG, RSL	Alt, ASL	TG, RSL	Alt, ASL
A	Fort Myers	1965/2012	2.37±0.27	0.79±1.29	1.48±1.50	1.67±1.86
A	Key Colony Beach	1977/1998	2.68±0.55	1.26±1.70	-	0.37±2.36
A	Key West	1960/2012	2.53±0.20	1.05±1.03	1.67±0.89	0.78±1.41
A	Naples	1965/2012	2.06±0.21	1.12±1.22	1.61±0.85	1.19±1.75
A	Vaca Key	1987/2012	2.83±0.37	1.26±1.70	2.14±0.81	0.37±2.36
A	Virginia Key	1994/2012	1.25±0.60	1.21±0.87	0.96±1.06	1.25±1.18
A	Settlement Point	1986/2002	1.23±1.40	0.99±0.64	-	1.08±0.91
Region A average:			2.14±0.51	1.10±1.21	1.57±1.02	0.96±1.69
				(1.07±0.89)		(1.16±1.29)
B	Cabo San Antonio	1972/2010	3.13±0.35	0.31±1.01	1.80±2.33	0.11±1.40
B	Casilda II	1983/2012	1.55±0.41	0.28±0.65	-	-0.04±0.93
B	Gibara	1974/2010	1.10±0.28	0.20±0.59	0.60±1.31	-0.31±0.83
B	North Sound	1976/1997	1.42±0.80	0.20±0.77	-	-0.13±1.08
B	South Sound	1976/1997	1.46±0.91	0.20±0.77	-	-0.13±1.08
Region B average:			1.73±0.55	0.24±0.76	1.20±1.82	-0.10±1.06
				(0.63±0.93)		(0.46±1.34)
C	Magueyes Island	1960/2012	1.27±0.10	1.54±0.70	2.52±0.67	1.49±1.02
C	San Juan	1962/2012	1.63±0.13	1.38±0.68	2.09±0.71	1.53±0.94
C	Charlotte Amalie	1975/2012	1.35±0.14	1.37±0.66	2.43±0.58	1.58±0.91
C	Lime Tree Bay	1978/2012	2.00±0.19	1.37±0.66	2.26±0.83	1.58±0.91
C	Pointe a Pitre	1991/2012	0.75±0.60	1.77±0.62	-	1.37±0.87
Region C average:			1.40±0.23	1.49±0.66	2.33±0.70	1.51±0.93
				(2.43±0.70)		(2.38±0.99)
D	Panama*	1960/1996	2.91±0.26	2.23±0.65		2.48±0.89
Region D average:			-	-	-	-
				(2.66±0.67)		(2.77±0.96)
Average all regions:			2.05±0.49	1.27±0.82	1.70±1.18	1.21±1.14
				(1.69±0.80)		(1.69±1.15)

* Panama is a combination of tide gauges, Cristobal and Coco Sol, which have the similar locations. Baseline corrections are described in PSMSL station documentation.

Variations between the tide gauge and altimetry solutions may be the result of local tectonics affecting the tide gauge. Simply, if there is local subsidence (or uplift), a tide gauge connected to the ground will record a sea-level rise (or fall) in response. This will mask true sea-level changes. Furthermore, if the land motion is discontinuous, the tide gauge could record apparently abrupt rises/falls in sea level. Understanding the local setting of the tide gauge is therefore important when trying to reconcile relative and ASL changes.

It is also likely that annual to multi-decadal cycles are recorded differently between tide gauges and altimetry. Vinogradov and Ponte (2010) found substantial differences

in variability of annual cycles between the two data types. Annual cycles on marine shelves were enhanced relative to the open ocean and phase differences of 1-2 months were typical. In particular, we note that near shore dynamics are more heavily influenced by wind/wave setup, bathymetry and river outflows (Tsimplis and Woodworth, 1994). By removing the annual signal over the duration of the time series, it is possible to negate the effect of this annual cycle. Furthermore, each time series at each altimetric node and tide gauge is treated individually for this correction, which accounts for the spatial differences in annual variability (Vinogradov and Ponte, 2010).

Long term effects on sea-level estimation should not be forgotten either. Various papers have commented upon the appearance of multi-decadal cycles (e.g. Woodworth et al. (2009), Sturges and Douglas (2011)). The nature of these fluctuations is not well understood (Chambers et al., 2012) and links have been made to volcanism, surface temperature, solar radiation and land water storage. (Chambers et al., 2012) suggest the presence of a ∼20 mm amplitude 60-year global sea-level oscillation. In their North Atlantic/Gulf of Mexico/Mediterranean averaged basin, a peak lies at 1954 and troughs at 1922, 1985. The sinusoid is therefore on an upwards trend at present time, thus analyses of 20 year time series needs care when interpreting. Chambers et al. (2012) note that modelling a 60-year oscillation does not change the estimated trend in any reconstruction time-series of global mean sea level by more than 0.1 mm yr^{-1}, which is lower than the uncertainty. Likewise, this is the case for the 18.6 year nodal cycle, whose sinusoid is on an upward trend at the present time (Baart et al., 2012b) with amplitude ∼22 mm.

The methods shown in this chapter improve the estimates and errors of sea-level change by removing temporal and regionally coherent signals from the both tide gauges and satellite altimetry. The method also shows that time series of 15 years can be useful to estimate trends in sea level. This is shown by the similarity in spatial distribution of trends between full span and 1997-2012 processed results in Figure 4.22. Other than the central Gulf of Mexico and north eastern South American coast, differences do not exceed 0.5 mm yr^{-1} in the long term trends.

The application of these processing steps show locally distinct ASL changes across the Caribbean from satellite altimetry. These rates are generally in line with the 20^{th} century global estimate of 1.8 mm yr^{-1} (Douglas, 1991, 2001), but at least 1 mm yr^{-1} less than present day global estimate of 3.4±0.4 mm yr^{-1} (Nerem et al., 2010). This is

for the most part supported by findings using tide gauges though local tectonic effects (uplift/subsidence) may contribute to observed differences. I will investigate the short and long term land uplift contributions in the next chapter to attempt to reconcile absolute and relative sea-level observations.

Chapter 5

Measuring uplift and assessing the sea-level budget

5.1 Introduction

In the previous chapter I processed tide gauge (TG) and satellite altimetry data to assess the relative sea-level (RSL) and absolute sea-level (ASL) changes occurring around the Caribbean during the last few decades. With these results I can study vertical ground motion (VGM) and compare the results to Global Positioning System (GPS) observations. Furthermore, I can use the results from Chapters 2 and 3, Holocene RSL rates and an representative Glacial Isostatic Adjustment (GIA) model for the region, to calculate the GIA induced sea level and VGM contributions. These results will allow me to ascertain the overall state of sea-level rise in the Caribbean during the last decades and if there are significant differences between this region at present compared to the past.

5.2 Measures of vertical ground motion

5.2.1 GPS

GPS devices measure the travel time of microwaves from source transmitters on orbiting satellites to a receiver on the ground. Since the early 1990s, steady improvements in estimates of three-dimensional land motion have been made from GPS and other geodetic data (DeMets et al., 2010). Of the three dimensions, the horizontal components (north and east) have been used extensively to quantify global plate motions (e.g. Argus and Heflin (1995), Sella et al. (2002), Kogan and Steblov (2008),

DeMets et al. (2010)). More recently, the vertical component (radially outward from the Earth's centre) has been used to study subduction (e.g. Bergeot et al. (2009)), collision (e.g. Fu and Freymueller (2012)) and regions affected by post-glacial rebound (e.g. Sella et al. (2007)) as well as being used to correct long term TG records (e.g. Nerem and Mitchum (2002), Wöppelmann et al. (2009)). All of these applications require unbiased velocities and realistic uncertainties (Santamaría-Gómez et al., 2011).

GPS derived vertical velocities and errors from four recent publications are shown in Figure 5.1. Global velocity field solutions from University of La Rochelle (ULR) (accessed from http://www.sonel.org/) are ULR3 (Wöppelmann et al. (2009), extended by Bouin and Wöppelmann (2010)), ULR4 (Santamaría-Gómez et al., 2011) and ULR5 (Santamaría-Gómez et al., 2011). These have improved upon each other incrementally in the main by increasing the length of the records but also through processing improvements. Another difference in each is the International Terrestrial Reference Frame (ITRF) to which they are applied; ULR3 - ITRF2000, Bouin and Wöppelmann (2010) - ITRF2005, ULR4 and ULR5 - ITRF2008. GPS velocities from NASA's Jet Propulsion Lab (JPL, accessed from http://sideshow.jpl.nasa.gov/post/series.html) use a greater number of sites in the Caribbean with errors of the same magnitude as the ULR data. Heflin (September 2013) process the JPL GPS (henceforth Hefl) results into ITRF2008. Vertical velocities are the mostly poorly constrained of the three components, whose errors are on average 0.6 mm yr^{-1} for the best 400 sites (Heflin, September 2013).

I use ULR5 and Hefl GPS vertical velocities to perform inter-comparisons with TG, altimetry and GIA modelling from the previous chapters. It is important to note that the reference frames of GIA models and GPS velocities differ. GIA models are produced in a reference frame where the origin lies at the centre-of-mass of the solid Earth (CE) whereas GPS velocities are in ITRF(2000,2005,2008), which is at secular timescales, a centre-of-mass of the entire Earth system reference frame (CM). Thomas et al. (2011) found negligible differences in the component velocities between CE using ICE-5G (Peltier, 2004) and CM, therefore it is appropriate to perform direct inter-comparison between the two data.

In addition to the previous assumption, I also assume continuous VGM as measured by the GPS stations. This is because the average time series lengths of the two GPS data sets are 8.1 and 6.1 years for ULR5 and Hefl respectively. Furthermore, for many of the tide gauges, there is little or no overlap in time with the nearest GPS station.

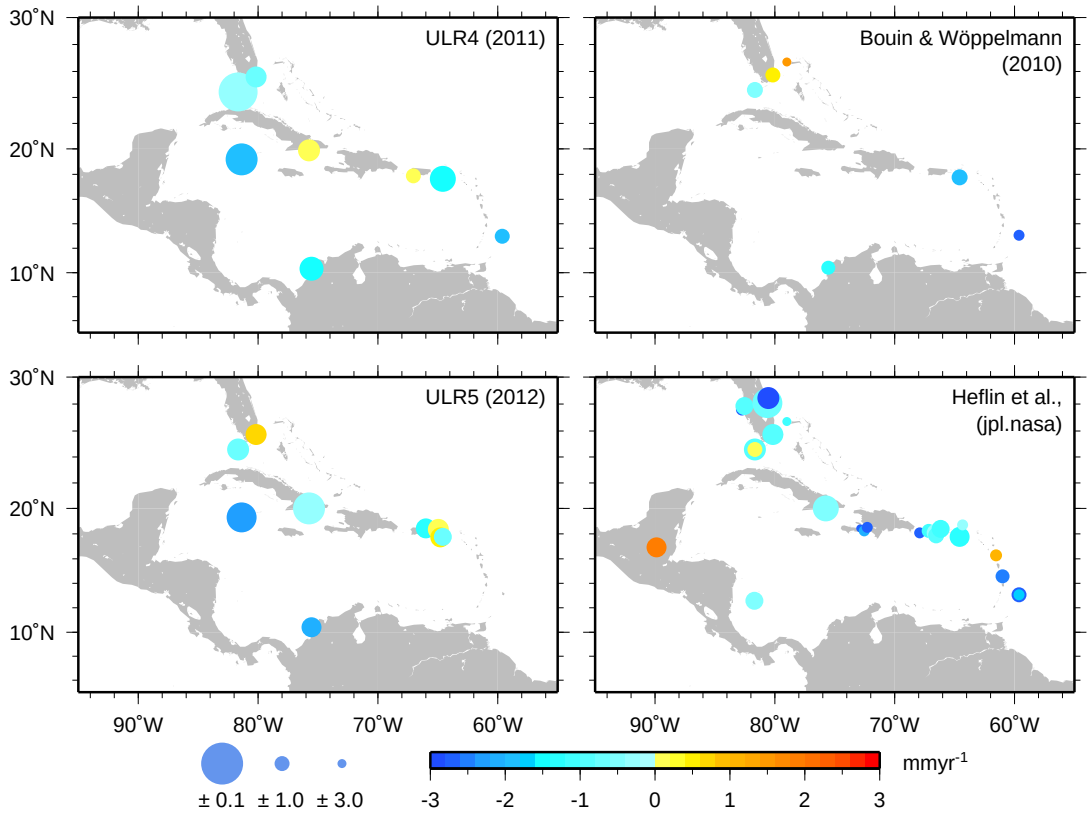

Figure 5.1: GPS sites in the Caribbean region from four separate sources: ULR4 (Santamaría-Gómez et al., 2011), ULR5 (Santamaría-Gómez et al., 2012), Bouin and Wöppelmann (2010) and Heflin (September 2013). Circle colour and size represent rate and error of vertical ground motion.

5.2.2 GIA contribution

The range of GIA model Earth parameters, which minimise the misfit between model RSL curves and RSL data (derived curves and indicators, Chapter 2) for the regions around the Caribbean, are assumed to provide bounds upon realistic lithospheric thickness, upper and lower mantle viscosity parameters (see Chapter 3). Using a similar concept, I investigate the sensitivity of uplift rates from GPS to variations in model Earth parameters. Whereas the χ^2 misfit was used to ascertain representative model Earth parameter combinations for the sea-level curves, I use the weighted root-mean-square (WRMS) error to assess the degree of fit between the GIA model uplift output and GPS observations (e.g. Whitehouse et al. (2012)):

$$WRMS = \sqrt{\frac{\sum_i (o_i - p_i)^2 w_i}{\sum_i w_i}} \tag{5.1}$$

where o_i and p_i are observed and predicted uplift rates, respectively, and w_i is the weighting for each datum. The weighting of the root mean square value uses the standard deviation of the GPS uplift (σ_i^{GPS}) and the standard deviation of the range of GIA uplift values (σ_i^{GIA}) for the range of models tested,

$$w_i = \frac{1}{(\sigma_i^{\mathrm{GPS}})^2 + (\sigma_i^{\mathrm{GIA}})^2} \tag{5.2}$$

I perform the WRMS calculation between the full range of model Earth parameters and the GPS velocities (Figure 5.2). I partition Hefl into north, central and south regions as well as calculating WRMS for the whole Hefl set and ULR5. Figures 5.2, E-1 and E-2 (Appendix E) show that there is a general invariance to model Earth parameters that satisfy GPS velocities across the region. This is to be expected as the GIA uplift in the region is unlikely to be the sole contributor to the VGM at any given site given the tectonics in the region and the far-field position of the region relative to the centre of deglaciation.

Although the range of WRMS values are low in Figure 5.2b-f, there is an indication that model viscosity parameters in the range 0.4 - 1.0 x 10^{21} Pa s (upper mantle) and 10 - 50 x 10^{21} Pa s (lower mantle) give lower misfits. This indicates a weak preference towards models in this parameter range, though lithospheric thickness shows no such preference.

On the basis that GPS results weakly prefer an GIA model with higher upper and lower mantle viscosity ranges, I utilise the representative model Earth parameters from Chapter 3 to assess the contribution to uplift in the Caribbean region (Figure 5.3). The model Earth parameters used are, lithospheric thickness 71 km, upper mantle viscosity 0.5 x 10^{21} Pa s and lower mantle viscosity 10 x 10^{21} Pa s. The range of parameters that lie within the 95 per cent confidence limit of RSL data are lithospheric thickness 71 - 120 km (lithospherically invariant), upper mantle viscosity 0.5 - 0.8 x 10^{21} Pa s and lower mantle viscosity 10 - 30 x 10^{21} Pa s. The result of these model runs (Figure 5.3a,b) show present day predicted subsidence, which is greater to the north than in the south. Greater levels of subsidence occur in the ocean basins (Gulf of Mexico, -2 mm yr^{-1}; Atlantic, -2 mm yr^{-1}; Caribbean, -1.2 to -1.4 mm yr^{-1}) compared to the land (-0.6 to -1.0 mm yr^{-1}). It is important to note that the model parameter range shows an uplift rate range the same order of magnitude as the representative model uplift (0.4 mm yr^{-1} in the south to 1.2 mm yr^{-1} in the north). The higher

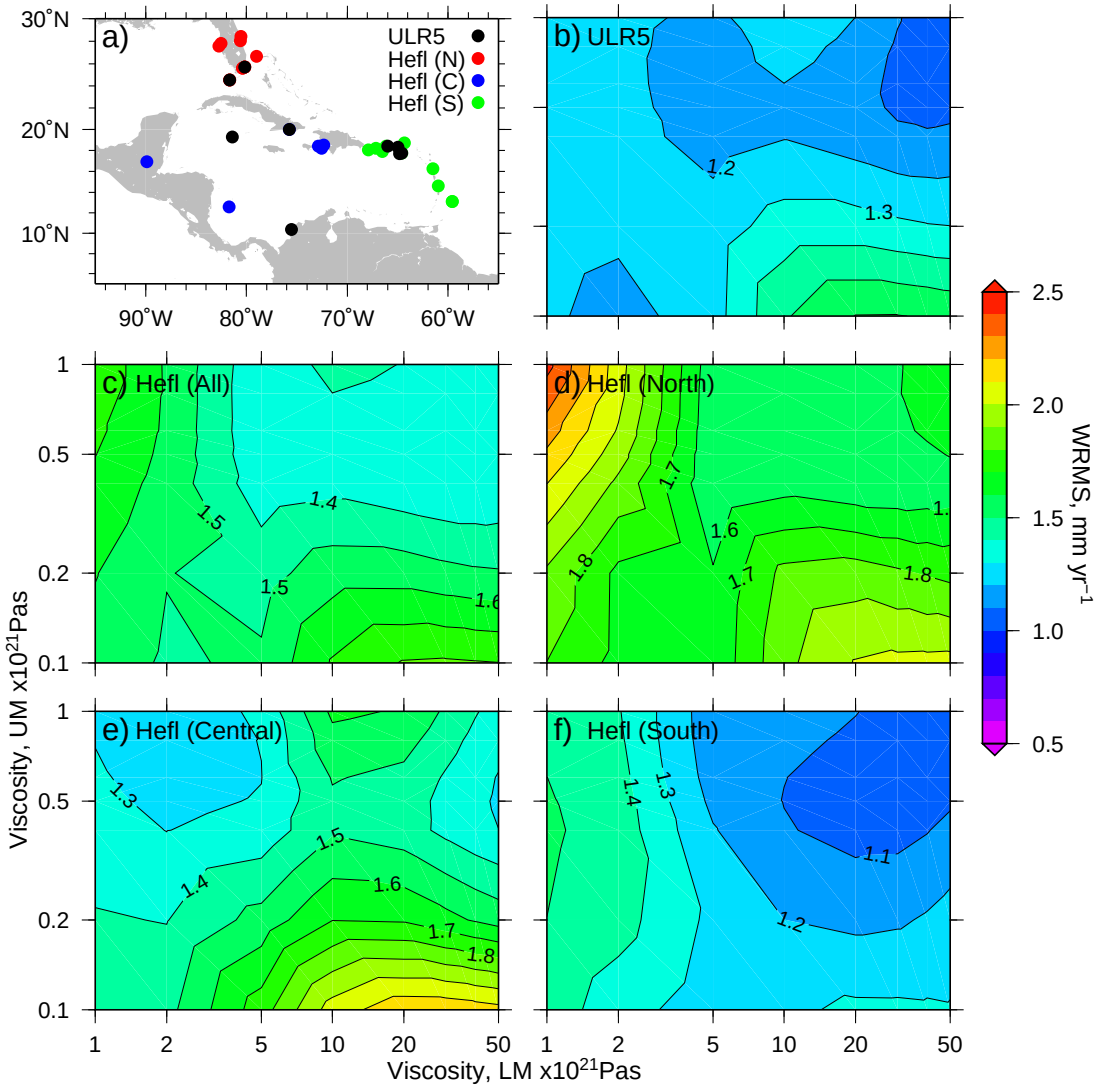

Figure 5.2: **a**: GPS sites (circles) used for analysis: Heflin (September 2013), north (red), central (blue) and south-east (green); Santamaría-Gómez et al. (2012), ULR5 (black). **b - d**: WRMS values between GIA model predicted uplift rate (for range of upper and lower mantle viscosity parameters) and GPS uplift rates (b: ULR5, Santamaría-Gómez et al. (2012); c: All sites (Heflin, September 2013); d,e,f: north, central and south-east sites (Heflin, September 2013). Lithospheric thickness is 71 km.

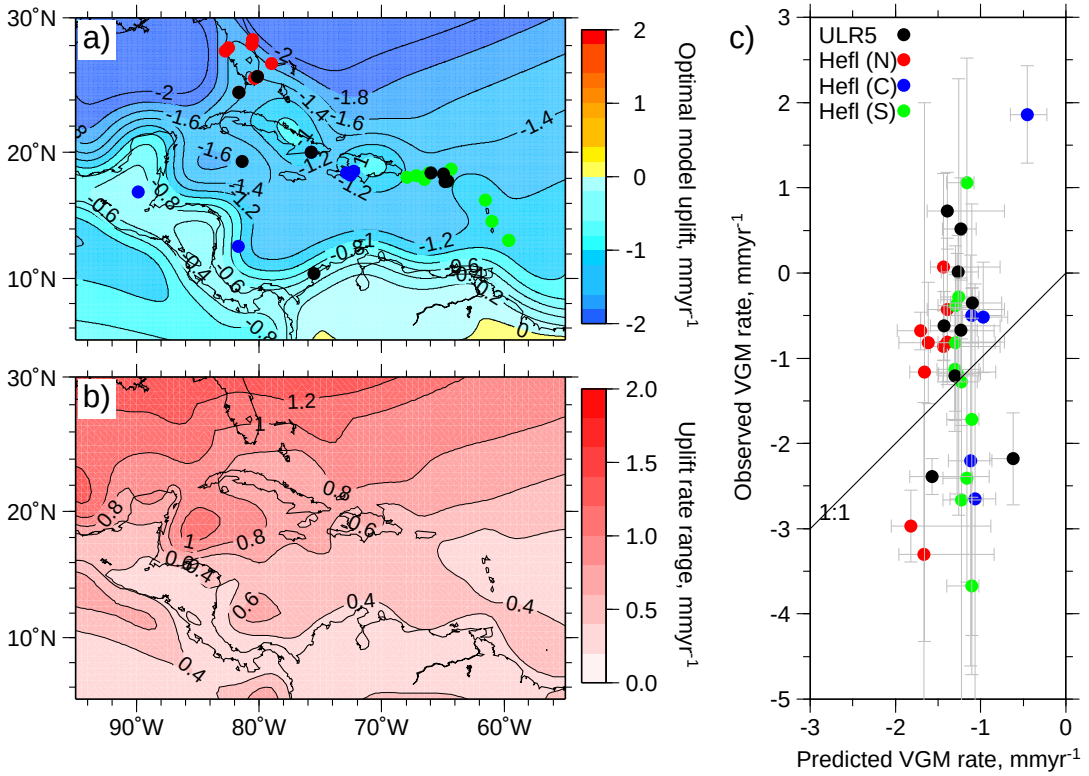

Figure 5.3: **a**: Radial uplift from GIA model using representative model Earth parameters (see text). Coloured circles represent north (red), central (blue) and south-east (green) GPS sites of Heflin (September 2013) and ULR5 (black) of Santamaría-Gómez et al. (2012). **b**: Uplift rate range of the representative model Earth parameters. **c**: Model predicted versus observed radial uplift at GPS locations labelled in (a). Horizontal error bars represent range of model representative model solutions (see **b**).

rate of subsidence and range of rates in the north of the region (Florida) is expected since it is closer to the centre of deglaciation (Laurentide), which I established as the dominant melt-water source for this region (in agreement with Milne et al. (2005)) and therefore will be more sensitive to changes in the parameters used, in particular lower mantle viscosity (Figure 3.5). The lack of coherence between GPS and GIA uplift is shown in Figure 5.3c and in agreement with Ostanciaux et al. (2012) (VGM calculated using altimetry minus TG, see next section). The range of local uplift across the sites is around seven times greater than the predicted GIA uplift rate range showing that GIA uplift is only a small contribution to uplift in this region.

5.2.3 Altimetry minus Tide Gauge

Nerem and Mitchum (2002) first implemented an alternative method to derive VGM by subtracting TG (RSL) from altimetry (ASL) time series that overlap in time and calculating the least squares residual. Since the primary limitation of this approach was the short length of the time series involved, Kuo et al. (2004) and Kuo et al. (2008) used long TG records, regionally averaged sea-level records and altimetry to solve the same problem except that rates of each were calculated first then subtracted to give VGM rate. The same approach was applied by Fenoglio-Marc et al. (2004) and García et al. (2007) in the Mediterranean and Ostanciaux et al. (2012) globally, except that the nearest node of the altimetry grid to each TG location was used rather than a regional ASL average rate (Kuo et al., 2004). As with Nerem and Mitchum (2002) this shortened the total series length.

The relationship between the RSL rate measured by the tide gauge ($\dot{S}$) and ASL rate measured by altimetry ($\dot{g}$) for the same location (θ, ϕ) can be written as,

$$\dot{u}_{\mathrm{AMT}}(\theta, \phi) = \dot{g}(\theta, \phi) - \dot{S}(\theta, \phi) \tag{5.3}$$

where $\dot{u}_{\mathrm{AMT}}$ is the rate of VGM (AMT is Altimetry Minus Tide Gauge). Equation 5.3 assumes that land motion is linear for the time scale considered (up to 50 years). I can now directly compare rates of VGM from GPS ($\dot{u}_{\mathrm{GPS}}$) and equation 5.3. I also assume the same land motion affects the ground to which the TG and GPS antenna are anchored (Bouin and Wöppelmann, 2010). As the distance between TG and GPS instruments increase, the weaker this assumption becomes. The TG stations are paired to their nearest GPS station. The TG-GPS station pairs are grouped into four categories: A, $dx \leq 20$ km, B, $20 < dx \leq 50$ km, C, $50 < dx \leq 100$ km and D, $100 < dx \leq 200$ km, where dx is the inter-station distance. The results from those station pairs in group A and B are likely to be the most well resolved.

I calculate $\dot{g} - \dot{S}$ in four different ways: I use altimetry rates interpolated from the 1^o x 1^o grid to the TG locations (Figure 5.4a,c) and also average altimetry rates of the regions delimited for the regional common mode TG correction (Figure 4.9 in Section 4.3.1) in Figure 5.4b,d. For each of these options, I use either the full TG and altimetry spans (Figure 5.4a,b) or restrict the comparison to altimetry and TG time series that exactly overlap (1997-2012: Figure 5.4c,d).

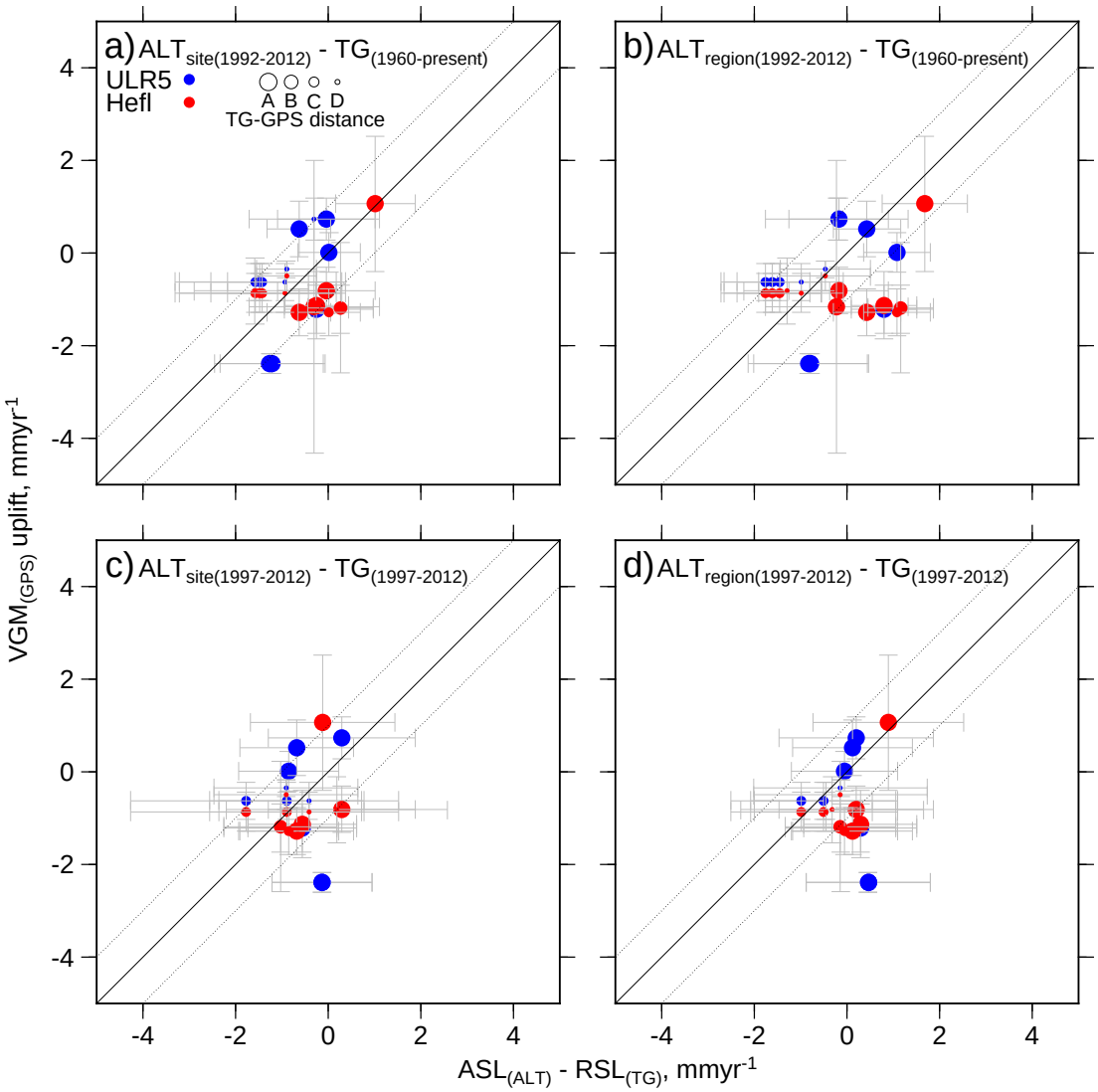

Figure 5.4: Vertical Ground Motion from $\dot{u}_{\mathrm{AMT}}$ compared to $\dot{u}_{\mathrm{GPS}}$. **a**: Altimetry (1992-2012) at nearest node to each TG (Full span). **b**: Altimetry (1992-2012) averaged by region for each TG (Full span). **c**: Altimetry (1997-2012) at nearest node to each TG (1997-2012). **d**: Altimetry (1997-2012) averaged by region for each TG (1997-2012). GPS stations are those nearest to TGs. Size of circle denotes inter-station (TG-GPS) distance denoted by letters A to D. These correspond to: A, $dx < 20$ km; B, $20 < dx \leq 50$ km; C, $50 < dx \leq 100$ km; D, $100 < dx \leq 200$ km

By subtracting one rate from another, I remove the need to formerly subtract the two overlapping time series, which would likely result in the degradation of the signal by reducing the time period for which both the satellite altimetry and TG records overlap to a maximum of 19.5 years, i.e. a short time interval, when considering the uncertainties, gaps and other device related issues. The error in the $\dot{g} - \dot{S}$ measurement is simply the square root of the sum of the squares of the two rate errors since they are independently measured and calculated,

$$\sigma_{\dot{u}_{\mathrm{AMT}}} = \sqrt{\sigma_{\dot{g}}^2 + \sigma_{\dot{S}}^2}. \tag{5.4}$$

Figure 5.4 shows that there is a general agreement between $\dot{g} - \dot{S}$ and GPS calculations. Some minor exceptions exist and these lie well outside the ± 1 mm line shown on the graphs. Table 5.1 shows the average RMS misfits between $\dot{u}_{\mathrm{AMT}}$, $\dot{u}_{\mathrm{GPS}}$ pairs and 1:1 line (Figure 5.4) for the four span/interpolation combinations. There is a small improvement between the average misfit for site interpolated versus regionally interpolated altimetry for both ULR5 and Hefl GPS data sets. Using exact or partially overlapping spans of TG and altimetry time series does not appear to have a significant effect upon the average RMS misfit. Contrary to expectation, the TG-GPS inter-station distance does not appear to have any discernible effect upon the misfit.

In fact, those distances less than 50 km (A and B) appear more poorly fitted than those greater than 50 km (C and D) with the exception of ULR5 GPS, full TG and altimetry spans where altimetry is interpolated at the TG site. Here the average RMS misfit is practically the same regardless of inter-station distance. For Hefl GPS, the best RMS solutions are found for the 15 year TG and altimetry spans, where the altimetry is also interpolated at the TG site. It is also apparent that the inter-station distance range D give unusually low average RMS misfits. Some of the TG-GPS pairs for this distance have extremely high agreements between $\dot{g} - \dot{S}$ and GPS calculations. It is therefore more likely that the hypothesis of smaller inter-station distances exhibiting higher agreements is skewed by the distant inter-station pairs, rather than poor fitting of near inter-station pairs. This is supported by the sub-mm accuracy for eight out of twelve average RMS misfits whose inter-station distance is less than 50 km.

Table 5.1: Average RMS misfit between $\dot{u}_{\mathrm{AMT}}$, $\dot{u}_{\mathrm{GPS}}$ paired sites and 1:1 line for four TG/Altimetry span/interpolation combinations (shown in Figure 5.4). RMS values are for TG-GPS station pairs of different distances, A-D and for all station pairs including those at distances greater than D (see text for distances)

TG/Alt spans/interpolation	Average RMS misfit to 1:1 line, mm				
GPS set	A	B	C	D	All
TG: 1960 - 2012, Alt: 1992 - 2012 site interpolated					
ULR5 (2012)	0.68		0.62	0.68	0.66
Hefl (2013)	0.50	1.03	0.60	0.35	0.56
TG: 1960 - 2012, Alt: 1992 - 2012 regionally averaged					
ULR5 (2012)	0.96		0.71	0.91	0.89
Hefl (2013)	0.91	1.65	0.96	0.20	0.91
TG: 1997 - 2012, Alt: 1997 - 2012 site interpolated					
ULR5 (2012)	1.04		0.59	0.25	0.82
Hefl (2013)	0.64	0.11	0.41	0.48	0.51
TG: 1997 - 2012, Alt: 1997 - 2012 regionally averaged					
ULR5 (2012)	1.26		0.19	0.45	0.96
Hefl (2013)	0.79	0.74	0.52	0.30	0.61

For the sites in this study within 50 km of the sites used by Ostanciaux et al. (2012), there is general agreement in $\dot{g} - \dot{S}$ within calculated error (Figure 5.5). The misfit between the two sets of results is 0.85 mm yr^{-1}, though most of the of this deviation is due to discrepancies at three tide gauge locations, Vaca Key (Florida), Cabo San Antonio (Cuba) and Lime Tree Bay (US Virgin Islands). Figure 5.5 shows that of these, Cabo San Antonio and Lime Tree Bay lie outside the error bars of my results. Ostanciaux et al. (2012) do not discuss errors in the VGM rates calculated, though since they subtract annual mean ASL and RSL data from each other it is likely that their cumulative error (Equation 5.4) would be small (since a maximum and minimum of 16 and 5 points [years] would be used to fit the trend).

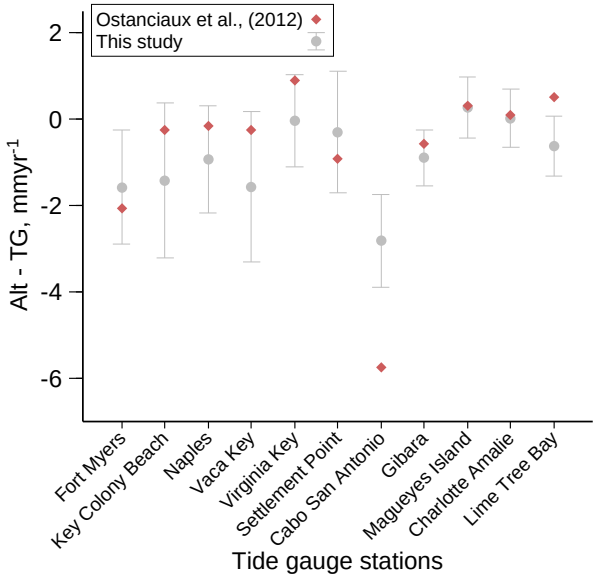

Figure 5.5: Comparison between Alt-TG from this study versus results from global assessment (Ostanciaux et al., 2012) for same tide gauge locations.

5.3 Relative sea level

5.3.1 Present day GIA contribution

In this section I consider the contribution of GIA induced sea-level rise to present-day RSL rates. To do so, I follow on from section 5.2.2 and show the present day predicted RSL rate and range for the representative model Earth parameters (Figure 5.6a: lithospheric thickness 71 km, upper and lower mantle viscosity 0.5 and 10 x 10^{21} Pa s respectively) and its associated parameter range respectively (Figure 5.6b). The predicted RSL rates range from -0.2 to 0 mm yr^{-1} around the south and western coasts of the Caribbean, to 1.4 mm yr^{-1}, in the northern Gulf of Mexico and Atlantic coast of Florida. The range of the model predicted RSL rates increase from 0.2 - 0.3 mm yr^{-1} in the south to 0.8 mm yr^{-1} in the north of the region. In a similar fashion to the uplift result, the range of present day observed RSL rates is approximately 2.8 times greater than the range of predicted rates. This result initially indicates that GIA induced present day RSL rise contributes around a third to present day RSL rise.

5.3.2 Present versus past RSL/ASL rates

To ascertain the increase in modern sea-level rates compared to prehistoric sea-level rates, I plot selected TG RSL rates versus the youngest prehistoric RSL rates (Fig-

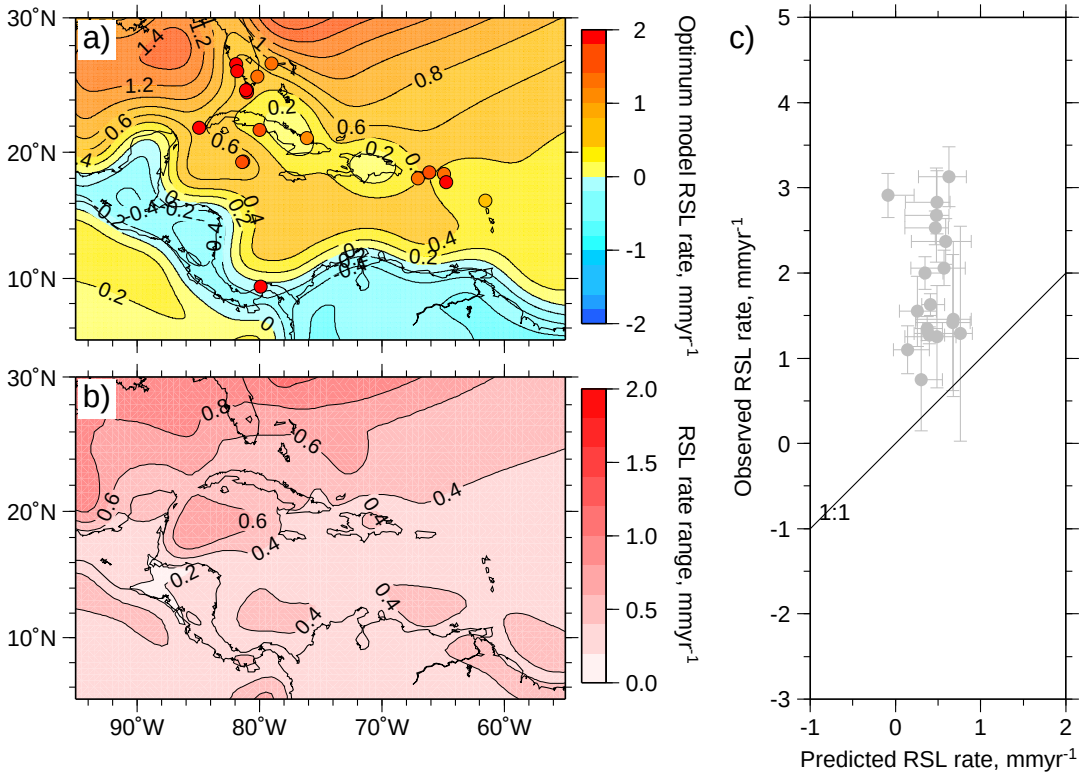

Figure 5.6: **a**: RSL rate from GIA model using representative model Earth parameters (see text). **b**: RSL rate range of the representative model Earth parameters. **c**: Model predicted versus observed RSL rate at TG locations labelled in (a). Grey circles are positions of TGs. Horizontal error bars represent range of model representative model solutions (see **b**).

ure 5.7a) from the curve construction method outlined in Chapter 2 and also prehistoric RSL rates corrected for model predicted GIA uplift to give pseudo-ASL rates versus ASL rates from altimetry at the selected TG locations (Figure 5.7b). I select the prehistoric RSL rate whose region is closest to the TG location.

Whilst the late Holocene RSL rates at selected TG locations have an average of 0.61 $\pm$ 0.39 mm yr^{-1}, the modern RSL rates have an average of 2.05 $\pm$ 0.49 mm yr^{-1}. This translates to a modern RSL rate almost three times that of RSL rates in the late Holocene. The prehistoric pseudo-ASL rates at selected TG locations have an average of 1.97 $\pm$ 0.58 mm yr^{-1} whilst the modern ASL rates have an average of 1.27 $\pm$ 0.82 mm yr^{-1}. This translates to a modern ASL rate almost twice that of ASL rates in the late Holocene. The increase in both types of measured rate (RSL and ASL) of between a factor of two and three from late Holocene to modern times is supported by the findings of Gehrels and Woodworth (2013), who identify that within a 40 year

period, centred around 1925, global sea-level rise started to exceed the late Holocene background global rate.

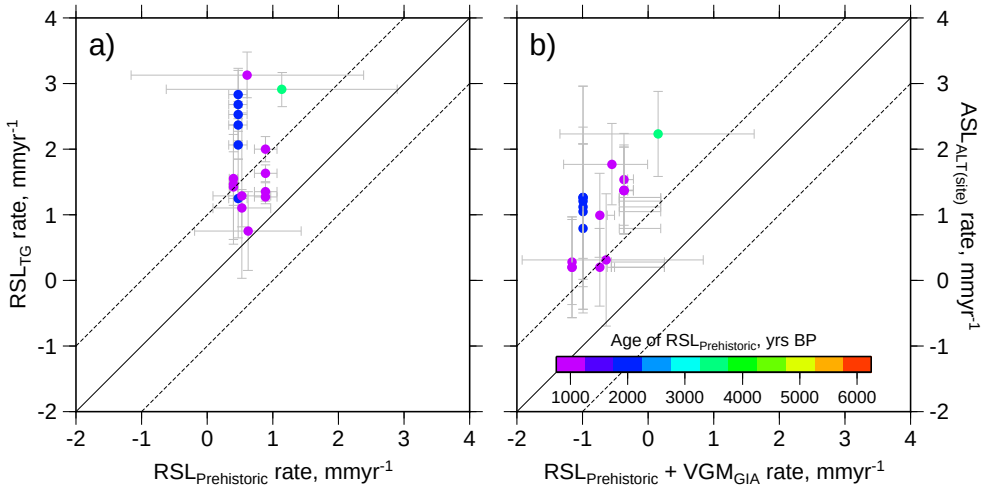

Figure 5.7: **a**: Prehistoric RSL rates derived from sea-level curve construction method versus present day RSL rates for TG positions (select smallest distance between TG and prehistoric node locations) **b**: Prehistoric RSL rates (at TG locations) corrected for VGM predicted by representative GIA model (to give pseudo-ASL rate) versus satellite altimetry (ASL rate) at TG locations. Coloured circles show age of prehistoric RSL rate measurement.

5.3.3 Closing the loop: Unaccounted Sea-level change

To understand if the modern sea-level change can be accounted for, I rearrange Equation 5.3 to bring all the terms to one side and use $\dot{u}_{\mathrm{GPS}}$ instead of $\dot{u}_{\mathrm{AMT}}$ (i.e. sea-level change should be perfectly explained by volumetric sea-level change and GPS VGM rate),

$$\delta\dot{d} = \dot{g}(\theta,\phi) - \dot{S}(\theta,\phi) - \dot{u}_{\mathrm{GPS}}(\theta,\phi) \tag{5.5}$$

where $\delta\dot{d}$ is the deficit in the sea-level rate, which should equal zero if the assumption that RSL rate corrected by GPS VGM rate equals ASL rate.

Figure 5.8 shows the sea-level rate deficit for all and selected TG locations (series longer than 15 years, ending after 1997: see Section 4.3.2 in Chapter 4) using four combinations of the TG, altimetry and GPS observables. From the full set and subset of TG locations, only TG-GPS sites with inter-station distances less than 200 km are used (see Table E-2 in Appendix E). The combinations use the two GPS sets, ULR5 (Santamaría-Gómez et al., 2012) and Hefl (Heflin, September 2013), full span for TG

and altimetry and restricted spans (1997 - 2012) for TG and altimetry.

The error of the rate deficit at each site is calculated in the same way as equation 5.4 but adding the GPS error term ($\sigma_{\dot{u}_{\mathrm{GPS}}}$) to give,

$$\sigma_{\delta\dot{d}} = \sqrt{\sigma^2_{\dot{g}} + \sigma^2_{\dot{S}} + \sigma^2_{\dot{u}_{\mathrm{GPS}}}}. \tag{5.6}$$

The different combinations of observables give slightly mixed results, though all of them lie within 1 mm yr^{-1} of zero rate deficit. Using the ULR5 GPS VGM rates in equation 5.5 and taking the median of the deficits and their errors ($\sigma_{\delta\dot{d}}$) gives a deficit ranging from -0.36 to -0.56 mm yr^{-1} for all and selected stations for both time series combinations (Figure 5.8a,c). By contrast, using the Hefl GPS VGM rates gives median rate deficits with a larger range from -0.04 to 0.79 mm yr^{-1} for all and selected stations for both time series combinations (Figure 5.8b,d).

The error bounds for all the average rate deficits extend across zero indicating that the assumption made above (equation 5.5) holds true, at least to the first order. This is an encouraging result given most studies have concentrated their efforts upon closing the sea-level loop from a VGM point of view and have either focused upon high latitude regions where GIA dominates VGM observations (e.g. Kuo et al. (2004, 2008)) or global studies to ascertain the first order VGM signals using brute force techniques and statistical evaluation (Ostanciaux et al., 2012).

Although there is a first order agreement, a rate deficit nonetheless remains. This deficit ranges from $\sim$ -0.5 mm yr^{-1} for ULR5 results to $\sim$ 0.4 mm yr^{-1} for Hefl results. Since all the observables have been carefully calculated, the deficit is likely to be due to a combination of small effects. These are, the interpolation of the altimetric grid to the TG positions, local coastal effects upon sea level recorded by the TG, the local uplift variations between TG and GPS stations.

As I stated in the previous chapter (Section 4.2.3), the interpolation of the altimetric grid to a TG position relies on the grid nodes that surround the TG station (up to four nodes, but more likely two or three given the TG is on the coast). The altimetry time series at each node is averaged to the TG position. Although this prevents bias towards any particular node, the nodes themselves are each up to 156 km ($\sqrt{2}^o$) away from the TG position. It is therefore appropriate to use the interpolated altimetry and the tide gauge together because the two data sources have been processed to remove their inter-annual variability and over multi-annual time scales it has been shown that

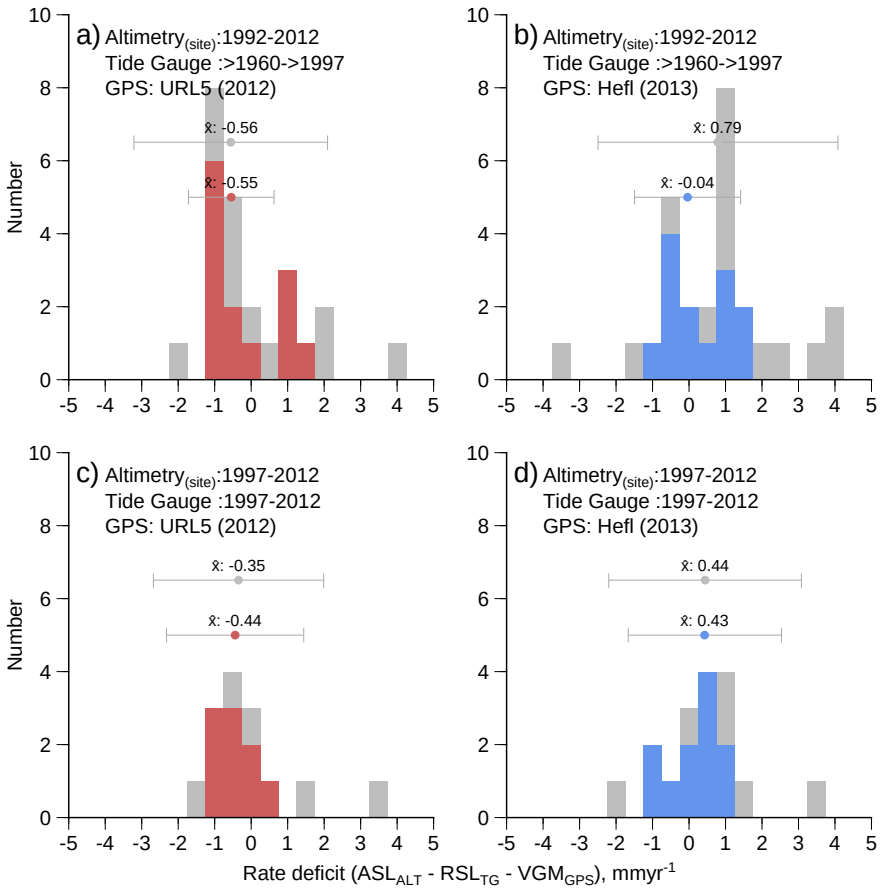

Figure 5.8: Distribution of sea-level rate deficits for all tide gauge locations (grey) and selected tide gauge locations (coloured). Median deficit and error range plotted for each distribution (all tide gauge locations, grey; selected tide gauge locations, coloured). **a** and **c** use ULR5 (2012) GPS data sets, **b** and **d** use Hefl (2013) GPS data sets. **a** and **b** use rates from full tide gauge and altimetry spans, **c** and **d** use rates from limited tide gauge and altimetry spans (1997-2012).

the two data sources are comparable with the exception of VGM.

The coastal geometry of each TG that results in local coastal effects has not been taken into account and may be considered a source of error (García et al., 2007). As mentioned previously, the assumption that increasing distance between TG and GPS stations reduces the coherence of uplift between the two sites is valid. However, given the low misfits between Alt-TG and GPS (Figure 5.4 and Table 5.1), sites up to 200 km apart can be used in comparison to Alt-TG studies at least to the first order.

5.4 Summary

In this chapter I have performed a series of inter-comparisons between past and modern sea-level rate estimates and models. These results show that GIA induced RSL rise accounts for up to one third of the total present day RSL rise. The local effects of land uplift near to TGs are important in balancing the ASL rate budget, which can be approximated to the sum of RSL and VGM rates. Furthermore, independent RSL and ASL (at the RSL site) measurements can be used to calculate VGM. The misfit between GPS and $\dot{g}(\theta,\phi)-\dot{S}(\theta,\phi)$ can be minimised by using TG and Altimetry records either with both their maximum time extent, or both overlapping such that the TG is truncated. To the first order, the budget for sea-level rise can be closed using the, $\dot{g}(\theta,\phi) - \dot{S}(\theta,\phi) - \dot{u}_{\mathrm{GPS}}(\theta,\phi) = 0$, assumption yet there remains a rate deficit, which I reason is caused by three sources of error: interpolation of altimetry grid to TG location, inter-station distance between TG and GPS pairs and local coastal effects.

Chapter 6

Discussion and Summary

6.1 Introduction

In the four previous chapters I have calculated how sea level has changed across the Caribbean, on millennial timescales using Holocene sea-level indicators, on decadal timescales during the twentieth century using tide gauges and on decadal timescales using satellite altimetry from the last twenty years. To make sense of this array of information, I present the relative sea-level (RSL) and absolute sea-level (ASL) trends at various time slices in the past at selected tide gauge locations. In the following sections I describe these sea-level changes, then I discuss the societal and environmental implications of long term sea-level rise across the region and recommendations for further study based upon the issues raised during this investigation.

6.2 Around the Caribbean in 10,000 years

To describe sea-level change around the Caribbean over the last 10,000 years I consider the changes occurring at or near to selected tide gauge locations. Each tide gauge location falls within a region used for the regional common mode correction with other tide gauges (Chapter 4) and within or in close proximity to a prehistoric sea-level curve derived in (Chapter 2), shown in Figure 6.1. Three tide gauges fall outside the prehistoric sub-regions and these, Cabo San Antonio, Casilda and Gibara lie between four sub-regions (1a, 1b, 2, 4a). Although Casilda is closer geographically to region 1a and 1b, I ascribe it to region 4a since it is on the south Cuban coast whilst Gibara is ascribed to region 1b as it is on the north Cuban coast. Cabo San Antonio is ascribed to region 2.

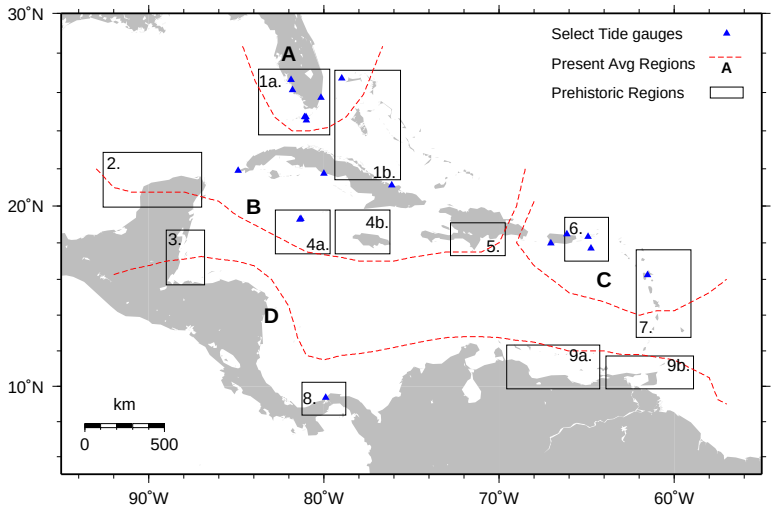

Figure 6.1: Tide gauges and two sets of sub-regions for the Caribbean. The first set of sub-regions (boxes) are those which were used to group Holocene sea-level indicators for sea-level curve construction (Chapter 2). The second set of sub-regions (red dashed lines) delineate groups of tide gauges used together for the regional common mode correction (Chapter 4).

Table 6.1 shows the RSL rates at the different locations for the last 15 and 50 years and at 1000, 4000 and 7000 cal yr BP. The gaps in the table are due to insufficient data availability to calculate a reasonable rate, which is in line with other nearby estimates (e.g. Key Colony Beach has a RSL rate over the last 15 years of 88 mm yr^{-1}, because the time span post-1997 is 1.3 years). Results in brackets for prehistoric RSL rates are the result of the curve construction of two adjacent regions of data. For example, Fort Myers is in region 1a, but region 1a doesn't give a 1000 cal yr BP RSL rate so I use the result of combined regions 1a and 1b (region 1: Chapter 2) to give rate at 1000 cal yr BP.

Table 6.2 shows the ASL rates across the Caribbean for the last 15, 50 and 1000 years BP. The 50 year and 1000 year time slices shown here are pseudo-ASL rates, which I calculate using equation 5.3. The RSL rates ($\dot{S}$) are those from Table 6.1 and I assume the GIA representative model predicted vertical ground motion ($\mathrm{VGM_{GIA}}$) is the major source of uplift ($\dot{u}_{\mathrm{VGM}}$). The 15 year time slice is directly from satellite altimetry, which is the only direct measure of ASL (see also Table 4.5).

Figure 6.2 shows graphically the RSL and ASL rates in Tables 6.1 and 6.2. The RSL and ASL rates are grouped by sub-region. It is easy to see that certain sub-regional rates (RSL and ASL) are distinct at given time slices, which demonstrates the spatial variation that exists across the region. There is a significant change in the rates of sea-

Table 6.1: Relative Sea-Level rise in mm yr^{-1} at tide gauge locations and within prehistoric regions (see Figure 6.1) over the last 15 and 50 years (tide gauge derived) and at 1000, 4000 and 7000 (Sea-level indicator derived) cal yr BP. Gaps are where insufficient data exists to derive rate. Bracketed rates are from combined prehistoric regions; 1a and 1b, region 1; 4a and 4b, region 4.

	Holocene	Years BP				
Tide gauge	region	15	50	1000	4000	7000
Region A						
Fort Myers	1a	1.48 ± 1.50	2.37 ± 0.27	(1.53 ± 0.82)	0.82 ± 0.16	1.99 ± 0.74
Key Colony Beach	1a		2.68 ± 0.55	(1.53 ± 0.82)	0.82 ± 0.16	1.99 ± 0.74
Key West	1a	1.67 ± 0.89	2.53 ± 0.20	(1.53 ± 0.82)	0.82 ± 0.16	1.99 ± 0.74
Naples	1a	1.61 ± 0.85	2.06 ± 0.21	(1.53 ± 0.82)	0.82 ± 0.16	1.99 ± 0.74
Vaca Key	1a	2.14 ± 0.81	2.83 ± 0.37	(1.53 ± 0.82)	0.82 ± 0.16	1.99 ± 0.74
Virginia Key	1a	0.96 ± 1.06	1.25 ± 0.60	(1.53 ± 0.82)	0.82 ± 0.16	1.99 ± 0.74
Settlement Point	1b		1.29 ± 1.26	0.53 ± 0.44	0.64 ± 0.45	1.65 ± 0.44
Region B						
Cabo San Antonio	2	1.80 ± 2.33	3.13 ± 0.35	0.61 ± 1.77	1.21 ± 2.68	
Casilda II	4a	1.50 ± 7.38	1.55 ± 0.41	0.40 ± 0.06	(0.96 ± 0.32)	2.28 ± 2.20
Gibara	1b	0.60 ± 1.31	1.10 ± 0.28	0.53 ± 0.44	0.64 ± 0.45	1.65 ± 0.44
North Sound	4a		1.42 ± 0.80	0.40 ± 0.06	(0.96 ± 0.32)	2.28 ± 2.20
South Sound	4a		1.46 ± 0.91	0.40 ± 0.06	(0.96 ± 0.32)	2.28 ± 2.20
Region C						
Magueyes Island	6	2.52 ± 0.67	1.27 ± 0.10	0.89 ± 0.17	0.70 ± 0.21	0.74 ± 0.19
San Juan	6	2.09 ± 0.71	1.63 ± 0.13	0.89 ± 0.17	0.70 ± 0.21	0.74 ± 0.19
Charlotte Amalie	6	2.43 ± 0.58	1.35 ± 0.14	0.89 ± 0.17	0.70 ± 0.21	0.74 ± 0.19
Lime Tree Bay	6	2.26 ± 0.83	2.00 ± 0.19	0.89 ± 0.17	0.70 ± 0.21	0.74 ± 0.19
Pointe a Pitre	7	1.49 ± 1.29	0.75 ± 0.60	0.62 ± 0.81	1.15 ± 0.69	0.95 ± 1.93
Region D						
Panama*	8		2.91 ± 0.26		1.14 ± 1.76	2.51 ± 1.34

* Panama is a combination of tide gauges Cristobal and Coco Sol, which have similar locations. Baseline corrections are described in PSMSL documentation.

Table 6.2: Absolute Sea-Level rise in mm yr^{-1} at tide gauge locations and within prehistoric regions (see Figure 6.1) over the last 15 (altimetry derived), 50 (TG and VGM_{GIA} derived) and 1000 (Sea-level indicator and VGM_{GIA} derived) years. Bracketed rates are from combined prehistoric regions; 1a and 1b, region 1.

	Holocene	Years BP		
Tide gauge	region	15	50	1000
Region A				
Fort Myers	1a	1.67 ± 1.86	0.89 ± 0.58	(0.07 ± 0.94)
Key Colony Beach	1a	0.37 ± 2.36	1.30 ± 0.69	(0.07 ± 0.94)
Key West	1a	0.78 ± 1.41	1.15 ± 0.45	(0.07 ± 0.94)
Naples	1a	1.19 ± 1.75	0.59 ± 0.52	(0.07 ± 0.94)
Vaca Key	1a	0.37 ± 2.36	1.44 ± 0.56	(0.07 ± 0.94)
Virginia Key	1a	1.25 ± 1.18	-0.14 ± 0.75	(0.07 ± 0.94)
Settlement Point	1b	1.08 ± 0.91	-0.37 ± 1.36	-0.74 ± 0.58
Region B				
Cabo San Antonio	2	0.11 ± 1.40	1.60 ± 0.56	-0.64 ± 1.81
Casilda II	4a	-0.04 ± 0.93	0.39 ± 0.54	-1.16 ± 0.47
Gibara	1b	-0.31 ± 0.83	0.06 ± 0.43	-0.74 ± 0.58
North Sound	4a	-0.13 ± 1.08	-0.14 ± 0.93	-1.16 ± 0.47
South Sound	4a	-0.13 ± 1.08	-0.11 ± 1.02	-1.16 ± 0.47
Region C				
Magueyes Island	6	1.49 ± 1.02	-0.02 ± 0.26	-0.37 ± 0.27
San Juan	6	1.53 ± 0.94	0.32 ± 0.28	-0.37 ± 0.27
Charlotte Amalie	6	1.58 ± 0.91	0.09 ± 0.26	-0.37 ± 0.27
Lime Tree Bay	6	1.58 ± 0.91	0.77 ± 0.27	-0.37 ± 0.27
Pointe a Pitre	7	1.37 ± 0.87	-0.41 ± 0.62	-0.55 ± 0.83
Region D				
Panama*	8	2.48 ± 0.89	2.26 ± 0.30	

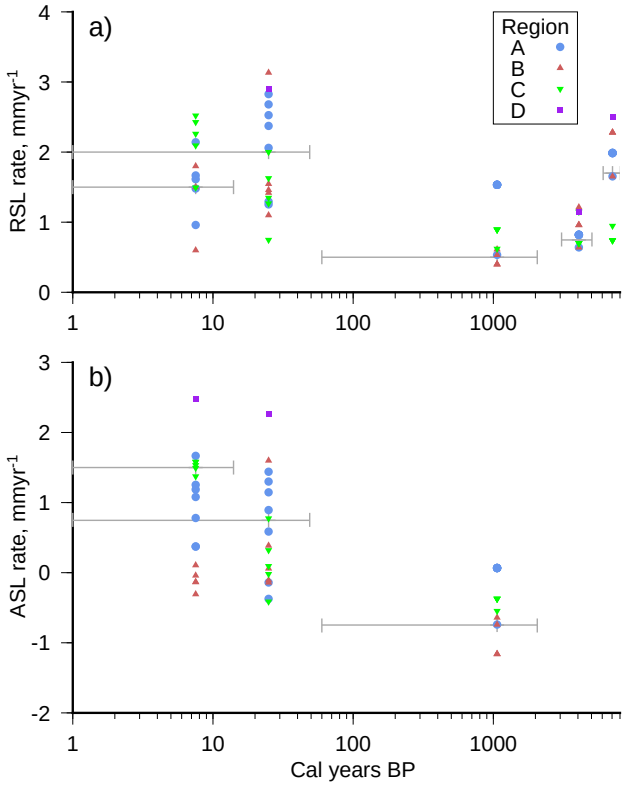

Figure 6.2: Sub-regional RSL (**a**) and ASL (**b**) rates from the Holocene to present day at tide gauge locations stated in Tables 6.1 and 6.2. The tide gauges are separated into their sub-regions by shape and colour. Details of the data sources are in Tables 6.1 and 6.2. Horizontal grey bars show the time span covered by each rate. They are symmetrical, but appear asymmetric because of the logarithmic time axis.

level rise from the late Holocene to the present. In the modern era, the rate changes depending upon the time span one views.

6.2.1 Mid to late Holocene: end of a rapid rise

In the Caribbean, as with much of the rest of the world, the mid to late Holocene (7000 - 4000 year BP) marked a significant reduction in the rate of sea-level rise relative to the previous 10,000 years (Carlson and Clark, 2002). The 7000 year BP time slice coincides with the end of significant melting of the Laurentide ice sheet, which was the dominant contributor to Caribbean Late-Pleistocene/Holocene sea-level change, at 6800 $\pm$ 300 years BP (Carlson et al., 2008) at which time RSL rates were between 0.7 to

2.5 mm yr^{-1} (Figure 6.2). These rates varied spatially and were $\sim$2 mm yr^{-1} in Cuba and along the Florida Keys, around 1 mm yr^{-1} along the Lesser Antilles (including the

US Virgin Islands) and 2.5 mm yr^{-1} in the south western Caribbean. Elsewhere in the Caribbean, rates were around 1.9 mm yr^{-1} along the Belize Barrier Reef System and ∼0.6 mm yr^{-1} (at 6000 years BP) in the Venezuela and Trinidad region.

During the next three thousand years RSL rise slowed by up to a half, with RSL rates between 0.6 to 1.2 mm yr^{-1} (Figure 6.2). Spatial variations of the RSL rate became smaller. Whilst other sub-regions experienced this slow down, the Lesser Antilles (including the US Virgin Islands) remained the same as their 7000 year BP rate. This time period coincides with a sparse coral/peat record in the Lesser Antilles.

6.2.2 The last thousand years

The sea level in the Caribbean, at the turn of the first millennium AD, was within 0.5 m of its present position. From 4000 to 1000 years BP sea level rose by up to 2.5 m (US Virgin Islands) though in some sub-regions as little as 1 m (Belize). Whilst the RSL rate of change continued to slow further in the central Caribbean (0.4 - 0.6 mm yr^{-1}) it was slightly elevated along Florida Keys (1 - 1.5 mm yr^{-1}) and remained similar along the Lesser Antilles (including US Virgin Islands) to the previous 6000 years (0.6 - 0.8 mm yr^{-1}).

At this time, the RSL rate was larger than the ASL rate in the Caribbean due to long term subsidence caused by GIA. The subsidence, which I predicted by fitting sea-level curves to the suite of model parameters and finding a regionally representative fit (lithospheric thickness, 71 km, upper and lower mantle viscosities, 0.5 and 10 x 10^{21} Pa s), varies from -1.2 to -0.2 mm yr^{-1} from north to south across the region, which is consistent with published rates (e.g. Mitrovica et al. (2001b)). Most of the RSL rise is caused by subsidence due to ocean syphoning and the small ASL change shows a minimal melt water component.

Although there is insufficient data to calculate the rate of sea-level change (either ASL or RSL) from peat and coral records between 1000 years BP and the second half of the twentieth century, the agreement between the 1000 year RSL rates and the model derived rates (Figure 3.14) at this time allow model projection of rates at 500 years BP, which is towards the end of the pre-industrial era. By using the representative model and projecting forwards, I find that RSL rates were 0.3 - 0.5 mm yr^{-1} along the Florida Keys, Bahamian platform and central Caribbean. RSL rate along the Lesser Antilles (including US Virgin Islands) had finally come into line with the

rest of the Caribbean after remaining constant from 7000 years BP. Exceptions to this RSL rate lie along Venezuelan and Trinidad coasts where it is predicted to have been zero or slightly negative (i.e. a sea level fall), which is consistent with published model results (Milne et al., 2005) for this region. These negative rates (zero within model error range) are also predicted at present day in the south eastern Caribbean along the northern South American coastline (Figure 5.6). Rates in Belize are also around zero.

The prehistoric curves calculated by sub-region across the Caribbean demonstrate the differences between rates of sea-level change across the Caribbean and argues against the use of the Western Atlantic Sea-Level (WASL) curve (Toscano and Macintyre, 2003) at this spatial scale. I have explicitly demonstrated the subtle spatial sea-level variations between locations, for example between Belize and US Virgin Islands, which is possible with good temporal coverage (during the Holocene) of sea-level indicators.

Fitting these curves using a computer code that models Glacial Isostatic Adjustment (GIA) with sea-level response has given representative model Earth parameters in agreement with those previously published (Milne et al., 2005). It is important to understand that the parameters are used to best fit the curves in this region and not near field sites surrounding the centres of deglaciation (region I and II, Figure 3.2). The sensitivity of the viscosity parameters in the Caribbean (though specifically to the Barbados sea-level curve) are mainly due to peripheral bulge dynamics (Milne and Mitrovica, 2008) rather than far field continental levering, ocean syphoning or rotational feedback (Mitrovica and Peltier, 1991, Mitrovica and Milne, 2002, Milne et al., 2005, Milne and Mitrovica, 2008).

6.2.3 Second half of 20$^{\text{th}}$ Century

A dearth of tide gauges that span more than 20 years and extend further back in time than 1950 prevent an analysis of 20$^{\text{th}}$ century sea-level change in the Caribbean. However, Table's 6.1 and 6.2 show the RSL and ASL ($\dot{S} + \dot{u}_{\text{GIA}}$) rates occurring across the region during the last 50 years.

The sites in region A can be considered as two groups, those bordering the Gulf of Mexico (including Florida Keys), which record RSL and ASL rates of 2 - 2.8 and 0.6 - 1.4 mm yr^{-1} respectively, and those on the Atlantic coast with RSL and ASL rates of 1.3 and -0.4 - -0.1 mm yr^{-1} respectively. These differences between Gulf of Mexico

versus Atlantic coast sites are also evident for the Cuban stations (region B), where Cabo San Antonio (Gulf of Mexico) and Gibara (Atlantic) have RSL rates of 3.1 and 1.1 mm yr^{-1} and ASL rates of 1.6 and 0.1 mm yr^{-1} respectively. Casilda (South Cuban coast) can be grouped with North and South Sound (Cayman Islands) where RSL rates lie between 1.4 - 1.6 mm yr^{-1}, however the ASL rates differ from -0.14 mm yr^{-1} in the open ocean (Cayman Islands) to 0.39 mm yr^{-1} at the coast (Casilda). The rates indicate that sub-regional sea-level trends exist for the Atlantic coast, Gulf of Mexico and Northern Caribbean Sea.

In region C, there are two regionally distinct sea-level trends. The Puerto Rico and Virgin Islands group show RSL and ASL rates in the ranges 1.3 - 2.0 and 0.0 - 0.8 mm yr^{-1} respectively and Pointe a Pitre, which has smaller RSL and ASL rates, akin to those 1000 years BP of 0.8 and -0.4 mm yr^{-1} respectively. A trend appears to exist of smaller RSL and ASL rise from north to south east along the Greater and Lesser Antilles island chains. Although there is not a tide gauge of sufficient length in the extreme south east to demonstrate the continuation of this trend, the Port of Spain record (1984 - 1992) hints at a RSL rate of 0.6 mm yr^{-1} supported by Miller (2005) (1 mm yr^{-1}, raw rate using annual means). This is consistent with the modelled VGM rates, which show subsidence rates becoming smaller from north-west to south-east (Figure 5.3a). The Panama record, composed of Coco Sol and Cristobal has RSL and ASL rates of 2.9 and 2.3 mm yr^{-1} respectively. Although this is the only record in the southern Caribbean for this time span, the ASL and RSL rates can be reconciled within error by the GIA modelled VGM of $\sim$0.4 mm yr^{-1}. This is unfortunately the only record in the southern Caribbean in this time span.

The RSL rates across the Caribbean vary significantly. I correct each TG site (Table 6.1) by the optimal RSL_{GIA} at each site and average the difference between them and the global average (1.8 $\pm$ 0.3 mm yr^{-1}, 1950-2000, GIA corrected, Church et al. (2004)) giving a deviation of -0.4 $\pm$ 0.7 mm yr^{-1}. This reveals that sea level in the the Caribbean was close to the global average (Church et al., 2004) during the second half of the 20^{th} century.

Recent work by Gehrels and Woodworth (2013) has shown that a deviation from late Holocene sea-level rates (0 to 0.2 mm yr^{-1}), which are in agreement with my observed and modelled results, to modern sea-level rates (1.8 mm yr^{-1}) occurred globally in a 40 year span centred about 1925. Although my modern results do cover the 87 year

span (1925 - 2012), nor do my Holocene sea-level rates extend beyond 1000 cal yr BP, the change in magnitude of the sea-level rate is consistent with Gehrels and Woodworth (2013).

6.2.4 The last 15 years

Seven of the tide gauges in Table 6.1 do not record RSL from 1997 to 2012. The limited records that do exist show RSL rates on the Gulf of Mexico side of Florida fell during the last 15 years by ∼0.5 mm yr^{-1} to 1.5 - 2.1 mm yr^{-1}. Virginia Key remains constant relative to the last 50 years with an RSL rate of 1.0 mm yr^{-1}, which is supported by the RSL rate at Gibara, 0.6 mm yr^{-1}. The errors associated with these values does mean the rates fall in line with those mentioned on the Gulf of Mexico side of Florida (including the Keys). The RSL rate in this part of the Gulf of Mexico is supported by the rate at Cabo San Antonio, 1.8 mm yr^{-1} though here again the error is high.

One region with lower errors of RSL rates is US Virgin Islands with a narrow range, 2.1 - 2.5 mm yr^{-1} and average errors of 0.7 mm yr^{-1}. On Guadeloupe, Pointe a Pitre records a lower RSL rate, 1.5 mm yr^{-1} though yet again the error is sufficiently high to overlap with RSL rate in the US Virgin Islands. As mentioned in Chapter 4, there are no tide gauge records between 1997 - 2012 in the southern Caribbean, which prevents any further assessment of RSL rates across the region.

ASL rates are directly from the satellite altimetry and are on average 0.4 ± 1.4 mm yr^{-1} larger than those estimated using RSL - VGM_{GIA} for the last 50 years. This average value does not tell the whole story though, as ASL rates within each sub-region are consistent revealing the caution that must be adopted when interpreting pseudo-ASL rates from the past. The Florida sites on both east and west sides range from 0.4 to 1.7 mm yr^{-1} though the two sites with ASL rates of 0.4 mm yr^{-1} have errors exceeding 2 mm yr^{-1}, whilst those remaining average to 1.2 ± 1.4 mm yr^{-1}. This drops significantly to the range -0.3 to 0.1 mm yr^{-1} for region B, averaging at -0.1 ± 1.1 mm yr^{-1}. Region C ASL rates average 1.5 ± 0.9 mm yr^{-1} in the range, 1.4 to 1.6 mm yr^{-1}. Finally, the site at Panama has ASL rate of 2.5 mm yr^{-1}.

In short, regions B and C show a difference between recent RSL and ASL rates (-1.4 and -0.8 mm yr^{-1}), which can be ascribed to subsidence due to GIA. The discrepancy between RSL and ASL rates in region A is smaller than the predicted subsidence suggesting that a volumetric increase to sea level is overprinting the subsidence effects.

6.3 Pre-historic comparisons and future projections

6.3.1 Interglacial to Holocene to Modern sea-level rates

Figure 6.2 shows that there has been a distinct change in sea-level rates from the Holocene to the present. Rates of sea-level change have gone from sub-millimetre to millimetres per year during the last thousand years and much of the evidence indicates this will only continue. The root cause in equatorial regions also appears to have changed from primarily being meltwater redistribution (ocean syphoning) and GIA caused by the last deglaciation to steric changes caused by a warming world (Milne et al., 2009) (though this will feedback to meltwater redistribution if large portions of grounded ice sheets are melted).

It is interesting to consider how late Holocene and modern rates of sea-level change compare to the previous interglacial. This is a useful proxy for future sea-level rise scenarios as global mean surface temperatures were at least 2^oC warmer than present, which is in line with climate projections for 2100 AD (Otto-Bliesner et al., 2006). Rohling et al. (2008) suggest that the sea-level highstand (4 - 6 m above present sea level) occurring during the last interglacial (123.5 to 119 kyr BP) would have required an ice sheet comparable to the size of Greenland melting in roughly four centuries (1000 years or more from modelling, Gregory et al. (2004)).

This gives average sea-level rates of $\sim 1.6 \pm 0.8$ cm yr^{-1} during this time (Rohling et al., 2008), which is up to ten times faster than the 20^{th} century globally averaged sea-level rate (1.8 mm yr^{-1}, Church et al. (2004)), up to four times faster than the modern globally averaged sea level rate (3.4 mm yr^{-1}, Nerem et al. (2010) and up to 15 mm yr^{-1} greater than modern ASL rates in the Caribbean. Not since the middle Holocene have rates of this magnitude been observed in the Caribbean (Figure 2.17). If modern sea-level rates continue to rise as is expected with rising CO_2 concentrations (Forster et al., 2007), increasing ocean temperatures (Bindoff et al., 2007) and retreating ice margins (Lemke et al., 2007) then it is quite plausible for rates of sea-level change to increase by a significant factor.

6.3.2 Implications and impacts upon coastline communities

Using the IPCC 2007 global climate model (GCM) ensemble mean for scenario A1B, the most recent estimate for global sea-level rise between 1980 - 1999 and 2090 - 2099

is 34 ± 13 cm (Meehl et al., 2007). This range gives a range of ASL rates of 2.1 to 4.7 mm yr^{-1}. Coupled to this, the regional variation in the Caribbean is ±5 cm from this mean based on the ensemble of 16 GCMs (Meehl et al., 2007).

I calculate the RSL rise at tide gauge locations in 2100 using the following steps (Mazzotti et al., 2008). Firstly, I assume the IPCC projection start date is 1989.5 ($\frac{(1999+1980)}{2}$). Next I using my satellite altimetry ASL rate estimates (1992-2012) to calculate the ASL rise from 1989.5 to 2012 at each tide gauge location. This value is subtracted from the 34 ± 13 cm global ASL rise estimate. The difference then is a local ASL estimated rise from 2012 to 2100.

Assuming land motion is going to be constant over the next 88 years (2012 - 2100), I calculate the total land motion (VGM, mm yr^{-1} x 100 yrs = mm) at each tide gauge location and subtract this from the locally estimated ASL rise. This gives a projection of the RSL rise that each tide gauge location could experience. For this I use both $\dot{g} - \dot{S}$ solutions and GPS measurements (ULR5 Santamaría-Gómez et al. (2012) and Hefl Heflin (September 2013)) from Chapter 5.

Figure 6.3 shows the projected RSL rise at tide gauge locations in the Caribbean between 2012 and 2100, with their associated errors. The colour scale shows that the RSL rises across the region are positive, and in the range 20 to 60 cm. Furthermore the average RSL rise for the tide gauge locations shown is 39 ± 16 cm, 37 ± 14 cm and 41 ± 13 cm for the $\dot{g} - \dot{S}$, GPS: ULR5 and GPS: Hefl respectively. The regional variation appears to change with the method used to calculate the rise. For example using $\dot{g} - \dot{S}$, RSL rise increases from south-east (20 ± 15 cm: Pointe a Pitre, Guadeloupe) to north-west (46 ± 18 cm: Fort Myers, Florida) along the Antilles, whereas using Heflin (September 2013) shows the opposite trend, 38 ± 13 cm in the north-west (Fort Myers, Florida) increasing to 58 ± 13 cm in the south-east (Pointe a Pitre, Guadeloupe). The average Caribbean RSL rise is consistent for GPS based projections when I use all the tide gauge locations across the region (see Figure F-1 in Appendix F). The average RSL rise (maximum range in parentheses) for all tide gauge locations is 29 ± 28cm (-163 to 151 cm), 35 ± 14 cm (25 to 55 cm) and 43 ± 13 cm (17 to 68 cm) for the $\dot{g} - \dot{S}$, GPS: ULR5 and GPS: Hefl based projections respectively.

As mentioned in the introduction, the Caribbean region is at risk from sea-level rise in a variety of different ways. It is important to stress that although the exercise performed above makes a series of assumptions, the magnitude of the sea-level

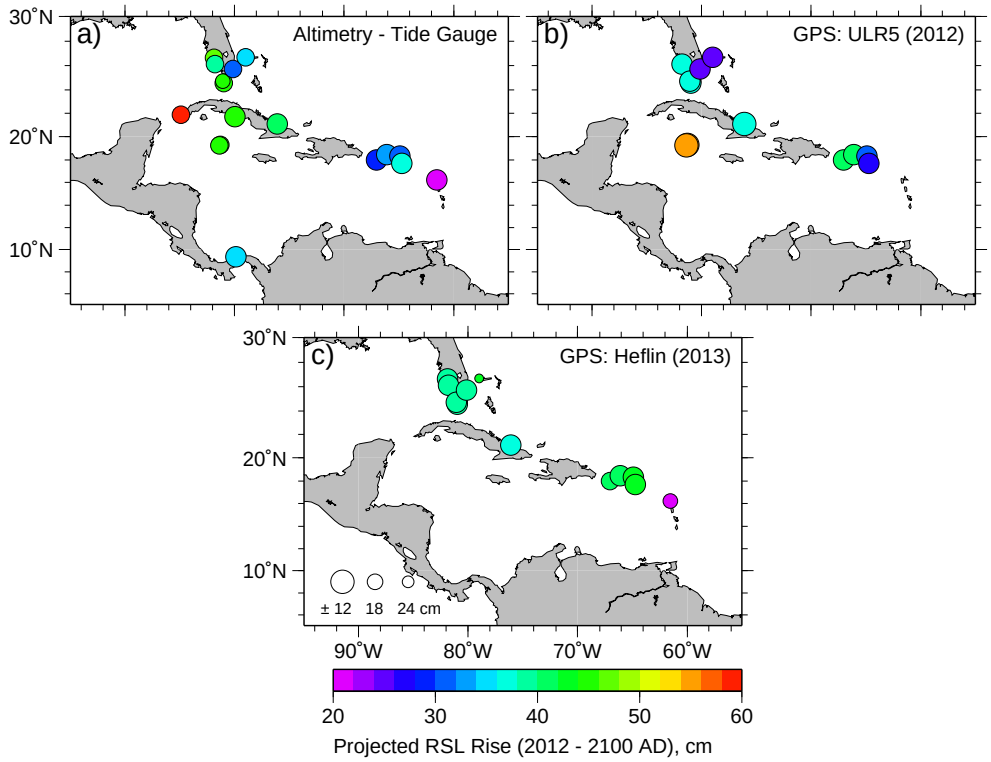

Figure 6.3: Projected relative sea-level rise by 2100 using vertical ground motion estimates and IPCC2007 ASL rise estimates from 1980-1999 to 2090-2099. Vertical ground motion estimates using **a**: Altimetry - Tide Gauge, **b**: GPS ULR5 (Santamaría-Gómez et al., 2012) and **c**: GPS Hefl (Heflin, September 2013). Size of circle corresponds to error in projection.

rise projected is conservative in comparison to assessments of financial loss and socio-economic risk, which tend to promote 1 and 2 metre sea-level rise by 2100 scenarios (Stanton and Ackerman, 2007, Bueno et al., 2008, Simpson et al., 2010). These scenarios are at the extreme end of those made by IPCC and should be treated with care. This does not means that they should be dismissed. The projected rise shown in Figure 6.3 has up to 20 cm errors, which gives an upper envelope of ∼70 cm at some sites. To demonstrate the difficulty of projecting into the future but also the need to do so, I present two examples of sites that require detailed site knowledge.

The Forte de France tide gauge record extends from 2005 to 2012. Although this is only seven years, the corrected RSL rate for this span is 12.59 ± 3.94 mm yr^{-1} (Figure D in Appendix D). This is very high, particularly given the ASL rate is only 1.99 ± 0.6 mm yr^{-1}. This results in a VGM for the time span of -10.6 ± 3.99 mm yr^{-1}. A GPS site, LMMF (Heflin, September 2013) lies 6.2 km from the tide gauge and has a VGM of -4.35 ± 0.1 mm yr^{-1}. Although this does not close the

deficit for the site, it should be noted that LMMF only extends 2 years from 2010 to 2012. Upon closer inspection, I suggest two reasons for the deficit. The first is the inter-station distance of 6.2 km between the tide gauge (in Forte de France harbour) and GPS station (at Forte de France airport above the harbour bay). The second is centimetre scale land subsidence due to shaking caused by a 7.4 moment magnitude earthquake on 29$^{\text{th}}$ November 2007, 30 km north of Martinique in the Dominica channel (Lachassagne et al., 2011). Although the earthquake occurred at depth (143 km, USGS estimate), there was strong shaking in the city of Forte de France (up to MMI VII, Modified Mercalli Intensity scale) that caused damage to buildings. The amount of subsidence required to close this deficit, assuming the measurements are correct, would be up to 12 mm (two years between earthquake and GPS start date, deficit of $\sim$6 mm yr^{-1}). The RLR tide gauge record does not appear to record a sudden jump in sea level, but an inflexion (causing a much higher rate) occurs from mid-2008 after which sea level rises much faster than before. This delayed response could be interpreted as postseismic relaxation though alternatives could give similar magnitude signals. For example, coastal subsidence may affect a tide gauge in a city like Forte de France, much of which lies on reclaimed swamp. Wang et al. (2012) have measured subsidence rates up to 6 mm yr^{-1} using Interferometric Synthetic Aperture Radar (InSAR) in the heavily populated coastal environment of the Pearl River, China. Though much smaller, Forte de France may experience a similar effect.

Cartagena on the Colombian coast records corrected RSL and ASL rates of 5.5 ± 0.6 (Figure D in Appendix D) and 2.6 ± 0.7 mm yr^{-1} respectively. The difference between the two rates is supported by GPS within error from ULR5 (Santamaría-Gómez et al., 2012), which gives total VGM, including GIA subsidence, of -2.2 $\pm$ 0.5 mm yr^{-1} ($\dot{g} - \dot{S}$ = -2.9 $\pm$ 0.9 mm yr^{-1}). The representative GIA model predicts long term subsidence of -0.6 $\pm$ 0.2 mm yr^{-1} at Cartagena inferring a local tectonically induced subsidence of -2.3 $\pm$ 0.9 mm yr^{-1} ($\dot{g} - \dot{S} - \dot{u}_{\text{GIA}}$).

Both of these sites are experiencing high rates of RSL change, mainly due to VGM. Although both GPS stations are relatively close to their respective tide gauge stations, Forte de France has a significant deficit in the rate of sea-level change, whilst subsidence at Cartagena can be explained within error. In view of these results, accurately quantifying VGM is critical to projecting sea-level rise at the local scale into the future. By assuming constant rates of VGM and ASL, it is possible to make conservative pro-

jections. In fact, rapid VGM like a thrust or normal earthquake will cause many short term problems (e.g. damage to infrastructure) and greatly increase the risk associated with a site if it lies at or near the coastline.

6.4 Recommendations for future study

During the thesis I have illuminated problems with the various methods, assumptions and data that have been used. Here I make a series of recommendations based upon these problems to enable a clearer understanding of sea level in this diverse region to emerge.

Firstly, I acknowledge the limitations of the sea-level curve construction method. The approach assumes coral and mangrove species live at well defined positions relative to sea level. To the first order this is correct and I have used growth distribution and abundance records as well as other *a priori* information from publications to develop probability distribution functions of coral and mangrove habitable ranges. Of course this is not straight forward as the materials dealt with here are organic and depend very much upon their environmental setting. For example, Bard et al. (2010) found *A Palmata* corals living at 17 m depth, 5 m outside my distribution for the same coral.

Therefore, it is of critical importance to build up the coral and mangrove habitable range record. Applying a careful, palynological approach to present day species for a wide spatial distribution of coral reefs and mangrove swamps is key to modelling past sea-level position more accurately. This approach has been used along the US eastern seaboard to great success (e.g. Engelhart and Horton (2012)). Furthermore, with a few exemptions (Rull et al., 1999, Ramcharan, 2004, Milne et al., 2005) there is a complete lack of Holocene (or Pleistocene) sea-level records along the north coast of South America (Colombia and Venezuela) and south western Caribbean coastline (Costa Rica, Nicaragua and Honduras). This problem must be addressed to place the sea-level curve at Panama in context.

Secondly, I acknowledge the limitations of the method of Mazzotti et al. (2008), which relies upon reasonable correlation between tide gauges within a region. This approach was initially used along the west coast of the United States and Canada where the average tide gauge length is 45 years (Mazzotti et al., 2008). Although the time spans of tide gauges in the Caribbean were much less (average of 49 tide gauges, 18.6 years; 18 selected tide gauges, 33 years), the method was generally successful in

reducing regionally correlated high frequency noise, which affected the estimated rate.

However, the largest region (D) suffered from much the same problem as those of prehistoric sea-level records, lack of records. There is not one active tide gauge along a coastline of 5000 km from the eastern tip of the Yucatan Peninsula south and east along the Caribbean coastline until one reaches Forte de France on Martinique half way along the Lesser Antilles island chain. Network improvements along north coast of South America (Colombia, Venezuela, Trinidad and Tobago) and south western Caribbean coastlines (Costa Rica, Nicaragua and Honduras), either tide gauge or GPS stations (preferably both) would allow the southern Caribbean to be monitored far more effectively.

6.5 Conclusions

My investigation into sea-level change in the Caribbean has revealed the following results.

Firstly, I have devised a method to reconstruct past sea-level positions using Holocene sea-level indicators. The resulting sea-level curves show sub-regional variations in sea-level position during the Holocene.

Secondly, by comparing these sea-level curves to GIA model derived sea-level curves I have ascertained a set of representative parameters for upper and lower mantle viscosities. The inter-comparison is generally invariant to lithospheric thickness. Furthermore, the dominant meltwater source for the Caribbean is the Laurentide ice sheet, which is also contributing to modern VGM.

Thirdly, by calculating modern rates of sea-level change using tide gauges and satellite altimetry I have found that present sea-level rates are up to 2 mm yr^{-1} greater than at the end of the Holocene ($\sim$500 - 1000 Cal yr BP). In addition, the noise reduction processing allows one to use shorter time series and still derive long term rates of sea-level change with a reduction in the error.

Fourthly, the difference between ASL and RSL rates is, to the first order, due to the ground motion that the tide gauge (RSL) experiences. Excluding the posibility of local tectonics, the primary driver of VGM should be GIA (subsidence across the Caribbean, becoming greater to the north). Central and Southern Caribbean sites can generally be explained by this assumption, but those in the Florida region show VGM that is smaller than the predicted GIA induced subsidence.

References

Adey, W. (1975), The Algal Ridges and Coral Reefs of St.Croix: their structure and Holocene development, *Atol Res Bull*, *187*.

Adey, W. H., and R. Burke (1976), Holocene bioherms (algal ridges and bank-barrier reefs) of the eastern Caribbean, *Geol Soc Am Bull*, *87*, 95–109.

Adey, W. H., I. G. Macintyre, R. Stuckenrath, and R. F. Dill (1977), Relict barrier reef system off St. Croix: Its implications with respect to Late Cenozoic Coral Reef development in the Western Atlantic, in *Proceedings of the Third International Coral Reef Symposium, Florida*, vol. 2, edited by D. L. Taylor, pp. 15–21.

Agnew, D. C. (1992), The time-domain behaviour of power-law noises, *Geophys Res Lett*, *19*(4), 333–336.

Aitken, M. J. (1990), *Science-based dating in Archaeology*, 296 pp., Longman.

Argus, D. F., and M. B. Heflin (1995), Plate Motion and Crustal Deformation Estimated With Geodetic Data From the Global Positioning System, *Geophys Res Lett*, *22 (15)*, 1973–1976.

Baart, F., M. van Koningsveld, and M. J. F. Stive (2012a), Trends in Sea-Level Trend Analysis, *J Coast Res*, *28 (2)*, 311–315, doi:10.2112/JCOASTRES-11A-00024.1.

Baart, F., P. H. A. J. M. van Gelder, J. de Ronde, M. van Koningsveld, and B. Wouters (2012b), The Effect of the 18.6-Year Lunar Nodal Cycle on Regional Sea-Level Rise Estimates, *J Coast Res*, *28 (2)*, 511–516, doi:10.2112/JCOASTRES-D-11-00169.1.

Bak, R. P. M., and M. S. Engel (1979), Distribution, Abundance and Survival of Juvenile Hermatypic Corals (Scleractinia and the Importance of Life History Strategies in the Parent Coral Community, *Mar Biol*, *54*, 341–352.

Bard, E., B. Hamelin, and R. G. Fairbanks (1990), U-Th ages obtained by mass spectrometry in corals from Barbados: sea level during the past 130,000 years, *Nature*, *346*, 456–458.

Bard, E., B. Hamelin, and D. Delanghe-Sabatier (2010), Deglacial Meltwater Pulse 1B and Younger Dryas Sea Levels Revisited with Boreholes at Tahiti, *Science*, *327*, 1235–1237, doi:10.1126/science.1180557.

Barham, A. J., and D. R. Harris (1983), Prehistory and Palaeoecology of Torres Strait, in *Quaternary Coastlines and Marine Archaeology*, edited by P. Masters and N. C. Fleming, pp. 529–557, Academic Press.

Bartlett, A. S., and E. S. Barghoorn (1973), Phytogeographic History of the Isthmus of Panama during the Past 12,000 years (A History of Vegetation, Climate and Sea-level Change, in *Vegetation and Vegetational History of Northern Latin America*, edited by A. Graham, pp. 203–299, Elsevier.

Bassett, S. E., G. A. Milne, J. X. Mitrovica, and P. U. Clark (2005), Ice Sheet and Solid Earth Influences on Far-Field Sea-Level Histories, *Science*, *309*, 925–928, doi:10.1126/science.1111575.

Bentley, M. J. (1999), Volume of Antarctic Ice at the Last Glacial Maximum, and its impact on global sea level change, *Quat Sci Rev*, *18*, 1569–1595.

Benz, H. M., A. C. T. anf G. P. Hayes, A. V. nor, K. P. Furlong, R. L. .Dart, and S. Rhea (2011), Seismicity of the Earth 1900-2010 caribbean plate and vicinity, *Open-File Report 2010-1083-A*, U.S. Geological Survey.

Bergeot, N., M. N. Bouin, M. Diament, B. Pelletier, M. Régnier, S. Calmant, and V. Ballu (2009), Horizontal and vertical interseismic velocity fields in the Vanuatu subduction zone from GPS measurements: Evidence for a central Vanuata locked zone, *J Geophys Res*, *114*, B06,405, doi:10.1029/2007JB005249.

Bezada, M. J., A. Levander, and B. Schmandt (2010), Subduction in the southern Caribbean: Images from finite-frequency P wave tomography, *J Geophys Res*, *115*, B12,333, doi:10.1029/2010JB007682.

Biasutti, M., A. H. Sobel, S. J. Camargo, and T. T. Creyts (2012), Projected changes in physical climate of the Gulf Coast and Caribbean, *Climatic Change*, *112*, 819–845, doi:10.1007/s10584-011-0254-y.

Bindoff, N. L., J. Willebrand, V. Artale, A. Cazenave, J. Gregory, S. Gulev, K. Hanawa, C. L. Quéré, S. Levitus, Y. Nojiri, C. K. Shum, L. D. Talley, and A. Unnikrishnan (2007), 2007: Oceanic Climate Change and Sea Level, in *IPCC, 2007: Climate Change 2007: The Physical Science Basis. Contribution of Working Group I to the Fourth Assessment Report of the Intergovernmental Panel on Climate Change*, edited by S. Solomon, D. Qin, M. Manning, Z. Chen, M. Marquis, K. B. Averyt, M. Tignor, and H. L. Miller, Cambridge University Press, Cambridge, United Kingdom and New York, NY, USA.

Bingham, R. J., and C. W. Hughes (2012), Local diagnostics to estimate density-induced sea level variations over topography and along coastlines, *J Geophys Res*, *117*, C01,013, doi:10.1029/2011JC007276.

Blanchon, P. (2000), Discovery of an early Holocene relict reef and shoreline off Grang Cayman, in *Proceedings of the Ninth International Coral Reef Symposium, Bali*, vol. 1, edited by M. K. Moosa, S. Soemodihardjo, A. Soegiarto, K. Romimohtarto, A. Nontji, Soekarno, and Suharsono, pp. 223–230.

Blanchon, P. (2005), Comments on "Corrected western Atlantic sea-level curve for the last 11,000 years based on calibrated 14C dates from Acropora palmata framework and intertidal mangrove peat" by Toscano and Macintyre [Coral Reefs (2003) 22:257-270], *Coral Reefs*, *124*, 183–186, doi:10.1007/s00338-004-0472-0.

Blanchon, P., and C. T. Perry (2004), Taphonomic differentiation of Acropora palmata facies in cores from Campeche Bank Reefs, Gulf of Mexico, *Sedimentology*, *51*, 53–76, doi:10.1046/j.1365-3091.2003.00610.x.

Blanchon, P., and J. Shaw (1995), Reef drowning during the last deglaciation: Evidence for catastrophic sea-level rise and ice-sheet collapse, *Geology*, *23*, 4–8.

Boardman, M. R., A. C. Neumann, and K. A. Rasmussen (1989), Holocene Sea Level in the Bahamas, in *Proceedings of the Fourth Symposium on the Geology of the Bahamas*, edited by J. E. Mylroie and D. T. Gerace, pp. 45–52.

Bosscher, H., and W. Schlager (1992), Computer simulation of reef growth, *Sedimentology*, *39*, 503–512.

Bouin, M. N., and G. Wöppelmann (2010), Land motion estimates from GPS at tide gauges: a geophysical evaluation, *Geophys J Int*, *180*, 193–209, doi:10.111/j.1365-246X.2009.04411.x.

Bradley, S., G. A. Milne, I. Shennan, and R. Edwards (2011), An improved Glacial Isostatic Adjustment model for the British Isles, *J Quaternary Sci*, *26(5)*, 541–552, doi:10.1002/jqs.1481.

Broecker, W. S., and J. L. Kulp (1957), Lamont Natural Radiocarbon Measurements IV, *Science*, *126*(3287), 1324–1334.

Broecker, W. S., and E. A. Olson (1961), Lamont radiocarbon measurements viii, *Radiocarbon*, *3*, 176–204.

Bueno, R., C. Herzfeld, E. A. Stanton, and F. Ackerman (2008), The Caribbean and Climate Change: The Costs of Inaction, *Tech. rep.*, Stockholm Environment Institute - US Center and Global Development and Environment Institute, Tufts University.

Burke, R. B., W. H. Adey, and I. G. Macintyre (1989), Overview of the Holocene history architecture and structural components of Tague Reef and Lagoon, in *Terrestrial and Marine Geology of St. Croix, U.S. Virgin Islands.*, vol. 8, edited by D. K. Hubbard, pp. 105–110, West Indies Laboratory Special Publication.

Calafat, F. M., D. P. Chambers, and M. N. Tsimplis (2012), Mechanisms of decadal sea level variability in the eastern North Atlantic and the Mediterranean Sea, *J Geophys Res*, *117*, C09,022, doi:10.1029/2012JC008285.

Carew, J. L., and J. E. Mylroie (1995), Quaternary tectonic stability of the Bahamian Archipelago: Evidence from fossil coral reefs and flank margin caves, *Quat Sci Rev*, *14*, 145–153.

Carlson, A. E., and P. U. Clark (2002), Ice sheet sources of sea level rise and freshwater discharge during the last deglaciation, *Rev Geophys*, *50*, RG4007, doi:10.1029/2011RG000371.

Carlson, A. E., A. N. Legrande, D. W. Oppo, R. E. Came, G. A. Schmidt, F. S. Anslow, J. M. Licciardi, and E. A. Obbink (2008), Rapid early Holocene deglaciation of the Laurentide ice sheet, *Nature Geosci*, *1*, 620–624, doi:10.1038/ngeo285.

Cazenave, A., and W. Llovel (2010), Contemporary Sea Level Rise, *Annu Rev Mar Sci*, *2*, 145–173, doi:10.1146/annurev-marine-120308-081105.

Chalker, B. E. (1981), Simulating light-saturation curves for photosynthesis and calcification by reef-building corals, *Mar Biol*, *63*, 135–141.

Chalker, B. E., D. J. Barnes, W. C. Dunlop, and P. L. Jokiel (1988), Light and reef-building corals, *Interdisc Sci Rev*, *13*, 222–237.

Chambers, D. P., M. A. Merrifield, and R. S. Nerem (2012), Is the a 60-year oscillation in global mean sea level?, *Geophys Res Lett*, *39*(L18607), doi:10.1029/2012GL052885.

Chérubin, L. M., W. Sturges, and E. P. Chassignet (2005), Deep flow variability in the vicinity of the Yucatan Straits from a high-resolution numerical simulation, *J Geophys Res*, *110*(C04009), doi:10.1029/2004JC002280.

Church, J. A., and N. J. White (2011), Sea-Level Rise from the Late 19th to the Early 21st Century, *Surv Geophys*, *32*, 585–602, doi:10.1007/s10712-011-9119-1.

Church, J. A., N. J. White, R. Coleman, K. Lambeck, and J. X. Mitrovica (2004), Estimates of the Regional Distribution of Sea Level Rise over the 1950-2000 Period, *J Climate*, *17*, 2609–2625.

Church, J. A., N. J. White, L. F. Konikow, C. M. Domingues, J. G. Cogley, E. Rignot, J. M. Gregory, M. R. van den Broeke, A. J. Monaghan, and I. Velicogna (2011), Revisiting the Earth's sea-level and energy budgets from 1961 to 2008, *Geophys Res Lett*, *38*(L18601), doi:10.1029/2011GL048794.

Clark, J. A., W. E. Farrell, and W. R. Peltier (1978), Global Changes in Postglacial Sea Level: A Numerical Calculation, *Quaternary Res*, *9*, 265–287.

Coke, J., E. C. Perry, and A. Long (1991), Sea-level curve, *Nature*, *353*, 25.

Cuevas, D. N., C. E. Sherman, W. Ramírez, and D. K. Hubbard (2009), Coral growth rates from the Holocene Cañada Honda fossil reef, Southwestern Dominican Republic: Comparisons with modern counterparts in high sedimentation settings, *Caribb J Sci*, *45(1)*, 94–109.

Dalca, A. V., K. L. Ferrier, J. X. Mitrovica, J. T. Perron, G. A. Milne, and J. R. Creveling (2013), On postglacial sea level - III. Incorporating sediment redistribution, *Geophys J Int*, doi:10.1093/gji/ggt089.

Davies, P. J., and L. Montaggioni (1985), Reef growth and sea-level change: the environmental signature, in *Proceedings of the Fifth International Coral Reef Congress, Tahiti*, vol. 3, pp. 477–511.

DeMets, C., R. G. Gordon, and D. F. Argus (2010), Geologically current plate motions, *Geophys J Int*, *181*, 1–80, doi:10.1111/j.1365-246X.2009.04491.x.

Digerfeldt, G., and M. D. Hendry (1987), An 8000 year Holocene sea-level record from Jamaica: implications for interpretation of Caribbean reef and coastal history, *Coral Reefs*, *5*, 165–169.

Dillon, W. P., and J. G. Vedder (1973), Structure and development of the continental margin of British Honduras, *Geol Soc Amer Bull*, *84*, 2713–2732.

Douglas, B. C. (1991), Global Sea Level Rise, *J Geophys Res*, *96*, 6981–6992.

Douglas, B. C. (2001), Sea level change in the era of recording tide gauge, in *Sea Level Rise History*, *Int Geophys*, vol. 75, edited by B. C. Douglas, M. S. Kearney, and S. P. Leatherman, pp. 37–64, doi:10.1016/S0074-6142(01)80006-1.

Druffel, E. M., and T. W. Linick (1978), Radiocarbon in annual coral rings of Florida, *Geophys Res Lett*, *5*, 913–916.

Dullo, W.-C. (2005), Coral growth and reef growth: a brief review, *Facies*, *51*, 33–48, doi:10.1007/s10347-005-0060-y.

Dziewonski, A. M., and D. L. Anderson (1981), Preliminary Reference Earth Model (PREM), *Phys Earth planet Inter*, *25*, 297–356.

Engelhart, S., and B. P. Horton (2012), Holocene sea level database for the Atlantic coast of the United States, *Quat Sci Rev*, *54*, 12–25, doi:10.1016/j.quascirev.2011.09.013.

Fairbanks, R. G. (1989), A 17,000-year glacio-eustatic sea level record: influence of glacial melting rates on the Younger Dryas event and deep-ocean circulation, *Nature*, *342*, 637–642.

Fairbanks, R. G., R. A. Mortlock, T. C. Chiu, L. Cao, A. Kaplan, T. P. Guilderson, T. W. Fairbanks, A. L. Bloom, P. M. Grootes, and M. J. Nadeau (2005), Radiocarbon calibration curve spanning 0 to 50,000 years BP based on paired ^{230}Th/^{234}U/^{238}U and ^{14}C dates on pristine corals, *Quaternary Sci Rev*, *24*, 1781–1796, doi:10.1016/j.quascirev.2005.04.007.

Farrell, W. E., and J. A. Clark (1976), On Postglacial Sea Level, *Geophys J Roy Astr S*, *46*(3), 647–667.

Feller, C., M. Fournier, D. Imbert, C. Caratini, and L. Martin (1990), Datations ^{14}c et Palynologie d'un sediment tourbeux continu (0-7 m) dans la mangrove de Guadeloupe (F.W.I.). Resultats preliminaires, in *Evolution des Littoraux de Guyane et de la Zone Carabe Mridionale Pendant le Quaternaire, ORSTROM, Paris*, pp. 193–202.

Feng, M., Y. Li, and G. Meyers (2004), Multidecadal variations of Fremantle sea level: Footprint of climate variability in the tropical Pacific, *Geophys Res Lett*, *31*, L16,302, doi:10.1029/2004GL019947.

Fenoglio-Marc, L., C. Dietz, and E. Groten (2004), Vertical Land Motion in the Mediterranean Sea from Altimetry and Tide Gauge Stations, *Mar Geod*, *27*, 683–701, doi:10.1080/01490410490883441.

Feuillet, N., F. Beauducel, and P. Tapponnier (2011), Tectonic context of moderate to large historical earthquakes in the Lesser Antilles and mechanical coupling with volcanoes, *J Geophys Res*, *116*(B10308), doi:10.1029/2011JB008443.

Field, C. B., L. D. Mortsch, M. Brklacich, D. L. Forbes, P. Kovacs, J. A. Patz, S. W. Running, and M. Scott (2007), 2007: North America, in *Climate Change 2007: Impacts, Adaptation and Vulnerability. Contribution of Working Group II to the Fourth Assessment Report of the Intergovernmental Panel on Climate Change*, edited by M. L. Parry, O. F. Canziani, J. P. Palutikof, P. J. van der Linden, and C. E. Hanson, pp. 617–652, Cambridge University Press, Cambridge, UK.

Forster, P., V. Ramaswamy, P. Artaxo, T. Berntsen, R. Betts, D. W. Fahey, J. Haywood, J. Lean, D. C. Lowe, G. Myhre, J. Nganga, R. Prinn, G. Raga, M. Schulz, and R. V. Dorland (2007), 2007: Changes in Atmospheric Constituents and in Radiative Forcing, in *IPCC, 2007: Climate Change 2007: The Physical Science Basis. Contribution of Working Group I to the Fourth Assessment Report of the Intergovernmental Panel on Climate Change*, edited by S. Solomon, D. Qin, M. Manning, Z. Chen, M. Marquis, K. B. Averyt, M. Tignor, and H. L. Miller, Cambridge University Press, Cambridge, United Kingdom and New York, NY, USA.

Fu, Y., and J. T. Freymueller (2012), Seasonal and long-term vertical deformation in the Nepal Himalaya constrained by GPS and GRACE measurements., *J Geophys Res*, *117*, B03,407, doi:10.1029/2011JB008925.

García, D., I. Vigo, B. F. Chao, and M. C. Martínez (2007), Vertical crustal motion along the Mediterranean and Black Sea coast derived from ocean altimetry and tide gauge data, *Pure Appl Geophys*, *164*, 851–863, doi:10.1007/s00024-007-0193-8.

Gaspar, P., and R. M. Ponte (1997), Relation between sea level and barometric pressure determined from altimeter data and model simulations, *J Geophys Res*, *102*(C1), 961–971.

Gehrels, W. R., and P. L. Woodworth (2013), When did modern rates of sea-level rise start?, *Global Planet Change*, *100*, 263–277, doi:10.1016/j.gloplacha.2012.10.020.

Gischler, E. (2003), Holocene lagoonal development in the isolated carbonate platforms off Belize, *Sediment Geol*, *159*, 113–132, doi:10.1016/S0037-0738(03)00098-8.

Gischler, E. (2006), Comment on "Corrected western Atlantic sea-level curve for the last 11,000 years based on calibrated 14C dates from Acropora palmata framework and intertidal mangrove peat" by Toscano and Macintyre. Coral Reefs 22:257-270 (2003), and their response in Coral Reefs 24:187-190 (2005), *Coral Reefs*, *25*, 273–279, doi:10.1007/s00338-006-0101-1.

Gischler, E., and J. H. Hudson (1998), Holocene development of three isolated carbonate platforms, Belize, Central America, *Mar Geol*, *144*, 333–347.

Gischler, E., and J. H. Hudson (2004), Holocene development of the Belize Barrier Reef, *Sediment Geol*, *164*, 223–236, doi:10.1016/j.sedgeo.2003.10.006.

Gischler, E., and A. J. Lomando (2000), Isolated carbonate platforms of Belize, Central America: sedimentary facies, late Quaternary history and controlling factors, in *Carbonate Platform Systems: component sand interactions*, vol. 178, edited by E. Insalaco, P. W. Skelton, and T. J. Palmer, pp. 135–146, Geological Society, London, Special Publications.

González, O., L. Alvarez, M. Guidarelli, and G. F. Panza (2007), Crust and Upper Mantle Structure in the Caribbean Region by Group Velocity Tomography and Regionalization, *Pure Appl Geophys*, *164*, 1985–2007, doi:10.1007/s00024-007-0259-7.

Goreau, T. F., and N. I. Goreau (1973), The ecology of Jamaican Coral Reefs. II Geomorphology, zonation and sedimentary phases, *Bull Mar Sci*, *23*, 399–464.

Granger, O. E. (1985), Caribbean climates, *Prog Phys Geog*, *9*, 16–43.

Gregory, J. M., P. Huybrechts, and S. C. B. Raper (2004), Threatened loss of the Greenland ice-sheet, *Nature*, *428*, 616, doi:10.1038/428616a.

Guilderson, T. P., J. E. Cole, and J. R. Southon (2005), Pre-bomb ^{14}c variability and the Seuss effect in Cariaco Basin surface waters as recorded in hermatypic corals, *Radiocarbon*, *47(1)*, 57–65.

Halley, R. B., E. A. Shinn, J. H. Hudson, and B. Lidz (1977), Recent and relict topography of Boo Bee Patch Reef, Belize, in *Proceedings of the Third International Coral Reef Symposium, Florida*, vol. 2, edited by D. L. Taylor, pp. 29–35.

Haskell, N. A. (1935), The motion of a fluid under a surface load, 1, *Physics*, *6*, 265–269.

Heflin, M. (September 2013), http://sideshow.jpl.nasa.gov/mbh/series.html.

Hill, D. F., S. D. Griffiths, W. R. Peltier, B. P. Horton, and T. E. Törnqvist (2011), High-resolution numerical modeling of tides in the western Atlantic, Gulf of Mexico, and Caribbean Sea during the Holocene, *J Geophys Res*, *116*, C10,014, doi:10.1029/2010JC006896.

Holgate, S. J., and P. L. Woodworth (2004), Evidence for enhanced coastal sea level rise during the 1990s, *Geophys Res Lett*, *31*(L07305), doi:10.1029/2004GL019626.

Horta-Puga, G., and G. Barba-Santos (1999), Veracruz Reef System, Gulf of Mexico, *Agrra field reports*, INVEMAR, Lab. Biogeoquímica, UBIPRO, ENEP-Iztacala, Universidad Nacional Autónoma de México.

Horton, B. P., W. R. Peltier, S. J. Culver, R. Drummond, S. E. Engelhart, A. C. Kemp, D. Mallinson, E. R. Thieler, S. R. Riggs, D. V. Ames, and K. H. Thomson (2009), Holocene sea-level changes along the North Carolina Coastline and their implications for glacial isostatic adjustment models, *Quat Sci Rev*, *28*, 1725–1736, doi:10.1016/j.quascirev.2009.02.002.

Hubbard, D. K. (2009), Depth and Species-Related Patterns of Holocene Reef Accretion in the Caribbean and Western Atlantic: A Critical Assessment of Existing Models, in *Perspectives in Carbonate Geology: A Tribute to the Career of Robert Nathan Ginsburg*, edited by P. K. Swart, G. P. Eberli, J. A. McKenzie, I. Jarvis, and T. Stevens, John Wiley & Sons, Ltd, Chichester, West Sussex, UK, doi:10.1002/9781444312065.ch1.

Hubbard, D. K., H. Zankl, I. V. Heerden, and I. P. Gill (2005), Holocene Reef Development along the northeastern St. Croix Shelf, Buck Island, U.S. Virgin Islands, *J Sediment Res*, *75*(1), 97–113, doi:10.2110/jsr.2005.009.

Hughen, K. A., M. G. L. Baillie, E. Bard, A. Bayliss, J. W. Beck, C. J. H. Bertrand, P. G. Blackwell, C. E. Buck, G. S. Burr, K. B. Cutler, P. E. Damon, R. L. Edwards, R. G. Fairbanks, M. Friedrich, T. P. Guilderson, B. Kromer, G. McCormac, S. Manning, C. B. Ramsey, P. J. Reimer, R. W. Reimer, S. Remmele, J. R. Southon, M. Stuiver, S. Talamo, F. W. Taylor, J. van der Plicht, and C. E. Weyhenmeyer (2004), MARINE04 Marine radiocarbon age calibration, 26 - 0 ka BP, *Radiocarbon*, *46*, 1059–1086.

Huston, M. (1985), Variation in coral growth rates with depth at Discovery Bay, Jamaica, *Coral Reefs*, *4*, 19–25.

Jevrejeva, S., A. Grinsted, J. C. Moore, and S. Holgate (2006), Nonlinear trends and multiyear cycles in sea level records, *J Geophys Res*, *111*(C09012), doi:10.1029/2005JC003229.

Jevrejeva, S., J. C. Moore, A. Grinsted, and P. L. Woodworth (2008), Recent global sea level acceleration started over 200 years ago?, *Geophys Res Lett*, *35*(L08715), doi:10.1029/2008GL033611.

Johnson, G. C., and S. G. Purkey (2009), Deep Caribbean Sea warming, *Deep-Sea Res I*, *56*, 827–834, doi:10.1016/j.dsr.2008.12.011.

Johnston, P. (1993), The effect of spatially nonuniform water loads on prediction of sea-level change, *Geophys J Int*, *114*(3), 615–634.

Jury, M., B. Malmgren, and A. Winter (2007), Subregional precipitation climate of the Caribbean and relationships with ENSO and NAO, *J Geophys Res*, *112*(D16107), doi:10.1029/2006JD007541.

Jury, M. R., and B. A. Malmgren (2012), Joint modes of climate variability across the inter-Americas, *Int J Climatol*, *32*, 1033–1046, doi:10.1002/joc.2324.

Kalnay, E., M. Kanamitsu, R. Kistler, W. Collins, D. Deaven, L. Gandin, M. Iredell, S. Saha, G. White, J. Woollen, Y. Zhu, M. Chelliah, W. Ebisuzaki, W. Higgins, J. Janowiak, K. C. Mo, C. Ropelewski, J. Wang, A. Leetmaa, R. Reynolds, R. Jenne, and D. Joseph (1996), The NCEP/NCAR 40-Year Reanalysis Project, *B Am Meteorol Soc*, *77*, 437–471.

Keith, M. L., G. M. Anderson, and R. Eichler (1964), Carbon and oxygen isotope composition of mollusk shells from marine and fresh-water environments, *Geochim Cosmoshim Ac*, *28*, 1757–1786.

Kendall, R. A., J. X. Mitrovica, and G. A. Milne (2005), On post-glacial sea level - II. Numerical formulation and comparative results on spherically symmetric models, *Geophys J Int*, *161*, 679–706, doi:10.1111/j.1365-246X.2005.02553.x.

Kilbourne, K. H., T. Quinn, T. P. Guilderson, R. S. Webb, and F. W. Taylor (2007), Decadal to interannual-scale source water variations in the Caribbean Sea recorded by Puerto Rican coral radiocarbon, *Clim Dynam*, *29*, 51–62.

Kjerfve, B. (1981), Tides of the Caribbean Sea, *J Geophys Res-Oc Atm*, *86*(C5), 4243–4247.

Klosowska, B. (2003), Late Holocene embayment and salina record of Curacao (Dutch Antilles): criteria to monitor environmental change and biodiversity, Ph.D. thesis, Vrije Universiteit, Amsterdam, The Netherlands.

Kogan, M. G., and G. M. Steblov (2008), Current global plate kinematics from GPS (1995-2007) with the plate-consistent reference frame, *J Geophys Res*, *113*, B04,416, doi:10.1029/2007JB005353.

Kuo, C. Y., C. K. Shum, A. Braun, and J. X. Mitrovica (2004), Vertical crustal motion determined by satellite altimetry and tide gauge data in Fennoscandia, *Geophys Res Lett*, *31*(L01608), doi:10.1029/2003GL019106.

Kuo, C. Y., C. K. Shum, A. Braun, K. C. Cheng, and Y. Yi (2008), Vertical Motion Determined Using Satellite Altimetry and Tide Gauges, *Terr Atmos Ocean Sci*, *19*(1-2), 21–35, doi:10.3319/TAO.2008.19.1-2.21(SA).

Lachassagne, P., V. Léonardi, B. Vittecoq, and A. Henriot (2011), Interpretation of the piezometric fluctuations and precursors associated with the November 29, 2007, magnitude 7.4 earthquake in Martinique (Lesser Antilles), *C R Geosci*, *343*, 760–776, doi:10.1016/j.crte.2011.09.002.

Lambeck, K., and J. Chappell (2001), Sea Level Cange Through the Last Glacial Cycle, *Science*, *292*, 679–685, doi:10.1126/science.1059549.

Lambeck, K., M. Anzidei, F. Antonioli, A. Benini, and A. Esposito (2004), Sea level in Roman time in the Central Mediterranean and implications for recent change, *Earth Planet Sc Lett*, *224*, 563–575, doi:10.1016/j.epsl.2004.05.031.

Lambeck, K., C. D. Woodroffe, F. Antonioli, M. Anzidei, W. R. Gehrels, J. Laborel, and A. J. Wright (2010), Paleoenvironmental Records, Geophysical Modelling, and Reconstruction of Sea-Level Trends and Variability on Centenial and Longer Timescales, in *Understanding Sea-Level Rise and Variability*, edited by J. Church, P. Woodworth, T. Aarup, and W. Wilson, pp. 61–121, Wiley-Blackwell.

Lemke, P., J. Ren, R. B. Alley, I. Allison, J. Carrasco, G. Flato, Y. Fujii, G. Kaser, P. Mote, R. H. Thomas, and T. Zhang (2007), 2007: Changes in Snow, Ice and Frozen Ground, in *IPCC, 2007: Climate Change 2007: The Physical Science Basis. Contribution of Working Group I to the Fourth Assessment Report of the Intergovernmental Panel on Climate Change*, edited by S. Solomon, D. Qin, M. Manning, Z. Chen, M. Marquis, K. B. Averyt, M. Tignor, and H. L. Miller, Cambridge University Press, Cambridge, United Kingdom and New York, NY, USA.

Leuliette, E. W., R. S. Nerem, and G. T. Mitchum (2004), Calibration of TOPEX/Poseidon and Jason Altimeter Data to Construct a Continuous Record of Mean Sea Level Change, *Mar Geod*, *22*, 79–94, doi:10.1080/01490410490465193.

Lighty, R. G., I. G. Macintyre, and R. Stuckenrath (1978), Submerged early Holocene barrier reef south-east Florida shelf, *Nature*, *276*, 59–60.

Lighty, R. G., I. G. Macintyre, and R. Stuckenrath (1982), Acropora Palmata Reef Framework: A Reliable Indicator of Sea Level in the Western Atlantic for the Past 10,000 Years, *Coral Reefs*, *1*, 125–130.

Machin, D., M. J. Campbell, and S. J. Walters (2010), *Medical statistics: a textbook for the health sciences*, fourth ed., 346 pp., John Wiley & Sons Inc.

Macintyre, I. G., and W. H. Adey (1990), Buck Island Bar, St. Croix, USVI: A reef that cannot catch up with sea level, *Atol Res Bull*, *336*.

Macintyre, I. G., and P. W. Glynn (1976), Evolution of Modern Caribbean Fringing Reef, Galeta Point, Panama, *Am Assoc Petrol Geol Bull*, *60*, 1054–1072.

Macintyre, I. G., R. B. Burke, and R. Stuckenrath (1977), Thickest recorded Holocene reef section, Isla Pérez core hole, Alacran Reef, Mexico, *Geology*, *5*, 749–754.

Macintyre, I. G., B. Raymond, and R. Stuckenrath (1982), Recent History of a Fringing Reef, Bahia Salina Del Sur, Vieques Island, Puerto Rico, *Atol Res Bull*, *268*.

Macintyre, I. G., H. G. Multer, H. L. Zankl, D. K. Hubbard, M. P. Weiss, and R. Stukenrath (1985), Growth and depositional facies of a windward reef complex (Nonesuch Bay, Antigua, W.I., in *Proc 5th Int Coral Reef Congr Tahiti*, vol. 6, pp. 605–610.

Macintyre, I. G., M. M. Littler, and D. S. Littler (1995), Holocene history of Tobacco Range, Belize, Central America, *Atol Res Bull*, *430*.

Macintyre, I. G., R. P. Reid, and R. S. Steneck (1996), Growth History of Stromatolites in a Holocene Fringing Reef, Stocking Island, Bahamas, *J Sediment Res*, *66*(1), 231–242.

Macintyre, I. G., M. A. Toscano, R. G. Lighty, and G. B. Bond (2004), Holocene history of the mangrove islands of Twin Cays, Belize, Central America., *Atol Res Bull*, *510*.

Macintyre, I. G., M. A. Toscano, and J. Lundberg (2008), Complex environemental patterns and Holocene sea-level changes controlling reef histories along Northeastern St. Croix, USVI, *Atol Res Bull*, *556*.

Magrin, G., C. G. García, D. C. Choque, J. C. Giménez, A. R. Moreno, G. J. Nagy, C. Nobre, and A. Villamizar (2007), 2007: Latin America, in *Climate Change 2007: Impacts, Adaptation and Vulnerability. Contribution of Working Group II to the Fourth Assessment Report of the Intergovernmental Panel on Climate Change*, edited by M. L. Parry, O. F. Canziani, J. P. Palutikof, P. J. van der Linden, and C. E. Hanson, pp. 581–615, Cambridge University Press, Cambridge, UK.

Mann, P., F. W. Taylor, K. Burke, and R. Kulstad (1984), Subaerially exposed Holocene coral reef, Enriquillo Valley, Dominican Republic, *Geol Soc Am Bull*, *95*, 1084–1092.

Mann, P., C. Schubert, and K. Burke (1990), Review of Caribbean neotectonics, in *The Caribbean Region*, vol. H, The Geology of North America, edited by G. Dengo and J. E. Case, chap. 11, pp. 307–338, The Geological Society of North America.

Mann, P., E. Calais, J.-C. Ruegg, C. DeMets, P. E. Jansma, and G. S. Mattioli (2002), Oblique collision in the northeastern Caribbean from GPS measurements and geological observations, *Tectonics*, *21 (6)*, doi:10.1029/2001TC001304.

Mao, A., C. G. A. Harrison, and T. H. Dixon (1999), Noise in GPS coordinate time series, *J Geophys Res*, *104*, 2797–2816.

Martínez, J. I., Y. Yokoyama, A. Gomez, A. Delgado, H. Matsuzaki, and E. Rendon (2010), Late Holocene marine terraces of the Cartagena region, southern Caribbean: The product of neotectonism or a former high stand in sea-level?, *J S Am Earth Sci*, *29*, 214–224, doi:10.1016/j.jsames.2009.08.010.

Mason, R. O., D. A. Lind, and W. G. Marchal (1983), *Statistics: An Introduction*, 368–383 pp., New York: Harcourt Brace Jovanovich, Inc.

Mazzotti, S., C. Jones, and R. E. Thomson (2008), Relative and absolute sea level rise in western Canada and northwestern United States from a combined tide gauge-GPS analysis, *J Geophys Res*, *113*(C11019), doi:10.1029/2008JC004835.

McCann, W. R., and W. D. Pennington (1990), Seismicity, large earthquakes, and the margin of the Caribbean Plate, in *The Caribbean Region*, vol. H, The Geology of North America, edited by G. Dengo and J. E. Case, chap. 11, pp. 291–306, The Geological Society of North America.

Meehl, G. A., T. F. Stocker, W. D. Collins, P. Friedlingstein, A. T. Gaye, J. M. Gregory, A. Kitoh, R. Knutti, J. M. Murphy, A. Noda, S. C. B. Raper, I. G. Watterson, A. J. Weaver, and Z.-C. Zhao (2007), 2007: Global Climate Projections, in *IPCC, 2007: Climate Change 2007: The Physical Science Basis. Contribution of Working Group I to the Fourth Assessment Report of the Intergovernmental Panel on Climate Change*, edited by S. Solomon, D. Qin, M. Manning, Z. Chen, M. Marquis, K. B. Averyt, M. Tignor, and H. L. Miller, Cambridge University Press, Cambridge, United Kingdom and New York, NY, USA.

Miall, A. D. (1990), *Principles of Sedimentary Basin Analysis*, 2nd ed., Springer-Verlag, New York.

Miller, K. M. (2005), Variations in sea level on the West Trinidad coast, *Mar Geod*, *28*, 219–229, doi:10.1080/01490410500204561.

Miller, M. S., A. Levander, F. Niu, and A. Li (2009), Upper mantle structure beneath the Caribbean-South American plate boundary from surface wave tomography, *J Geophys Res*, *114*, B01,312, doi:10.1029/2007JB005507.

Milliken, K. T., J. B. Anderson, and A. B. Rodriguez (2008), A new composite Holocene sea-level curve for the northern Gulf of Mexico, in *Response of Upper Gulf Coast Estuaries to Holocene Climate Change and Sea-Level Rise: Geological Society of America Special Paper 443*, edited by J. B. Anderson and A. B. Rodriguez, pp. 1–11, The Geological Society of America, doi:10.1130/2008.2443(01).

Milne, G. A., and J. X. Mitrovica (1998a), The influence of time-dependant ocean-continent geometry on predictions of post-glacial sea level change in Australia and New Zealand, *Geophys Res Lett*, *25 (6)*, 793–796.

Milne, G. A., and J. X. Mitrovica (1998b), Postglacial sea-level change on a rotating Earth, *Geophys J Int*, *133*, 1–19.

Milne, G. A., and J. X. Mitrovica (2008), Searching for eustacy in deglacial sea-level histories, *Quat Sci Rev*, *27*, 2292–2302, doi:10.1016/j.quascirev.2008.08.018.

Milne, G. A., A. J. Long, and S. E. Bassett (2005), Modelling Holocene relative sea-level observations from the Caribbean and South America, *Quaternary Sci Rev*, *24*, 1183–1202, doi:10.1016/j.quascirev.2004.10.005.

Milne, G. A., W. R. Gehrels, C. W. Hughes, and M. E. Tamisiea (2009), Identifying the causes of sea-level change, *Nat Geosci*, *2*(7), 471–478, doi:10.1038/ngeo544.

Mimura, N., L. Nurse, R. F. McLean, J. Agard, L. Briguglio, P. Lefale, R. Payet, and G. Sem (2007), 2007: Small islands, in *Climate Change 2007: Impacts, Adaptation and Vulnerability. Contribution of Working Group II to the Fourth Assessment Report of the Intergovernmental Panel on Climate Change*, edited by M. L. Parry, O. F. Canziani, J. P. Palutikof, P. J. van der Linden, and C. E. Hanson, pp. 687–716, Cambridge University Press, Cambridge, UK.

Mitchum, G. T., R. S. Nerem, M. A. Merrifield, and W. R. Gehrels (2010), Modern Sea-Level-Change Estimates, in *Understanding Sea-Level Rise and Variability*, edited by J. Church, P. Woodworth, T. Aarup, and W. Wilson, pp. 122–142, Wiley-Blackwell.

Mitrovica, J. X. (1996), Haskell [1935] revisited, *J Geophys Res*, *101*(B1), 555–569.

Mitrovica, J. X., and A. M. Forte (1997), Radial profile of mantle viscosity: Results from the joint inversion of convection and postglacial rebound observables, *J Geophys Res*, *102(B2)*, 2751–2769, doi:10.1029/96JB03175.

Mitrovica, J. X., and A. M. Forte (2004), A new inference of mantle viscosity based upon joint inversion of convection and glacial isostatic adjustment data, *Earth Planet Sc Lett*, *225*, 177–189, doi:10.1016/j.epsl.2004.06.005.

Mitrovica, J. X., and G. A. Milne (2002), On the origin of late holocene sea-level highstands within equatorial ocean basins, *Quaternary Sci Rev*, *21*, 2179–2190.

Mitrovica, J. X., and G. A. Milne (2003), On post-glacial sea level: I. General Theory, *Geophys J Int*, *154*(2), 253–267.

Mitrovica, J. X., and W. R. Peltier (1991), On Postglacial Geoid Subsidence over the Equatorial Oceans, *J Geophys Res*, *96*(B12), 20,053–20,071.

Mitrovica, J. X., M. E. Tamisiea, J. L. Davis, and G. A. Milne (2001a), Recent mass balance of polar ice sheets inferred from patterns of global sea-level change, *Nature*, *409*, 1026–1029.

Mitrovica, J. X., G. A. Milne, and J. L. Davis (2001b), Glacial isostatic adjustment on a rotating earth, *Geophys J Int*, *147*, 562–578.

Mitrovica, J. X., M. E. Tamisiea, E. R. Ivins, L. L. A. Vermeersen, G. A. Milne, and K. Lambeck (2010), Surface Mass Loading on a Dynamic Earth: Complexity and Contamination in the Geodetic Analysis of Global Sea-Level Trends, in *Understanding Sea-Level Rise and Variability*, edited by J. Church, P. Woodworth, T. Aarup, and W. Wilson, pp. 285–325, Wiley-Blackwell.

Mitrovica, J. X., N. Gomez, E. Morrow, C. Hay, K. Latychec, and M. E. Tamisiea (2011), On the robustness of predictions of sea level fingerprints, *Geophys J Int*, *187*, 729–742.

Mooers, C. N. K., and G. A. Maul (1998), Intra-Americas sea circulation, coastal segment(3,w), in *The Sea*, edited by A. Robinson and K. H. Brink, pp. 183–208, John Wiley and Sons.

Mullins, H. T., and A. C. Neumann (1979), Geology of the Miami Terrace and its paleogeographic implications, *Mar Geol*, *30*, 205–232.

Nerem, R. S., and G. T. Mitchum (2002), Estimates of vertical crustal motion derived from differences of TOPEX/POSEIDON and tide gauge sea level measurements, *Geophys Res Lett*, *29 (19)*(1934), doi:10.1029/2002GL015037.

Nerem, R. S., D. P. Chambers, C. Choe, and G. T. Mitchum (2010), Estimating Mean Sea Level Change from the TOPEX and Jason Altimeter Missions, *Mar Geod*, *33(S1)*, 435–446, doi:10.1080/01490419.2010.491031.

noz, E. M., A. J. Busalacchi, S. Nigam, and A. Ruiz-Barradas (2008), Winter and Summer Structure of the Caribbean Low-Level Jet, *J Climate*, *21*(1260–1276), doi:10.1175/2007JCLI1855.1.

Ostanciaux, E., L. Husson, G. Choblet, C. Robin, and K. Pedoja (2012), Present-day trends of vertical ground motion along the coast lines, *Earth-Sci Rev*, *110*, 74–92, doi:10.1016/j.earscirev.2011.10.004.

Otto-Bliesner, B. L., S. J. Marshal, J. T. Overpeck, G. H. Miller, A. Hu, and C. L. I. P. Members (2006), Simulating Arctic Climate Warmth and Icefield Retreat in the Last Interglaciation, *Science*, *311*, 1751–1753, doi:10.1126/science.1120808.

Palanisamy, H., M. Becker, B. Meyssignac, O. Henry, and A. Cazenave (2012), Regional Sea Level Change and Variability in the Caribbean Sea since 1950, *J Geod Sci*, doi:10.2478/v10156-011-0029-4.

Parry, M. L., O. F. Canziani, J. P. Palutikof, P. J. van der Linden, and C. E. Hanson (Eds.) (2007), *IPCC, 2007: Climate Change 2007: Impacts, Adaptation and Vulnerability. Contribution of Working Group II to the Fourth Assessment Report of the Intergovernmental Panel on Climate Change*, 976 pp., Cambridge University Press, Cambridge, UK.

Paulson, A., S. Zhong, and J. Wahr (2009), Modelling post-glacial rebound with lateral viscosity variations, *Geophys J Int*, *163*, 357–371, doi:10.1111/j.1365-246X.2005.02645.x.

Peltier, W. R. (1974), Impulse Response of a Maxwell Earth, *Rev Geophys*, *12*, 649–669.

Peltier, W. R. (1994), Ice Age Paleotopography, *Science*, *265*(5169), 195–201.

Peltier, W. R. (2004), Global Glacial Isostacy and the Surface of the Ice-age Earth: The ICE-5G (VM2) Model and GRACE, *Annu Rev Earth Pl Sc*, *32*, 111–149, doi:10.1146/annurev.earth.32.082503.144359.

Peltier, W. R., and J. T. Andrews (1976), Glacial-Isostatic Adjustment-I. The Forward Problem, *Geophys J Roy Astr S*, *46*, 605–646.

Peltier, W. R., and R. G. Fairbanks (2006), Global glacial ice volume and Last Glacial Maximum duration from an extended Barbados sea level record, *Quaternary Sci Rev*, *25*, 3322–3337, doi:10.1016/j.quascirev.2006.04.010.

Penland, C., and L. Matrasova (1998), Prediction of Tropical Atlantic Sea Surface Temperatures Using Linear Inverse Modeling, *J Climate*, *11*, 483–496.

Peros, M. C., E. D. Reinhardt, and A. M. Davis (2007), A 6000-year record of ecological and hydrological changes from Laguna de la Leche, north coastal Cuba, *Quaternary Res*, *67*, 69–82, doi:10.1016/j.yqres.2006.08.004.

Pindell, J. L., and L. Kennan (2009), Tectonic Evolution of the Gulf of Mexico, Caribbean and northern South America in the mantle reference frame: an update, in *The Origin and Evolution of the Caribbean Plate*, vol. 328, edited by K. H. James, M. A. Lorentre, and J. L. Pindell, pp. 1–55, Geological Society, London, Special Publications, doi:10.1144/SP328.1.

Pinter, N., and T. W. Gardner (1989), Construction of a polynomial model of glacio-eustatic fluctuation: Estimating paleo-sea levels continuously through time, *Geology*, *17*, 295–298.

Pirazzoli, P. A. (1991), *World Atlas of Holocene Sea-Level Changes*, *Elsevier Oceanography Series*, vol. 58, Elsevier.

Purdy, E. G. (1974), Karst-Determined Facies Patterns in British Honduras: Holocene Carbonate Sedimentation Model, *Am Assoc Petr Geol B*, *58*(5), 825–855.

Ramcharan, E. K. (2004), Mid-to-late Holocene sea level influence on coastal wetland development in Trinidad, *Quatern Int*, *120*, 145–151, doi:10.1016/j.quaint.2004.01.013.

Ramcharan, E. K., and J. H. McAndrews (2006), Holocene Development of Coastal Wetland at Maracas Bay, Trinidad, West Indies, *J Coast Res*, *22 (3)*, 581–586.

Riley, K. F., M. P. Hobson, and S. J. Bence (2006), *Mathematical Methods for Physics and Engineering*, third ed., 1333 pp., Cambridge University Press, Cambridge, UK.

Robbin, D. M. (1984), A new Holocene sea-level curve for the upper Florida Keys and Florida reef tract, in *Environments of south Florida, present and past*, edited by P. J. Gleason, pp. 437–458, Miami Geological Society.

Rogers, C. S., H. C. F. III, M. Gilnack, J. Beets, and J. Hardin (1984), Scleractinian Coral Recruitment Patterns at Salt River Submarine Canyon, St. Croix, U.S. Virgin Islands, *Coral Reefs*, *3*, 69–76.

Rohling, E. J., K. Grant, C. Hemleben, M. Siddal, B. A. A. Hoogakker, M. Bolshaw, and M. Kucera (2008), High rates of sea-level rise during the last interglacial period, *Nature Geosci*, *1*, 38–42, doi:10.1038/ngeo.2007.28.

Rubin, M., and H. E. Suess (1955), U.S. Geological Survey Radiocarbon Dates II, *Science*, *121*(3145), 481–488.

Rull, V., T. Vegas-Vilarrúbia, and N. E. de Pernía (1999), Palynological Record of an Early-Mid Holocene Mangrove in Eastern Venezuela. Implications for Sea-Level Rise and Disturbance history, *J Coastal Res*, *15*(2), 496–504.

Santamaría-Gómez, A., M.-N. Bouin, X. Collilieux, and G. Wöppelmann (2011), Correlated errors in GPS position time series: Implications for velocity estimates, *J Geophys Res*, *116*(B01405), doi:10.1029/2010JB007701.

Santamaría-Gómez, A., M. Gravelle, X. Collilieux, M. Guichard, B. M. Miguez, P. Tiphaneau, and G. Wöppelmann (2012), Mitigating the effects of vertical land motion in tide gauge records using state-of-the-art GPS velocity field, *Global Planet Change*, *98–99*, 6–17, doi:10.1016/j.gloplacha.2012.07.007.

Scholl, D. W., and M. Stuiver (1967), Recent Submergence of Southern Florida: A Comparison with Adjacent Coasts and Other Eustatic Data, *Geol Soc Am Bull*, *78*(4), 437–454.

Sella, G. F., T. H. Dixon, and A. Mao (2002), REVEL:A model for Recent plate velocities from space geodosy, *J Geophys Res*, *107*, B42,081, doi:10.1029/2000JB000033.

Sella, G. F., S. Stein, T. H. Dixon, M. Craymer, T. S. James, S. Mazzotti, and R. K. Dokka (2007), Observation of glacial isostatic adjustment in "stable" North America with GPS, *Geophys Res Lett*, *34*(L02306), doi:10.1029/2006GL027081.

Sheng, J., and L. Tang (2003), A Numerical Study of Circulation in the Western Caribbean Sea, *J Phys Oceanogr*, *33*, 2049–2069.

Shennan, I., G. Milne, and S. Bradley (2012), Late Holocene vertical land motion and relative sea-level changes: lessons from the British Isles, *J Quaternary Sci*, *27(1)*, 64–70, doi:10.1002/jqs.1532.

Shinn, E. A., J. H. Hudson, R. B. Halley, and B. Lidz (1977), Topographic control and accumulation rate of some holocene coral reefs: South Florida and Dry Tortugas, in *Proceedings of the Third International Coral Reef Congress, Miami*, vol. 2, edited by D. L. Taylor, pp. 1–7.

Shinn, E. A., J. H. Hudson, R. B. Halley, B. Lidz, D. M. Robbin, and I. G. Macintyre (1982), Geology and sediment accumulation rates at Carrie Bow Cay, Belize, *Smithsonian Contr Mar Sci*, *12*, 63–75.

Simpson, M. C., D. Scott, M. Harrison, R. Sim, N. Silver, E. O'Keeffe, S. Harrison, M. Taylor, G. Lizcano, M. Rutty, H. Stager, J. Oldham, M. Wilson, M. New, J. Clarke, O. J. Day, N. Fields, J. Georges, R. Waite, and P. McSharry (2010), Quantification and Magnitude of Losses and Damages and Costs of Sea Level Rise in the Caribbean (Full Document), *Tech. rep.*, United Nations Development Programme (UNDP), Barbados, West Indies.

Snay, R., M. Cline, W. Dillinger, R. Foote, S. Hilla, W. Kass, J. Ray, J. Rohde, G. Sella, and T. Soler (2007), Using global positioning system-derived crustal velocities to estimate rates of absulute sea level change from North American tide gauge records, *J Geophys Res*, *112*(B04409), doi:10.1029/2006JB004606.

Solomon, S., D. Qin, M. Manning, Z. Chen, M. Marquis, K. B. Averyt, M. Tignor, and H. L. Miller (Eds.) (2007), *IPCC, 2007: Climate Change 2007: The Physical Science Basis. Contribution of Working Group I to the Fourth Assessment Report of the Intergovernmental Panel on Climate Change*, 996 pp., Cambridge University Press, Cambridge, United Kingdom and New York, NY, USA.

Spada, G., and G. Galassi (2012), New estimates of secular sea level rise from tide gauge data and GIA modelling, *Geophys J Int*, *191 (3)*, 1067–1094, doi:10.1111/j.1365-246X.2012.05663.x.

Spada, G., and P. Stocchi (2007), SELEN: A Fortran 90 program for solving the "sea-level equation", *Comput Geosci*, *33*(4), 538–562, doi:10.1016/j.cageo.2006.08.006.

Stanton, E. A., and F. Ackerman (2007), Florida and Climate Change: The Costs of Inaction, *Tech. rep.*, Tufts University.

Stuiver, M., and T. F. Braziunas (1993), Modeling atmospheric ^{14}c influences and ^{14}c ages of marine samples back to 10,000BC, *Radiocarbon*, *35*, 137–189.

Stuiver, M., and H. A. Polach (1977), Discussion: Reporting of 14c data, *Radiocarbon*, *19*, 355–363.

Stuiver, M., and P. J. Reimer (1993), Extended 14c database and revised CALIB radiocarbon calibration program, *Radiocarbon*, *35*, 215–230.

Stuiver, M., P. J. Reimer, and R. W. Reimer (2005), Calib 5.0.

Sturges, W., and B. C. Douglas (2011), Wind effects on estimates of sea level rise, *J Geophys Res*, *116*(C06008), doi:10.1029/2010JC006492.

Sturges, W., and B. G. Hong (2001), Decadal variability in sea level, in *Sea Level Rise History*, *Int Geophys*, vol. 75, edited by B. C. Douglas, M. S. Kearney, and S. P. Leatherman, pp. 165–180, doi:10.1016/S0074-6142(01)80010-3.

Tamisiea, M. E., J. X. Mitrovica, G. A. Milne, and J. L. Davis (2001), Global geoid and sea level changes due to present-day ice mass fluctuations, *J Geophys Res*, *106 (B12)*, 30,849–30,863.

Taylor, F. W., P. Mann, S. V. (Jr), and K. Burke (1985), Stratigraphy and radiocarbon chronology of a subaerially exposed Holocene coral reef, Dominican Republic, *J Geol*, *93*(3), 311–332.

Taylor, R. (1990), Interpretation of the Correlation Coefficient: A Basic Review, *JDMS*, *1*, 35–39.

Thomas, I. D., M. A. King, M. J. Bentley, P. L. Whitehouse, N. T. Penna, S. D. P. Williams, R. E. M. Riva, D. A. Lavallee, P. J. Clarke, E. C. King, R. C. A. Hindmarsh, and H. Koivula (2011), Widespread low rates of Antartic glacial isostatic adjustment revealed by GPS observations, *Geophys Res Lett*, *38*, L22,302, doi:10.1029/2011GL049277.

Thomson, R. E., and S. Tabata (1982), Baroclinic oscillations of tidal frequency at Ocean Weather Station P, *Atmos Ocean*, *20*, 242–257.

Torres, R. R., and M. N. Tsimplis (2011), Tides and long-term modulations in the Caribbean Sea, *J Geophys Res*, *116*(C10022), doi:10.1029/2011JC006973.

Torres, R. R., and M. N. Tsimplis (2012), Seasonal sea level cycle in the Caribbean Sea, *J Geophys Res*, *117*(C07011), doi:10.1029/2012JC008159.

Toscano, M. A., and J. Lundberg (1998), Early Holocene sea-level record from submerged fossil reefs on the southeast Florida margin, *Geology*, *26*, 255–258.

Toscano, M. A., and I. G. Macintyre (2003), Corrected western Atlantic sea-level curve for the last 11,000 years based on calibrated 14C dates from Acropora palmata framework and intertidal mangrove peat, *Coral Reefs*, *22*, 257–270, doi:10.1007/s00338-003-0315-4.

Toscano, M. A., and I. G. Macintyre (2005), Blanchon P, Comment on Toscano MA and Macintyre IG (2003): Corrected western Atlantic sea-level curve for the last 11,000 years based on calibrated 14C dates from Acropora palmata framework and intertidal mangrove peat. Coral Reefs 22:257-270, *Coral Reefs*, *24*, 187–190, doi:10.1007/s00338-005-0481-7.

Toscano, M. A., and I. G. Macintyre (2006), Reply to Gischler E, Comment on Toscano and Macintyre (2005): corrected western Atlantic sea-level curve for the last 11,000 years based on calibrated 14C dates from Acropora palmata framework and intertidal mangrove peat Coral Reefs 22: 257-270 (2003) and their response in Coral Reefs 24:187–190 (2005), *Coral Reefs*, *25*, 281–286, doi:10.1007/s00338-006-0102-0.

Toscano, M. A., W. R. Peltier, and R. Drummond (2011a), Ice-5g and ICE-6G models of postglacial relative sea-level history applied to the Holocene coral reef record of northeastern St Croix, USVI - investigating the influence of rotational feedback on GIA processes at tropical latitudes, *Quat Sci Rev*, *30*, 3032–3042, doi:10.1016/j.quascirev.2011.07.018.

Tsimplis, M. N., and P. L. Woodworth (1994), The global distribution of the seasonal sea level cycle calculated from coastal tide gauge data, *J Geophys Res*, *99*(C8), 16,031–16,039.

Tushingham, A. M., and W. R. Peltier (1991), ICE-3G: A new global model of late Pleistocene deglaciation based upon geophysical predictions of post-glacial relative sea level change, *J Geophys Res*, *96*(B3), 4497–4523.

van der Wal, W., P. Wu, H. Wang, and M. G. Sideris (2010), Sea levels and uplift rate from composite rheology in glacial isostatic adjustment modelling, *J Geodyn*, *50*, 38–48, doi:10.1016/j.jog.2010.01.006.

Vinogradov, S. V., and R. M. Ponte (2010), Annual cycle in coastal sea level from tide gauges and altimetry, *J Geophys Res*, *115*(C04021), doi:10.1029/2009JC005767.

Wagner, A. J., T. P. Guilderson, N. C. Slowey, and J. E. Cole (2009), Pre-bomb Surface Water Radiocarbon of the Gulf of Mexico and Caribbean as Recorded in Hermatypic Corals, *Radiocarbon*, *51(3)*, 947–954.

Wang, C., and D. B. Enfield (2001), The tropical Western Hemisphere warm pool, *Geophys Res Lett*, *28*(8), 1635–1638.

Wang, C., and S. Lee (2007), Atlantic warm pool, Caribbean low-level jet, and their potential impact on Atlantic hurricanes, *Geophys Res Lett*, *34*(L02703), doi:10.1029/2006GL028579.

Wang, H., T. J. Wright, Y. Yu, H. Lin, L. Jiang, C. Li, and G. Qui (2012), InSAR reveals coastal subsidence in the Pearl River Delta, China, *Geophys J Int*, *191*, 1119–1128, doi:10.1111/j.1365-246X.2012.05687.x.

Wang, Y., and R. Rapp (1994), Estimation of sea surface dynamic topography, ocean tides, and secular changes from Topex altimeter data, *Tech. Rep. 430*, Department of Geodetic Science and Surveying, Ohio State University.

Warne, A. G., E. H. Guevara, and A. Aslan (2002), Late Quaternary Evolution of the Orinoko Delta, Venezuela, *J Coast Res*, *18 (2)*, 225–253.

Weil, E., and N. Knowlton (1994), A multi-character analysis of the Caribbean coral *Montastraea annularis* (ellis and solander, 1786) and its two sibling species, *M. faveolata* (ellis and solander, 1786) and *M. franksi* (gregory, 1895), *B Mar Sci*, *55*(1), 151–175.

Weiss, M. P. (1979), A saline lagoon on Cayo Sal, Western Venezuela, *Atol Res Bull*, *232*.

Whitehouse, P. L., M. J. Bentley, G. A. Milne, M. A. King, and I. D. Thomas (2012), A new glacial isostatic adjustment model for Antarctica: calibrated and tested using observations of relative sea-level change and present-day uplift rates, *Geophys J Int*, *190*, 1464–1482, doi:10.1111/j.1365-246X.2012.05557.x.

Wieczerkowski, K., J. X. Mitrovica, and D. Wolf (1999), A revised relaxation-time spectrum for Fennoscandia, *Geophys J Int*, *139*, 69–86.

Williams, S. D. P. (2003), The effect of colored noise on the uncertainties of rates estimated from geodetic series, *J Geod*, *76*, 483–494, doi:10.1007/s00190-002-0283-4.

Wolter, K., and M. S. Timlin (1998), Measuring the strength of ENSO events: How does 1997/98 rank?, *Weather*, *53*, 315–324.

Woodroffe, C. D. (1981), Mangrove Swamp Stratigraphy and Holocene Transgression, Grand Cayman Island, West Indies, *Mar Geol*, *41*, 271–294.

Woodroffe, C. D. (1990), The impact of sea-level rise on mangrove shorelines, *Prog Phys Geog*, *14*, 483–520, doi:10.1177/030913339001400404.

Woodward, R. S. (1888), On the form and position of mean sea level, *USGS Bull*, *48*, 87–170.

Woodworth, P. L., and R. Player (2003), The permanent service for mean sea level: An update to the 21st century, *J Coastal Res*, *19*, 287–295.

Woodworth, P. L., N. J. White, S. Jevrejeva, S. J. Holgate, J. A. Church, and W. R. Gehrels (2009), Evidence for the accelerations of sea level on multi-decade and century timescales, *Int. J. Climatol.*, *29*, 777–789, doi:10.1002/joc.1771.

Wooler, M. J., H. Behling, B. J. Smallwood, and M. Fogel (2004), Mangrove ecosystem dynamics and elemental cycling at Twin Cays, Belize, during the Holocene, *J Quaternary Sci*, *19(7)*, 703–711, doi:10.1002/jqs.877.

Wooler, M. J., R. Morgan, S. Fowell, H. Behling, and M. Fogel (2007), A multiproxy peat record of Holocene mangrove palaeoecology from Twin Cays, Belize, *The Holocene*, *17(8)*, 1129–1139, doi:10.1177/0959683607082553.

Wooler, M. J., H. Behling, J. L. Guerrero, N. Jantz, and M. E. Zweigert (2009), Late Holocene hydrological and vegetation changes at Turneffe Atoll, Belize, comared with records from mainland Central Americal and Mexico, *PALAIOS*, *24*, 650–656, doi:10.2110/palo.2009.p09-036r.

Wöppelmann, G., B. M. Miguez, M. N. Bouin, and Z. Altamimi (2007), Geocentric sea-level trend estimates from GPS analyses at relevant tide gauges world-wide, *Global Planet Change*, *57*(3-4), 396–406, doi:10.1016/j.gloplacha.2007.02.002.

Wöppelmann, G., C. Letetrel, A. Santamaría, M.-N. Bouin, X. Collilieux, Z. Altamimi, S. D. P. Williams, and B. M. Miguez (2009), Rates of sea-level change over the past century in a geocentric reference frame, *Geophys Res Lett*, *36*(L12607), doi:10.1029/2009GL038720.

Wu, P., and W. R. Peltier (1983), Glacial isostatic adjustment and the free air gravity anomaly as a constraint on deep mantle viscosity, *Geophys J Roy Astr S*, *74*, 377–449.

Zhang, J., Y. Bock, H. Johnson, P. Fang, S. Williams, J. Genrich, S. Wdowinsky, and J. Behr (1997), Southern California permanent GPS geodetic array: Error analysis pf daily position estimated and site velocity, *J Geophys Res*, *102*, 18,035–18,055, doi:10.1029/97JB01380.

Zhang, X., and J. A. Church (2012), Sea level trends, interannual and decadal variability in the Pacific Ocean, *Geophys Res Lett*, *39*(L21701), doi:10.1029/2012GL053240.

Appendix A

Sea-level indicators, habitable ranges and RSL curves

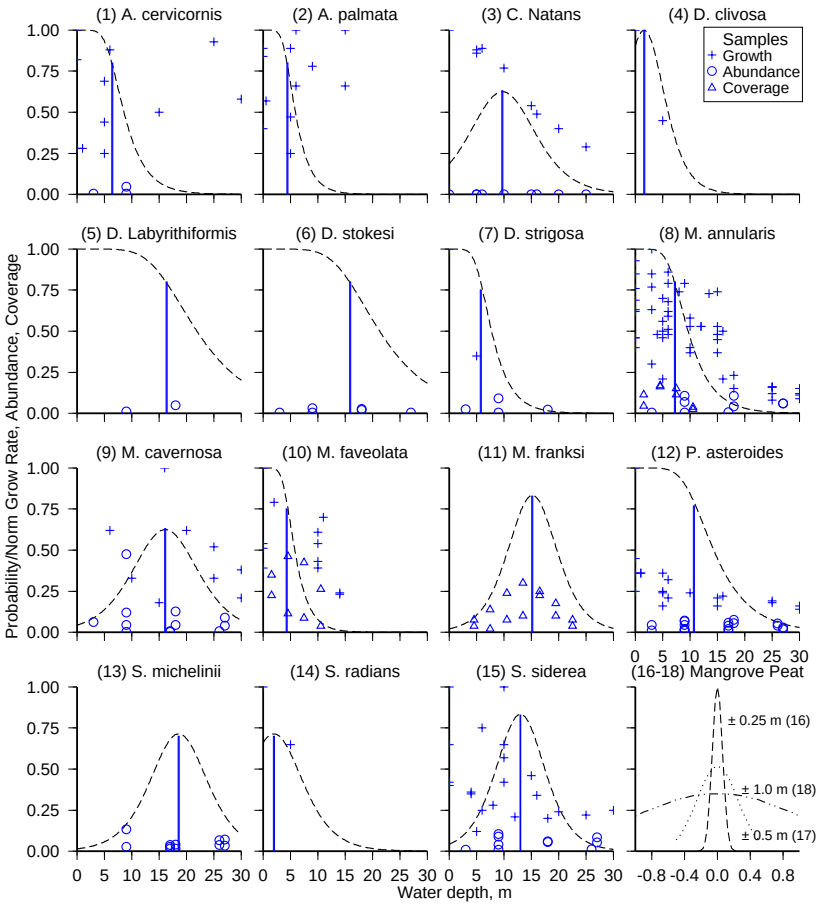

Figure A-1: Probability depth distributions of corals (1-15) and peats (16-18). Symbols show the recorded growth, abundance and coverage coral samples, discussed in text. Probability distributions based upon: Tanh (1,2,5,6,7,8,10,12), logistical (3,4,9,11,13,14,15) and Gaussian (16-18). Mangrove peat distributions discussed in text.

Table A-1: List of sea-level indicators used in this study. The following are listed: location by region (from text), site location, longitude, latitude, material (follow labelling in Figure A-1), limiting factor (terrestrial, 1; intertidal, 0; marine, -1), elevation in metres relative to present mean sea level, ^{14}C age, $\delta^{13}C$ fraction, Calibrated age range and median age, U/Th age and Source which first published the data presented.

Region	Site	Longitude	Latitude	Material	Sea level limit	Elevation RMSL, m	14C age, years BP (1950) ± Error		δ13C	2σ Calibrated age, years BP			U/Th age ± error, years BP		Source
										Lower	Upper	Median			
	Florida														
1a	Shelf Edge Reef	279.94	26.25	2	(-1)	-17.5	7145	80	0	7810	8190	8001			Lighty et al., (1978)
1a	Shelf Edge Reef	279.94	26.25	2	(-1)	-20.5	7595	70	0	8290	8640	8453			Lighty et al., (1978)
1a	Shelf Edge Reef	279.94	26.25	2	(-1)	-16.5	7840	65	0	8550	8980	8762			Lighty et al., (1978)
1a	Shelf Edge Reef	279.94	26.25	2	(-1)	-26.5	9440	85	0	10530	11060	10746			Lighty et al., (1978)
1a	Shelf Edge Reef	279.94	26.25	2	(-1)	-17.5	7740	65	0	8410	8880	8620			Lighty et al., (1978)
1a	Shelf Edge Reef	279.94	26.25	2	(-1)	-18	8295	90	0	9090	9530	9344			Lighty et al., (1978)
1a	Shelf Edge Reef	279.94	26.25	2	(-1)	-24.5	8900	95	0	9770	10380	10105			Lighty et al., (1978)
1a	Shelf Edge Reef	279.94	26.25	2	(-1)	-23	7295	70	0	7980	8320	8150			Lighty et al., (1978)
1a	Shelf Edge Reef	279.94	26.25	2	(-1)	-27	8405	80	0	9250	9670	9462			Lighty et al., (1978)
1a	Bal Harbour	279.93	25.9	14	(-1)	-16.1	6300	120	0	6920	7450	7209			Shinn et al., (1977)
1a	Sewer Trench	279.85	25.74	9	(-1)	-9.8	4930	70	0	5540	5890	5692			Shinn et al., (1977)
1a	Long Reef	279.87	25.5	8	(-1)	-8.3	5630	120	0	6190	6730	6450			Shinn et al., (1977)
1a	Caysfort Reef	279.79	25.22	8	(-1)	-5.8	4570	85	0	5030	5550	5297			Shinn et al., (1977)
1a	Caysfort Reef	279.79	25.22	8	(-1)	-9.1	5250	95	0	5820	6280	6047			Shinn et al., (1977)
1a	Marker G	278.66	24.55	8	(-1)	-12.1	6170	80	0	6850	7270	7072			Shinn et al., (1977)
1a	Marker G	278.66	24.55	8	(-1)	-13.6	7160	85	0	7810	8220	8017			Shinn et al., (1977)
1a	Marker G	278.66	24.55	3	(-1)	-11.1	4735	85	0	5280	5680	5481			Shinn et al., (1977)
1a	Tortugas SE Reef	277.12	24.61	8	(-1)	-5.2	3585	80	0	3720	4230	3981			Shinn et al., (1977)
1a	Tortugas SE Reef	277.12	24.61	8	(-1)	-9.4	4762	85	0	5300	5700	5508			Shinn et al., (1977)
1a	Tortugas SE Reef	277.12	24.61	8	(-1)	-13.4	5883	224	0	6260	7250	6740			Shinn et al., (1977)
1a	Tortugas SE Reef	277.12	24.61	8	(-1)	-14	6017	90	0	6660	7140	6893			Shinn et al., (1977)
1a	Pulaski Reef	277.23	24.69	8	(-1)	-11.3	5865	90	0	6460	6950	6710			Shinn et al., (1977)
1a	Pulaski Reef	277.23	24.69	8	(-1)	-13.4	6585	115	0	7250	7690	7475			Shinn et al., (1977)
1a	Pulaski Reef	277.23	24.69	7	(-1)	-14.9	7165	90	0	7820	8250	8023			Shinn et al., (1977)
1a	Whitewater Bay	278.97	25.3	16	(1)	-1.86	4000	125	-27	3610	4330	3951			Scholl & Stuiver (1967)
1a	Whitewater Bay	278.99	25.25	16	(1)	-1.92	3930	265	-27	3200	4590	3873			Scholl & Stuiver (1967)
1a	S. of Flamingo	279.1	25.1	16	(1)	-1.7	3650	125	-27	3190	3850	3509			Scholl & Stuiver (1967)
1a	Ten Thousand Is.	278.6	25.82	16	(0)	-1.49	3344	245	-27	2510	3750	3132			Scholl & Stuiver (1967)
1a	Long Sound	279.51	25.21	16	(1)	-0.91	3408	271	-27	2530	3900	3210			Scholl & Stuiver (1967)
1a	Whitewater Bay	278.99	25.25	16	(0)	-1.46	2985	169	-27	2280	3160	2691			Scholl & Stuiver (1967)
1a	Whitewater Bay	279.05	25.3	16	(0)	-1.19	2894	273	-27	1910	3260	2580			Scholl & Stuiver (1967)
1a	Harney River	278.83	25.42	16	(0)	-3.82	4420	200	-27	3930	5040	4514			Scholl & Stuiver (1967)
1a	South Shark River	278.84	25.28	16	(1)	-2.36	4210	80	-27	3970	4480	4235			Scholl & Stuiver (1967)
1a	Sand Key Outlier Reef	278.13	24.43	2	(-1)	-9.3							6900	170	Toscano & Lundberg (1998)
1a	Sand Key Outlier Reef	278.13	24.43	2	(-1)	-9.6							6700	130	Toscano & Lundberg (1998)
1a	Sand Key Outlier Reef	278.13	24.43	3	(-1)	-12.4							8900	930	Toscano & Lundberg (1998)
1a	Sand Key Outlier Reef	278.13	24.43	2	(-1)	-11.5							8000	90	Toscano & Lundberg (1998)
1a	Sand Key Outlier Reef	278.13	24.43	2	(-1)	-11.3							8200	100	Ludwig et al., (1996)
1a	Sand Key Shelf Edge	278.13	24.43	8	(-1)	-10.1							7700	680	Toscano & Lundberg (1998)
1a	Sand Key Shelf Edge	278.13	24.43	3	(-1)	-15.4							8600	130	Toscano & Lundberg (1998)
1a	Carysfort Outlier Reef	279.79	25.22	2	(-1)	-9.7							7000	190	Toscano & Lundberg (1998)
1a	Carysfort Outlier Reef	279.79	25.22	3	(-1)	-10.5							7500	150	Toscano & Lundberg (1998)
1a	Carysfort Outlier Reef	279.79	25.22	8	(-1)	-11.9							7300	350	Toscano & Lundberg (1998)
1a	Carysfort Outlier Reef	279.79	25.22	8	(-1)	-9.2							5000	170	Toscano & Lundberg (1998)
1a	Carysfort Outlier Reef	279.79	25.22	8	(-1)	-15.2							7100	140	Toscano & Lundberg (1998)
1a	Carysfort Outlier Reef	279.79	25.22	3	(-1)	-12.5							7500	210	Toscano & Lundberg (1998)
1a	Carysfort Outlier Reef	279.79	25.22	8	(-1)	-13.5							7400	80	Toscano & Lundberg (1998)
1a	Carysfort Outlier Reef	279.79	25.22	8	(-1)	-15.3							6100	80	Toscano & Lundberg (1998)
1a	Carysfort Outlier Reef	279.79	25.22	8	(-1)	-20							6600	150	Toscano & Lundberg (1998)
1a	Crane Key	279.38	25.01	18	(0)	-2	3300	240	-27	2470	3670	3081			Rubin & Suess (1955)
1a	Upper Florida Keys	279.92	26.26	2	(-1)	-7.8	5950	90	0	6570	7080	6812			Toscano & Macintyre (2003)
1a	Upper Florida Keys	279.92	26.26	2	(-1)	-7.8	6200	80	0	6890	7300	7105			Toscano & Macintyre (2003)
1a	Upper Florida Keys	279.92	26.26	2	(-1)	-7.9	6070	60	0	6770	7150	6959			Toscano & Macintyre (2003)
1a	Upper Florida Keys	279.92	26.26	2	(-1)	-8.5	6360	70	0	7120	7430	7281			Toscano & Macintyre (2003)
1a	Upper Florida Keys	279.92	26.26	2	(-1)	-8.6	6350	60	0	7140	7420	7273			Toscano & Macintyre (2003)
1a	Upper Florida Keys	279.92	26.26	2	(-1)	-8.7	6470	90	0	7190	7560	7374			Toscano & Macintyre (2003)
1a	Upper Florida Keys	279.92	26.26	2	(-1)	-8.7	6520	60	0	7280	7550	7422			Toscano & Macintyre (2003)
1a	Upper Florida Keys	279.92	26.26	2	(-1)	-8.7	6310	60	0	7060	7400	7232			Toscano & Macintyre (2003)
1a	Upper Florida Keys	279.92	26.26	2	(-1)	-9.5	6080	60	0	6780	7150	6972			Toscano & Macintyre (2003)
1a	Upper Florida Keys	279.92	26.26	2	(-1)	-9.5	6240	80	0	6930	7350	7152			Toscano & Macintyre (2003)
1a	Sands Key/Elliot Key	279.82	25.49	18	(0)	-0.5	1740	60	-27	1070	1380	1244			Toscano & Macintyre (2003)
1a	Sands Key/Elliot Key	279.82	25.49	18	(0)	-1	2530	80	-27	1910	2330	2138			Toscano & Macintyre (2003)
1a	Sands Key/Elliot Key	279.82	25.49	18	(0)	-1.5	2580	70	-27	1970	2380	2196			Toscano & Macintyre (2003)
1a	Sands Key/Elliot Key	279.82	25.49	18	(0)	-2	3980	80	-27	3670	4170	3921			Toscano & Macintyre (2003)
1a	Sands Key/Elliot Key	279.82	25.49	18	(0)	-2.5	4080	90	-27	3800	4360	4056			Toscano & Macintyre (2003)
1a	Sands Key/Elliot Key	279.82	25.49	17	(0)	-2.9	4160	140	-27	3760	4560	4166			Toscano & Macintyre (2003)
1a	Swan Key	279.75	25.35	18	(0)	-1	2090	90	-27	1380	1850	1613			Toscano & Macintyre (2003)
1a	Swan Key	279.75	25.35	18	(0)	-1.5	2650	90	-27	2020	2600	2279			Toscano & Macintyre (2003)
1a	Swan Key	279.75	25.35	18	(0)	-2	2850	60	-27	2340	2710	2542			Toscano & Macintyre (2003)
1a	Swan Key	279.75	25.35	18	(0)	-2.5	3170	70	-27	2740	3130	2913			Toscano & Macintyre (2003)
1a	Swan Key	279.75	25.35	18	(0)	-3	3710	70	-27	3380	3790	3571			Toscano & Macintyre (2003)
1a	Swan Key	279.75	25.35	18	(0)	-3.5	3970	100	-27	3620	4220	3909			Toscano & Macintyre (2003)
1a	Swan Key	279.75	25.35	18	(0)	-4	4050	90	-27	3720	4300	4016			Toscano & Macintyre (2003)
1a	Swan Key	279.75	25.35	18	(0)	-4.5	4150	150	-27	3710	4560	4153			Toscano & Macintyre (2003)
1a	Swan Key	279.75	25.35	17	(0)	-4.8	4220	80	-27	3990	4490	4248			Toscano & Macintyre (2003)
1a	Swan Key	279.75	25.35	17	(0)	-4.9	4800	100	-27	4770	5310	5024			Toscano & Macintyre (2003)
1a	Key Largo	279.55	25.05	18	(0)	-1.5	2460	1	-27	1920	2160	2046			Toscano & Macintyre (2003)
1a	Key Largo	279.55	25.05	18	(0)	-4.3	5550	1	-27	5750	5980	5886			Toscano & Macintyre (2003)
1a	Middle Keys	279.38	24.85	18	(0)	-7.2	7595	85	-27	7800	8210	8012			Toscano & Macintyre (2003)
1a	Middle Keys	279.38	24.85	17	(0)	-7.4	8010	165	-27	8070	8910	8446			Toscano & Macintyre (2003)
1a	West Marquesas	277.73	24.54	18	(0)	-6.7	6060	60	-27	6280	6600	6430			Toscano & Macintyre (2003)

Region	Site	Longitude	Latitude	Material	Sea level limit	Elevation RMSL, m	14C age, years BP (1950) ± Error		δ13C	2σ Calibrated age, years BP			U/Th age ± error, years BP		Source
										Lower	Upper	Median			
	Bahamas														
1b	San Salvador	282.85	26.36	17	(0)	-0.08	1074.1	100	-27	440	800	605			Boardman et al., (1989)
1b	San Salvador	282.85	26.36	17	(0)	-1.5	3750	100	-27	3360	3890	3625			Boardman et al., (1989)
1b	San Salvador	282.85	26.36	17	(0)	-1.76	4703.7	100	-27	4600	5240	4898			Boardman et al., (1989)
1b	San Salvador	282.85	26.36	17	(0)	-2.8	4963	100	-27	4900	5500	5222			Boardman et al., (1989)
1b	San Salvador	282.85	26.36	17	(0)	-4.8	6296.3	100	-27	6440	6960	6701			Boardman et al., (1989)
1b	San Salvador	282.85	26.36	17	(0)	-8.56	7259.3	100	-27	7490	7910	7685			Boardman et al., (1989)
1b	San Salvador	282.85	26.36	17	(0)	-11	7888.9	100	-27	8060	8530	8301			Boardman et al., (1989)
1b	San Salvador	282.85	26.36	17	(0)	-9.6	6600	100	-15	7020	7470	7273			Boardman et al., (1989)
1b	Bimini Islands	280.75	25.74	18	(0)	-2.7	4370	110	-27	4140	4790	4456			Broecker & Kulp (1957)
1b	Stocking Island	284.24	23.53	12	(-1)	-0.64	430	60	0	290	550	446			Macintyre et al., (1996)
1b	Fish Cays, Abaco Reef	282.28	27.01	2	(-1)	-6.8	4515	80	0	4950	5460	5213			Lighty et al., (1982)
1b	Umbrella Cays, Abaco Reef	282.28	27.01	2	(-1)	-5.5	3985	90	0	4270	4810	4533			Lighty et al., (1982)
1b	Umbrella Cays, Abaco Reef	282.28	27.01	2	(-1)	-6.4	3795	90	0	3970	4520	4267			Lighty et al., (1982)
1b	Umbrella Cays, Abaco Reef	282.28	27.01	2	(-1)	-7	3685	70	0	3890	4360	4118			Lighty et al., (1982)
1b	Umbrella Cays, Abaco Reef	282.17	25.48	2	(-1)	-7.3	3580	90	0	3690	4250	3975			Lighty et al., (1982)
	Cuba														
1b	Laguna de Leche	281.3	22.27	17	(0)	0.25							1230	80	Peros et al., (2007)
1b	Laguna de Leche	281.3	22.27	17	(0)	-0.35							1730	60	Peros et al., (2007)
1b	Laguna de Leche	281.43	22.21	17	(0)	0.05							920	50	Peros et al., (2007)
	North West Yucatan, Mexico														
2	Cayos Arcas	268.02	20.22	8	(-1)	-2	750	50	-1.5	540	800	676			Blanchon & Perry (2004)
2	Cayos Arcas	268.02	20.22	8	(-1)	-2.2	840	60	-1	650	910	766			Blanchon & Perry (2004)
2	Cayos Arcas	268.02	20.22	2	(-1)	-4.05	870	60	-0.2	660	940	804			Blanchon & Perry (2004)
2	Cayos Arcas	268.02	20.22	2	(-1)	-4.35	850	50	1.1	670	920	805			Blanchon & Perry (2004)
2	Cayos Arcas	268.02	20.22	2	(-1)	-5.05	1200	40	-0.6	1000	1260	1140			Blanchon & Perry (2004)
2	Cayos Arcas	268.02	20.22	8	(-1)	-7.9	4200	70	-0.8	4540	5000	4782			Blanchon & Perry (2004)
2	Cayos Arcas	268.02	20.22	2	(-1)	-8.2	4070	60	-0.3	4440	4810	4639			Blanchon & Perry (2004)
2	Cayos Arcas	268.02	20.22	2	(-1)	-8.35	4580	80	0.2	5050	5540	5318			Blanchon & Perry (2004)
2	Cayos Arcas	268.02	20.22	2	(-1)	-8.85	4260	50	1.6	4770	5170	4914			Blanchon & Perry (2004)
2	Cayos Arcas	268.02	20.22	8	(-1)	-5.2	170	60	-2.2	0	280	154			Blanchon & Perry (2004)
2	Cayos Arcas	268.02	20.22	2	(-1)	-0.85	910	40	1.3	720	980	861			Blanchon & Perry (2004)
2	Cayos Arcas	268.02	20.22	2	(-1)	-1.1	1080	50	0.6	900	1190	1033			Blanchon & Perry (2004)
2	Cayos Arcas	268.02	20.22	2	(-1)	-4.45	1340	50	-0.7	1130	1410	1273			Blanchon & Perry (2004)
2	Cayos Arcas	268.02	20.22	2	(-1)	-4.65	1840	50	1	1690	2020	1853			Blanchon & Perry (2004)
2	Cayos Arcas	268.02	20.22	2	(-1)	-5.25	1830	60	0.7	1650	2030	1835			Blanchon & Perry (2004)
2	Triangulos	267.78	20.9	2	(-1)	-3.05	2820	60	1.6	2850	3260	3060			Blanchon & Perry (2004)
2	Alacran Reef, Isla Perez	270.31	22.38	8	(-1)	-5.56	3485	70	0	3630	4070	3845			Macintyre et al., (1977)
2	Alacran Reef, Isla Perez	270.31	22.38	8	(-1)	-15.08	4260	80	0	4630	5200	4890			Macintyre et al., (1977)
2	Alacran Reef, Isla Perez	270.31	22.38	8	(-1)	-22.27	5435	60	0	6060	6400	6244			Macintyre et al., (1977)
	East Yucatan, Mexico														
2	Car Wash, Tulum	272.51	20.27	18	(1)	-27.4	8250	80	-24	9030	9440	9253			Coke et al., (1991)
	Belize														
3	Glovers Reef	272.22	16.89	17	(0)	-15.6	7660	90	-25	7920	8320	8108			Gischler (2003)
3	Glovers Reef	272.16	16.74	17	(0)	-17.3	8450	130	-25	8640	9390	9040			Gischler (2003)
3	Turneffe Islands	272.06	17.24	17	(0)	-5.3	5610	60	-25	5840	6190	5996			Gischler (2003)
3	Turneffe Islands	272.08	17.39	17	(0)	-5.7	4620	70	-25	4570	5040	4821			Gischler (2003)
3	Turneffe Islands	272.11	17.39	17	(0)	-9.3	6010	80	-25	6250	6630	6416			Gischler (2003)
3	Turneffe Islands	272.17	17.47	17	(0)	-3.3	2690	80	-25	2150	2660	2389			Gischler (2003)
3	Lighthouse Reef	272.47	17.41	17	(0)	-7.4	6950	70	-25	7280	7580	7443			Gischler (2003)
3	Lighthouse Reef	272.39	17.14	17	(0)	-8.4	6660	90	-25	6930	7380	7165			Gischler (2003)
3	Turneffe Islands	272.1	17.17	17	(0)	-2.8	5470	50	-27	5640	5930	5793			Gischler & Hudson (1998)
3	Turneffe Islands	272.21	17.33	2	(-1)	-3	4750	80	0	5300	5680	5497			Gischler & Hudson (1998)
3	Turneffe Islands	272.25	17.56	2	(-1)	-2.7	1940	60	0	1770	2140	1953			Gischler & Hudson (1998)
3	Glovers Reef	272.14	16.78	7	(-1)	-11	7370	70	0	8040	8380	8230			Gischler & Hudson (1998)
3	Glovers Reef	272.14	16.78	8	(-1)	-8.75	6170	90	0	6830	7290	7071			Gischler & Hudson (1998)
3	Glovers Reef	272.14	16.78	8	(-1)	-4.6	5210	90	0	5760	6220	6006			Gischler & Hudson (1998)
3	Glovers Reef	272.2	16.75	8	(-1)	-8	6570	80	0	7290	7620	7465			Gischler & Hudson (1998)
3	Glovers Reef	272.2	16.75	2	(-1)	-5.6	6280	80	0	6980	7390	7197			Gischler & Hudson (1998)
3	Glovers Reef	272.2	16.75	1	(-1)	-1	3040	70	0	3070	3500	3303			Gischler & Hudson (1998)
3	Glovers Reef	272.18	16.77	1	(-1)	-2.8	3590	80	0	3720	4240	3988			Gischler & Hudson (1998)
3	Glovers Reef	272.18	16.77	1	(-1)	-1.25	2970	80	0	2970	3430	3217			Gischler & Hudson (1998)
3	Lighthouse Reef	272.47	17.22	7	(-1)	-7.9	6430	60	0	7200	7470	7342			Gischler & Hudson (1998)
3	Lighthouse Reef	272.47	17.22	8	(-1)	-5.1	4460	60	0	4900	5320	5144			Gischler & Hudson (1998)
3	Lighthouse Reef	272.47	17.22	2	(-1)	-3.5	4390	70	0	4850	5270	5058			Gischler & Hudson (1998)
3	Lighthouse Reef	272.47	17.22	8	(-1)	-2	3880	50	0	4180	4560	4383			Gischler & Hudson (1998)
3	Lighthouse Reef	272.47	17.37	17	(0)	-10							6660	50	Gischler & Lomando (2000)
3	Lighthouse Reef	272.48	17.35	17	(0)	-7							6410	50	Gischler & Lomando (2000)
3	Lighthouse Reef	272.43	17.37	17	(0)	-6.5							5990	60	Gischler & Lomando (2000)
3	Lighthouse Reef	272.47	17.37	8	(-1)	-6.5							4510	60	Gischler & Lomando (2000)
3	Lighthouse Reef	272.51	17.46	7	(-1)	-7.5							6620	60	Gischler & Lomando (2000)
3	Lighthouse Reef	272.47	17.37	8	(-1)	-5.5							3650	70	Gischler & Lomando (2000)
3	Turneffe Islands	272.1	17.17	17	(0)	-3.8							5850	50	Gischler & Lomando (2000)
3	Turneffe Islands	272.42	17.41	18	(0)	-0.74	2480	30	-27	1930	2250	2072			Wooler et al., (2009)
3	Turneffe Islands	272.42	17.41	18	(0)	-4.4	5390	30	-27	5590	5850	5704			Wooler et al., (2009)
3	Tobacco Cay	271.95	16.93	2	(-1)	-3.1	4230	70	0	4570	5070	4845			Gischler & Hudson (2004)
3	Tobacco Cay	271.95	16.93	8	(-1)	-8.4	5610	60	0	6270	6600	6419			Gischler & Hudson (2004)
3	Tobacco Cay	271.95	16.93	8	(-1)	-14.2	6390	60	0	7160	7430	7309			Gischler & Hudson (2004)
3	Emily	271.98	17.06	2	(-1)	-2.3	4350	70	0	4820	5250	5003			Gischler & Hudson (2004)
3	Emily	271.98	17.06	2	(-1)	-4.7	5810	70	0	6440	6840	6643			Gischler & Hudson (2004)

Region	Site	Longitude	Latitude	Material	Sea level limit	Elevation RMSL, m	14C age, years BP (1950) ± Error		δ13C	2σ Calibrated age, years BP			U/Th age ± error, years BP		Source
										Lower	Upper	Median			
3	Rendezvous Cay	271.96	17.24	2	(-1)	-4.4	5780	80	0	6400	6830	6608			Gischler & Hudson (2004)
3	Rendezvous Cay	271.96	17.24	2	(-1)	-9.3	6810	80	0	7500	7860	7673			Gischler & Hudson (2004)
3	Rendezvous Cay	271.96	17.24	2	(-1)	-20.9	6880	60	0	7600	7900	7737			Gischler & Hudson (2004)
3	Gallow's Point Reef	271.96	17.48	2	(-1)	-2.3	2970	70	0	2980	3410	3220			Gischler & Hudson (2004)
3	Gallow's Point Reef	271.96	17.48	2	(-1)	-6.6	5760	70	0	6390	6780	6584			Gischler & Hudson (2004)
3	Gallow's Point Reef	271.96	17.48	2	(-1)	-9.9	6810	60	0	7540	7830	7670			Gischler & Hudson (2004)
3	Gallow's Point Reef	271.96	17.48	2	(-1)	-11.4							8148	52	Gischler & Hudson (2004)
3	Gladden Spit	271.96	16.45	2	(-1)	-3.7	1010	60	0	780	1130	951			Gischler & Hudson (2004)
3	Gladden Spit	271.96	16.45	12	(-1)	-8.2	5330	70	0	5930	6280	6127			Gischler & Hudson (2004)
3	Gladden Spit	271.96	16.45	8	(-1)	-14.9	6770	90	0	7450	7830	7637			Gischler & Hudson (2004)
3	Carrie Bow Cay 1	271.92	16.69	2	(-1)	-3.8	3900	70	0	4150	4650	4411			Gischler & Hudson (2004)
3	Carrie Bow Cay 1	271.92	16.69	8	(-1)	-8.2	5030	80	0	5590	5980	5791			Gischler & Hudson (2004)
3	Carrie Bow Cay 1	271.92	16.69	8	(-1)	-8.6							6259	48	Gischler & Hudson (2004)
3	Carrie Bow Cay 1	271.92	16.69	8	(-1)	-12.8							6963	66	Gischler & Hudson (2004)
3	Carrie Bow Cay 2	271.92	16.69	2	(-1)	-3.6	4120	70	0	4450	4880	4697			Gischler & Hudson (2004)
3	Carrie Bow Cay 2	271.92	16.69	8	(-1)	-7	5070	70	0	5630	6020	5831			Gischler & Hudson (2004)
3	Carrie Bow Cay 2	271.92	16.69	8	(-1)	-9.5							6705	89	Gischler & Hudson (2004)
3	Nicholas Cay	271.78	16.19	2	(-1)	-3.2	2760	70	0	2750	3170	2949			Gischler & Hudson (2004)
3	Nicholas Cay	271.78	16.19	2	(-1)	-8.6	5170	80	0	5740	6180	5958			Gischler & Hudson (2004)
3	Nicholas Cay	271.78	16.19	8	(-1)	-14.8	6090	60	0	6790	7160	6985			Gischler & Hudson (2004)
3	Nicholas Cay	271.78	16.19	8	(-1)	-20.3	7380	60	0	8060	8380	8240			Gischler & Hudson (2004)
3	Ranguana Cay	271.87	16.34	2	(-1)	-4.1	680	60	0	510	760	636			Gischler & Hudson (2004)
3	Ranguana Cay	271.87	16.34	2	(-1)	-11.9	4570	70	0	5040	5510	5302			Gischler & Hudson (2004)
3	Ranguana Cay	271.87	16.34	8	(-1)	-16.7	6160	70	0	6870	7250	7064			Gischler & Hudson (2004)
3	Ranguana Cay	271.87	16.34	8	(-1)	-21	7160	60	0	7860	8170	8015			Gischler & Hudson (2004)
3	Cross Cay 1	271.96	16.98	2	(-1)	-2.5	4590	70	0	5070	5540	5331			Gischler & Hudson (2004)
3	Cross Cay 1	271.96	16.98	2	(-1)	-4.5	5400	80	0	5980	6390	6204			Gischler & Hudson (2004)
3	Cross Cay 1	271.96	16.98	2	(-1)	-7.3	6530	60	0	7290	7560	7432			Gischler & Hudson (2004)
3	Cross Cay 2	271.96	16.98	2	(-1)	-2.3	4580	70	0	5050	5520	5317			Gischler & Hudson (2004)
3	Cross Cay 2	271.96	16.98	2	(-1)	-4.7	5680	60	0	6320	6660	6498			Gischler & Hudson (2004)
3	Cross Cay 2	271.96	16.98	2	(-1)	-7.1	6070	60	0	6770	7150	6959			Gischler & Hudson (2004)
3	Boo Bee Patch Reef	271.88	16.75	18	(0)	-18	8780	100	-27	9100	9620	9390			Halley et al., (1977)
3	Tobacco Range	271.92	16.9	18	(0)	-0.97	2090	70	-27	1410	1810	1613			Macintyre et al., (1995)
3	Tobacco Range	271.92	16.9	18	(0)	-3.3	2670	90	-27	2050	2650	2309			Macintyre et al., (1995)
3	Tobacco Range	271.92	16.9	18	(0)	-7.91	6920	80	-27	7230	7550	7383			Macintyre et al., (1995)
3	Tobacco Range	271.92	16.9	18	(0)	-1.16	1710	60	-27	1050	1350	1214			Macintyre et al., (1995)
3	Tobacco Range	271.92	16.9	18	(0)	-3.01	3550	90	-27	3140	3630	3388			Macintyre et al., (1995)
3	Tobacco Range	271.92	16.9	18	(0)	-3.84	5450	75	-27	5590	5940	5773			Macintyre et al., (1995)
3	Tobacco Range	271.92	16.9	18	(0)	-8.34	6550	95	-27	6750	7240	7006			Macintyre et al., (1995)
3	Tobacco Range	271.92	16.9	18	(0)	-0.62	2380	90	-27	1700	2230	1956			Macintyre et al., (1995)
3	Tobacco Range	271.92	16.9	18	(0)	-3.51	4790	80	-27	4810	5260	5007			Macintyre et al., (1995)
3	Tobacco Range	271.92	16.9	18	(0)	-5.82	6040	100	-27	6200	6660	6416			Macintyre et al., (1995)
3	Tobacco Range	271.92	16.9	18	(0)	-6.33	5510	110	-27	5590	6120	5836			Macintyre et al., (1995)
3	Tobacco Range	271.92	16.9	18	(0)	-6.75	6010	80	-27	6200	6590	6382			Macintyre et al., (1995)
3	Tobacco Range	271.92	16.9	18	(0)	-7.53	6230	90	-27	6450	6930	6693			Macintyre et al., (1995)
3	Tobacco Range	271.92	16.9	18	(0)	-4.81	5470	100	-27	5570	6050	5793			Macintyre et al., (1995)
3	Tobacco Range	271.92	16.9	18	(0)	-7.34	6310	90	-27	6470	6960	6717			Macintyre et al., (1995)
3	Tobacco Range	271.92	16.9	17	(0)	-9.93	6920	100	-27	7180	7570	7383			Macintyre et al., (1995)
3	Tobacco Range	271.92	16.9	18	(0)	-6.97	5790	110	-27	5900	6390	6144			Macintyre et al., (1995)
3	Tobacco Range	271.92	16.9	18	(0)	-8.25	6570	90	-27	6780	7250	7029			Macintyre et al., (1995)
3	Tobacco Range	271.92	16.9	18	(0)	-9.38	6850	90	-27	7140	7510	7323			Macintyre et al., (1995)
3	Tobacco Range	271.92	16.9	18	(0)	-2.42	3050	80	-27	2520	3020	2783			Macintyre et al., (1995)
3	Tobacco Range	271.92	16.9	18	(0)	-8.04	6570	80	-27	6800	7240	7031			Macintyre et al., (1995)
3	Tobacco Range	271.92	16.9	18	(0)	-1.5	3550	80	-27	3160	3610	3388			Macintyre et al., (1995)
3	Tobacco Range	271.92	16.9	18	(0)	-7.19	5770	110	-27	5880	6380	6123			Macintyre et al., (1995)
3	Twin Cays	271.89	16.82	18	(0)	-1.76	3655	80	-27	3310	3750	3509			Macintyre et al., (2004)
3	Twin Cays	271.89	16.82	18	(0)	-4.59	6065	75	-27	6270	6630	6439			Macintyre et al., (2004)
3	Twin Cays	271.89	16.82	17	(0)	-4.73	6030	105	-27	6180	6660	6407			Macintyre et al., (2004)
3	Twin Cays	271.89	16.82	17	(0)	-7.06	6070	110	-27	6210	6710	6449			Macintyre et al., (2004)
3	Twin Cays	271.89	16.82	18	(0)	-1.77	2835	130	-27	2170	2820	2517			Macintyre et al., (2004)
3	Twin Cays	271.89	16.82	18	(0)	-5.76	5745	150	-27	5740	6420	6096			Macintyre et al., (2004)
3	Twin Cays	271.89	16.82	17	(0)	-7.19	6060	145	-27	6110	6790	6443			Macintyre et al., (2004)
3	Twin Cays	271.89	16.83	18	(0)	-1.55	3960	95	-27	3610	4180	3895			Macintyre et al., (2004)
3	Twin Cays	271.89	16.83	18	(0)	-4.25	5915	90	-27	6030	6500	6285			Macintyre et al., (2004)
3	Twin Cays	271.9	16.83	18	(0)	-1.53	3400	105	-27	2890	3460	3200			Macintyre et al., (2004)
3	Twin Cays	271.9	16.83	18	(0)	-4.5	6520	160	-27	6580	7320	6964			Macintyre et al., (2004)
3	Twin Cays	271.9	16.83	18	(0)	-1.05	800	70	-27	250	520	386			Macintyre et al., (2004)
3	Twin Cays	271.89	16.83	18	(0)	-2.31	2490	60	-27	1910	2290	2088			Macintyre et al., (2004)
3	Twin Cays	271.89	16.83	18	(0)	-6.75	6920	110	-27	7160	7580	7382			Macintyre et al., (2004)
3	Twin Cays	271.89	16.83	18	(0)	-3.3	5870	100	-27	5970	6460	6234			Macintyre et al., (2004)
3	Twin Cays	271.89	16.83	18	(0)	-6.35	6310	90	-27	6470	6960	6717			Macintyre et al., (2004)
3	Twin Cays	271.89	16.83	17	(0)	-8.71	6730	90	-27	6980	7410	7206			Macintyre et al., (2004)
3	Twin Cays	271.89	16.83	18	(0)	-4.45	5210	90	-27	5300	5720	5516			Macintyre et al., (2004)
3	Twin Cays	271.89	16.83	18	(0)	-6.43	5870	90	-27	5990	6440	6235			Macintyre et al., (2004)
3	Twin Cays	271.9	16.84	17	(0)	-3.71	5420	70	-27	5580	5900	5744			Macintyre et al., (2004)
3	Twin Cays	271.9	16.83	18	(0)	-3.08	4270	80	-27	4060	4570	4313			Macintyre et al., (2004)
3	Twin Cays	271.9	16.83	18	(0)	-6.15	5670	80	-27	5840	6250	6028			Macintyre et al., (2004)
3	Twin Cays	271.9	16.83	17	(0)	-8.49	6920	90	-27	7200	7560	7383			Macintyre et al., (2004)
3	Twin Cays	271.89	16.83	17	(0)	-8.12	6450	90	-27	6660	7140	6885			Macintyre et al., (2004)
3	Carrie Bow Cay	271.92	16.8	17	(0)	-13.98	7619	320	-27	7410	8770	8050			Toscano & Macintyre (2003)
3	Carrie Bow Cay	271.92	16.8	17	(0)	-14.87	8237	270	-27	8150	9410	8737			Toscano & Macintyre (2003)
3	Carrie Bow Cay	271.92	16.8	18	(0)	-7	6804	150	-27	6930	7560	7268			Toscano & Macintyre (2003)
3	Carrie Bow Cay	271.92	16.8	17	(0)	-5.22	2861	190	-27	2050	3020	2540			Toscano & Macintyre (2003)
3	Twin Cays	271.9	16.83	18	(0)	-1.03	925	50	-26.2	400	630	506			Wooler et al., (2004)

Region	Site	Longitude	Latitude	Material	Sea level limit	Elevation RMSL, m	14C age, years BP (1950) ± Error		δ13C	2σ Calibrated age, years BP			U/Th age ± error, years BP		Source
										Lower	Upper	Median			
3	Twin Cays	271.9	16.83	18	(0)	-1.49	3700	30	-26.2	3430	3710	3572			Wooler et al., (2004)
3	Twin Cays	271.9	16.83	18	(0)	-2.6	3860	35	-26.2	3620	3930	3774			Wooler et al., (2004)
3	Twin Cays	271.9	16.83	18	(0)	-4.26	5900	50	-26.2	6160	6430	6284			Wooler et al., (2004)
3	Twin Cays	271.9	16.83	18	(0)	-8.27	6990	55	-26.2	7320	7570	7461			Wooler et al., (2004)
3	Twin Cays	271.9	16.83	18	(0)	-1.5	2880	65	-27	2350	2730	2572			Wooler et al., (2007)
3	Twin Cays	271.9	16.83	18	(0)	-2.26	4650	70	-27	4570	5030	4817			Wooler et al., (2007)
3	Twin Cays	271.9	16.83	18	(0)	-2.95	5190	40	-27	5330	5600	5505			Wooler et al., (2007)
3	Twin Cays	271.9	16.83	18	(0)	-4.25	6090	40	-27	6320	6610	6462			Wooler et al., (2007)
3	Twin Cays	271.9	16.83	18	(0)	-4.65	6320	35	-27	6600	6880	6727			Wooler et al., (2007)
3	Twin Cays	271.9	16.83	18	(0)	-6.2	6610	45	-27	6930	7230	7078			Wooler et al., (2007)
3	Twin Cays	271.9	16.83	18	(0)	-7.12	7040	45	-27	7390	7600	7490			Wooler et al., (2007)
	Grand Cayman														
4a	South East Grand Cayman	278.92	19.3	5	(-1)	-20							4916	205	Blanchon (2000)
4a	South East Grand Cayman	278.92	19.3	2	(-1)	-21							8198	82	Blanchon (2000)
4a	South East Grand Cayman	278.92	19.3	2	(-1)	-20.7							8122	101	Blanchon (2000)
4a	South East Grand Cayman	278.92	19.3	5	(-1)	-22							6025	350	Blanchon (2000)
4a	South East Grand Cayman	278.92	19.3	2	(-1)	-22.8							8354	75	Blanchon (2000)
4a	South East Grand Cayman	278.92	19.3	2	(-1)	-23.5							8933	180	Blanchon (2000)
4a	South East Grand Cayman	278.92	19.3	2	(-1)	-21							8658	74	Blanchon (2000)
4a	South East Grand Cayman	278.92	19.3	2	(-1)	-21.9							8953	149	Blanchon (2000)
4a	South East Grand Cayman	278.92	19.3	2	(-1)	-22.2							9878	97	Blanchon (2000)
4a	South East Grand Cayman	278.62	19.37	16	(0)	-1.84	2132	40	-27	1520	1810	1660			Woodroffe (1981)
4a	South East Grand Cayman	278.62	19.37	16	(0)	-0.47	842	50	-27	290	520	424			Woodroffe (1981)
4a	South East Grand Cayman	278.62	19.37	16	(0)	-2.09	928	80	-27	320	640	495			Woodroffe (1981)
4a	South East Grand Cayman	278.62	19.37	16	(0)	-1.4	2160	75	-27	1490	1900	1693			Woodroffe (1981)
4a	South East Grand Cayman	278.62	19.37	16	(0)	-1.13	1404	50	-27	750	1050	898			Woodroffe (1981)
4a	South East Grand Cayman	278.62	19.37	16	(0)	-0.5	567	55	-27	0	270	147			Woodroffe (1981)
4a	South East Grand Cayman	278.62	19.37	16	(0)	-1.16	1549	70	-27	900	1240	1055			Woodroffe (1981)
4a	South East Grand Cayman	278.62	19.37	16	(0)	-1.14	1856	60	-27	1220	1520	1358			Woodroffe (1981)
4a	South East Grand Cayman	278.62	19.37	16	(0)	-1.3	878	60	-27	290	570	454			Woodroffe (1981)
	Jamaica														
4b	Negril	281.67	18.29	17	(0)	-1.1	3560	60	-27	3220	3580	3400			Digerfeldt & Hendry (1987)
4b	Negril	281.67	18.29	18	(0)	-1.15	3810	60	-27	3490	3890	3699			Digerfeldt & Hendry (1987)
4b	Negril	281.67	18.29	17	(0)	-1.75	4370	60	-27	4230	4690	4455			Digerfeldt & Hendry (1987)
4b	Negril	281.67	18.29	17	(0)	-2.1	4450	60	-27	4390	4790	4567			Digerfeldt & Hendry (1987)
4b	Negril	281.67	18.29	18	(0)	-3	3190	50	-27	2760	3120	2931			Digerfeldt & Hendry (1987)
4b	Negril	281.67	18.29	18	(0)	-3.15	4740	60	-27	4780	5210	4934			Digerfeldt & Hendry (1987)
4b	Negril	281.67	18.29	17	(0)	-3.35	5100	60	-27	5270	5570	5406			Digerfeldt & Hendry (1987)
4b	Negril	281.67	18.29	17	(0)	-4.09	5680	60	-27	5880	6210	6038			Digerfeldt & Hendry (1987)
4b	Negril	281.67	18.29	17	(1)	-4.75	5970	70	-27	6180	6520	6342			Digerfeldt & Hendry (1987)
4b	Negril	281.67	18.29	17	(0)	-5	5310	60	-27	5460	5830	5628			Digerfeldt & Hendry (1987)
4b	Negril	281.67	18.29	18	(0)	-5	4480	60	-27	4420	4800	4608			Digerfeldt & Hendry (1987)
4b	Negril	281.67	18.29	18	(0)	-5.45	6220	70	-27	6400	6800	6607			Digerfeldt & Hendry (1987)
4b	Negril	281.67	18.29	18	(0)	-7	5240	60	-27	5350	5720	5550			Digerfeldt & Hendry (1987)
4b	Negril	281.67	18.29	17	(0)	-7.22	6610	70	-27	6880	7260	7074			Digerfeldt & Hendry (1987)
4b	Negril	281.67	18.29	18	(0)	-9	5910	70	-27	6100	6460	6281			Digerfeldt & Hendry (1987)
4b	Negril	281.67	18.29	17	(0)	-8.8	6960	70	-27	7270	7560	7422			Digerfeldt & Hendry (1987)
4b	Negril	281.67	18.29	18	(0)	-11	6670	70	-27	6940	7310	7143			Digerfeldt & Hendry (1987)
4b	Negril	281.67	18.29	17	(0)	-11.45	7880	80	-27	8100	8500	8293			Digerfeldt & Hendry (1987)
4b	Negril	281.67	18.29	17	(0)	-11.7	8080	80	-27	8320	8750	8499			Digerfeldt & Hendry (1987)
4b	Negril	281.67	18.29	17	(0)	-12.6	8070	80	-27	8310	8730	8489			Digerfeldt & Hendry (1987)
4b	Negril	281.67	18.29	17	(0)	-8.2	6300	80	-27	6480	6930	6704			Digerfeldt & Hendry (1987)
4b	Negril	281.67	18.29	17	(0)	-6.1	6220	70	-27	6400	6800	6607			Digerfeldt & Hendry (1987)
4b	Black River	282.18	18.02	18	(0)	-1.2	3240	60	-27	2800	3210	3000			Digerfeldt & Hendry (1987)
4b	Black River	282.18	18.02	17	(0)	-1.05	3590	60	-27	3260	3620	3434			Digerfeldt & Hendry (1987)
4b	Black River	282.18	18.02	17	(0)	-1.65	4140	60	-27	3930	4370	4139			Digerfeldt & Hendry (1987)
4b	Black River	282.18	18.02	17	(1)	-1.7	4410	60	-27	4320	4770	4510			Digerfeldt & Hendry (1987)
4b	Black River	282.18	18.02	18	(0)	-2.35	3890	60	-27	3590	4000	3797			Digerfeldt & Hendry (1987)
4b	Black River	282.18	18.02	18	(0)	-2.2	4180	60	-27	3980	4400	4196			Digerfeldt & Hendry (1987)
4b	Black River	282.18	18.02	18	(0)	-4.2	5680	70	-27	5870	6230	6038			Digerfeldt & Hendry (1987)
4b	Black River	282.18	18.02	17	(1)	-4.4	6080	70	-27	6280	6640	6454			Digerfeldt & Hendry (1987)
4b	Black River	282.18	18.02	17	(1)	-4.85	6030	70	-27	6250	6600	6400			Digerfeldt & Hendry (1987)
4b	Black River	282.18	18.02	17	(0)	-5.65	6320	70	-27	6520	6930	6728			Digerfeldt & Hendry (1987)
4b	Black River	282.18	18.02	17	(1)	-6.4	6470	70	-27	6720	7140	6908			Digerfeldt & Hendry (1987)
4b	Black River	282.18	18.02	17	(0)	-6.7	6500	70	-27	6740	7150	6947			Digerfeldt & Hendry (1987)
4b	Black River	282.18	18.02	18	(0)	-6.8	5950	70	-27	6160	6510	6323			Digerfeldt & Hendry (1987)
	Dominican Republic														
5	Canada Honda	288.43	18.53	10	(-1)	-33	8560	40	-3.51	9440	9710	9553			Cuevas et al., (2009)
5	Canada Honda	288.43	18.53	10	(-1)	-28	7390	45	-3.75	8030	8330	8192			Cuevas et al., (2009)
5	Canada Honda	288.43	18.53	10	(-1)	-23	6240	30	-2.13	6980	7240	7121			Cuevas et al., (2009)
5	Canada Honda	288.43	18.53	10	(-1)	-17	7200	45	-3	7880	8150	8004			Cuevas et al., (2009)
5	Canada Honda	288.43	18.53	15	(-1)	-32	8130	45	-4.53	8920	9270	9069			Cuevas et al., (2009)
5	Canada Honda	288.43	18.53	15	(-1)	-26	7350	40	-3.07	8000	8280	8127			Cuevas et al., (2009)
5	Canada Honda	288.43	18.53	15	(-1)	-23	6910	40	-3.47	7590	7840	7717			Cuevas et al., (2009)
5	Enriquillo Valley	288.26	18.53	8	(-1)	-10	4760	90	0	5290	5710	5505			Mann et al., (1984)
5	Enriquillo Valley	288.68	18.41	14	(-1)	-20	5930	100	0	6520	7070	6789			Mann et al., (1984)
5	Canada Honda	288.38	18.53	8	(-1)	-3.5	5180	80	0	5740	6180	5971			Taylor et al., (1985)
5	Canada Honda	288.38	18.53	8	(-1)	-5.9	6200	80	0	6890	7300	7105			Taylor et al., (1985)
5	Canada Honda	288.38	18.53	15	(-1)	-26	6490	130	0	7140	7640	7389			Taylor et al., (1985)
5	Canada Honda	288.38	18.53	6	(-1)	-32.5	8400	190	0	8990	10030	9466			Taylor et al., (1985)
5	Canada Honda	288.38	18.53	14	(-1)	-32.5	8740	110	0	9550	10180	9891			Taylor et al., (1985)

Region	Site	Longitude	Latitude	Material	Sea level limit	Elevation RMSL, m	14C age, years BP (1950) ± Error		δ13C	2σ Calibrated age, years BP			U/Th age ± error, years BP		Source
										Lower	Upper	Median			
5	Canada Honda	288.38	18.53	14	(-1)	-34.2	8990	60	0	10070	10460	10232			Taylor et al., (1985)
5	Canada Honda	288.38	18.53	14	(-1)	-35	7930	110	0	8550	9210	8872			Taylor et al., (1985)
	Puerto Rico														
6	Bahia Salina	294.7	18.13	2	(-1)	-0.61	190	90	0	0	400	207			Macintyre et al., (1982)
6	Bahia Salina	294.7	18.13	2	(-1)	-1.83	2155	80	0	1970	2440	2210			Macintyre et al., (1982)
6	Bahia Salina	294.7	18.13	2	(-1)	-1.83	860	90	0	630	1000	802			Macintyre et al., (1982)
6	Bahia Salina	294.7	18.13	2	(-1)	-3.35	2020	70	0	1860	2280	2051			Macintyre et al., (1982)
	St Croix, US Virgin Islands														
6	Fancy Algal Ridge	295.36	17.72	2	(-1)	-2	355	60	0	260	500	384			Adey (1975)
6	Hess Channel, Mid Shelf	295.26	17.68	2	(-1)	-3.63	970	95	0	690	1130	907			Adey (1975)
6	Hess Channel, Mid Shelf	295.26	17.68	8	(-1)	-5.21	1070	100	0	780	1250	1016			Adey (1975)
6	Hess Channel, Mid Shelf	295.26	17.68	15	(-1)	-10.53	3180	100	0	3210	3750	3471			Adey (1975)
6	Hess Channel, Mid Shelf	295.26	17.68	7	(-1)	-11.4	4360	100	0	4770	5310	5023			Adey (1975)
6	Isaac's Algal Ridge	295.42	17.75	2	(-1)	-8.5	4040	95	0	4330	4850	4604			Adey (1975)
6	Hess Channel, shelf edge	295.26	17.69	2	(-1)	-13.1	7240	70	0	7930	8280	8093			Adey et al., (1977a)
6	East Point	295.44	17.76	2	(-1)	-15.49	5010	70	0	5590	5930	5773			Adey et al., (1977a)
6	East Point	295.44	17.76	2	(-1)	-17.06	6110	70	0	6790	7200	7009			Adey et al., (1977a)
6	Shelf-edge reef, East Point	295.44	17.76	2	(-1)	-20.98	6945	70	0	7640	7960	7800			Adey et al., (1977a)
6	Shelf-edge reef, East Point	295.44	17.76	2	(-1)	-23.5	9075	70	0	10170	10500	10326			Adey et al., (1977a)
6	Tague Reef	295.4	17.76	8	(-1)	-5.5							1661	3	Macintyre et al., (2008)
6	Tague Reef	295.4	17.76	7	(-1)	-7.75							2295	4	Macintyre et al., (2008)
6	Tague Reef	295.4	17.76	8	(-1)	-12.3							3889	8	Macintyre et al., (2008)
6	Tague Reef	295.4	17.76	2	(-1)	-4.8							1873	5	Macintyre et al., (2008)
6	Tague Bay	295.4	17.76	2	(-1)	-7.98	3220	75	0	3320	3740	3514			Burke et al., (1989)
6	Tague Bay	295.4	17.76	2	(-1)	-8.62	4525	80	0	4960	5460	5229			Burke et al., (1989)
6	Tague Lagoon	295.4	17.76	2	(-1)	-7.9	1115	65	0	910	1230	1061			Burke et al., (1989)
6	Sand Cay/Candlelight Reef	295.35	17.77	2	(-1)	-3	1495	60	0	1280	1600	1435			Burke et al., (1989)
6	North Shore Reef	295.38	17.76	8	(-1)	-2	1455	80	0	1230	1610	1400			Burke et al., (1989)
6	North Shore Reef	295.38	17.76	2	(-1)	-2.7	1850	65	0	1650	2050	1846			Burke et al., (1989)
6	Tague Bay	295.39	17.76	8	(-1)	-3	2035	80	0	1860	2300	2070			Burke et al., (1989)
6	Tague Bay	295.39	17.76	7	(-1)	-8	3415	80	0	3500	3990	3754			Burke et al., (1989)
6	Tague Bay	295.4	17.76	2	(-1)	-1.5	120	80	0	0	300	147			Burke et al., (1989)
6	Tague Bay Romney Pt	295.4	17.76	2	(-1)	-1	803	50	0	640	890	745			Burke et al., (1989)
6	Tague Bay Romney Pt	295.4	17.76	2	(-1)	-7.2	5490	85	0	6090	6530	6302			Burke et al., (1989)
6	Tague Bay Romney Pt	295.4	17.76	2	(-1)	-10.4	6135	80	0	6810	7240	7036			Burke et al., (1989)
6	Tague Bay Romney Pt	295.41	17.76	2	(-1)	-1.2	720	80	0	520	860	674			Burke et al., (1989)
6	Boiler Bay, Shark Reef	295.42	17.76	2	(-1)	-2.8	315	60	0	150	500	355			Lighty et al., (1982)
6	Buck Island	295.39	17.8	7	(-1)	-6.02	1785	45	0	1600	1920	1770			Macintyre & Adey (1990)
6	Buck Island	295.39	17.8	8	(-1)	-8	2745	50	0	2760	3110	2925			Macintyre & Adey (1990)
6	Buck Island	295.39	17.8	12	(-1)	-9.32	3555	50	0	3750	4130	3939			Macintyre & Adey (1990)
6	Buck Island	295.39	17.8	2	(-1)	-12.39	4145	50	0	4530	4870	4729			Macintyre & Adey (1990)
6	Buck Island	295.39	17.79	2	(-1)	-3.9									Hubbard et al., (2005)
6	Buck Island	295.39	17.79	2	(-1)	-5.45									Hubbard et al., (2005)
6	Buck Island	295.39	17.79	2	(-1)	-7.15									Hubbard et al., (2005)
6	Buck Island	295.39	17.79	2	(-1)	-3.35									Hubbard et al., (2005)
6	Buck Island	295.39	17.79	2	(-1)	-4.6									Hubbard et al., (2005)
6	Buck Island	295.39	17.79	2	(-1)	-4.6									Hubbard et al., (2005)
6	Buck Island	295.39	17.79	2	(-1)	-14.25									Hubbard et al., (2005)
6	Buck Island	295.39	17.79	2	(-1)	-2.05									Hubbard et al., (2005)
6	Buck Island	295.39	17.78	2	(-1)	-4.9									Hubbard et al., (2005)
6	Buck Island	295.39	17.79	2	(-1)	-2.9									Hubbard et al., (2005)
6	Buck Island	295.39	17.79	2	(-1)	-4.65									Hubbard et al., (2005)
6	Buck Island	295.39	17.79	2	(-1)	-6.2									Hubbard et al., (2005)
6	Buck Island	295.39	17.78	2	(-1)	-5.75									Hubbard et al., (2005)
6	Buck Island	295.38	17.8	2	(-1)	-5.05									Hubbard et al., (2005)
6	Buck Island	295.38	17.8	2	(-1)	-8.15									Hubbard et al., (2005)
6	Buck Island	295.38	17.8	2	(-1)	-12.75									Hubbard et al., (2005)
6	Buck Island	295.38	17.8	2	(-1)	-13.7									Hubbard et al., (2005)
6	Buck Island	295.39	17.79	2	(-1)	-7.9									Hubbard et al., (2005)
6	Buck Island	295.39	17.79	2	(-1)	-7.9									Hubbard et al., (2005)
6	Buck Island	295.39	17.78	4	(-1)	-0.5									Hubbard et al., (2005)
6	Buck Island	295.39	17.78	5	(-1)	-2.35									Hubbard et al., (2005)
6	Buck Island	295.39	17.78	8	(-1)	-8.5									Hubbard et al., (2005)
6	Buck Island	295.39	17.78	10	(-1)	-10.5									Hubbard et al., (2005)
6	Buck Island	295.39	17.79	10	(-1)	-11									Hubbard et al., (2005)
6	Buck Island	295.39	17.79	10	(-1)	-12.5									Hubbard et al., (2005)
6	Buck Island	295.39	17.79	10	(-1)	-7.85									Hubbard et al., (2005)
6	Buck Island	295.39	17.79	10	(-1)	-7.85									Hubbard et al., (2005)
6	Buck Island	295.39	17.79	10	(-1)	-11.8									Hubbard et al., (2005)
6	Buck Island	295.39	17.78	10	(-1)	-5.9									Hubbard et al., (2005)
6	Buck Island	295.39	17.78	10	(-1)	-8.2									Hubbard et al., (2005)
6	Buck Island	295.39	17.79	10	(-1)	-8.35									Hubbard et al., (2005)
6	Buck Island	295.39	17.78	10	(-1)	-13.1									Hubbard et al., (2005)
6	Buck Island	295.39	17.78	10	(-1)	-7.9									Hubbard et al., (2005)
6	Buck Island	295.39	17.78	10	(-1)	-12.25									Hubbard et al., (2005)
6	Buck Island	295.39	17.78	10	(-1)	-16.05									Hubbard et al., (2005)
6	Buck Island	295.39	17.79	15	(-1)	-14.25									Hubbard et al., (2005)
6	Long Reef	295.29	17.76	2	(-1)	-5.52	270	50	0	140	450	313			Macintyre et al., (2008)
6	Long Reef	295.29	17.76	7	(-1)	-2.02	700	50	0	530	770	653			Macintyre et al., (2008)
6	Long Reef	295.29	17.76	8	(-1)	-4.43	1970	50	0	1820	2150	1988			Macintyre et al., (2008)
6	Long Reef	295.29	17.76	2	(-1)	-3.08	3250	120	0	3250	3880	3555			Macintyre et al., (2008)
6	Long Reef	295.29	17.76	4	(-1)	-4.17	3620	60	0	3820	4240	4026			Macintyre et al., (2008)

Region	Site	Longitude	Latitude	Material	Sea level limit	Elevation RMSL, m	14C age, years BP (1950) ± Error		δ13C	2σ Calibrated age, years BP			U/Th age ± error, years BP		Source
										Lower	Upper	Median			
6	Long Reef	295.29	17.76	2	(-1)	-6.08	3890	70	0	4140	4630	4396			Macintyre et al., (2008)
	Antigua														
7	Nonsuch Bay	298.32	17.07	2	(-1)	-3.06	2245	85	0	2090	2650	2329			Macintyre et al., (1985)
7	Nonsuch Bay	298.32	17.07	2	(-1)	-11.32	4115	85	0	4420	4910	4689			Macintyre et al., (1985)
7	Nonsuch Bay	298.32	17.07	2	(-1)	-14.62	4830	85	0	5330	5800	5584			Macintyre et al., (1985)
7	Nonsuch Bay	298.32	17.07	2	(-1)	-7.4	2005	75	0	1840	2280	2033			Macintyre et al., (1985)
7	Nonsuch Bay	298.32	17.07	2	(-1)	-1.38	670	75	0	500	780	629			Macintyre et al., (1985)
7	Nonsuch Bay	298.32	17.07	2	(-1)	-5.42	2705	66	0	2720	3090	2882			Macintyre et al., (1985)
7	Nonsuch Bay	298.32	17.07	2	(-1)	-3.7	3710	55	0	3960	4370	4153			Macintyre et al., (1985)
7	Nonsuch Bay	298.32	17.07	2	(-1)	-13.39	5330	80	0	5920	6300	6126			Macintyre et al., (1985)
7	Nonsuch Bay	298.32	17.07	2	(-1)	-15.55	6745	90	0	7430	7810	7614			Macintyre et al., (1985)
7	Nonsuch Bay	298.32	17.07	2	(-1)	-6.1	3365	80	0	3450	3920	3692			Macintyre et al., (1985)
	Guadeloupe														
7	Belle-Plaine canal	298.46	16.28	18	(-1)	-1.65	905	214	-27	0	790	459			Feller et al., (1990)
7	Belle-Plaine canal	298.46	16.28	18	(-1)	-2.26	2000	167	-27	1170	1920	1523			Feller et al., (1990)
7	Belle-Plaine canal	298.46	16.28	18	(-1)	-2.7	2381	214	-27	1410	2490	1963			Feller et al., (1990)
7	Belle-Plaine canal	298.46	16.28	18	(-1)	-3.22	3381	143	-27	2800	3520	3172			Feller et al., (1990)
7	Belle-Plaine canal	298.46	16.28	18	(-1)	-3.65	3929	190	-27	3390	4380	3863			Feller et al., (1990)
7	Belle-Plaine canal	298.46	16.28	18	(-1)	-4.17	4333	143	-27	4000	4800	4401			Feller et al., (1990)
7	Belle-Plaine canal	298.46	16.28	18	(-1)	-6.17	4690	405	-27	3820	5840	4850			Feller et al., (1990)
	Martinique														
7	Vauclin Point Reef	299.17	14.57	2	(-1)	-0.9	560	110	0	320	730	552			Adey & Burke (1976)
7	Vauclin Point Reef	299.17	14.57	2	(-1)	-4	1670	120	0	1340	1920	1637			Adey & Burke (1976)
7	Pinsonelle Reef	299.17	14.61	2	(-1)	-4.5	2110	120	0	1830	2480	2159			Adey & Burke (1976)
7	Rameville Reef	299.17	14.57	2	(-1)	-2	1980	65	0	1810	2230	2002			Lighty et al., (1982)
7	Vauclin Reef	299.17	14.61	2	(-1)	-1	805	55	0	640	900	748			Lighty et al., (1982)
	Barbados														
7	South Coast	300.46	13.04	2	(-1)	-1.3							726	10	Peltier & Fairbanks (2006)
7	South Coast	300.46	13.04	2	(-1)	-21.4							9930	17	Peltier & Fairbanks (2006)
7	South Coast	300.46	13.04	2	(-1)	-24.7							8936	22	Peltier & Fairbanks (2006)
7	South Coast	300.46	13.04	2	(-1)	-25.4							8934	30	Peltier & Fairbanks (2006)
7	South Coast	300.46	13.04	2	(-1)	-28.6							9155	18	Peltier & Fairbanks (2006)
7	South Coast	300.46	13.04	2	(-1)	-33.3							9618	23	Peltier & Fairbanks (2006)
7	South Coast	300.46	13.04	2	(-1)	-33.6							9922	21	Peltier & Fairbanks (2006)
7	South Coast	300.46	13.04	2	(-1)	-36.5							9941	33	Peltier & Fairbanks (2006)
7	South Coast	300.46	13.04	2	(-1)	-41.4							10571	39	Peltier & Fairbanks (2006)
7	South Coast	300.46	13.04	2	(-1)	-42.8							10808	23	Peltier & Fairbanks (2006)
7	South Coast	300.46	13.04	2	(-1)	-44.5							11078	37	Peltier & Fairbanks (2006)
7	South Coast	300.46	13.04	2	(-1)	-93.5							14082	28	Peltier & Fairbanks (2006)
7	South Coast	300.46	13.04	2	(-1)	-94.4							14295	29	Peltier & Fairbanks (2006)
7	South Coast	300.46	13.04	2	(-1)	-95.6							14255	20	Peltier & Fairbanks (2006)
7	South Coast	300.46	13.04	2	(-1)	-97.4							14408	20	Peltier & Fairbanks (2006)
7	South Coast	300.46	13.04	2	(-1)	-97.5							14396	18	Peltier & Fairbanks (2006)
7	South Coast	300.46	13.04	2	(-1)	-98.9							14539	23	Peltier & Fairbanks (2006)
7	South Coast	300.46	13.04	2	(-1)	-111.4							18116	37	Peltier & Fairbanks (2006)
7	South Coast	300.46	13.04	2	(-1)	-112							18174	33	Peltier & Fairbanks (2006)
7	South Coast	300.46	13.04	2	(-1)	-112.2							18448	50	Peltier & Fairbanks (2006)
7	South Coast	300.46	13.04	2	(-1)	-112.2							18218	44	Peltier & Fairbanks (2006)
7	South Coast	300.46	13.04	2	(-1)	-112.2							18176	56	Peltier & Fairbanks (2006)
7	South Coast	300.46	13.04	2	(-1)	-113.2							18549	26	Peltier & Fairbanks (2006)
7	South Coast	300.46	13.04	2	(-1)	-113.7							18746	64	Peltier & Fairbanks (2006)
7	South Coast	300.46	13.04	2	(-1)	-113.9							18783	80	Peltier & Fairbanks (2006)
7	South Coast	300.46	13.04	2	(-1)	-115.5							18716	28	Peltier & Fairbanks (2006)
7	South Coast	300.46	13.04	2	(-1)	-115.7							18806	33	Peltier & Fairbanks (2006)
7	South Coast	300.46	13.04	2	(-1)	-120.3							19075	55	Peltier & Fairbanks (2006)
7	South Coast	300.46	13.04	2	(-1)	-56.9							11392	22	Peltier & Fairbanks (2006)
7	South Coast	300.46	13.04	2	(-1)	-58.6							11511	37	Peltier & Fairbanks (2006)
7	South Coast	300.46	13.04	2	(-1)	-61.5							12002	25	Peltier & Fairbanks (2006)
7	South Coast	300.46	13.04	2	(-1)	-61.8							12203	38	Peltier & Fairbanks (2006)
7	South Coast	300.46	13.04	2	(-1)	-61.9							12170	15	Peltier & Fairbanks (2006)
7	South Coast	300.46	13.04	2	(-1)	-64.8							12798	25	Peltier & Fairbanks (2006)
7	South Coast	300.46	13.04	2	(-1)	-66.6							12844	39	Peltier & Fairbanks (2006)
7	South Coast	300.46	13.04	2	(-1)	-68.2							12993	17	Peltier & Fairbanks (2006)
7	South Coast	300.46	13.04	2	(-1)	-69.8							13088	56	Peltier & Fairbanks (2006)
7	South Coast	300.46	13.04	2	(-1)	-70.3							13179	16	Peltier & Fairbanks (2006)
7	South Coast	300.46	13.04	2	(-1)	-73.7							13555	19	Peltier & Fairbanks (2006)
7	South Coast	300.46	13.04	2	(-1)	-74							13574	26	Peltier & Fairbanks (2006)
7	South Coast	300.46	13.04	2	(-1)	-74.2							13578	26	Peltier & Fairbanks (2006)
7	South Coast	300.46	13.04	2	(-1)	-74.5							13632	16	Peltier & Fairbanks (2006)
7	South Coast	300.46	13.04	2	(-1)	-87.5							29540	41	Peltier & Fairbanks (2006)
7	South Coast	300.46	13.04	2	(-1)	-87.8							30147	57	Peltier & Fairbanks (2006)
7	South Coast	300.46	13.04	2	(-1)	-88.2							30225	75	Peltier & Fairbanks (2006)
7	South Coast	300.46	13.04	2	(-1)	-88.8							30298	110	Peltier & Fairbanks (2006)
7	South Coast	300.46	13.04	2	(-1)	-88.9							30242	48	Peltier & Fairbanks (2006)
7	South Coast	300.46	13.04	2	(-1)	-111.9							17580	69	Peltier & Fairbanks (2006)
7	South Coast	300.46	13.04	2	(-1)	-96.3							14573	15	Peltier & Fairbanks (2006)
7	South Coast	300.46	13.04	2	(-1)	-107.9							18408	26	Peltier & Fairbanks (2006)
7	South Coast	300.46	13.04	2	(-1)	-108.3							19392	29	Peltier & Fairbanks (2006)
7	South Coast	300.46	13.04	2	(-1)	-109.9							19518	33	Peltier & Fairbanks (2006)
7	South Coast	300.46	13.04	2	(-1)	-110.3							19708	26	Peltier & Fairbanks (2006)

Region	Site	Longitude	Latitude	Material	Sea level limit	Elevation RMSL, m	14C age, years BP (1950) ± Error		δ13C	2σ Calibrated age, years BP			U/Th age ± error, years BP		Source
										Lower	Upper	Median			
7	South Coast	300.46	13.04	2	(-1)	-58.2							11512	17	Peltier & Fairbanks (2006)
7	South Coast	300.46	13.04	2	(-1)	-58.3							11391	36	Peltier & Fairbanks (2006)
7	South Coast	300.46	13.04	8	(-1)	-82.2							12179	33	Peltier & Fairbanks (2006)
7	South Coast	300.46	13.04	8	(-1)	-82.4							12029	30	Peltier & Fairbanks (2006)
7	South Coast	300.46	13.04	8	(-1)	-82.5							11774	41	Peltier & Fairbanks (2006)
7	South Coast	300.46	13.04	8	(-1)	-82.9							12212	64	Peltier & Fairbanks (2006)
7	South Coast	300.46	13.04	8	(-1)	-83.7							12016	28	Peltier & Fairbanks (2006)
7	South Coast	300.46	13.04	8	(-1)	-84.1							12103	39	Peltier & Fairbanks (2006)
7	South Coast	300.46	13.04	8	(-1)	-84.4							12309	36	Peltier & Fairbanks (2006)
7	South Coast	300.46	13.04	8	(-1)	-85.4							12303	14	Peltier & Fairbanks (2006)
7	South Coast	300.46	13.04	8	(-1)	-85.8							12680	75	Peltier & Fairbanks (2006)
7	South Coast	300.46	13.04	8	(-1)	-133.2							22160	62	Peltier & Fairbanks (2006)
7	South Coast	300.46	13.04	8	(-1)	-134.5							22536	46	Peltier & Fairbanks (2006)
7	South Coast	300.46	13.04	8	(-1)	-134.7							22574	48	Peltier & Fairbanks (2006)
7	South Coast	300.46	13.04	8	(-1)	-136.5							23044	37	Peltier & Fairbanks (2006)
7	South Coast	300.46	13.04	8	(-1)	-136.7							23296	61	Peltier & Fairbanks (2006)
7	South Coast	300.46	13.04	8	(-1)	-136.7							23039	38	Peltier & Fairbanks (2006)
7	South Coast	300.46	13.04	8	(-1)	-138.1							23867	44	Peltier & Fairbanks (2006)
7	South Coast	300.46	13.04	8	(-1)	-138.2							23858	69	Peltier & Fairbanks (2006)
7	South Coast	300.46	13.04	8	(-1)	-141.6							25645	40	Peltier & Fairbanks (2006)
7	South Coast	300.46	13.04	8	(-1)	-141.8							25743	61	Peltier & Fairbanks (2006)
7	South Coast	300.46	13.04	8	(-1)	-142							25639	45	Peltier & Fairbanks (2006)
7	South Coast	300.46	13.04	8	(-1)	-142.2							25741	53	Peltier & Fairbanks (2006)
7	South Coast	300.46	13.04	8	(-1)	-142.3							25866	53	Peltier & Fairbanks (2006)
7	South Coast	300.46	13.04	8	(-1)	-142							25622	63	Peltier & Fairbanks (2006)
7	South Coast	300.46	13.04	8	(-1)	-142.3							26044	40	Peltier & Fairbanks (2006)
7	South Coast	300.46	13.04	8	(-1)	-100.5							14563	65	Peltier & Fairbanks (2006)
7	South Coast	300.46	13.04	8	(-1)	-85.4							11988	61	Peltier & Fairbanks (2006)
7	South Coast	300.46	13.04	8	(-1)	-87.5							12533	25	Peltier & Fairbanks (2006)
7	South Coast	300.46	13.04	8	(-1)	-89.6							12783	65	Peltier & Fairbanks (2006)
7	South Coast	300.46	13.04	8	(-1)	-111.5							19770	31	Peltier & Fairbanks (2006)
7	South Coast	300.46	13.04	8	(-1)	-112.7							19483	27	Peltier & Fairbanks (2006)
7	South Coast	300.46	13.04	8	(-1)	-112.9							19638	25	Peltier & Fairbanks (2006)
7	South Coast	300.46	13.04	8	(-1)	-113							19650	110	Peltier & Fairbanks (2006)
7	South Coast	300.46	13.04	8	(-1)	-114.8							19913	34	Peltier & Fairbanks (2006)
7	South Coast	300.46	13.04	8	(-1)	-118.1							20575	31	Peltier & Fairbanks (2006)
7	South Coast	300.46	13.04	8	(-1)	-119.3							20632	31	Peltier & Fairbanks (2006)
7	South Coast	300.46	13.04	12	(-1)	-20.3							7376	17	Peltier & Fairbanks (2006)
7	South Coast	300.46	13.04	12	(-1)	-86.1							12937	33	Peltier & Fairbanks (2006)
7	South Coast	300.46	13.04	12	(-1)	-86.1							12873	24	Peltier & Fairbanks (2006)
7	South Coast	300.46	13.04	12	(-1)	-126.7							20339	79	Peltier & Fairbanks (2006)
7	South Coast	300.46	13.04	12	(-1)	-131.5							21714	41	Peltier & Fairbanks (2006)
7	South Coast	300.46	13.04	12	(-1)	-131.8							21802	41	Peltier & Fairbanks (2006)
7	South Coast	300.46	13.04	12	(-1)	-132							21858	41	Peltier & Fairbanks (2006)
7	South Coast	300.46	13.04	12	(-1)	-132.8							21966	39	Peltier & Fairbanks (2006)
7	South Coast	300.46	13.04	7	(-1)	-138.6							24883	55	Peltier & Fairbanks (2006)
7	South Coast	300.46	13.04	7	(-1)	-138.8							24579	41	Peltier & Fairbanks (2006)
7	South Coast	300.46	13.04	7	(-1)	-140.6							25265	225	Peltier & Fairbanks (2006)
7	South Coast	300.46	13.04	7	(-1)	-140.7							25045	30	Peltier & Fairbanks (2006)
7	South Coast	300.46	13.04	7	(-1)	-150.5							31366	56	Peltier & Fairbanks (2006)
7	South Coast	300.46	13.04	7	(-1)	-86.2							12411	69	Peltier & Fairbanks (2006)
7	South Coast	300.46	13.04	7	(-1)	-111.7							19434	30	Peltier & Fairbanks (2006)
7	South Coast	300.46	13.04	7	(-1)	-114.2							19595	44	Peltier & Fairbanks (2006)
7	South Coast	300.46	13.04	7	(-1)	-114.3							19627	34	Peltier & Fairbanks (2006)
7	South Coast	300.46	13.04	1	(-1)	-52							10527	46	Peltier & Fairbanks (2006)
	Panama														
8	Gatun Basin	280.05	9.18	18	(0)	-13.11	6230	80	-27	6400	6840	6620			Bartlett & Bargoorn (1973)
8	Gatun Basin	280.12	9.18	18	(0)	-15.54	7300	130	-27	7470	7970	7725			Bartlett & Bargoorn (1973)
8	Gatun Basin	280.08	9.18	18	(0)	-19.51	8560	130	-27	8760	9460	9141			Bartlett & Bargoorn (1973)
8	Gatun Basin	280.13	9.27	18	(0)	-32.92	9600	300	-27	9630	11150	10408			Bartlett & Bargoorn (1973)
8	Gatun Basin	280.13	9.27	18	(0)	-48.16	11300	200	-27	12260	13190	12757			Bartlett & Bargoorn (1973)
8	Galeta Point Reef	280.14	9.41	2	(-1)	-7.56	6285	110	0	6920	7420	7195			Macintyre & Glynn (1976)
8	Galeta Point Reef	280.14	9.41	2	(-1)	-5.5	3535	80	0	3660	4160	3914			Macintyre & Glynn (1976)
8	Galeta Point Reef	280.14	9.41	2	(-1)	-3.8	3755	85	0	3950	4480	4214			Macintyre & Glynn (1976)
8	Galeta Point Reef	280.14	9.41	2	(-1)	-8.99	4790	85	0	5310	5730	5537			Macintyre & Glynn (1976)
8	Galeta Point Reef	280.14	9.41	2	(-1)	-12.5	6150	95	0	6790	7270	7049			Macintyre & Glynn (1976)
8	Galeta Point Reef	280.14	9.41	2	(-1)	-1.88	2605	55	0	2610	2950	2776			Macintyre & Glynn (1976)
8	Galeta Point Reef	280.14	9.41	2	(-1)	-6	5120	65	0	5700	6110	5893			Macintyre & Glynn (1976)
8	Galeta Point Reef	280.14	9.41	2	(-1)	-6.8	5610	95	0	6210	6650	6426			Macintyre & Glynn (1976)
8	Galeta Point Reef	280.14	9.41	2	(-1)	-1.27	2090	50	0	1970	2310	2141			Macintyre & Glynn (1976)
8	Galeta Point Reef	280.14	9.41	2	(-1)	-12.3	6500	100	0	7200	7590	7401			Macintyre & Glynn (1976)
8	Galeta Point Reef	280.14	9.41	2	(-1)	-2.04	3030	80	0	3050	3520	3289			Macintyre & Glynn (1976)
8	Galeta Point Reef	280.14	9.41	2	(-1)	-11.5	6860	110	0	7510	7940	7723			Macintyre & Glynn (1976)
8	Galeta Point Reef	280.14	9.41	2	(-1)	-5.8	4840	85	0	5360	5850	5596			Macintyre & Glynn (1976)
	Venezuela														
9a	Playa Medina	296.99	10.71	18	(-1)	-9.29	6960	70	-27	7270	7560	7422			Rull et al., (1999)
9a	Cayo Sal	294.74	10.95	18	(-1)	-1.49	2690	75	-27	2110	2640	2336			Weiss (1979)
	Curacao														
9a	Curacao	291.18	12.12	16	(0)	-3.1	5346	47	-27	5550	5850	5662			Milne et al., (2005)
9a	Curacao	291.18	12.12	16	(0)	-4.5	6220	50	-27	6440	6770	6607			Milne et al., (2005)
9a	Curacao	291.18	12.12	16	(0)	-0.4	1692	37	-27	1060	1300	1202			Milne et al., (2005)

Region	Site	Longitude	Latitude	Material	Sea level limit	Elevation RMSL, m	14C age, years BP (1950) ± Error		δ13C	2σ Calibrated age, years BP			U/Th age ± error, years BP	Source
										Lower	Upper	Median		
9a	Curacao	291.18	12.12	16	(0)	-0.3	1745	37	-27	1130	1360	1251		Milne et al., (2005)
9a	Curacao	291.18	12.12	16	(0)	-1.1	2659	40	-27	2130	2450	2288		Milne et al., (2005)
	Trinidad													
9b	Maracas Swamp	298.56	10.76	18	(-1)	-2.18	2930	80	-27	2360	2820	2623		Ramcharan (2004)
9b	Maracas Swamp	298.56	10.76	18	(-1)	-3.68	3960	60	-27	3680	4090	3893		Ramcharan (2004)
9b	Maracas Swamp	298.56	10.76	18	(-1)	-8.23	5880	60	-27	6060	6410	6250		Ramcharan (2004)
9b	Nariva Swamp (Sand Hill West)	298.91	10.44	18	(-1)	-2.13	2720	55	-27	2170	2640	2379		Ramcharan (2004)
9b	Nariva Swamp (Sand Hill West)	298.91	10.44	17	(0)	-5	4790	70	-27	4820	5250	5004		Ramcharan (2004)
9b	Nariva Swamp (Sand Hill West)	298.91	10.44	18	(-1)	-6.66	5260	70	-27	5330	5750	5573		Ramcharan (2004)
9b	Nariva Swamp (Trough)	298.95	10.46	17	(0)	-5.58	4250	70	-27	4060	4510	4288		Ramcharan (2004)

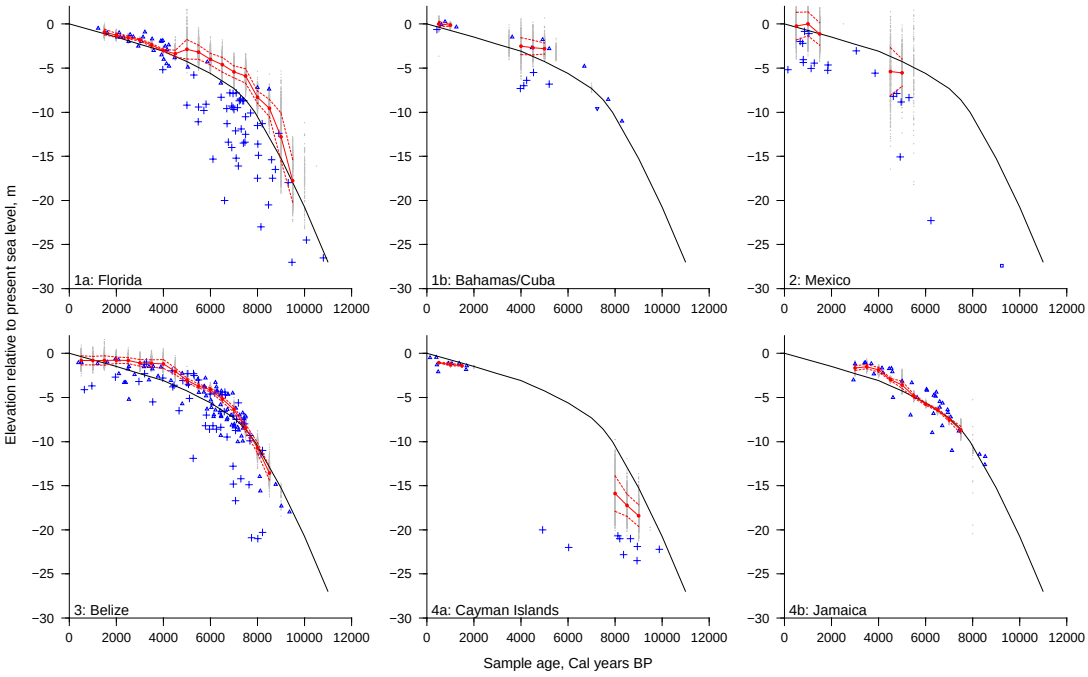

Figure A-2: Relative sea-level curves: Regions 1a to 4b (1 kyr window)

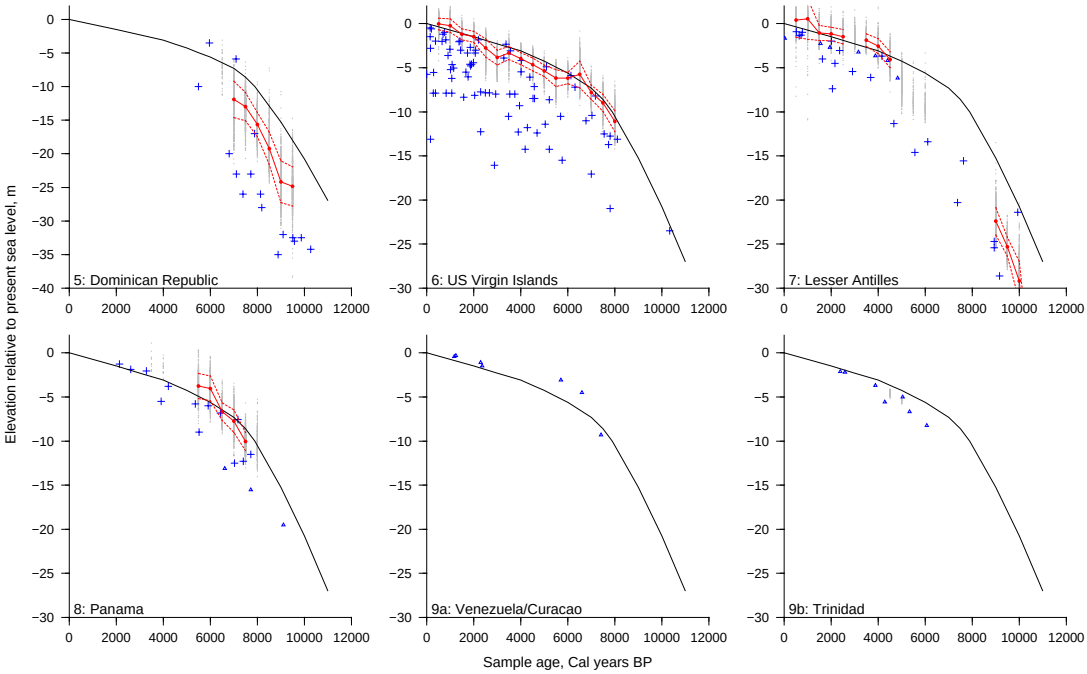

Figure A-3: Relative sea-level curves: Regions 5 to 9b (1 kyr window)

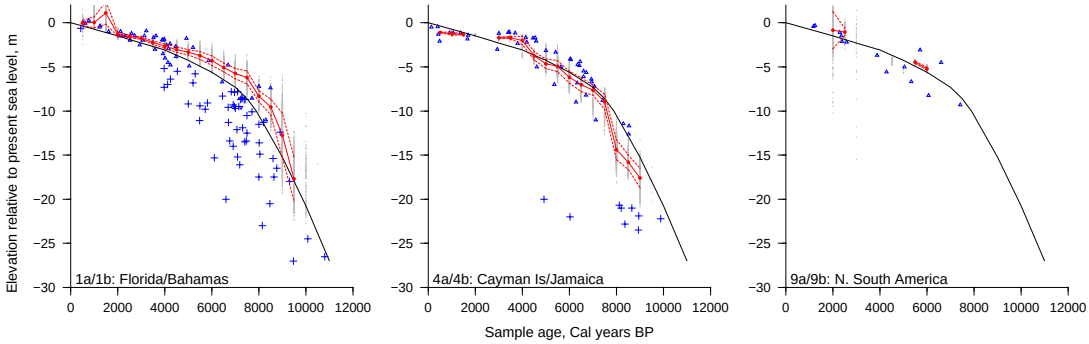

Figure A-4: Relative sea-level curves: Regions 1, 4, 9 (1 kyr window)

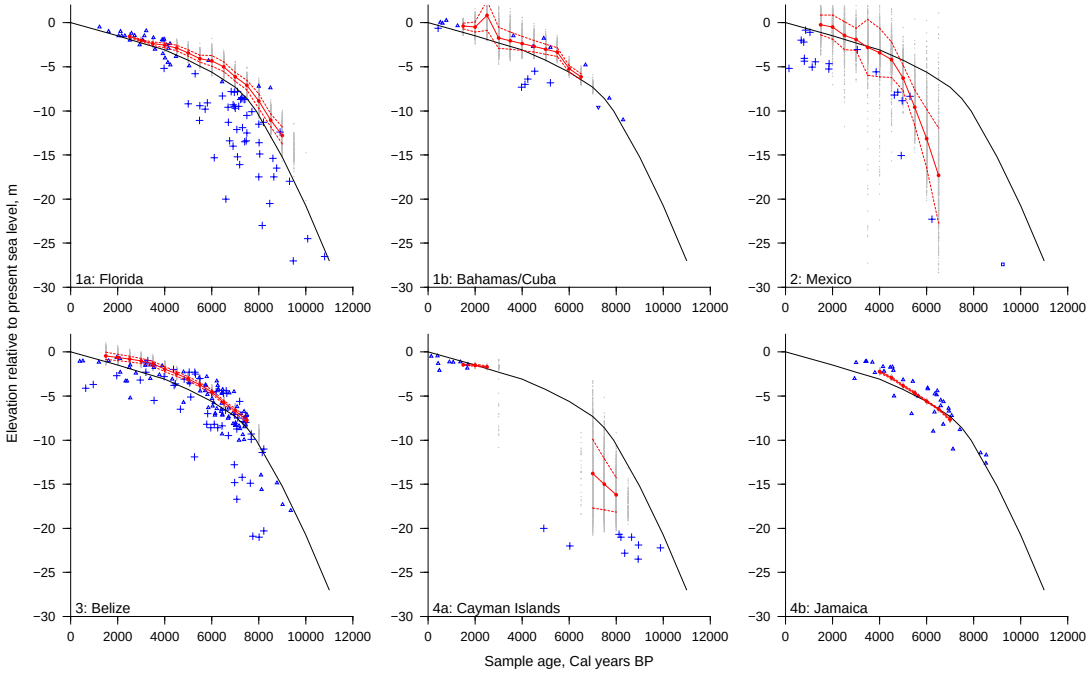

Figure A-5: Relative sea-level curves: Regions 1a to 4b (3 kyr window)

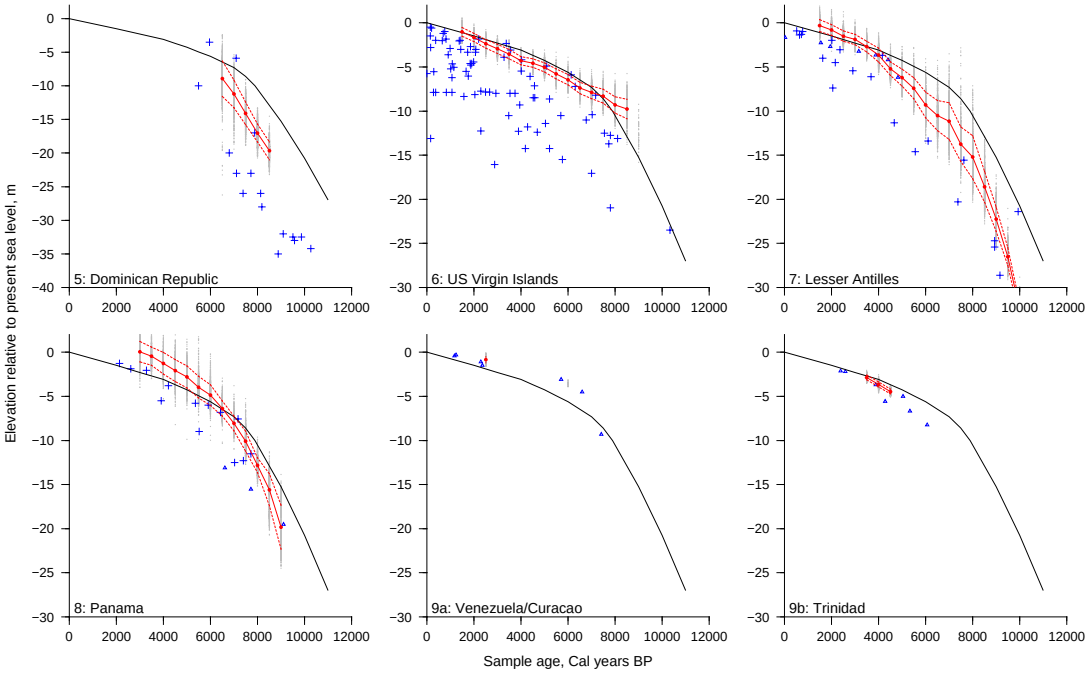

Figure A-6: Relative sea-level curves: Regions 5 to 9b (3 kyr window)

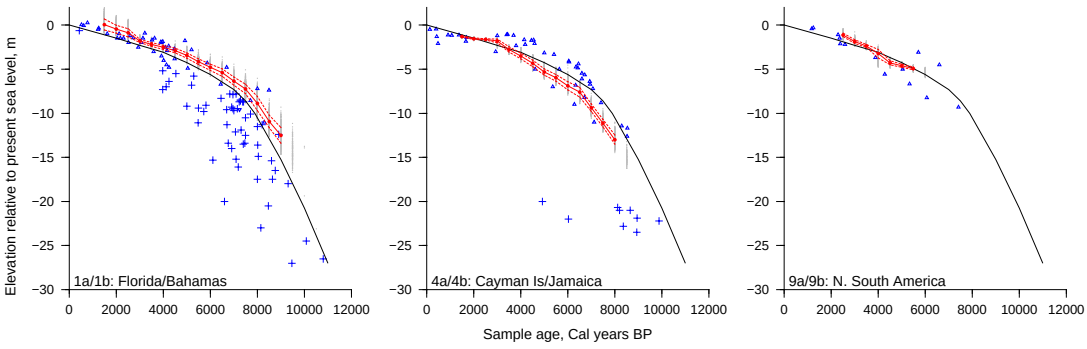

Figure A-7: Relative sea-level curves: Regions 1, 4, 9 (3 kyr window)

Appendix B

RSL curves using uniform distributions

This Appendix shows relative sea-level curves derived using the same method as in Chapter 2 and Appendix A. However, instead of using data derived depth probability distributions, I use uniform depth distributions. Hence, depths from 0 to 30 m (for corals) and -1 to 1 m, -0.5 to 0.5 m and -0.25 to 0.25 m (for mangroves) have the same probability.

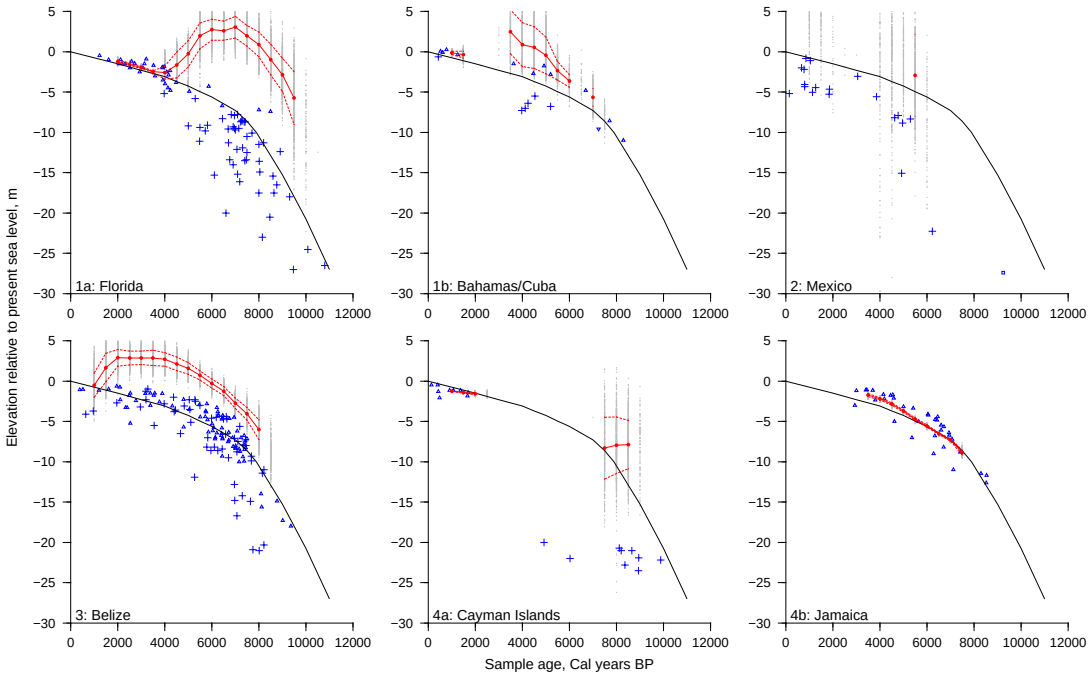

Figure B-1: Relative sea-level curves: Regions 1a to 4b (2 kyr window)

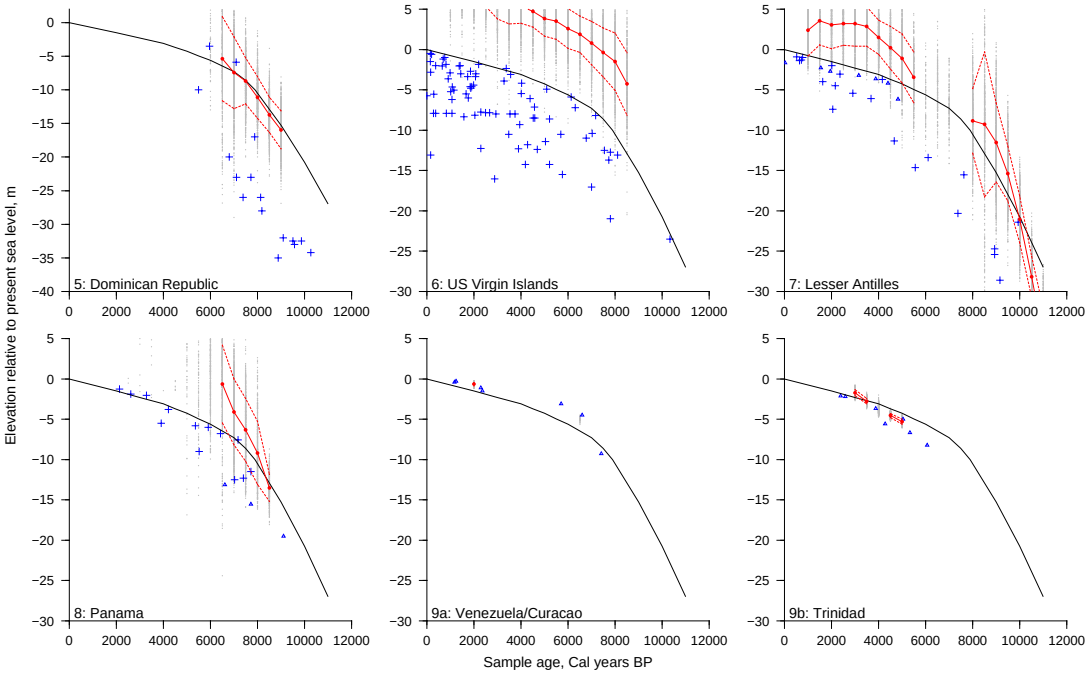

Figure B-2: Relative sea-level curves: Regions 5 to 9b (2 kyr window)

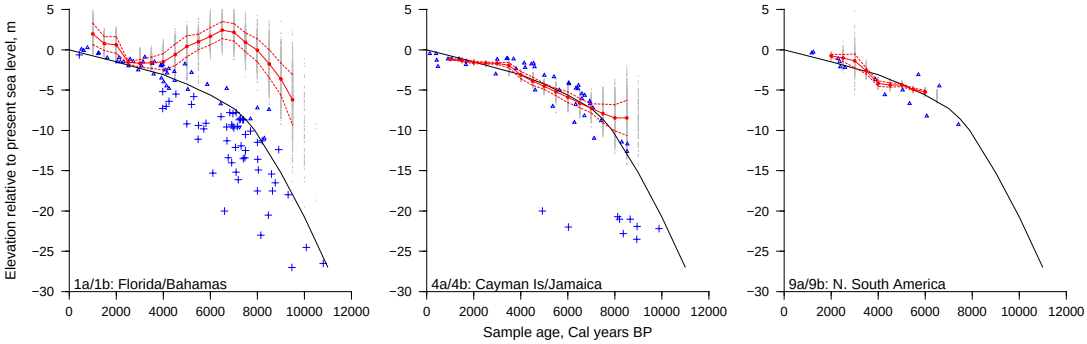

Figure B-3: Relative sea-level curves: Regions 1, 4, 9 (2 kyr window)

Appendix C

χ^2 misfit models

The following section shows a series of Figures each of which shows model relative sea-level (RSL) curves and contour plots of the χ^2 misfit between them and two types of data. First, the data derived RSL curves and second, the sea-level indicator derived RSL positions.

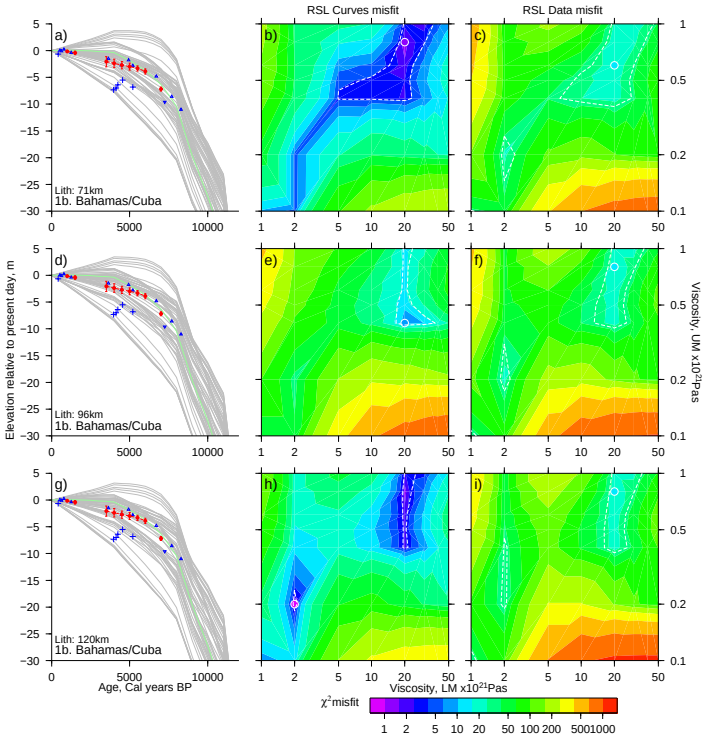

Figure C-1: Bahamas region (1b) χ^2 misfit: model, data and sea-level curves. **a**, **d**, **g**: age-elevation plots for lithospheric thicknesses, 71, 96 and 120 km respectively. GIA model RSL curves (grey), VM2 (Peltier, 2004) GIA model RSL curve (green), data derived RSL curve (red), RSL indicators (blue symbols). Contour plots **b**, **e**, **h** show χ^2 misfit between GIA model and data derived RSL curves ($N = 9$ points). Contour plots **c**, **f**, **i** show χ^2 misfit between GIA model RSL curves and RSL indicator realisations ($N = 18$ points). In both cases, the white outlined coloured circle represents the model upper and lower mantle viscosities which minimise the misfit and the dashed white line represents the 95% confidence contour (inside which the minimum χ^2 value lies).

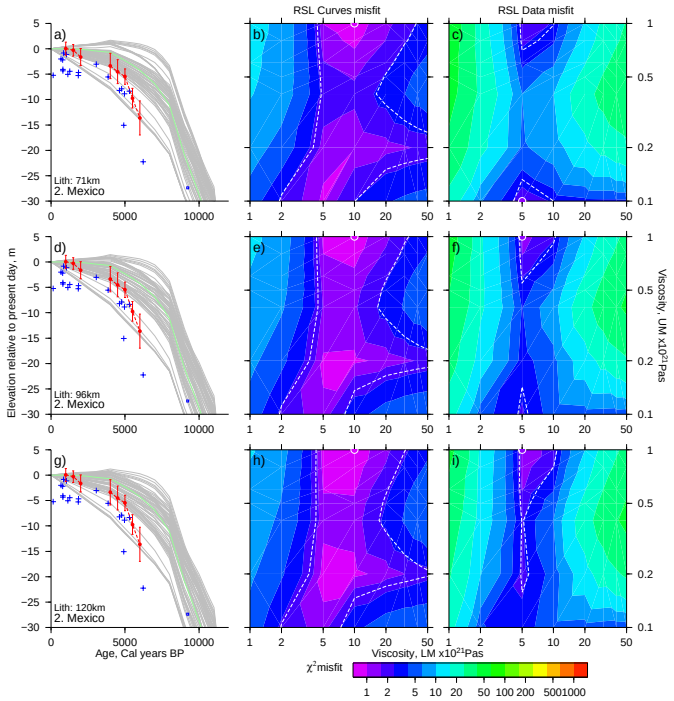

Figure C-2: As in Figure C-1 but for Mexico region (2). Data derived RSL curves ($N = 8$ points). Sea-level indicator derived RSL position ($N = 20$ points)

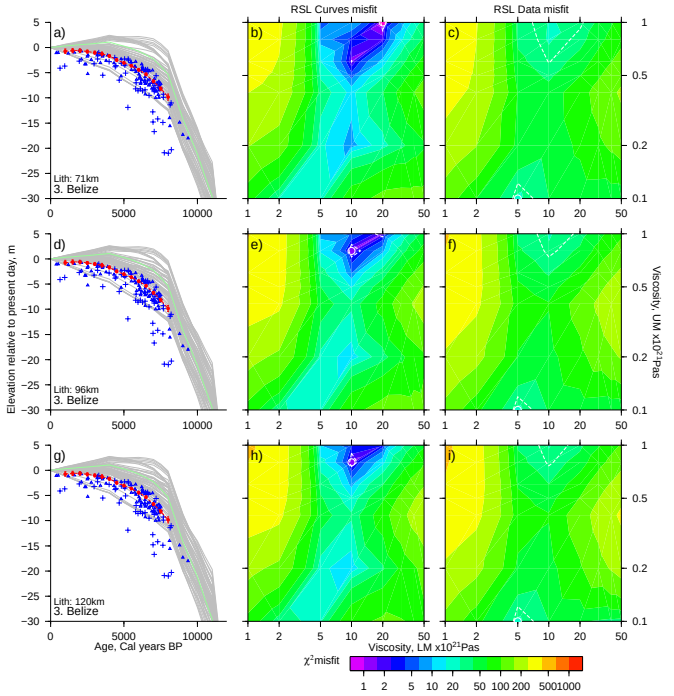

Figure C-3: As in Figure 3.5 but for Belize region (3). Data derived RSL curves ($N = 15$ points). Sea-level indicator derived RSL position ($N = 132$ points)

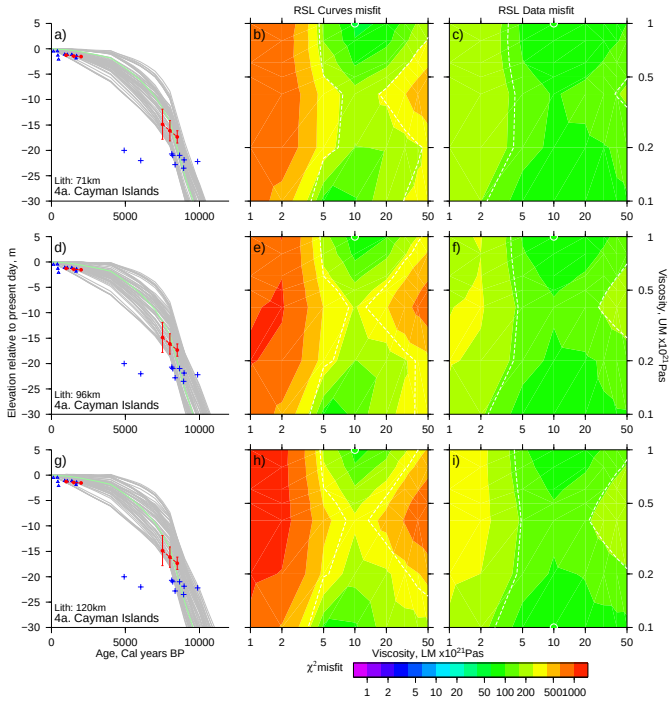

Figure C-4: As in Figure C-1 but for Cayman Islands region (4a). Data derived RSL curves ($N = 6$ points). Sea-level indicator derived RSL position ($N = 35$ points)

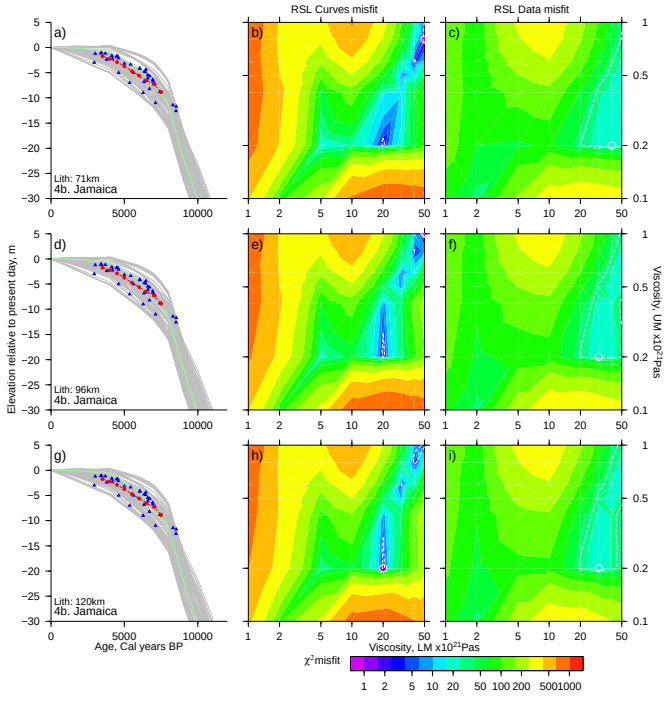

Figure C-5: As in Figure C-1 but for Jamaica region (4b). Data derived RSL curves ($N = 9$ points). Sea-level indicator derived RSL position ($N = 18$ points)

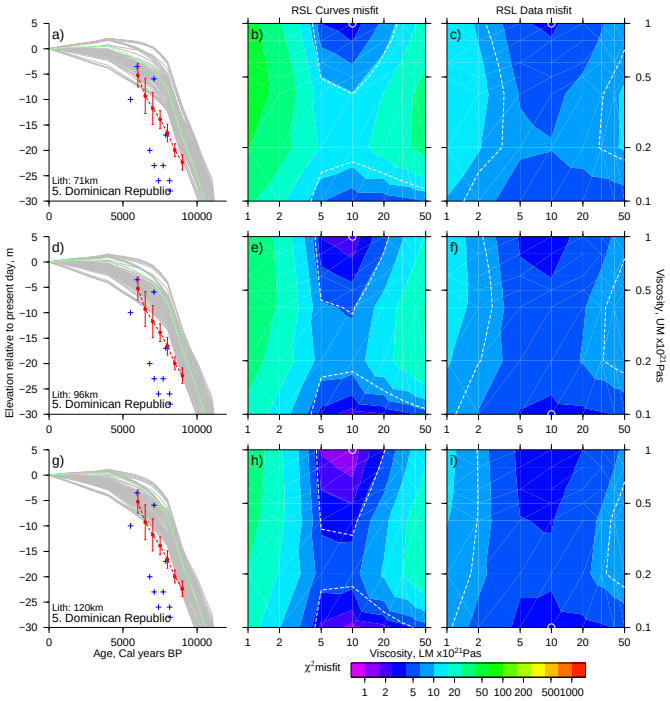

Figure C-6: As in Figure C-1 but for Dominican Republic region (5). Data derived RSL curves ($N = 7$ points). Sea-level indicator derived RSL position ($N = 16$ points)

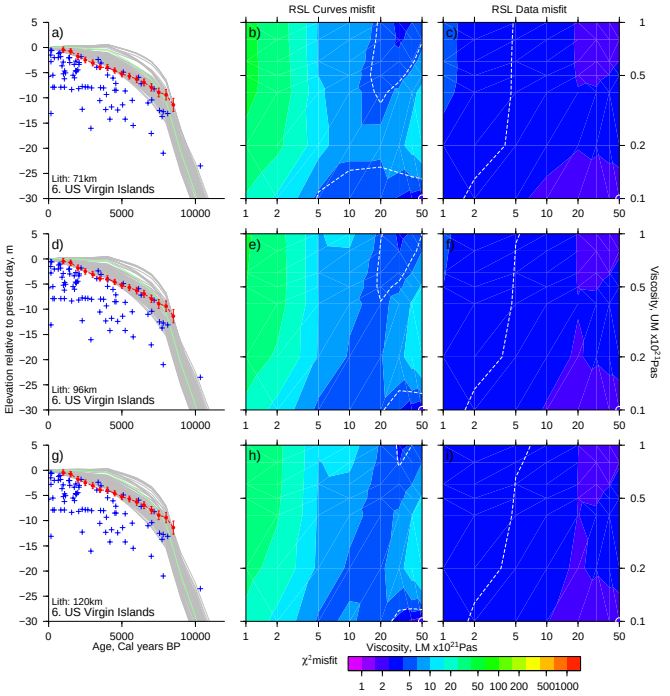

Figure C-7: As in Figure C-1 but for US Virgin Islands region (6). Data derived RSL curves ($N = 16$ points). Sea-level indicator derived RSL position ($N = 79$ points)

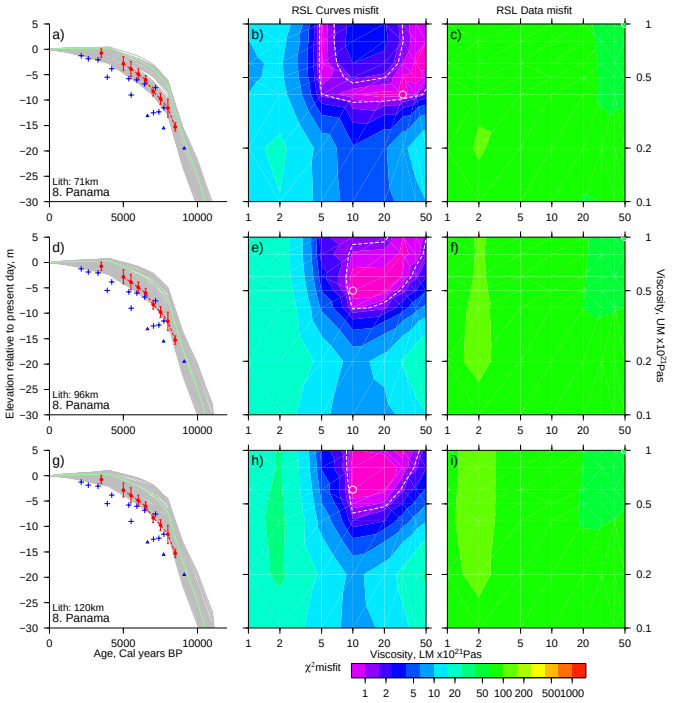

Figure C-8: As in Figure C-1 but for Panama region (8). Data derived RSL curves ($N = 9$ points). Sea-level indicator derived RSL position ($N = 18$ points)

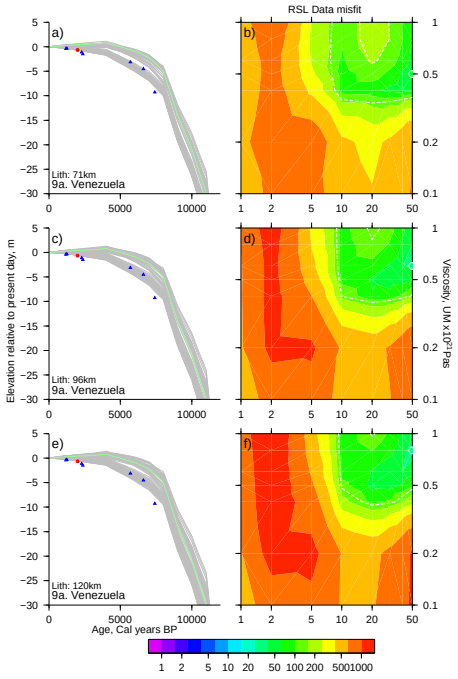

Figure C-9: As in Figure C-1 but for Venezuela region (9a). Data derived RSL curves ($N = 1$ points), therefore no misfit calculation attempted. Sea-level indicator derived RSL position ($N = 7$ points)

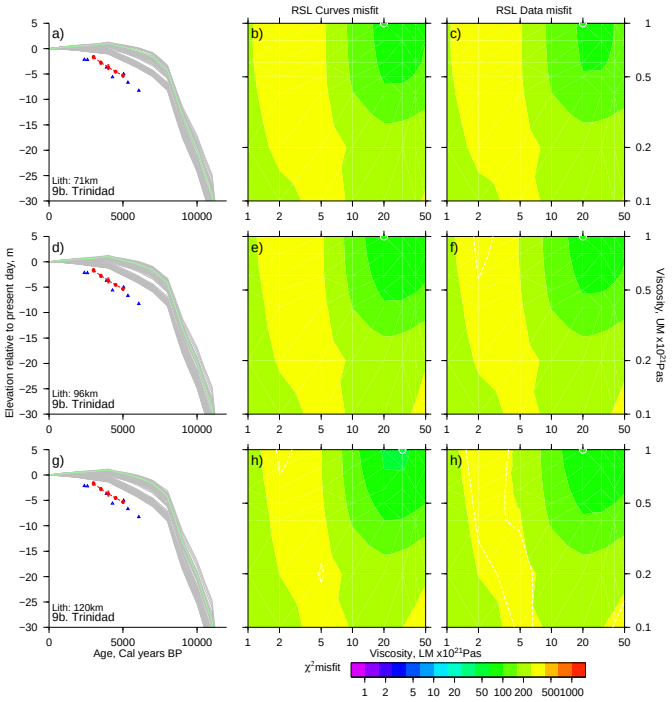

Figure C-10: As in Figure C-1 but for Trinidad region (9b). Data derived RSL curves (N = 7 points). Sea-level indicator derived RSL position (N = 5 points)

Appendix D

Tide gauge processing steps

The following section contains a selection of tide gauge RLR records from the 48 available on the PSMSL database (Woodworth and Player (2003), http://www.psmsl.org/). The layout is identical to that of Figure 4.4 and shows the different processing steps described in the text after Mazzotti et al. (2008).

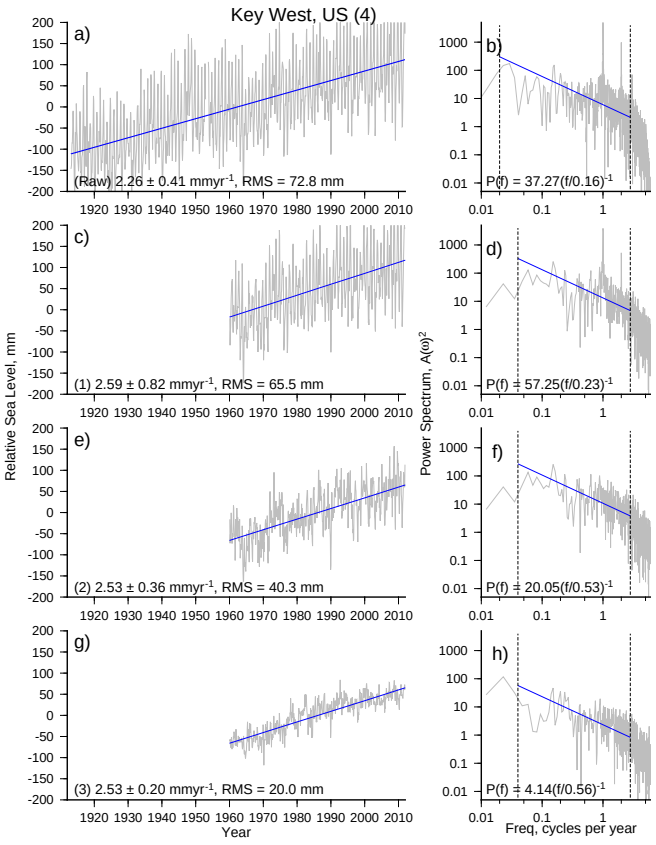

Figure D-1: Monthly mean tide gauge record for Key West (Florida, USA) (**a**, **c**, **e** and **g**). Grey lines show raw (**a**) and corrected (**c**, **e**, **g**) observations. In **a**, **c**, **e** and **g**, blue lines show linear RSL trends. **b**, **d**, **f**, **h** show power spectra of raw and corrected observations. Raw observations corrected in three ways following Mazzotti et al. (2008). (1) inverse barometric correction. (2) mean seasonal correction. (3) regional common mode correction.

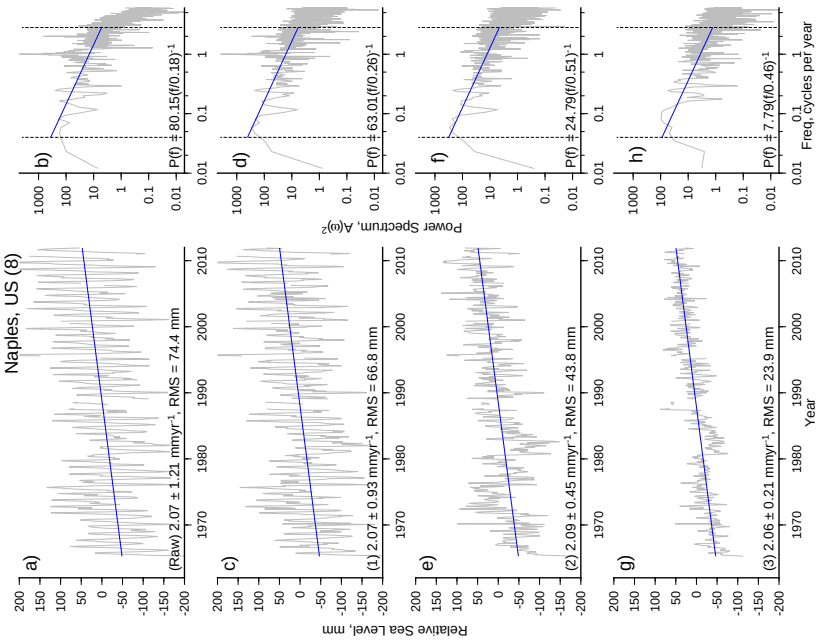

Figure D-2: Tide gauge processing steps: Naples (Florida, USA)

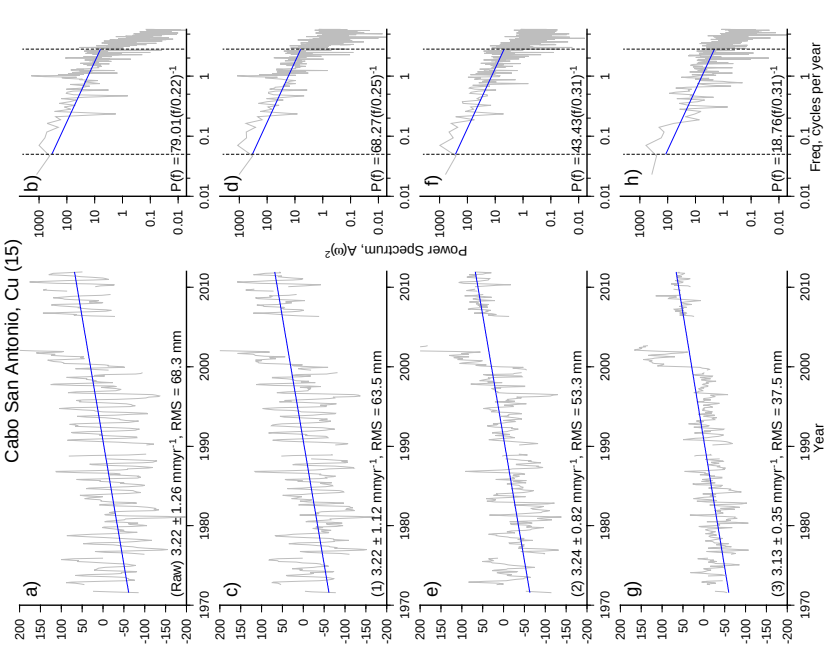

Figure D-3: Tide gauge processing steps: Cabo San Antonio (Cuba)

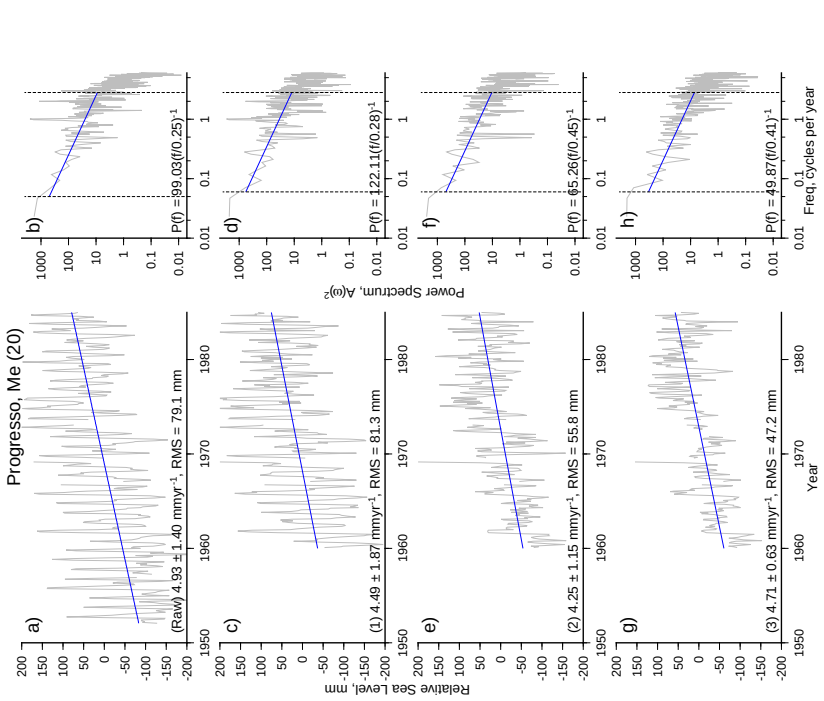

Figure D-4: Tide gauge processing steps: Progresso (Mexico)

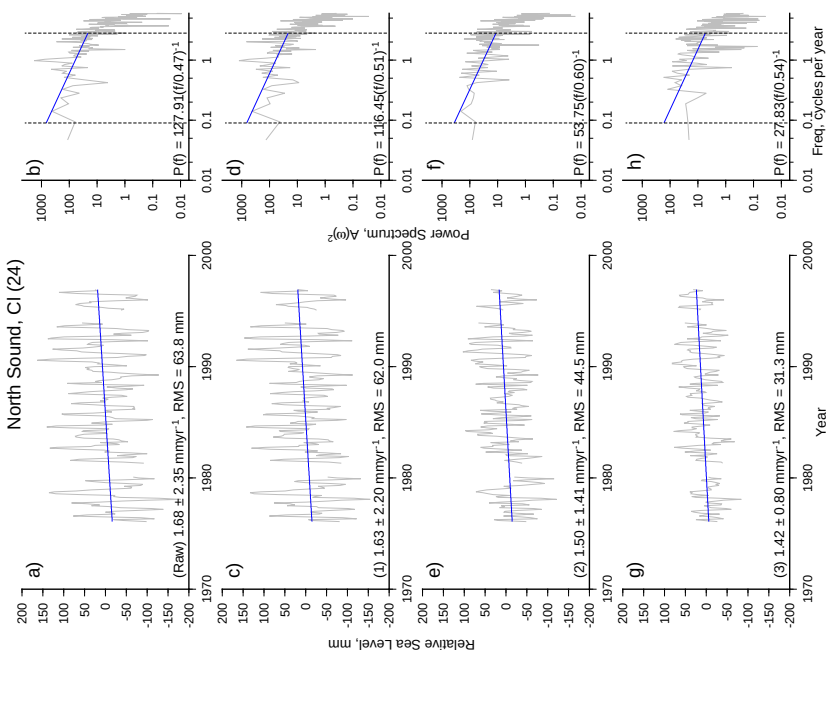

Figure D-5: Tide gauge processing steps: North South (Cayman Is.)

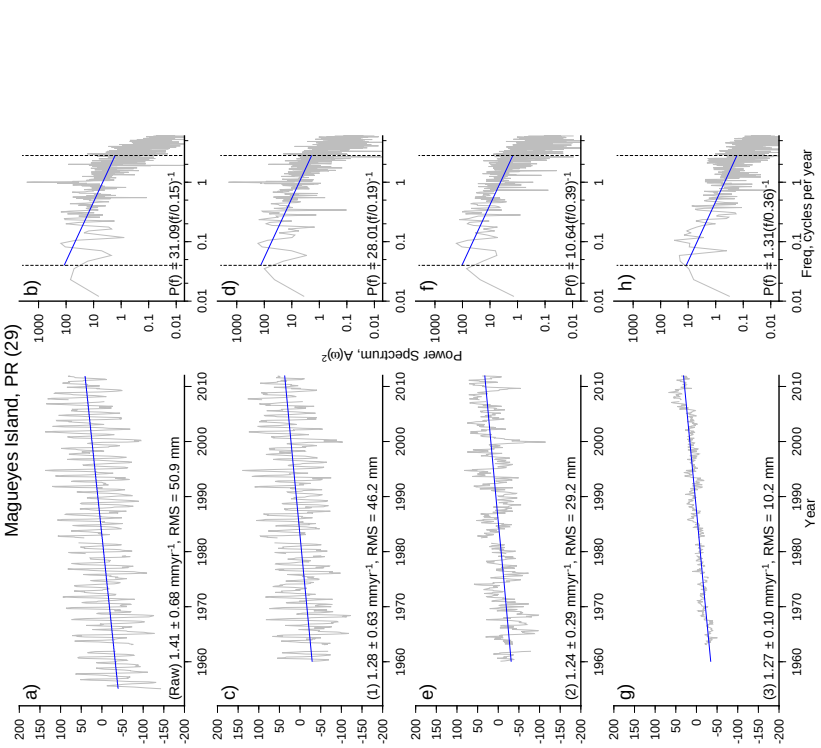

Figure D-6: Tide gauge processing steps: Magueyes Island (Puerto Rico)

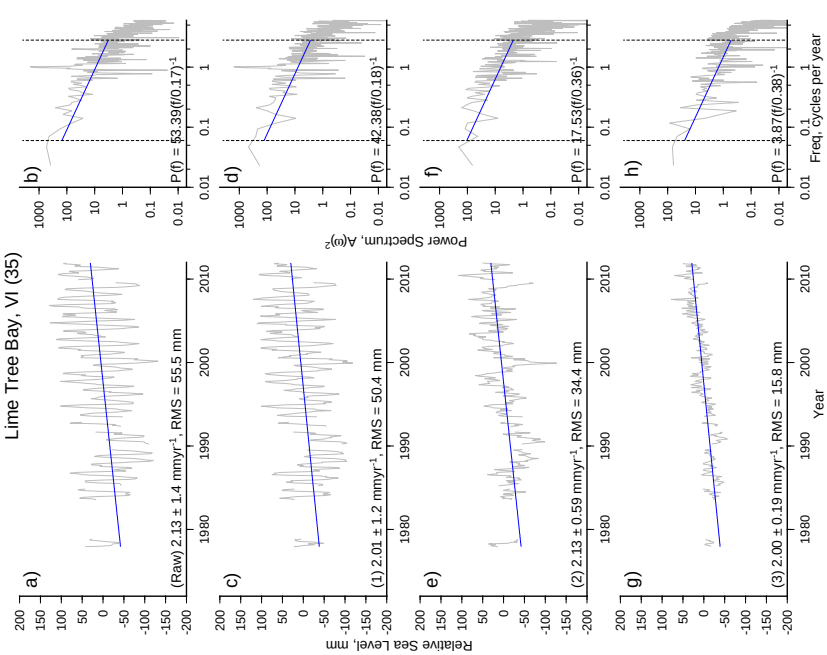

Figure D-7: Tide gauge processing steps: Lime Tree Bay (USVI)

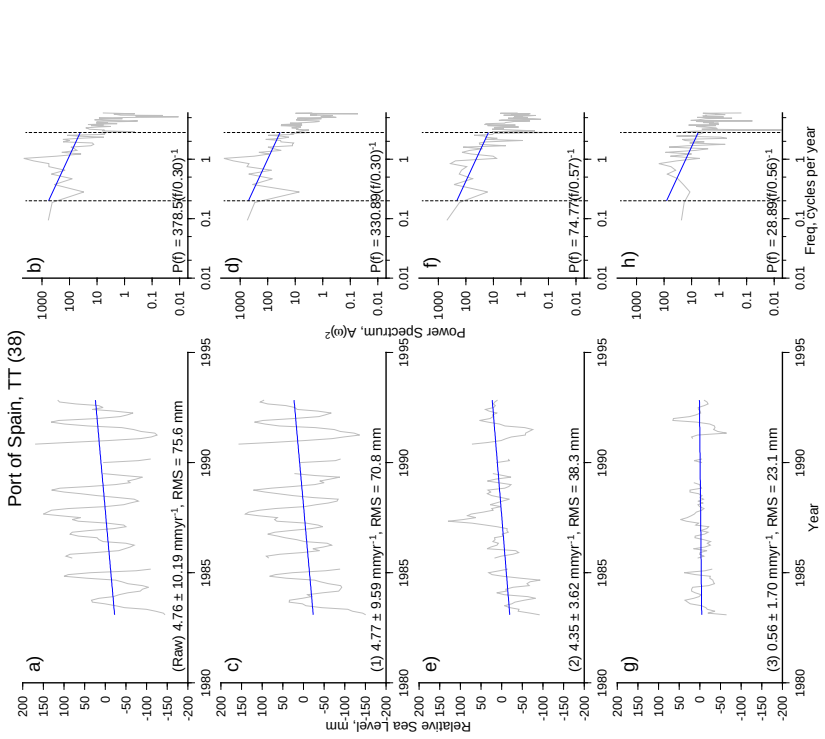

Figure D-8: Tide gauge processing steps: Port of Spain (Trinidad)

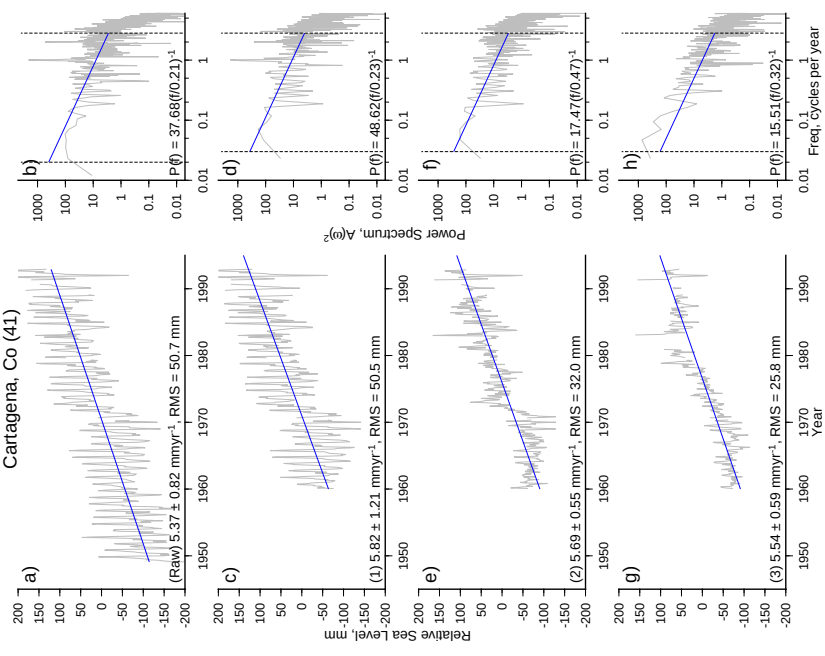

Figure D-9: Tide gauge processing steps: Cartagena (Colombia)

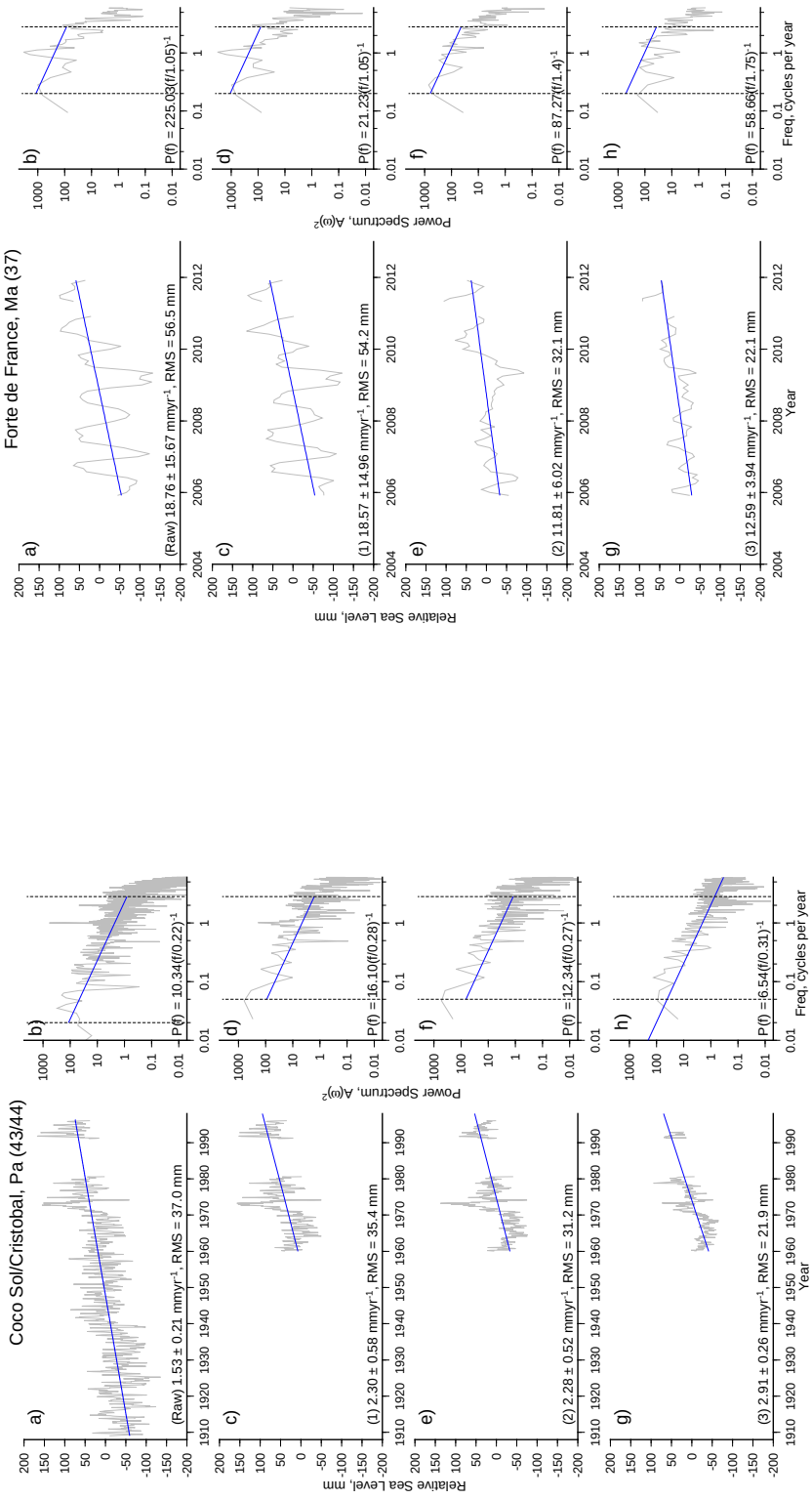

Figure D-10: Tide gauge processing steps: Forte de France (Martinique)

Figure D-11: Tide gauge processing steps: Cristobal & Coco Sol (Panama)

Appendix E

Collated Tide gauge, Altimetry, GPS and Prehistoric rates

The following section shows contour plots of WRMS misfit calculations between GIA model uplift rates and GPS velocities (see text for details). Also, there are tables showing, recent RSL rates calculated from the sea-level indicators (Chapter 2) and from the GIA model sea-level curves (Chapter 3), and RSL/ASL rates at tide gauge locations for two time spans with paired GPS sites and their vertical ground motion.

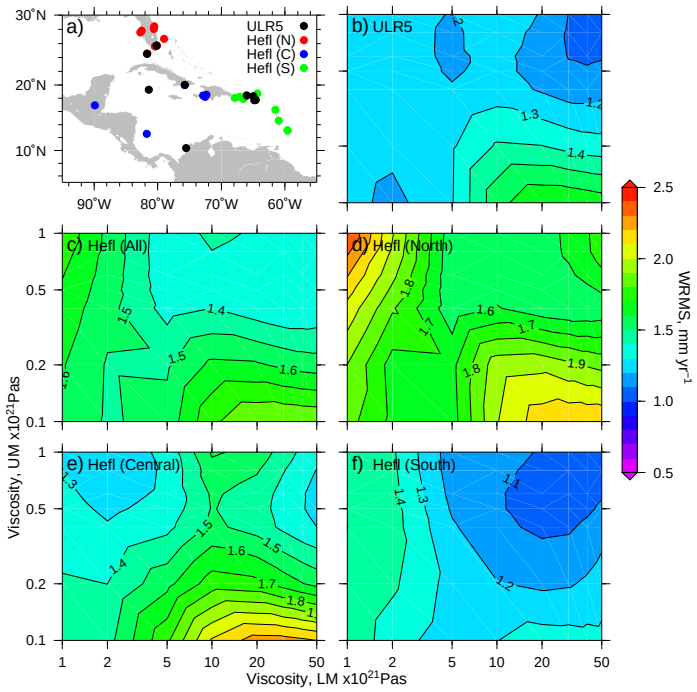

Figure E-1: **a**: GPS sites (circles) used for analysis: Heflin (September 2013), north (red), central (blue) and south-east (green); Santamaría-Gómez et al. (2012), ULR5 (black). **b - d**: WRMS values between GIA model predicted uplift rate (for range of upper and lower mantle viscosity parameters) and GPS uplift rates (b: ULR5, Santamaría-Gómez et al. (2012); c: All sites (Heflin, September 2013); d,e,f: north, central and south-east sites (Heflin, September 2013). Lithospheric thickness is 96 km.

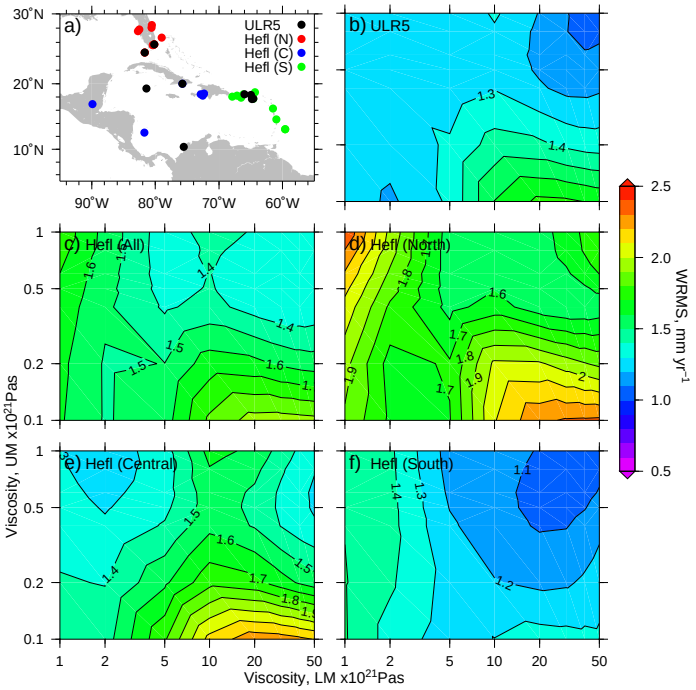

Figure E-2: As in Figure E-1 for GIA model parameter 120 km lithospheric thickness.

Table E-1: RSL rate of sea-level curves at closest age before present and optimal model (and range) predicted present RSL and VGM and RSL at 500 years BP. Optimal model Earth parameters: lithospheric thickness, 71km, upper and lower mantle viscosities, 0.5 and 10 x 10^{21} Pa s respectively

			Indicator derived RSL rates using 2000 year time window centred on Cal age BP, mm yr^{-1}			GIA model predictions, mm yr^{-1}											
						RSL rate at Cal age BP			RSL rate at 500 years BP			RSL rate at present			VGM rate at present		
Region	Lon	Lat	Cal age BP	Rate	error	opt	min	max	opt	min	max	opt	min	max	opt	min	max
1a	278.3	25.5	2000	0.47	0.14	0.74	0.27	0.94	0.54	0.13	0.73	0.56	0.16	0.76	-1.46	-1.68	-0.77
1b	282.5	24.3	1000	0.53	0.44	0.39	0.07	0.61	0.33	0.02	0.53	0.36	0.07	0.56	-1.27	-1.48	-0.71
2	269	21.5	1000	0.61	1.77	0.45	0.14	0.73	0.35	0.07	0.62	0.37	0.11	0.62	-1.25	-1.54	-0.76
3	272.1	18.2	1000	-0.03	0.47	0.1	-0.21	0.26	0.02	-0.26	0.17	0.05	-0.2	0.18	-0.9	-1.1	-0.43
4a	278.8	19.2	1000	0.4	0.06	0.81	0.3	1.02	0.69	0.22	0.9	0.67	0.25	0.88	-1.56	-1.83	-0.9
4b	282.2	18.2	3500	0.37	0.42	0.96	0.54	1.15	0.43	0.22	0.62	0.43	0.25	0.61	-1.31	-1.55	-0.92
5	288.8	18.2	6000	3.13	1.69	2.01	1.51	2.46	0.1	0.04	0.43	0.12	0.07	0.43	-1	-1.35	-0.79
6	295	18.2	1000	0.89	0.17	0.47	0.38	0.66	0.37	0.3	0.55	0.37	0.32	0.55	-1.26	-1.46	-1.03
7	299.4	15.2	1000	0.62	0.81	0.44	0.43	0.65	0.33	0.32	0.55	0.32	0.32	0.56	-1.17	-1.44	-1.1
8	279.2	10.9	3500	1.14	1.76	0.7	0.36	0.81	0.21	0.01	0.46	0.21	0.03	0.48	-0.99	-1.28	-0.72
9a	293.1	11.1	2000	0.38	0.27	0.24	0.09	0.48	-0.03	-0.16	0.25	-0.01	-0.14	0.28	-0.74	-1.05	-0.58
9b	298.6	10.8	3000	1.13	0.53	0.14	0.14	0.42	-0.15	-0.15	0.17	-0.12	-0.12	0.2	-0.62	-0.91	-0.61

Table E-2: List of relative and absolute sea-level rates for tide gauges spanning 1960-2012 and 1997-2012, satellite altimetry at tide gauge locations spanning 1992-2012 and 1997-2012. GPS station uplift rates presented for tide gauge-GPS station distance of less than 200 km for ULR5 (Santamaría-Gómez et al., 2012) and Hefl (Heflin, September 2013). Highlighted rows are tide gauges with length greater than 15 years and ending at or after 1997.

					Tide gauge (Relative sea level rate, mmyr^{-1})						Satellite Altimetry (Absolute sea level rate, mmyr^{-1})								GPS (Vertical Ground Motion, mmyr^{-1})											
					1960-present			1997-2012			1992-2012				1997-2012				Santa-Maria Gomez et al., (2012) ULR5						Heflin et al (jpl 2013)					
Tide Gauge	Country	Lon	Lat	End date	Span, years	Rate	σ	Rate	σ	% cmpt	Site rate	σ	Reg rate	σ	Site rate	σ	Reg rate	σ	Station	Lon	Lat	Span, years	Rate	Error	Station	Lon	Lat	Span, years	Rate	Error
Region A																													
Fort Myers	US	278.13	26.65	2012	46.67	2.37	0.27	1.48	1.5	0.91	0.79	1.29	1.07	0.89	1.67	1.86	1.16	1.29							MCD1	277.47	27.85	5.83	-0.82	0.71
Haulover Pier	US	279.88	25.9	1993	5.58	14.81	5.02				1.21	0.87	1.07	0.89	1.25	1.18	1.16	1.29	AOML	279.84	25.73	6.38	0.73	0.45	MIA3	279.84	25.73	11.04	-0.81	0.5
Key Colony Beach	US	278.98	24.72	1998	21.75	2.68	0.55	88.08	NaN	0.01	1.26	1.7	1.07	0.89	0.37	2.36	1.16	1.29	KYW1	278.35	24.58	10.46	-0.62	0.4	KYW1	278.35	24.58	10.78	-0.86	0.42
Key West	US	279	24.55	2012	51.96	2.53	0.2	1.67	0.89	0.99	1.05	1.03	1.07	0.89	0.78	1.41	1.16	1.29	KYW1	278.35	24.58	10.46	-0.62	0.4	KYW1	278.35	24.58	10.78	-0.86	0.42
Lake Worth Pier	US	279.97	26.62	1989	2.92	1.3	8.6				1.27	0.86	1.07	0.89	1.63	1.2	1.16	1.29	AOML	279.84	25.73	6.38	0.73	0.45	MIA3	279.84	25.73	11.04	-0.81	0.5
Marathon Shores	US	278.97	24.73	1975	8.75	1.29	1.51				1.26	1.7	1.07	0.89	0.37	2.36	1.16	1.29	KYW1	278.35	24.58	10.46	-0.62	0.4	KYW1	278.35	24.58	10.78	-0.86	0.42
Miami Beach	US	279.87	25.77	1981	21.46	1.22	0.62				1.21	0.87	1.07	0.89	1.25	1.18	1.16	1.29	AOML	279.84	25.73	6.38	0.73	0.45	MIA3	279.84	25.73	11.04	-0.81	0.5
Naples	US	278.2	26.13	2012	46.75	2.06	0.21	1.61	0.85	0.94	1.12	1.22	1.07	0.89	1.19	1.75	1.16	1.29	KYW1	278.35	24.58	10.46	-0.62	0.4	KYW1	278.35	24.58	10.78	-0.86	0.42
Palm Beach	US	279.95	26.7	1987	1.67	-1.61	19.09				1.27	0.86	1.07	0.89	1.63	1.2	1.16	1.29	AOML	279.84	25.73	6.38	0.73	0.45	MIA3	279.84	25.73	11.04	-0.81	0.5
Vaca Key	US	278.9	24.72	2012	24.92	2.83	0.37	2.14	0.81	0.93	1.26	1.7	1.07	0.89	0.37	2.36	1.16	1.29	KYW1	278.35	24.58	10.46	-0.62	0.4	KYW1	278.35	24.58	10.78	-0.86	0.42
Virginia Key	US	279.83	25.73	2012	17.83	1.25	0.6	0.96	1.06	0.98	1.21	0.87	1.07	0.89	1.25	1.18	1.16	1.29	AOML	279.84	25.73	6.38	0.73	0.45	MIA3	279.84	25.73	11.04	-0.81	0.5
Settlement Point	Ba	281.02	26.72	2002	15.83	1.29	1.26	-12.72	4.1	0.25	0.99	0.64	1.07	0.89	1.08	0.91	1.16	1.29	AOML	279.84	25.73	6.38	0.73	0.45	FREE	281.01	26.70	2.37	-1.16	3.16
Region B																													
Isabela de Sagua	Cu	279.98	22.93	2010	9.92	2.84	1.26	2.84	1.54	0.73	-0.02	0.87	0.63	0.93	-0.19	1.22	0.46	1.34												
Cabo Cruz	Cu	282.27	19.83	2010	9.92	2.06	1.14	2.06	1.38	0.67	0.15	0.66	0.63	0.93	-0.42	0.94	0.46	1.34							SCUB	284.24	20.01	13.45	-0.5	0.32
Cabo San Antonio	Cu	275.1	21.9	2010	38.25	3.13	0.35	1.8	2.33	0.7	0.31	1.01	0.63	0.93	0.11	1.4	0.46	1.34												
Casilda II	Cu	280.01	21.75	2012	28.92	1.55	0.41	1.5	7.38	0.3	0.28	0.65	0.63	0.93	-0.04	0.93	0.46	1.34												
Gibara	Cu	283.87	21.12	2010	35.5	1.1	0.28	0.6	1.31	0.98	0.2	0.59	0.63	0.93	-0.31	0.83	0.46	1.34	SCUB	284.24	20.01	10.97	-0.35	0.18	SCUB	284.24	20.01	13.45	-0.5	0.32
Guantanamo Bay	Cu	284.85	19.9	1972	11.96	0.21	1.34				0.07	0.94	0.63	0.93	0.72	1.36	0.46	1.34	SCUB	284.24	20.01	10.97	-0.35	0.18	SCUB	284.24	20.01	13.45	-0.5	0.32
Manzanillo	Cu	282.85	20.33	2010	5.92	-1.34	3.52	-1.34	4.59	0.41	0.15	0.66	0.63	0.93	-0.42	0.94	0.46	1.34	SCUB	284.24	20.01	10.97	-0.35	0.18	SCUB	284.24	20.01	13.45	-0.5	0.32
Progresso	Me	270.33	21.3	1991	30.96	4.71	0.63				1.95	0.63	0.63	0.93	2.14	0.9	0.46	1.34												
Port au Prince	Ha	287.65	18.57	1962	1.96	-21.41	14.71				-0.16	0.81	0.63	0.93	-0.78	1.15	0.46	1.34							JMEL	287.46	18.23	2.29	-2.2	2.41
Barahona	DR	288.92	18.2	1970	9.96	-1.68	2.14				0.13	0.77	0.63	0.93	-0.09	1.07	0.46	1.34							JMEL	287.46	18.23	2.29	-2.2	2.41
Puerto Plata	DR	289.3	19.82	1970	9.96	0.74	1.63				0.47	0.72	0.63	0.93	0.54	0.99	0.46	1.34							VOIL	287.69	18.53	2.33	-2.65	2.52
North Sound	CI	278.68	19.3	1997	20.92	1.42	0.8				0.2	0.77	0.63	0.93	-0.13	1.08	0.46	1.34	GCGT	278.62	19.29	5.55	-2.39	0.21						
South Sound	CI	278.62	19.27	1997	20.75	1.46	0.91				0.2	0.77	0.63	0.93	-0.13	1.08	0.46	1.34	GCGT	278.62	19.29	5.55	-2.39	0.21						
Port Royal	Ja	283.15	17.93	1970	9.96	-5.24	2.6				-0.35	1.02	0.63	0.93	-0.2	1.41	0.46	1.34												

					Tide gauge (Relative sea level rate, mmyr^{-1})						Satellite Altimetry (Absolute sea level rate, mmyr^{-1})								GPS (Vertical Ground Motion, mmyr^{-1})											
					1960-present			1997-2012			1992-2012				1997-2012				Santa-Maria Gomez et al., (2012) ULR5						Heflin et al (jpl 2013)					
Tide Gauge	Country	Lon	Lat	End date	Span, years	Rate	σ	Rate	σ	% cmpt	Site rate	σ	Reg rate	σ	Site rate	σ	Reg rate	σ	Station	Lon	Lat	Span, years	Rate	Error	Station	Lon	Lat	Span, years	Rate	Error
Region C																														
Aguadilla	PR	292.83	18.46	2012	5.42	-1.04	1.97	-1.04	2.96	0.32	1.54	0.7	2.43	0.7	1.49	1.02	2.38	0.99	ZSU1	294.01	18.43	7.16	-1.21	0.52	MAYZ	292.84	18.22	3.56	-1.18	1.41
Culebra	PR	294.7	18.3	2012	6.25	2.97	1.5	2.97	1.91	0.38	1.14	0.79	2.43	0.7	1.63	1.05	2.38	0.99	VITH	295.03	18.34	4.36	0.01	0.43	CRO1	295.42	17.76	17.88	-1.28	0.51
Magueyes Island	PR	292.95	17.97	2012	51.96	1.27	0.1	2.52	0.67	0.98	1.54	0.7	2.43	0.7	1.49	1.02	2.38	0.99	ZSU1	294.01	18.43	7.16	-1.21	0.52	MAYZ	292.84	18.22	3.56	-1.18	1.41
Mona Island	PR	292.06	18.09	2012	5.17	-4.14	2.84	-4.14	3.94	0.24	1.54	0.7	2.43	0.7	1.49	1.02	2.38	0.99							MOPR	292.07	18.08	2.69	-2.66	2.36
San Juan	PR	293.88	18.47	2012	49.58	1.63	0.13	2.09	0.71	0.97	1.38	0.68	2.43	0.7	1.53	0.94	2.38	0.99	ZSU1	294.01	18.43	7.16	-1.21	0.52	BYSP	293.84	18.41	5.32	-1.13	0.73
Charlotte Amalie	VI	295.08	18.33	2012	36.83	1.35	0.14	2.43	0.58	0.93	1.37	0.66	2.43	0.7	1.58	0.91	2.38	0.99	VITH	295.03	18.34	4.36	0.01	0.43	CRO1	295.42	17.76	17.88	-1.28	0.51
Christiansted Harbour	VI	295.3	17.75	2012	5.75	1.8	2.98	1.8	3.86	0.35	1.37	0.66	2.43	0.7	1.58	0.91	2.38	0.99	VIKH	295.2	17.72	4.34	0.52	0.6	CRO1	295.42	17.76	17.88	-1.28	0.51
Lameshur Bay	VI	295.28	18.32	2012	5.25	1.79	1.28	1.79	1.72	0.33	1.37	0.66	2.43	0.7	1.58	0.91	2.38	0.99	VITH	295.03	18.34	4.36	0.01	0.43	CRO1	295.42	17.76	17.88	-1.28	0.51
Lime Tree Bay	VI	295.25	17.7	2012	34.08	2	0.19	2.26	0.83	0.98	1.37	0.66	2.43	0.7	1.58	0.91	2.38	0.99	VIKH	295.2	17.72	4.34	0.52	0.6	CRO1	295.42	17.76	17.88	-1.28	0.51
Pointe a Pitre	Gu	298.47	16.23	2012	20.92	0.75	0.6	1.49	1.29	0.44	1.77	0.62	2.43	0.7	1.37	0.87	2.38	0.99							ABMF	298.47	16.26	3.68	1.06	1.46
Forte de France	Ma	298.95	14.58	2012	6.08	12.59	3.94	12.59	4.56	0.38	1.99	0.6	2.43	0.7	1.71	0.85	2.38	0.99							LMMF	299.00	14.59	3.68	-2.41	1.22
Region D																														
Port of Spain	TT	298.48	10.65	1993	9.83	0.56	1.7				3.19	0.64	2.66	0.67	3.26	0.87	2.77	0.96												
Guiria	Ve	297.72	10.57	1968	5.42	0.84	3.91				3.09	0.59	2.66	0.67	3.25	0.86	2.77	0.96												
Puerto de Hierro	Ve	297.92	10.62	1964	3.54	-4.12	5.94				3.09	0.59	2.66	0.67	3.25	0.86	2.77	0.96												
Cartagena	Co	284.47	10.38	1993	32.96	5.54	0.59				2.58	0.72	2.66	0.67	2.4	1.08	2.77	0.96	CART	284.47	10.39	8.54	-2.18	0.54						
Riohacha	Co	287.08	11.55	1970	9.96	7.76	2.46				2.47	0.74	2.66	0.67	2.8	1.13	2.77	0.96												
Coco Solo	Pa	280.12	9.37	1996	5.33	-19.58	4.12				2.23	0.65	2.66	0.67	2.48	0.89	2.77	0.96												
Cristobal	Pa	280.08	9.35	1981	20.63	3.42	0.55				2.23	0.65	2.66	0.67	2.48	0.89	2.77	0.96												
Panama*		280.1	9.36	1996	36.38	2.91	0.26				2.23	0.65	2.66	0.67	2.48	0.89	2.77	0.96												
Puerto Limon	CR	276.97	10	1969	8.96	1.59	2.31				-0.23	0.7	2.66	0.67	0	1.03	2.77	0.96												
Santo Tomas Castillo	Gu	271.38	15.7	1984	19.92	-1.73	0.8						2.66	0.67			2.77	0.96							ELEN	270.13	16.92	11.73	1.86	0.57
Puerto Castilla	Ho	273.97	16.02	1969	8.96	2.34	1.46				1.76	0.82	2.66	0.67	1.59	1.28	2.77	0.96												
Puerto Cortes	Ho	272.05	15.83	1969	8.96	3.4	1.71				1.86	0.79	2.66	0.67	1.7	1.21	2.77	0.96							ELEN	270.13	16.92	11.73	1.86	0.57

* Panama is a combination of tide gauges, Cristobal and Coco Sol which have similar locations (see Chapter 2)

Appendix F

Relative sea-level projection: 2012-2100

Figure F-1 shows the projected RSL rise at all tide gauge locations in the Caribbean (2012 to 2100), with their associated errors. The colour scale shows the RSL rises are mainly positive, and in the range 20 to 60 cm. The average RSL rise (ranges in parenthesis) for the tide gauge locations shown is 29 ± 28cm (-163 to 151 cm), 35 ± 14 cm (25 to 55 cm) and 40 ± 16 cm (14 to 56 cm) for the Altimetry-TG, GPS: ULR5 and GPS: Hefl respectively. The method of projection is detailed in Chapter 6.

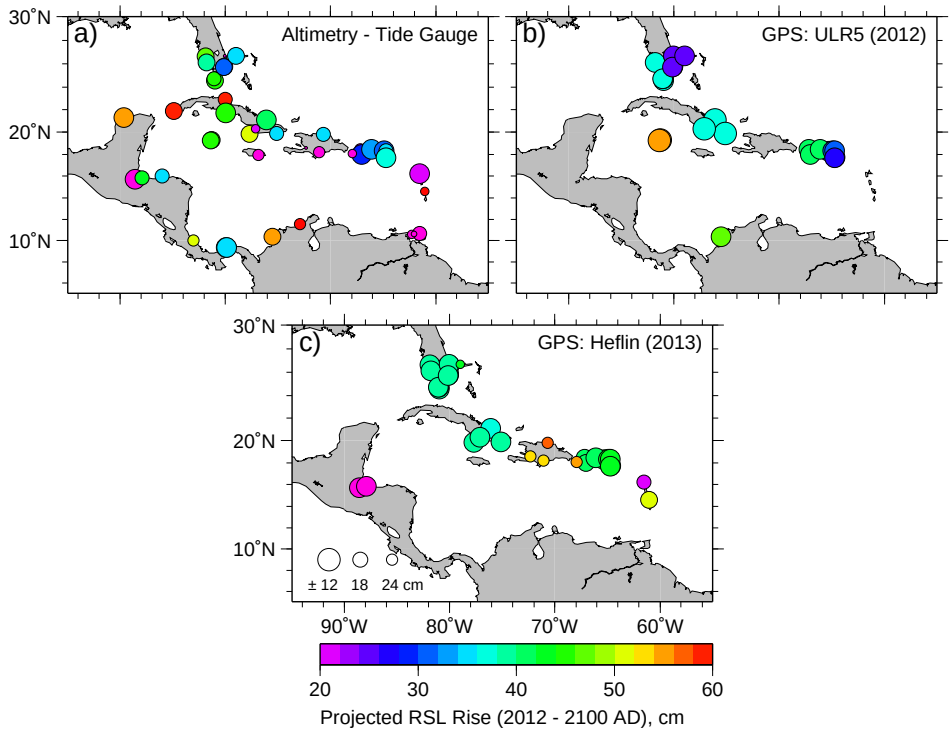

Figure F-1: Projected relative sea-level rise by 2100 using vertical ground motion estimates and IPCC2007 ASL rise estimates from 1980-1999 to 2090-2099. Vertical ground motion estimates using **a**: Altimetry - Tide Gauge, **b**: GPS ULR5 (Santamaría-Gómez et al., 2012) and **c**: GPS Hefl (Heflin, September 2013). Size of circle corresponds to error in projection.